The University of Nottingham
UNITED KINGDOM · CHINA · MALAYSIA

Lacinska, Alicja M (2016) Mineralogical and Experimental Study of Serpentine Minerals and Ultramafic Rocks with Application to Carbon Capture and Storage by Mineralisation. PhD thesis, University of Nottingham.

Access from the University of Nottingham repository:
http://eprints.nottingham.ac.uk/32938/3/Front%20Page.pdf

Copyright and reuse:

The Nottingham ePrints service makes this work by researchers of the University of Nottingham available open access under the following conditions.

- Copyright and all moral rights to the version of the paper presented here belong to the individual author(s) and/or other copyright owners.
- To the extent reasonable and practicable the material made available in Nottingham ePrints has been checked for eligibility before being made available.
- Copies of full items can be used for personal research or study, educational, or not-for-profit purposes without prior permission or charge provided that the authors, title and full bibliographic details are credited, a hyperlink and/or URL is given for the original metadata page and the content is not changed in any way.
- Quotations or similar reproductions must be sufficiently acknowledged.

Please see our full end user licence at:
http://eprints.nottingham.ac.uk/end_user_agreement.pdf

A note on versions:

The version presented here may differ from the published version or from the version of record. If you wish to cite this item you are advised to consult the publisher's version. Please see the repository url above for details on accessing the published version and note that access may require a subscription.

For more information, please contact eprints@nottingham.ac.uk



Mineralogical and Experimental Study of Serpentine Minerals and Ultramafic Rocks with Application to Carbon Capture and Storage by Mineralisation.

By

Alicja Lacinska, MSc

Thesis submitted to the University of Nottingham
for the degree of Doctor of Philosophy

2016

Abstract

The type of feedstock and host rock utilised in *ex situ* and *in situ* Carbon Capture and Storage by Mineralisation (CCSM) is an important aspect of these technologies, and detailed appraisal of candidate mineral/rock performance in the presence of CO_2 may greatly improve CCSM efficiency. Here, a detailed mineralogical and geochemical investigation of serpentine minerals and ultramafic rocks under laboratory-controlled experiments simulating *ex situ* and *in situ* process conditions is presented.

Feedstock serpentine minerals were analysed comprehensively, prior to experimental processing. The identification of antigorite was unequivocal using a combination of X-ray diffraction, Fourier Transform Infrared Spectroscopy and/or Thermo-gravimetric Analysis. However, the analysis of chrysotile and lizardite proved to be more challenging, especially when the two polymorphs were finely inter-grown. This study highlighted the structural, textural and chemical complexity of serpentines and showed that great care must be taken when analysing this mineral group for CCSM.

Investigation of the acid leaching of ***serpentine minerals*** under conditions of 70°C and 1.4M NH_4HSO_4 provided fundamental insights into the rate and extraction efficiency (EE) of Mg^{2+} and associated controlling factors, under conditions relevant for *ex situ* CCSM. It is demonstrated that EE is a function of mineral reactivity and depend on a complex interplay between crystal structure and chemistry. Generally, poorly crystalline and highly disordered phases with low levels of Al^{3+} were found to be suitable feedstock materials for acid digestion pre-treatment. Chrysotile, lizardite $2H_1$ and poorly crystalline serpentines showed up to 85% Mg^{2+} EE after 3 h of acid leaching, and hence are recommended as best feedstock materials for CCSM, whilst

antigorite and Al^{3+}-rich serpentines proved to be largely unsuitable, showing low levels of EE of ~ 20%.

Examination of ***dunite***, ***harzburgite*** and ***serpentinite*** under conditions relevant for *in situ* CCSM, *i.e.* 70°C and 100 bar CO_2 pressure, provided insights into rock reactivity as a function of composition and texture, and the progression of *in situ* mineral carbonation. The rate of net Mg release and thus the extent of subsequent carbonation were greatest for serpentinite, providing *ca.* 3% carbonation after six months. However, mineral reactivity within serpentinite was preferential, *i.e.* significantly enhanced within secondary vein serpentine, being thus, the main source of Mg^{2+} for magnesite precipitation. Reaction-induced transformation and hence mineral carbonation of dunite and harzburgite were less pronounced over the same time-scale. The reaction of serpentinite with wet supercritical CO_2, as opposed to CO_2-saturated brine, significantly affected rock integrity, with the exposure of more surface area and promotion of fluid-rock interaction. In particular, it is shown that ferric iron oxidation and the precipitation of goethite impacts upon surface mineral dissolution at exposed surfaces, thereby hindering subsequent carbonation. Overall, this study highlighted the importance of host rock choice for *in situ* CCSM and the need for detailed petrographical and geochemical investigation of any proposed CCSM repository prior to technological process modelling.

Table of Contents

Abstract	i
Table of Contents	iii
Acknowledgements	vi
CHAPTER 1 INTRODUCTION	1
CHAPTER 2 LITERATURE REVIEW	6
2.1 Overview of fundamental concepts and process routes of mineral carbonation	6
2.1.1 *Ex situ* CCSM	9
2.1.1.1 Direct *ex situ* CCSM	9
2.1.1.2 Indirect *ex situ* CCSM	11
2.1.2 *In situ* CCSM	12
2.2. Underpinning chemistry	15
2.2.1. Mineral dissolution	16
2.2.2. Metal-oxygen bonding in multi-oxide minerals	18
2.2.3. Rate of dissolution and reactive surface area	19
2.2.4. Saturation Index and Chemical Affinity	20
2.2.5. Reaction pathways in sheet silicates	20
2.2.6. Carbonate diversity in MgO-CO_2-H_2O system	21
2.2.7. Stability of Mg-carbonates	24
2.3. Feedstock and reservoir rocks	29
2.3.1. Serpentine minerals	29
2.3.2. Classification of ultramafic rocks in the context of CCSM	42
2.4 Summary	47
CHAPTER 3 MINERALOGICAL AND GEOCHEMICAL CHARACTERISATION OF SERPENTINE MINERALS FOR CCSM	50
3.1 Introduction	50
3.2 Materials	51
3.2.1 A brief description of the geological setting for samples collected at Lizard Peninsula and Montecastelli Pisano	52
3.2.2 Summary of nine samples used – mode of occurrence and hand specimen description	60
3.3 Methods	63
3.4 Results and discussion	63
3.4.1 Optical Microscopy	64
3.4.2 X-ray Diffraction	68

3.4.3 Scanning Electron Microscopy, including quantitative EDS 78
3.4.4 Transmission Electron Microscopy 84
3.4.5 X-ray Fluorescence 88
3.4.6 Fourier Transform Infrared Analysis 89
3.4.7 Thermogravimetric Analysis 94
3.5. Summary 101

CHAPTER 4 ACID EXTRACTION OF Mg^{2+} FROM SERPENTINE MINERALS IN THE CONTEXT OF CCSM

4.1. Introduction 105
4.2. Materials and Methods 108
4.2.1. Materials 106
4.2.2. Methods 116
4.3. Results 121
4.3.1 Leachate chemistry 121
4.3.2 Mineralogy of solid reaction residues 140
4.4 Discussion 179
4.4.1 Reaction rates and chemical affinity 179
4.4.2 The effect of rock texture 180
4.4.3 The effect of particle size and surface area 191
4.4.4 The effect of mineral chemistry 194
4.4.5 The effect of mineral structure 197
4.4.6 Comparison with other studies using ammonium bisulphate 203
4.5 Summary 206

CHAPTER 5 DISSOLUTION AND CARBONATION OF ULTRAMAFIC ROCKS AND SERPENTINITE AT CONDITIONS RELEVANT FOR *IN SITU* CO_2 SEQUESTRATION

5.1 Introduction 212
5.2 Materials and methods 214
5.2.1. Materials 214
5.2.2. Methods 224
5.3. Results 225
5.3.1. Leachate chemistry 225
5.3.2. Mineralogy and geochemistry of solid residues 255
5.4. Discussion 286
5.4.1. The extent of rock dissolution as a function of its composition and texture 286
5.4.2. Secondary mineralisation 291
5.4.3. Quantification of CO_2 captured in magnesite formed in the serpentinite sample 297
5.4.4. The reactivity of CO_2-saturated brine *versus* wet supercritical CO_2 300

5.4.5. Carbonate recycling and implications for long term system stability 304
5.4.6. Reaction driven cracking 308
5.5. Summary 309
CHAPTER 6 SYNTHESIS AND CONCLUSIONS 313

APPENDICES

APPENDIX A. Methodology and Analytical Techniques 320
APPENDIX B. Precision and Accuracy of SEM-EDS Analysis 345
APPENDIX C. Precision and Accuracy of ICP-AES Analysis 352
APPENDIX D. ICP-AES and XRF analytical data 354
APPENDIX E. Repeatability of short-term acid-leaching experiment 364

REFERENCES 368

Acknowledgements

First and foremost, I would like to express my special appreciation and gratitude to my three primary supervisors: Prof. Paul Brown, University of Nottingham (UoN); Dr Michael Styles, British Geological Survey (BGS) and Dr Matthew Hall (UoN), you all have been a remarkable support and inspiration. Thank you for our fascinating discussions; your great attitude, guidance and encouragement at every stage of my research. These past three years have been truly a memorable experience that has enriched me, both on a scientific and personal level.

I would also like to acknowledge Dr Jonathan Naden, Simon Kemp (BGS) and Professor Mercedes Maroto-Valer (University of Herriot Watt) for their advice and support.

My special thanks go to Keith Bateman, Dr Christopher Rochelle, Gemma Purser, Dr Jörgen Rosenqvist and Lauren Selby for providing me with the laboratory equipment at BGS; for their guidance and assistance in setting up and maintaining my hydrothermal experiments. Your help has been tremendous and it is my hope to collaborate with your team in the future. Dr Andrew Kilpatrick is thanked for making the PHREEQC modelling less daunting than originally "predicted".

Dr Jeremy Rushton, Doris Wagner, Gren Turner and Dr Barry Rawlins, all from BGS, are greatly appreciated for their assistance with undertaking SEM, XRD, BET, TGA and PSD analyses. Jon Fletcher and Phil Neep, also from BGS, are thanked for the preparation of thin sections. It was a great pleasure to work with you all and I'm looking forward to re-joining our team at BGS.

Dr Nigel Neate and Dr Martin Roe, from the Advanced Materials Group and Dr Michael Fay from the Nottingham Nanoscience and Nanotechnology Centre, (UoN) are thanked for their help and expertise in using TEM.

Dr Michael Watts, Dr Charles Gowing, Ian Mountaney (BGS) and Dr Mark Ingham, Neil Eatherington (PANanalytical Ltd.) are thanked for providing financial support for the ICP-AES and XRF analyses.

The financial support from BGS, UoN and Caterpillar Inc. is greatly appreciated. The BGS management, in particular, Dee Flight and Jeremy Rushton are thanked for their encouragement, support and for approving my three years career break.

Most importantly, none of this would have been possible without the love and patience of ***my immediate Family to whom this Thesis is dedicated to.*** You have been a constant source of support and strength throughout my life, especially in the past few years, thank you for everything.

Chapter 1 Introduction

Anthropogenic gas emissions have increased since the pre-industrial era, driven largely by economic and population growth. This has led to atmospheric concentrations of carbon dioxide, methane and nitrous oxide that are unprecedented over the past 800,000 years [*Field et al.*, 2014] (Figure 1.1). A recent Intergovernmental Panel on Climate Change (IPCC) report stated that human influence on the climate system is clear [*Field et al.*, 2014] and related to CO_2 release as a by-product of burning fossil fuels.

The latest direct measurement of atmospheric CO_2 at the Mauna Loa Earth System Research Laboratory returned a value of 400 ppm (November 2014 [*Tans and Keeling*, 2014]) being ~ 40% higher than 280 ppm during pre-industrial times (Figure 1.1). In 2013, the global CO_2 emission due to fossil fuel use (and cement production) was estimated at 36 Gt, being 60% higher than in 1990, with the main contributors being China (28%), USA (14%), EU (10%) and India (7%) [*CO_2Now.org*].

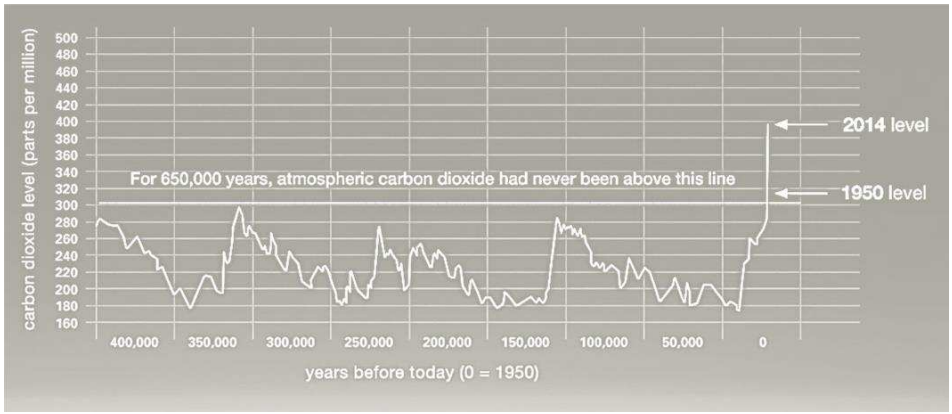


Figure 1.1 Comparison of atmospheric CO_2 levels from ice cores and more recent direct measurements (www.climate.nasa.gov; Vostok ice core data [Petit et al., 1997]; and the NOAA Mauna Loa CO_2 record). Regular cycles over the past 650 000 years represent glacial advance and retreat, with last abrupt end of the ice age about 7000 years ago.

The high emissions have augmented the natural greenhouse effect, causing perturbations in the Earth's climate leading to modifications of both terrestrial and marine ecosystems. Globally averaged, combined land and ocean surface temperature data, collated from multiple datasets over the period 1880 to 2012, show presently a warming of 0.85°C [*Field et al.*, 2014]. It is anticipated that an increase of 4°C or more above pre-industrial levels will impact very strongly, with consequences for global food security and the extinction of many species, *etc.* (*idem*.*)*

Various actions have been proposed to mitigate the effects of greenhouse gases. For example, the UK aims to reduce CO_2 emissions by 80% by 2050, with the government seeking to reduce emissions from the power sector through the promotion of alternative renewable energy sources; whilst investing £200 million for innovation in low-carbon technologies during 2011-2015 and creating industry for carbon capture and storage (www.gov.co.uk).

Carbon capture and storage (CCS), in addition to technologies aimed at reflecting the Sun's energy, is classified as geoengineering, *i.e.* a deliberate intervention in the planetary environment intended to counteract man-made climate change and/or its impacts (www.gov.co.uk). The term covers "conventional" underground CCS in saline aquifers or depleted carbon reservoirs, and CCS by mineralization (CCSM) of ultramafic rocks/serpentinites or wastes. Currently, "conventional" CCS constitutes the most developed technology for large-scale sequestration. Globally, there are 13 large-scale CCS projects in operation, with a further nine under construction. For example, the Sleipner Project in the central part of the North Sea (offshore Norway) is the world's first demonstration of CCS technology into a deep saline reservoir and the only development where CO_2 is both captured and injected offshore. It provides an injection rate of ~ 1 Mtpa making it one of the largest demonstrations of CCS in the world to date [*Global et al.*, 2014]. In the UK, two bids in the Carbon Capture and Storage Commercialization Programme Competition, both offering ~ 90% capture, have been shortlisted: the White Rose, a coal-fired power plant with full CCS

technology; and Peterhead, an existing combined cycle gas turbine power station, with capture of CO_2, offshore transportation and storage in a depleted gas field beneath the North Sea (www.gov.co.uk).

The present study, however, focuses on the alternative way of CO_2 sequestration, *i.e.* Carbon Capture and Storage by Mineralisation (CCSM), otherwise termed Mineral Carbonation. CCSM is a method for the chemical or "crystallographic" capture of CO_2 in newly formed carbonate minerals, and provides for long-term integrity of CO_2 and safe sequestration. Studies on CCSM to date have received considerable interest from research organizations and industry, especially now that mitigation of the effects of greenhouse gases has become an obligation for major fossil fuel suppliers and developed countries. Although CCSM constitutes a promising technology, it has yet to be implemented on an industrial scale, with barriers to large-scale deployment including concerns about process and operational technology costs.

CCSM technologies encompass the sequestration of CO_2 using externally derived feedstock material, termed *ex situ* CCSM, and the injection of CO_2 into underground reservoirs suitable for efficient chemical reaction and permanent crystallographic sequestration, termed *in situ* CCSM. The type of feedstock (*ex situ*) or host rock (*in situ*) utilised is one vital aspect of the evaluation of mineral carbonation technology, and detailed appraisal of candidate mineral performance in the presence of CO_2 may greatly improve CCSM technology efficiency. Despite a broad spectrum of research initiatives into CCSM to date [*Kelemen and Matter*, 2008; *Lackner*, 2002; *Oelkers et al.*, 2008; *Park and Fan*, 2004; *Paukert et al.*, 2012; *Power et al.*, 2013; *Zevenhoven et al.*, 2008 and references therein], many outstanding questions remain and improved understanding of the functional performance of candidate minerals under conditions relevant for CCSM is required in order to model effectively these processes, and thereby inform industry and policy makers on the viability of this technology.

The present study was initiated, following a three year project run by the Energy Technology Institute (ETI) on the feasibility of CCSM in the UK [*Sanna et al.*, 2014;

Sanna et al., 2013; *Styles et al.*, 2014], in collaboration with the British Geological Survey (BGS), Nottingham University, Caterpillar, Centre for Process Initiation CPI and Shell Global Solutions. The ETI study showed that significant problems and uncertainties regarding identification of serpentine minerals and their reactivity exist in the current literature. Thus, the mineralogy and geochemistry of a variety of feedstock and reservoir materials, *i.e.* serpentinites and ultramafic rocks were appraised under conditions approximating to industrial *ex situ* and *in situ* CCSM. In this context, two sets of well-defined, laboratory-controlled experiments were performed, to provide the data that constitutes this thesis.

The thesis has been organised into seven chapters. Chapter 1 introduces CCSM in the wider context of climate change and presents the objectives and the organisation of the thesis. Chapter 2 provides a review of relevant literature, whilst chapter 3 presents data on a detailed mineralogical and geochemical study of starting serpentine minerals, as feedstock material for *ex situ* CCSM, whilst Chapter 4 presents the results of an experimental study of *ex situ* CCSM using these serpentine minerals. In Chapter 5, dunite, harzburgite and serpentinite reservoir materials are investigated under conditions relevant for *in situ* CCSM. Chapter 6 presents the synthesis and conclusion of this thesis whilst prospect for future research are outlined in Section 6.1.

PhD Objectives

1.1. To investigate the mineralogical and geochemical factors that affect the reactivity of serpentine minerals under conditions relevant for *ex situ* CCSM; to be accomplished through investigation of:

- The chemistry and structure of serpentine minerals
- The reactivity of serpentine minerals during acid leaching at 70°C and the determination of extraction efficiency (EE) of Mg^{2+}
- The chemical, structural and textural changes in the remnants of original minerals

1.2. To investigate mineral carbonation in dunite, harzburgite and serpentinite under conditions relevant for the *in situ* injection of CO_2 into a reservoir at ~ 1 km depth, through study of:

- The reactivity of three host rocks, in terms of the degree and rate of carbonation under conditions of 70°C and 100 bar CO_2 pressure
- The factors driving rock reactivity
- The rock texture transformations: rock integrity, reaction driven cracking and distribution of carbonation

Chapter 2 Literature Review

2.1. Overview of fundamental concepts and process routes for mineral carbonation

Carbon capture and storage by mineralisation (CCSM), otherwise termed mineral carbonation or carbon mineralisation, is a proposed method to mitigate the excess of anthropogenic CO_2 in the atmosphere. As suggested by Seifritz [*Seifritz*, 1990]

> *'…it would be advantageous if there were an abundant mineral to which the CO_2 could be bound chemically via an exothermic reaction to form stable, permanent substance…'*

Reaction of CO_2 with divalent metal-rich resource material results in the formation of carbonate minerals, providing for the long-term, secure sequestration of CO_2. The carbonation reaction is exothermic and the amount of heat released depends on the resource material, *i.e.* for serpentine it is 64 kJ/mol CO_2, whereas for olivine it is 89 kJ/mol CO_2 [*Metz et al.*, 2005] Briefly:

$$\text{Metal oxide} + CO_2 \leftrightarrow \text{Metal carbonate} + \text{heat}$$

Carbonation is thus, spontaneous in nature; and carbonate minerals are thermodynamically more stable than isolated CO_2 and silicate minerals. There have been numerous investigations of field exposures of carbonated Mg-rich silicate rocks that constitute natural analogues for CCSM [*Boschi et al.*, 2009; *Lacinska et al.*, 2014; *J. M. Matter and Kelemen*, 2009; *O'Neil and Barnes*, 1971; *Power et al.*, 2009; *Stephen et al.*, 2013]. These studies have allowed improved understanding of natural CCSM reaction processes to be developed, with reference to substrates, reaction

products, kinetics and thermodynamics, scale of reaction; and shed light on the process control factors required to mitigate anthropogenic CO_2 in a laboratory scenario and on an industrial scale.

Several comprehensive overviews have been published in recent years [*Huijgen and Comans*, 2003a; *Lackner*, 2002; *Metz et al.*, 2005; *Olajire*, 2013; *A. Sanna et al.*, 2014; *Sipila et al.*, 2008], concluding that CCSM is a viable alternative to conventional CCS and provides for permanent sequestration over geological time-scales. However, as reported by the Intergovernmental Panel on Climate Change [IPCC, *Metz et al.*, 2005] *"…the current maturity of CCSM is still mostly at a research stage… and… significant technological breakthroughs will be needed before deployment can be considered…".*

The major drawback of CCSM technologies is the slow speeds of reaction, and although thermodynamically favourable, the reaction kinetics must be accelerated significantly to achieve economic viability.

Industrial CCSM includes processes associated with feedstock extraction (e.g. quarrying), pre-treatment and carbonation of the cation-charged solution to form solid carbonates. Three main types of pre-treatment are distinguished: mechanical (grinding), chemical (e.g. acid leaching) and thermal (heating in order to destroy and activate mineral crystal structure); all that can be used separately or combined to allow for the most efficient cation extraction.

The kinetics of silicate dissolution are, in most cases, slower than subsequent metal carbonation and hence rate limiting for CSSM [*Oelkers et al.*, 2008 and references therein]. The rate of cation release during dissolution can be enhanced by using chemical additives, and/or pulverisation and heating of the feedstock material (*e.g.* during pre-treatment), but these steps introduce a high energy penalty. By way of example, in ammonia based processes (also investigated during this study), NH_4 may

be used as an effective CO_2 capture medium and dissolution additive, but its recyclability is energy intensive, requiring 1300 kWh/t CO_2 sequestered [*Aimaro Sanna et al.*, 2013]; although it is noted that some costs could be reduced potentially by avoiding CO_2 separation and using flue gas directly [*Pasquier et al.*, 2014; *Werner et al.*, 2011; *Zevenhoven et al.*, 2013].

In practical terms, the viability of CCSM depends on the development of technologies that will (a) provide for fast reaction kinetics, (b) result in near-neutral costs and (c) impart low environmental impacts.

CCSM technologies can be categorised as: *in situ* CCSM - injection of CO_2 into deep underground reservoirs; or *ex situ* CCSM - carbonation above ground in a purposely built chemical/carbonation processing plant (Figure 2.1).

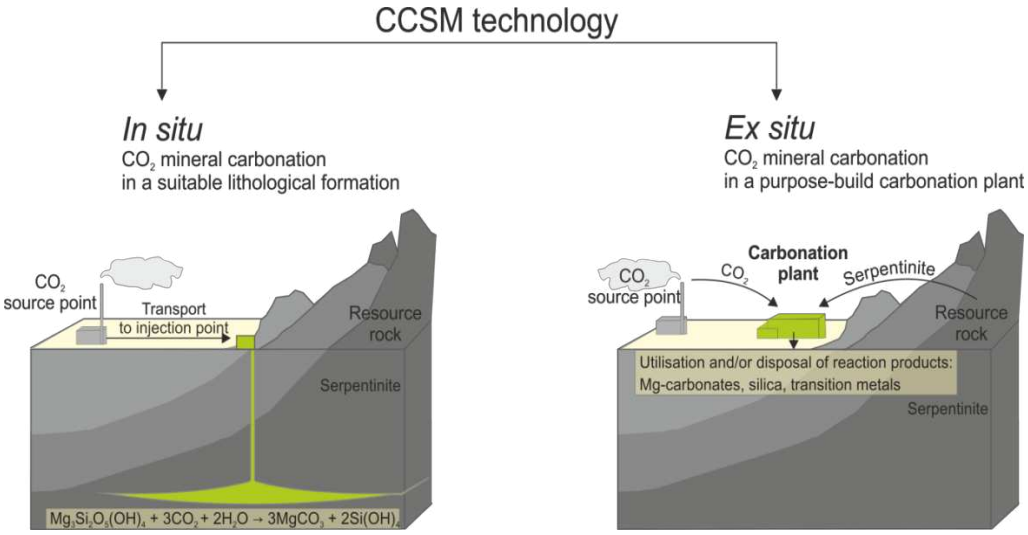


Figure 2.1 CCSM technologies using serpentinite as (left) reservoir or (right) feedstock material.

The following Sections give an overview of *ex situ* and *in situ* CCSM with examples of laboratory and field investigations. The underpinning chemistry is then presented, with a focus on mineral dissolution, reaction pathways in sheet silicates, stability of serpentine minerals and a diversity of carbonate minerals in $MgO\text{-}CO_2\text{-}H_2O$ system, focusing on their stability. The feedstock minerals and host rocks are then described with emphasis on crystal structure and chemistry of serpentine minerals and classification of ultramafic rocks in the context of CCSM, respectively.

2.1.1. *Ex situ* CCSM

Ex situ CCSM involves the carbonation of an externally supplied metal-rich resource material: *i.e.* mineral, rock or suitable industrial waste. The processes take place in a purpose-built carbonation plant. *Ex situ* CCSM processes can be categorised as being either direct (direct carbonation) or indirect (carbonation after metal ion release), following either a gas-solid or aqueous route (Figure 2.2).

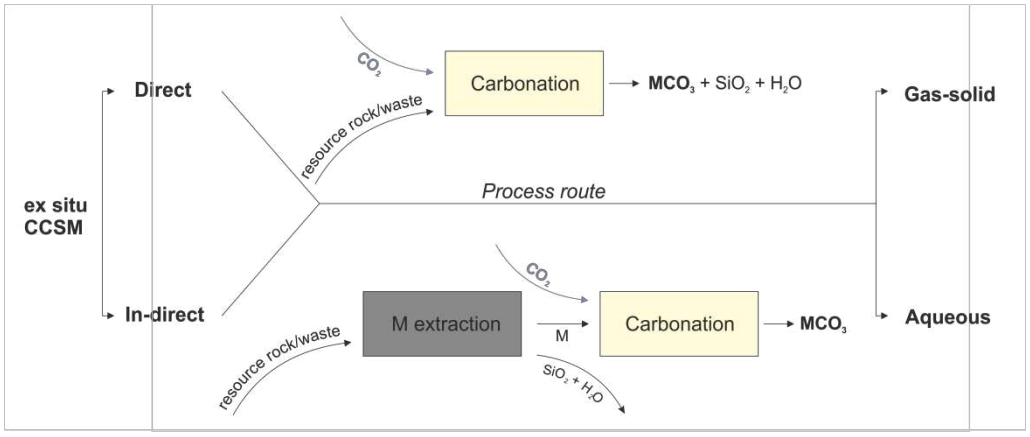


Figure 2.2 Overview of ex situ CCSM direct and indirect processing routes (M = metal (Mg, Ca, Fe)).

2.1.1.1. Direct *ex situ* CCSM

Direct *ex situ* gas–solid CCSM involves a direct reaction of flue gas or separated CO_2 with the feedstock material in one carbonation reactor. Its major advantage is simplicity, with lower energy input and lack of multi-step reactions as required for aqueous CCSM [*Huijgen and Comans*, 2003b]. Several studies have shown the key reactions to be too slow for practical applications, however, Huijgen *et al.* [*Huijgen and Comans*, 2003b] suggest that utilisation of supercritical CO_2 may present a more viable solution.

Direct *ex situ* aqueous route is also performed in one reactor but it consists of three coexisting aqueous mechanisms: a) dissolution of CO_2, b) cation leaching through material dissolution, and c) precipitation of carbonate [*Olajire*, 2013]. To enhance reaction rates studies have focused on using reaction catalysts instead of pure H_2O, as well as enhancing pressure and temperature conditions.

Table 2.1 Examples of direct solid-gas and aqueous processes relevant for CCSM.

Substrate	Product	Process conditions	Reaction (carbonation or *dissolution) Efficiency	Reference
		Direct gas-solid		
Brucite, CO_2	Magnesite	375°C, P~ 0.765 atm, CO_2 flow 50 cm^3/min	**16.7 wt%** in 12h	[*Butt et al.*, 1996]
Serpentinite	Mg -carbonate	140-300°C, 340 bar	**30%**	[*Lackner et al.*, 1997]
Brucite, CO_2	Magnesite and MgO	585°C, pCO_2 (1.4 – 183.8 atm), max carbonation at pCO_2 = 27.2 atm	Maximum carbonation **26.1 wt%** (16h), at this point magnesite coexists with 55.3 wt% MgO and 18.6 wt% of brucite	[*Bearat et al.*, 2002]
Thermally activated chrysotile	Magnesite	100-200°C, 3.2 MPa CO_2	negligible	[*F. Larachi et al.*, 2012]
		130°C, 0.1 MPa steam/ 3.1MPa CO_2	**70%** (0.7 CO_2 moles/ 1M Mg)	
Thermally activated serpentine	Nesquehonite	30, 50, 60, 90°C, pCO_2 0.1 bar and 1 bar, stiring rate 600 rpm	Max **20%**	[*Werner et al.*, 2013]

		Direct aqueous		
Thermally activated serpentine, olivine, wollastonite		185°C, 150 atm CO_2, NaCl+$NaHCO_3$ solution	Max carbonation: serpentine ~**60%** 6h, olivine ~ **85%** 6h, wollastonite ~**75%** 1h, not treated serpentine ~**3%** 1H	[*Gerdemann et al.*, 2007]
Antigorite	NA, focus on *dissolution	120°C, 20 bars CO_2, NaCl, NH4Cl, sodium citrate, sodium oxalate, sodium EDTA or sodium acetate. 6-24 h	Organic salts significantly enhance *dissolution: **60%** - 2 h**, 80%** - 7 h and near **100%** 10-20 h.	[*Samuel C. Krevor and Lackner*, 2009]
Olivine-Forsterite	Hydrated/hydrohylated Mg-carbonate and silica, magnesite, SiO_2	80°C, 76 bar, 20 h CO_2-saturated aqueous fluid and H_2O-saturated supercritical CO_2	NA. Effect of H_2O on carbonation investigated. For a given fluid/ mineral ratio there is a H_2O threshold above which a significant portion of the H_2O serves as a catalyst, unlocking carbonation reaction.	[*Kwak et al.*, 2011]
Thermally activated chrysotile		100°C, pCO_2 0.5-4 MPa, alkaline solution, 0.5M $NaHCO_3$, 1 h	**57%** at 3MPa	[*Ryu et al.*, 2011]
Gypsum	Calcite and vaterite	T_{room}, P_{atm}, ammonia solution	**5.3** wt%	[*Song et al.*, 2012]
Thermally activated serpentine mine tailings	Magnesite	40°C, total pressure 10.5 bar, 3 h	**60%,** giving 0.33 g CO_2 sequestered per g of residue	[*Pasquier et al.*, 2014]

2.1.1.2. Indirect *ex situ* CCSM

Indirect *ex situ* CCSM involves separate steps for metal extraction and carbonation and can also be divided into gas-solid and aqueous reaction routes. Similarly, to the direct route, the reaction kinetics of the indirect gas-solid route are considered too slow for practical applications (Table 2.2).

Table 2.2 Examples of indirect solid-gas and aqueous processes relevant for CCSM

Substrate	Product	Process conditions	Reaction (carbonation or *dissolution) Efficiency	Reference
		Indirect gas-solid		
$Mg(OH)_2$	Mg carbonate (not specified)	565°C, 52 bar, 30 min	**90%** conversion	Butt et al., 1997 from * [*Zevenhoven et al.*, 2008]
$Mg(OH)_2$ from serpentine and commercial $Mg(OH)_2$	Mg carbonate (not specified)	325°C, $P_{ambient}$, 2 h	**26%** conversion of serpentine-derived $Mg(OH)_2$ and **9%** of commercial $Mg(OH)_2$	[*P-C Lin et al.*, 2008]
$Mg(OH)_2$ from serpentinite and commercial $Mg(OH)_2$	$MgCO_3$	500°C, 20 bar, 10 min	**50%** conversion for serpentine –derived $Mg(OH)_2$	[*Fagerlund et al.*, 2011]
		Indirect aqueous		
Serpentine -Antigorite	$MgCO_3$▪$3H_2O$	pH swing: 1) dissolution of serpentine: 70°C in a) mixture of organic acids and b) 1.4M ammonium bisulphate, $P_{ambient.}$ 2) pH 8.6 to precipitate iron oxide 3) pH 9.5 to precipitate carbonates	Mg-leaching and carbonation: solvent a) **65%** and solvent b) **42%**	[*Park and Fan*, 2004]
Olivine - forsterite	Magnesite	130°C olivine dissolution, 250°C magnesite precipitation, 150 bar	Not given, but **11%** cited in [*A. Sanna et al.*, 2014]	[*Munz et al.*, 2009]
Chrysotile doped with Li, Na, K, Cs nitrate	Hydromagnesite – humid carbonation	300-1200°C, dry and humid atmosphere (up to 10mol % H_2O), 0.1 MPa	Nearly 15 atoms of 100 of the surface chrysotile brucitic Mg moiety was carbonated at optimal 375°C.	[*Faical Larachi et al.*, 2010]
Thermally activated serpentine	Nesquehonite	30-90°C, PCO_2 up to 1 bar	Carbonation limited to **20%**	[*Werner et al.*, 2011]
Serpentine- Antigorite	Hydromagnesite	70-100°C, 3h, $(NH_4)_2SO_4$, NH_4Cl, NH_4HSO_4, H_2SO_4 NH_4HSO_4	**100%** Mg-extraction at 100°C in 3 h using NH_4HSO_4	[*Wang and Maroto-Valer*, 2011]

2.1.2. *In situ* CCSM

In situ CCSM involves the injection of CO_2 into suitable underground reservoirs and hence is broadly related to conventional CCS underground storage. However, the predominant sequestration mechanism is different - CCSM proceeds via mineral trapping as opposed to structural, residual or solubility trapping in porous reservoirs, such as sandstones, relevant for conventional CCS.

The viability of CCSM technology is based on several assumptions, one being that deep underground, ultramafic and mafic reservoirs host sufficient porosity and fracture density to allow for efficient mineral carbonation. It is also assumed that the transformation kinetics are sufficiently fast to drive the overall reaction towards carbonation. To appraise this situation, backed up by complementary laboratory experiments, a few of test site studies have been initiated, including the CarbFix Project in Iceland and the Big Sky Carbon Sequestration Partnership in the US [*Gislason and Oelkers*, 2014; *Gislason et al.*, 2010; *Matter et al.*, 2009; *Matter et al.*, 2011; *McGrail et al.*, 2014; *McGrail et al.*, 2006]

2.1.2.1. CarbFix Project

CarbFix is a collaboration of the University of Iceland, Reykjavik Energy, Columbia University, USA, and CNRS, Toulouse, France; being the world's first fully integrated CCS project with CO_2 storage in basaltic rocks [*Matter et al., 2011*].

The project encompasses a number of studies on the field-scale injection of CO_2–charged waters into basaltic rocks, along with laboratory-based experiments, large-scale plug flow experiments, a study of natural CO_2 water as a natural analogue and

state-of-art geochemical modelling [*Alfredsson et al.*, 2008]. The injection site is located in SW Iceland, in the vicinity of the Hellisheidi geothermal power plant. The CO_2 injected into basalts originates from magmatic processes and is the by-product of geothermal energy production. The experimental phases progressed under the CarbFix CO_2 project include (pers. comm. with Matter, Apr 2014):

- The injection of 175 tons of pure, commercial CO_2 into a shallow basalt aquifer (400-800 m depth) in early 2012 (Figure 2.2). H_2O was co-injected with CO_2, but using different pipes. The two fluids were mixed at depth, with a static mixer located at 420 m to aid the CO_2 dissolution. The groundwater temperature at that depth ranges between 18-33°C (30-80°C quoted in [*Aradottir and Gunnlaugsson*, 2013]) with pH from 8.4-9.4. The permeable basalt flows are separated by low permeability hyaloclastites that act as a confining layer for the injection zone [*Matter et al.*, 2011].

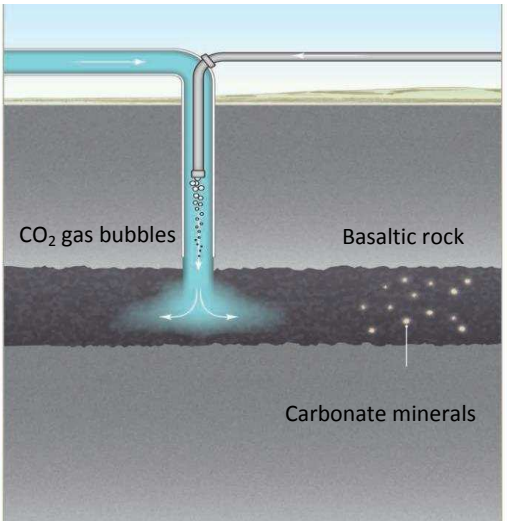


Figure 2.2 CarbFix method. CO_2 is dissolved into water during its injection into porous basaltic rocks. Solubility trapping occurs immediately, and the bulk of the carbon is trapped in minerals within 1 year [Gislason and Oelkers, 2014]

- The injection of ~1200 tons of geothermal CO_2-H_2S dissolved in water at depth; July 2012 - September 2012. This injection occurred in the same shallow basalt aquifer. However, CarbFix stopped the mixed gas injection into the shallow reservoir due to operational problems and there are currently no plans to resume this injection.
- Sulfix project: Injection of 100 tons of a mixture of CO_2 (64%), H_2S (35%) and H_2 (1%) in geothermal reservoir. The mixture was dissolved in water prior to injection. The Sulfix injection site and injection well were different. The storage reservoir was below 800 m at temperatures between 260-270 °C. This site experiment was aimed at a reduction of H_2S emissions.

The results of injected tracers monitoring suggest that more than 80% of CO_2 injected into the CarbFix injection site was carbonated within a year at 20°C to 50°C and 500 m to 800 m depth [*Gislason and Oelkers*, 2014]. Drilling into the injection site was accomplished in the end of November 2014 and approximately 150 m of core was recovered, and is currently undergoing characterisation (pers. comm. with Matter, January 2015).

2.1.2.2. Big Sky Carbon Sequestration Partnership (BSCSP)

The BSCSP partnership leads two carbon sequestration related projects, aimed at (a) storage in porous rocks, Kevin Dome Large Scale Storage Project; and (b) sequestration in continental basalts. The latter project, entitled Basalt Pilot Overview, is led by Montana State University and funded by the USA Department of Energy (DoE). The injection site is situated ~ 11 miles south of the town of Pasco in eastern Washington. The injection of CO_2 began on the 17th July 2013 and 977 metric

tons of compressed CO_2 was pumped into basalt breccia between depth interval of 828 and 887 m in the Grande Rhonde formation (Wallula pilot borehole) [*B. P. McGrail et al.*, 2014]. Cold CO_2 was heated and pressurised on site before entering the injection well as a supercritical fluid (*idem*.).

The injection was completed by August 2013 and surface soil gas monitoring and water samples collected from nearby monitoring wells have shown no evidence of CO_2 leakage. Fluid samples collected from reservoir depth showed elevated concentrations of Ca, Mg, Fe and Mn suggesting a rapid reaction of the injected CO_2 with the reservoir basalt (*idem*.). Fluid sampling and analysis will continue to 2015. There are currently plans to close the site in 2015, but prior to that core samples will be extracted and analysed for direct evidence of *in situ* carbonation [*B. P. McGrail et al.*, 2014].

2.2. Underpinning chemistry

Fundamental studies of CO_2-rock interaction mechanisms are highly important [*Chen et al.*, 2006; *Wolf et al.*, 2004] for predicting the fate of CO_2 when injected into underground formations. Mineral carbonation comprises two fundamental fluid-rock reactions: *i.e.* dissolution of the resource material and the precipitation of carbonate.

This section reviews the general concepts of dissolution and carbonation with emphasis on the dissolution of Mg-silicates and precipitation of Mg carbonates.

2.2.1. Mineral dissolution

Mineral dissolution proceeds via the transport of aqueous reactants to and from the mineral's surface [*Schott et al.*, 2009] leading to permanent alteration of material

structure and composition. Chemically, it is a proton - metal exchange with the number of protons exchanged proportional to the valency of the metal [*Ludwig and Casey*, 1996], *e.g.* each Mg^{2+} in serpentine would be exchanged with $2H^{+}$ [*Luce et al.*, 1972; *Siever and Woodford*, 1979] and each Al^{3+} in kaolinite would be exchanged for $3H^{+}$ [*Ward and Brady*, 1998]. Other studies have shown that charge balance is not always preserved during proton – metal exchange reactions [*Hellmann et al.*, 1990; *Oelkers et al.*, 2009] with Hellmann *et al.* [*Hellmann et al.*, 1997] concluding that the number of protons exchanged depended on pH. This finding was confirmed from leaching experiments on wollastonite, diopside, enstatite and forsterite, where the extent of divalent metal ion release was inversely related to pH. In practice, pH, leaching time, degree of under-saturation and ionic solution strength are the main factors that determine the depth from which cations are leached from the crystal [*Muir and Nesbitt*, 1997; *Oelkers et al.*, 2009]. The removal of metal ions from the near surface leads to the formation of new internal surfaces, readily accessible for the influx of new solvent molecules [*Hellmann et al.*, 1990; *Oelkers et al.*, 2009]. The adsorption of protons on the new internal sites causes further destabilization of the remaining bonds and the whole mineral structure undergoes deterioration (*idem.)* and dissolves congruently (*i.e.* stoichiometrically, with all mineral components dissolved into solution).

In many cases, however, dissolution is incongruent and proceeds towards the formation of a metal-leached microporous reaction residue, termed the 'leached-' or 'ash-layer' [*Kosuge et al.*, 1995; *Luce et al.*, 1972; *Ruiz-Agudo et al.*, 2012]. Kosuge *et al.* [*Kosuge et al.*, 1995] also reported the formation of 1 nm micropores between silica tetrahedra formed by the leaching of Mg^{2+} from antigorite, with the acid-treated reaction residue retained the morphology of the starting antigorite.

In addition to leached layer formation via incongruent dissolution of the original mineral, *i.e.* metal ion leaching, layer formation may also proceed through the coupled interface dissolution-precipitation process whereby the mineral dissolves congruently, and silica re-precipitates to form a siliceous residue [*Hellmann et al.*, 2003; *Ruiz-Agudo et al.*, 2012]. However, Schott *et al.* [*Schott et al.*, 2009] claims it is unlikely that siliceous layers form through the re-precipitation of amorphous silica because: (1) the aqueous solution in contact with these layers is strongly under-saturated with respect to quartz and amorphous silica; and (2) the leached layers are 'homogenous covers' rather than 'localized aggregates' that would involve point nucleation and crystallization. Schott *et al.* (*idem)* reported also that leached layers form when the surface reactions are fast and transport controlled. However, in surface-controlled reactions, the transport is fast and no cation depletion is observed [*Schott et al.*, 2009].

The formation of leached layer in partially acid-leached serpentine minerals is investigated in Chapter 4.

2.2.2. Metal - oxygen bonding in multi-oxide minerals

It is widely accepted that the destruction of the slowest breaking metal – oxygen bond constitutes the rate-limiting step during the dissolution of multi-oxide minerals [*Oelkers and Schott*, 2001; *Schott et al.*, 2009]. The relative rates at which each metal oxygen bond breaks within a multi-oxide is equivalent to the relative dissolution of that single metal (hydr)oxide (*idem.)* However, as pointed by Smyth [*Smyth*, 1913] "*…the solubility of an oxide varies greatly with the compound in which it occurs…*". This was later reiterated as: the composition and structure of a multi-oxide mineral

affect the extent of non-stoichiometric cation release, *i.e.* the destruction of specific bonds [*Schott et al.*, 2009] and is further ***investigated in the context of structurally different serpentine minerals in Chapter 4***.

At low pH, the ease of destruction of metal – oxygen bond decreases with increasing metal valency, *e.g.* Na – oxygen bond will break more easily than Si – O bonds. Oelkers [*Oelkers and Schott*, 2001] presented a comprehensive study on the dissolution kinetics of multi-oxides and summarised the dissolution mechanisms of selected minerals and basaltic glasses under acidic conditions (Figure 2.3). It was found that dissolution proceeds usually through several steps, with the "detachment" of alkali metals occurring initially, followed by Ca, Mg and Al.

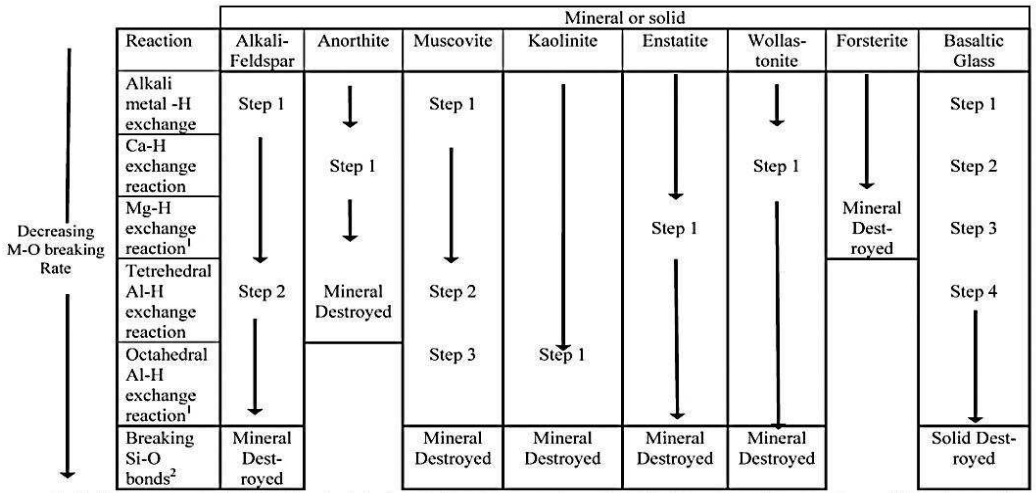


Figure 2.3 Overview of the dissolution mechanisms of various minerals and basaltic glass [Oelkers and Schott, 2001]

At low pH, it is noted that siloxane (Si-O-Si) bonds are relatively strong [*Oelkers*, 2001; *Westrich et al.*, 1993] and Si release is relatively slow compared to other metals [*Oelkers et al.*, 2009].

2.2.3. Rate of dissolution and reactive surface area

The rate at which a mineral dissolves is a measure of how its composition changes with time and is controlled by the slowest involved process [*Schott et al.*, 2009]. The rate of reaction R is expressed as the change in concentration of species originating from dissolved minerals per unit time, normalised for unit volume (if the volume changes with time) and surface area of a mineral, following [*Brantley et al.*, 2003],:

$$Ri = (\frac{V}{SA * m} * \frac{dC}{dt})/n$$

Where V is the volume of solution (l); SA is surface area (m^2/g); m is the <*starting*> mass of the sample (g); dC/dt is the change of elemental concentration (mol) with time (s); and n is a coefficient representing the mineral stoichiometry.

The rate of reaction depends on several factors including the type of material, the particle size distribution, the P-T conditions, and the availability of chemical catalysts. The other major factor that affects the reaction rates is the surface area [*F C Lin and Clemency*, 1981]. The total surface area is usually measured by geometric calculation or by the gas adsorption method of Brunauer, Edward and Teller (BET), and the value obtained, may further be used to calculate normalised mineral dissolution rates [*Brantley et al.*, 2008]. The total surface area when divided by the mass of sample analysed, gives the specific surface area (SSA), in m^2/g. Although difficult to determine, the third type of surface area, *i.e.* the reactive surface area, is most important for the rate calculation. The reactive surface area is related to the number of energetic sites present at the crystal surface [*Brantley et al.*, 2008], in the form of:

(1) atomically flat terraces; (2) steps; (3) kink sites; (4) corners; and (5) ad-atom positions. In crystals, some of these energetic sites could be categorised as crystal defects, with other sites being components of more complex structures. For example, in sheet silicates (*e.g.* serpentine minerals), the diversity of adjacent layer stacking arrangements could introduce more kinks and steps and less atomically flat surfaces, thereby enhancing the number of energetic sites; ***this aspect is further investigated in Chapter 4.***

2.2.4. Saturation Index and Chemical Affinity

Saturation index is a value used to determine whether the water is saturated, under-saturated or supersaturated with respect to a given mineral, and can be calculated from:

$$SI=\log_{10}(IAP/K_{sp})$$

Where IAP is ion activity product and Ksp is equilibrium constant. The solution is saturated with a respect to a mineral when SI=0, under-saturated when SI<0 and oversaturated when SI>0.

Chemical Affinity

The driving force for a reaction, ΔG, controls whether a mineral dissolves or precipitates under a given set of conditions [*Brantley et al.*, 2008]. The chemical affinity A, where A=- ΔG, describes the distance from equilibrium (equilibrium with a particular mineral being manifested by A=0), and is a measure of the energy driving a particular reaction at specific temperature and pressure [*Brantley et al.*, 2008]. It is

related to the saturation index (SI) of a given mineral, and can be calculated according to:

$$A = -R\,T\,\ln SI \quad [\textit{Schott et al.}, 2009]$$

where R is the gas constant 8.3145 J/mol·K, and T is the temperature in K. Chemical affinity is positive when the reactants are under-saturated favouring dissolution; and negative when the reactants are super-saturated, favouring precipitation [*Schott et al.*, 2009]

2.2.5. Reaction pathways in sheet silicates

In sheet silicates, a two-dimensional structure, there are two possible pathways for fluid penetration, enabling proton attack along: the edge of the Tetrahedral (T) – Octahedral (O) layers [*Kaviratna and Pinnavaia*, 1994; *Kline and Fogler*, 1981], or proceeding through the ditrigonal cavities of the basal surfaces, otherwise termed a gallery access mechanism [*Kaviratna and Pinnavaia*, 1994; *Rice and Strong*, 1974] (Figure 2.4). Kline and Fogler [*Kline and Fogler*, 1981] suggested also that three layer sheet silicates (2:1), such as talc, are attacked preferentially at cell edges, whilst two layer sheet silicates (*e.g.* serpentine minerals) are affected by both edge and gallery attack.

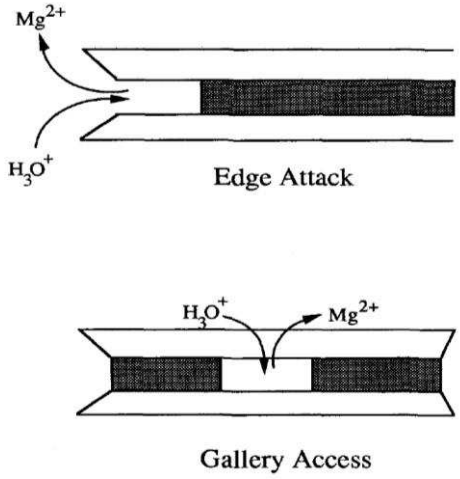


Figure 2.4. Illustration of the depletion of octahedral Mg^{2+} from 2:1 layered silicates by proton edge attack and gallery mechanism [Kaviratna and Pinnavaia, 1994].

It is recognised that irregularities in crystal structure and layer arrangements expose a substantial amount of potentially active interlayer surface to acid attack [*Kline and Fogler*, 1981]. ***However, the effect of layer stacking in serpentine minerals on the extent of dissolution has not received much attention and is a subject of this study***.

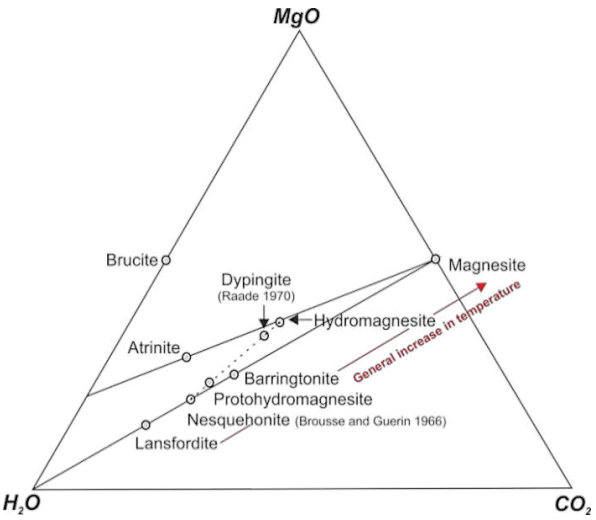
2.2.6. Carbonate diversity in MgO-CO_2-H_2O system

Carbonate minerals are the end products of both *in situ* and *ex situ* CCSM. For the Mg silicate-CO_2-H_2O system, relevant for the serpentinites and ultramafic rocks studied here, Mg carbonates (un-hydrous and hydrated) are the most likely reaction products and are ***investigated under the in situ CCSM conditions in Chapter 5***. In this context, however, as pointed out by Garcia [*Garcia*, 2005], the MgO-CO_2-H_2O system exhibits significant experimental discrepancies related to solubilities, the stabilities of solid phases at given P-T conditions, and even chemical formulae. For example, various amounts of water molecules or Mg cations have been associated with hydromagnesite, *e.g.* $4MgO{\cdot}3CO_2{\cdot}4H_2O$ [*Langmuir*, 1965], as distinct from the more

recently accepted $5MgO{\cdot}4CO_2{\cdot}5H_2O$ [*Haenchen et al.*, 2008; *Hopkinson et al.*, 2008]. The $MgO\text{-}CO_2\text{-}H_2O$ system can produce a large number of solid phases, from anhydrous magnesite to shelkovite with 24 water molecules (2.5) [*Davies and Bubela*, 1973].

Figure 2.5 (left) Composition of mineral phases across the $MgO\text{-}CO_2\text{-}H_2O$ system. (right) Adapted, showing the temperature trend, from the triangular composition plot of Davies and Bubela [Davies and Bubela, 1973].

Mineral name	Chemical formula
Magnesite	$MgCO_3$
Barringtonite	$MgCO_3.2H_2O$
Nesquehonite	$MgCO_3.3H_2O$
Lansfordite	$MgCO_3.5H_2O$
Pokrovskite	$Mg_2(CO_3)(OH)_2 . 0.5H_2O$
Artinite	$Mg_2(CO_3)(OH)_2 . 3H_2O$
Hydromagnesite	$Mg_5(CO_3)_4(OH)_2 . 4H_2O$
Dypingite	$Mg_5(CO_3)_4(OH)_2 . 5H_2O$
Giorgiosite	$Mg_5(CO_3)_4(OH)_2 . 5\text{-}6H_2O$
Shelkovite	$Mg_7(CO_3)_5(OH)_4 . 24H_2O$
Glushinskite	$Mg_5(C_2O_4) . 2H_2O$



The precipitation of Mg-carbonate is strongly controlled kinetically [*Hanchen et al.*, 2008], with the kinetics being influenced by temperature, pressure and solution composition [*Prigiobbe and Mazzotti*, 2013]. Under atmospheric conditions, the highly hydrated character of Mg^{2+} is responsible for the difficulty of forming the stable anhydrous $MgCO_3$ phase [*Christ and Hotetler*, 1970], being related to the rate of exchange of water molecules (desolvation) with carbonate or bicarbonate ions to

produce carbonate. The rate of exchange is faster for ions larger than Mg^{2+}, such as Ca^{2+}, and consequently calcite forms preferentially whilst the precipitation of magnesite and dolomite is inhibited (i*dem.)*

Schott *et al.* [*Schott et al.*, 2009] showed that the removal of one water molecule from $Metal{\cdot}(H_2O)_n^{m+}$, to form a reactive intermediate, is likely to be responsible for the much lower dissolution and precipitation rates of magnesite, siderite and dolomite, as compared to calcite. Further, Mg, Fe, Ni and Co are reluctant to form anhydrous carbonates (magnesite, dolomite, siderite and gaspeite) at ambient temperature (*idem.)* and for magnesite, Teng [*Teng*, 2013] reported that this may be related to the long-range ordered crystal structure, with $-CO_3$ groups securely interlocked between Mg-O octahedra. The energy barrier for forming such precise $Mg\text{-}CO_3$ arrangements may be too high to be overcome at low P-T conditions due to the entropic loss associated with the atoms' strict spatial distribution.

Mg carbonates tend to precipitate following the Oswald rule of stages; whereby a stable form is preceded by the crystallisation of several metastable forms, allowing for the smallest loss of free energy between transitions [*Mullin*, 1961 (2001); *Ostwald*, 1897]. There may be exceptions to this rule, but, as stated by Mullin [*Mullin*, 1961 (2001)], this process seems to operate often enough for it to be important in this system, especially for large-scale precipitation processes. The most probable explanation for this rule of stages lies in the kinetics of phase transformation, with the kinetics of the reaction often being more important that thermodynamics. This has implications for large scale (non-equilibrium) precipitating systems [*Mullin*, 1961 (2001)], such as industrial CCSM.

2.2.7. Stability of Mg carbonates

There have been many studies on the stability fields of various Mg carbonate minerals [*Christ and Hotetler*, 1970; *Davies and Bubela*, 1973; *Hanchen et al.*, 2008; *Langmuir*, 1965; *Marion*, 2001 and references therein]. Langmuir performed one of the first comparative studies [*Langmuir*, 1965] and concluded that magnesite is unstable below 60°C and at a low partial pressure of CO_2 of 1 bar. Between 10-60°C, depending on pCO_2, nesquehonite or hydromagnesite are stable, whilst < 10°C nesquehonite transforms to lansfordite (Figure 2.6). This is a reversible reaction and lansfordite rapidly transforms back to nesquehonite at 25°C (*idem.).* A more recent study showed that nesquehonite can be stable to ~ 99°C (373K) after which it decomposes to magnesite in the range ~ 149-209°C (423-483K) [*Ballirano et al.*, 2013]. It is generally considered that the most hydrated phases form during the initial stages of crystallisation, followed by less hydrated minerals, and according to Marion [*Marion*, 2001], the stability falls in the order from magnesite > hydromagnesite > nesquehonite (T ≥ 8.5 °C) & lansfordite (T ≤ 8.5 °C), being in a general agreement with Langmuir's work [*Langmuir*, 1965]. In general, an increase of temperature increases the rate of precipitation of solids in the $MgO\text{-}CO_2\text{-}H_2O$ system [*Case et al.*, 2011].

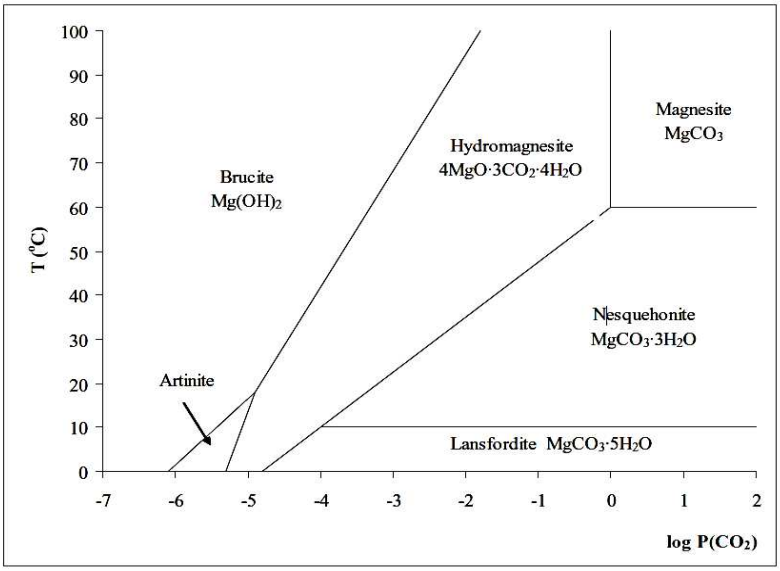


Figure 2.6 Phase diagram for the MgO-CO_2-H_2O system according to Langmuir [Langmuir, 1965]

Magnesite is considered the most stable phase in the MgO-CO_2±(H_2O) system, but its formation under conditions of ambient temperature and low salinity is virtually impossible [*Haenchen et al.*, 2008]. The transformation from hydromagnesite to magnesite under ambient conditions requires hundreds of years [*Zhang et al.*, 2000]. Ions of Mg^{2+} are small and in aqueous solution are completely surrounded by water molecules. The water molecule dipoles exhibit strong electrostatic interactions and form barriers around the Mg-cations (termed hydration layers). The molecules are easily incorporated into the carbonate structure, resulting in the formation of hydrated Mg carbonate [*Haenchen et al.*, 2008]. With increasing salinity, the activity of water is reduced and the proportion of less strongly hydrated Mg^{2+} increases [*Christ and Hotetler*, 1970], promoting the formation of unhydrous phases. This is in agreement with observations on the natural occurrences of authigenic magnesite in saline environments such as sabkha [*Melezhik et al.*, 2001] and in the laboratory scenarios where the magnesite was precipitated from brine solutions [*Pfaff*, 1894 and references therein]. For example, both Pfaff [*Pfaff*, 1894] who conducted

experiments in saturated NaCl and Anjos *et al.* [*Alves dos Anjos et al.*, 2011] who used solution with the salinity six times that of sea water, precipitated magnesite directly from solution at 50-60°C and ~ 40°C (42 days), respectively. The ionic strength of solution affects positively the rates of transformation from hydromagnesite to magnesite [*Zhang et al.*, 2000]. Zhang *et al.* (*ibid.)* found that the concentration of magnesium in solution has a negative effect on the transformation rate and distinguished two mechanisms: (i) in brines with low magnesium concentration – hydromagnesite dehydration with concomitant formation of brucite is favoured; whilst (ii) in brines with high magnesium concentration – hydromagnesite dissolution / magnesite precipitation is favoured [*Zhang et al.*, 2000].

Further, Hänchen *et al.* [*Hanchen et al.*, 2008] conducted a series of experiments using the H_2O-CO_2-Na_2CO_3-$MgCl_2$ system, under three different sets of conditions:

- T= 25°C and P_{CO2} = 1 bar
- T = 120°C and P_{CO2} = 3 bar
- T = 120°C and P_{CO2} = 100 bar

and concluded that the anhydrous form of magnesium carbonate can form at 120°C and low pCO_2 (3 bar), but it required the formation of hydromagnesite as an intermediate phase. However, this process was considered too slow for industrial applications. At 100 bar pCO_2, on the other hand, the kinetics of magnesite formation were greatly enhanced and co-precipitation of hydromagnesite and magnesite was observed, with subsequent transformation of hydromagnesite to the anhydrous form within a few hours.

Prigiobbe & Mazzotti [*Prigiobbe and Mazzotti*, 2013] performed experiments using magnesium chloride and sodium carbonate at 100 bar CO_2 and at 90°C, 120°C and 150°C; and observed the precipitation of magnesite at all temperatures, whilst at

120°C and 150°C the simultaneous precipitation of magnesite and hydromagnesite was observed. In a similar fashion to the experiment of Hänchen *et al.* [*Hanchen et al.*, 2008], hydromagnesite transformed to magnesite within 2 h at 120°C , and just 5 minutes at 150°C without affecting the magnesite precipitation.

In the context of industrial CCSM, magnesite is the desired form of Mg carbonate due to its long term stability and lowest process water requirements [*Swanson et al.*, 2014]. The hydrated minerals are less efficient in terms of the stoichiometric utilisation of Mg *(idem.).*

The formation of Mg-carbonates in CO_2-saturated brine and wet supercritical CO_2 under 100 bar pressure and 70°C is investigated in Chapter 5.

2.3. Feedstock and reservoir rocks

2.3.1. Serpentine minerals

Serpentine minerals have been studied widely [*Balan et al.*, 2002; *Cressey et al.*, 2008b; *Mellini and Zanazzi*, 1987; *Mellini et al.*, 2010; *Rucklidge and Zussman*, 1965; *Whittaker and Zussman*, 1956; *Wicks et al.*, 1995 and references therein]. Many aspects of the mineral composition, paragenesis, crystal structure and chemistry have been refined throughout many years of exploration and are comprehensively documented elsewhere. The following review focuses on the areas most relevant to the study of serpentine minerals as a feedstock material for CCSM. This section covers the themes of origin, crystal structure and chemistry, polymorphism and polytypism, and stability.

2.3.1.1. Origin of serpentine minerals

Serpentine minerals are hydrated, dominantly Mg-rich, silicates that form as a result of retrograde hydrothermal alteration of ultramafic rocks, or by prograde metamorphism of pre-existing serpentine [*Deer et al.*, 2009].

Retrograde hydrothermal alteration is defined as a group of processes that leads to compositional changes (including hydration) of the protolith rock with simultaneous decline of temperature. The hydration of ultramafic rocks (serpentinisation) is a complex and multistage process and occurs across a wide range of settings and temperatures, resulting in ~ 12-14 wt % water enrichment. Some serpentinites form within the ocean crust by the interaction of water with hot ultramafic rocks at spreading ridges, other form in fault zones that act as pathways for penetrating ocean water [*Prichard*, 1979]. Serpentines can also form concurrently with various phases of water ingress during the obduction of ophiolites and post-obduction tectonic events. At the Earth`s surface or near-surface environment, so called "present day serpentinisation" [*Barnes et al.*, 1978] is a result of meteoric water percolation through ultramafic massifs. Serpentinisation may be expressed by the following reactions [*Deer et al.*, 2009]:

$$2MgSiO_3 + 3H_2O \rightarrow Mg_3Si_2O_5(OH)_4 + Mg(OH)_2$$

or

$$3Mg_2SiO_4 + 4H_2O + SiO_2 \rightarrow Mg_3Si_2O_5(OH)_4$$

2.3.1.2. Serpentine mineral crystal structure and chemistry

The crystal structure of serpentine minerals has been the subject of many studies since the mid 1950`s [*Midgley*, 1951; *Whittaker and Zussman*, 1956] with a

reappraisal published in 1975 by Wicks and Whittaker [*Wicks and Whittaker*, 1975]. Since then the structure has been refined with new mineral species identified [*Cressey et al.*, 2008a and references therein; *Krstanovic*, 1997; *Mellini*, 1982; *Mellini and Zanazzi*, 1987; *Mellini et al.*, 2010].

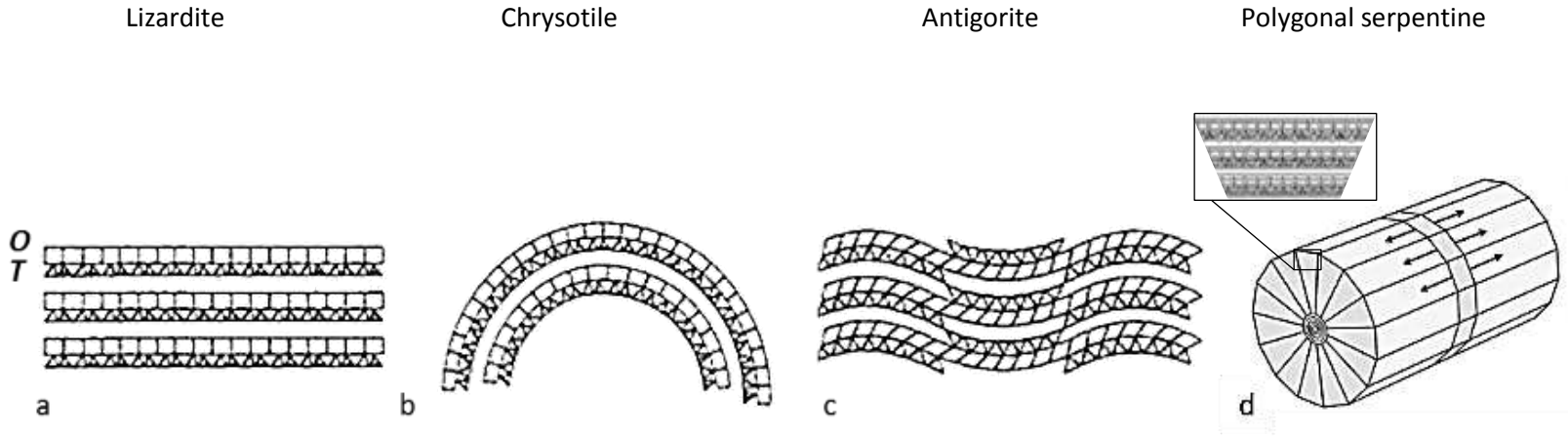
Three minerals commonly associated with the serpentine group are dominantly Mg-rich:

- Flat layered ***lizardite*** (Figure 2.7a);
- Curved (tubular) ***chrysotile*** (Figure 2.7b);
- Modulated ***antigorite*** (Figure 2.7c); (although due to $Mg(OH)_2$ depletion, this is not regarded as a true serpentine polymorph [*Capitani and Mellini*, 2004]).

Another two minerals belonging to this group are:

- ***Polygonal serpentine*** (Figure 2.7d); (also called Povlen type) - a fibrous variety consisting of a cylindrical core surrounded by 15 or 30 sectors of variably stacked layers of lizardite, which could be interpreted as structurally intermediate between chrysotile and lizardite [*Baronnet et al.*, 1994] ; and
- ***polyhedral serpentine*** with spherical or sub-spherical morphology. Based on the analysis of millimetre-sized crystals from Gew-graze, Lizard Peninsula, it is suggested that polyhedral spheres of this mineral comprise arrays of 92 triangular prisms of lizardite 1T [*Cressey et al.*, 2008a].

Figure 2.7 Basic structures of serpentine minerals: a) flat layer lizardite; b) tubular chrysotile, c) wavy antigorite and d) polygonal serpentine with polygons occupied by flat layer lizardite



Amesite, ***kellyite***, ***cronstedtite*** and ***népouite*** are other minerals with 1:1 layered structures similar to lizardite.

Serpentine minerals belong to a group of trioctahedral 1:1 layered silicates. They exhibit relatively simple chemical composition, of the form of $Mg_3Si_2O_5(OH)_4$, but a complex crystallographic structure. The basic tetrahedral (T) and octahedral (O) structural components are variably arranged and stacked one above another, giving rise to complex polymorphs and polytypes. Each tetrahedron is composed of a centralised Si and four corner-sited O atoms, although the substitution of Si^{4+} cations with Al^{3+} or Fe^{3+} (up to 8.8%) is common [*Fuchs et al.*, 1998]. The octahedral sheet is usually occupied by a divalent cation, predominantly Mg^{2+} and to a lesser extent Mn^{2+}, Fe^{2+}, Co^{2+} or Ni^{2+}. Substitutions in the octahedral sites by trivalent cations are also possible, usually paired with tetrahedral site substitutions. The dimensions of un-substituted tetrahedral and octahedral layers are not equivalent, with the latter exhibiting a larger unit cell [*Pauling*, 1930]. This misfit is compensated by the curvature of adjacent layers, with the tetrahedral layer positioned on the inside and the octahedral layer on the outside of the curve [*Fuchs et al.*, 1998]. The distance between each tetrahedral-octahedral (T-O) doublet, corresponding to the unit cell c-parameter, is ~ 7 Å for single layer serpentine minerals, and ~ n x7 Å (n integer) for a multi-layered structure.

The length of bond between O and Si within the tetrahedral site varies for the basal (B) and apical (A) oxygens (Figure 2.8), with the bond between the apical O and Si being shorter (1.577 - 1.617 Å) than one involving basal oxygens (1.637 - 1.651 Å). Mellini & Zanazzi [*Mellini and Zanazzi*, 1987] reported that minor modification affects the bond length from structure to structure and that the length of bonds between Si

and O in the tetrahedra varies depending on the degree of cation substitution [*Mellini and Viti*, 1994]. For instance, the degree of Al^{3+} substitution is inversely proportional to the size of the tetrahedral unit [*Mellini and Zanazzi*, 1987].

In the octahedral sheet, the cation is co-ordinated by 6 atoms (Figure 2.9) of O forming a slightly distorted "flattened octahedron" [*Mellini*, 1982]. The dimensions of an octahedral layer and the degree of distortion arise from the equilibrium of three forces: a) cation-cation repulsion across shared octahedral edges; b) anion-anion repulsion along shared edges; and c) cation-anion bonds within octahedra [*Radoslovich*, 1963]. As pointed out by Wicks and Whittaker [*Wicks and Whittaker*, 1975], the idealised serpentine mineral structure would involve a simple, not distorted stacking of octahedral and tetrahedral layers. Accordingly, the ideal "non-distorted" octahedral layer would exhibit b = 8.78 Å and a thickness of 2.43 Å, with shared and unshared edges of 2.97 Å and all the O-Mg-O angles at 90°. The layers would be linked by hydrogen bonds that develop between the basal oxygen in the tetrahedra and the hydroxyl groups of the adjacent layer. This ideal stacking would lead to a trigonal unit cell. However, in reality, the dimensions between un-substituted tetrahedral (Si-O) and octahedral (Mg-O) layers are not equivalent and in the brucite layer, the cation-cation repulsion between the Mg atoms extends the b to 9.43 Å and thins the sheet to 2.11 Å, with shared octahedral edges of 2.79 Å drawing the OH in, along the z-axis and unshared edges of 3.14 Å; the O-Mg-O angles shift from 90° to 83.3° and 96.8° [*Wicks and Whittaker*, 1975]. The layer misfit in serpentine minerals lead to curvature and modulation. This was first mentioned by Pauling [*Pauling*, 1930] who stated that *"…we expect that as a rule that two faces of a constituent layer of a crystal will be equivalent, for if they were not equivalent there would be a tendency for the layer to curve, one face becoming concave and one*

convex, and this tendency would in general not be overcome by the relatively weak forces operating between adjacent layers…"

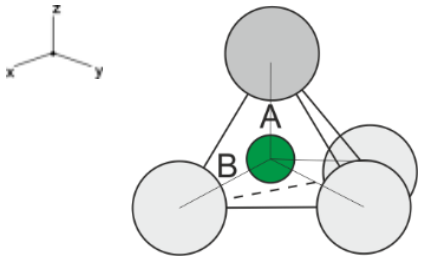


Figure 2.8 Basic tetrahedron – silicon atom (green) surrounded by grey atoms of oxygens, with the apical oxygen in the tetrahedron shaded dark grey. Apical and basal bonds marked A and B respectively.

a) b)

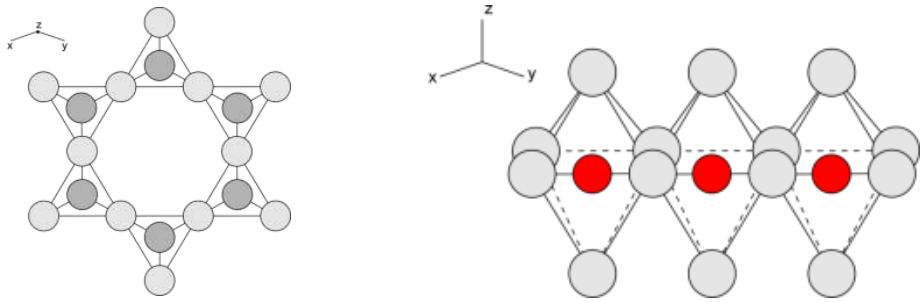


Figure 2.9 Arrangements of tetrahedrons and octahedrons in the layered silicate crystal structure: (a) hexagonal ring of SiO_4 tetrahedra and (b) linked octahedra. Note that the polygons are oriented differently with regards to the xyz axes.

2.3.1.4. Serpentine mineral polymorphism and polytypism

Lizardite and chrysotile exhibit similar compositions (complex solid-solutions) and are treated as polymorphs with general formula per unit cell: $M_3T_2O_5(OH)_4$, where M = Mg^{2+}, Fe^{2+}, Ni^{2+}, Al^{3+}; T=Si^{4+}, Al^{3+}, Fe^{3+}. However, *sensu stricto* polymorphism is not

simple for all serpentine minerals because of their structure complexity. The wavy structure of antigorite for instance, imposes differences in composition related to subtle $Mg(OH)_2$ depletion, given by: $M^{VI}_{3m-3}\,T^{IV}_{2m}\,O_{5m}(OH)_{4m-6}$, where m = number of unique tetrahedra per antigorite wavelength [*Capitani and Mellini*, 2004; *Page*, 1968]. Antigorite belongs to the serpentine minerals group but is not regarded as a serpentine polymorph.

Polytypism arises from the diverse stacking of basic structural components, *i.e.* the tetrahedral and octahedral sheets in serpentine minerals. Banfield *et al.* [*Banfield et al.*, 1995] suggested that polytypism results from: a) chemistry, temperature and pressure during growth; b) structural distortions within a crystal; c) the growth mechanism and d) the degree of super-saturation [*Amouric and Baronnet*, 1983]. The polytypism of trioctahedral 1:1 layered silicates was comprehensively described by Rucklidge & Zussman [*Rucklidge and Zussman*, 1965] and Bailey [*Bailey*, 1969] and definitions suggested by the latter author have been used ever since. The stacking diversity is determined by:

- ***Cation occupancy*** in the octahedral layer. The cations occupy either set I or set II positions above the tetragonal sheet (Figure 2.10).
- ***Interlayer rotations*** and ***shifts*** (Figures 2.11 & 2.12). The layers in the serpentine mineral structures are linked by hydrogen bonds that form by pairing oxygen on the basal tetrahedral surface of one layer with an OH group of the upper octahedral surface of the layer below. These bonds are generally long and weak, however they can be modified and strengthened by the degree of substitution (*e.g.* Al^{3+} in the tetrahedral layer promotes stronger hydrogen bonding and more stable structures [*Mellini*, 1982]). The hydrogen bond is maintained when the following arrangements of adjacent 1:1 layers occur [*Bailey*, 1969]:

- ***no shift of successive layer***. Polytypes **1T** and **$2H_1$**. Directly superimposed layers do not display any shift and these polytypes differ in the cation occupancy of the octahedral site. No difference in cation occupancy is observed for 1T polytypes, whereas $2H_1$ exhibits alternation of site I and II cation positions.

- ***shift of second layer by a/3 along the fixed x1, x2 and x3 axis***. Polytypes: **1M**, **2Or**, **$2M_1$**, **$2M_2$**, **3T** and **6H**. The shift of the succeeding interlayer may occur in six directions following ± x1, ± x2 and ± x3 (in the plane of x axis). The displacement of layers results in the development of distinct stacking angles between the initial and successive planes. These stacking angles are 0°, 60°, 120° and 180°, and 240° and 300° that are equivalent to 120° and 60°, respectively. The 1M polytype exhibits a shift along – x1 and no interlayer rotation; 2Or alternately shifts along + and – x1, with 180° stacking angle; $2M_1$ shifts along two different x-axes with continuous alteration of ± 120° stacking angles; $2M_2$ shifts along two different x-axes with continuous alteration of ± 60° stacking angles; 3T shifts along all three x-axes, whilst 6H shifts along all three x-axes with continuous stacking angles of 60° and 300°.

- ***shift of the second layer by b±3 along any of the three hexagonal y-axes*** of the initial layer (normal to the three x-axes), with or without rotation of the second layer. Polytypes **2T**, **$2H_2$**, **3R** and **6R** (Table 2.6). Shifts along the y-axis lead to equivalent results hence all shifts are taken along Y1. Polytypes 2T and $2H_2$ result from alternating positive and negative shift directions, whereas 3R and 6R result from the same shift direction between the layers.

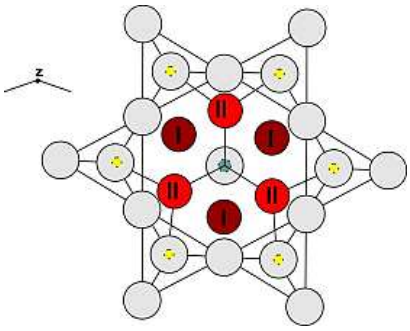


Figure 2.10 Positioning of site I and II octahedral cations above the tetrahedral sheet [Bailey, 1988]. Red – Mg atoms, Grey – oxygen atoms, Yellow – silicon atoms.

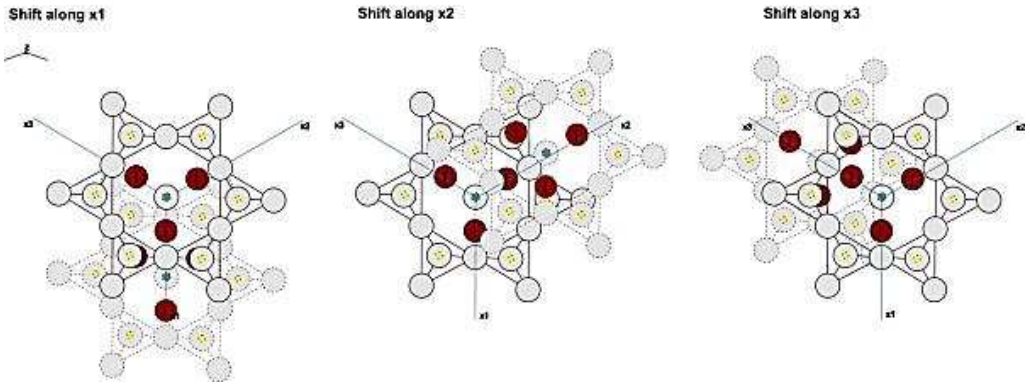


Figure 2.11 Three possible directions of interlayer shift along the hexagonal axes if octahedral site is occupied by cations I [Bailey, 1988].

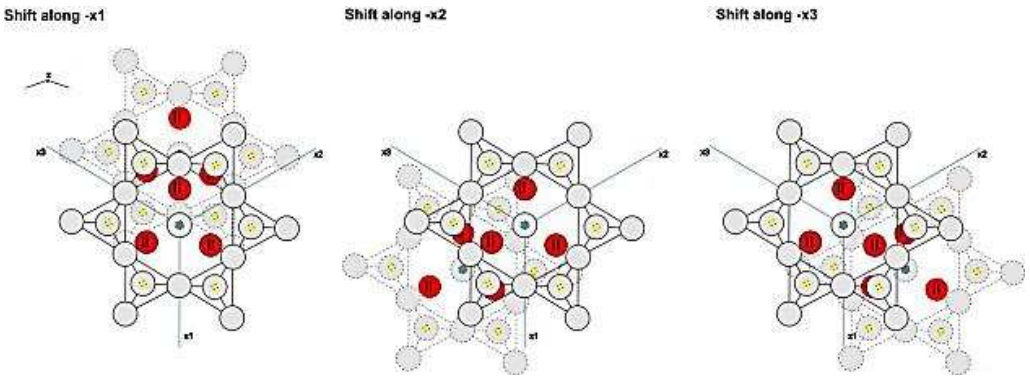


Figure 2.12 Three possible directions of interlayer shift along the hexagonal axes if octahedral site is occupied by cations II [Bailey, 1988].

Based on the combination of cation occupancy and interlayer shift direction and angle, Bailey [*Bailey*, 1969] divided the 12 polytypes into four groups (A, B, C and D) as listed in the Table 2.5.

Table 2.5 Groups of standard sheet layer polytypes [Bailey, 1969].

Polytype	A	B	C	D
Layer shift	± a/3	± a/3	0 or ± b/3	0 or ± b/3
Octahedral sites	I	II	I	II
Symmetry	1M, $2M_1$, 3T	2Or, $2M_2$, 6H	1T, 2T, 3R	$2H_1$, $2H_2$, $6R_1$

The serpentine crystal chemistry and structure, and their influence on the efficiency of Mg^{2+} leaching are investigated in Chapter 3 and Chapter 4, respectively.

2.3.1.5. Stability of serpentine minerals

Differences in the stability of chrysotile, lizardite and antigorite arise due to a complex interplay between composition and the structural adjustments required to reduce the misfit between the tetrahedral and octahedral layers [*Caruso and Chernosky*, 1979]. Amongst the serpentine minerals, antigorite exhibits the highest thermal stability over lizardite and chrysotile [*Bromiley and Pawley*, 2003; *Caruso and Chernosky*, 1979]. To accommodate the dimensional misfit, antigorite exhibits a wave-like modulation with periodically inverted tetrahedral sheets attached to the concave side of the octahedral sheets (Figure 2.13) [*Capitani and Mellini*, 2004 and references therein]. This modulation is attributed to the repulsion between adjacent

apical oxygens and tetrahedral cations, and the movement of oxygens, promoting layer curvature [*Capitani and Mellini*, 2004]. The tetrahedra arrangements result in a complex three-dimensional network of chemical bonds that extend through the entire crystal *(idem.),* acting as a highly stable "chemical cement".

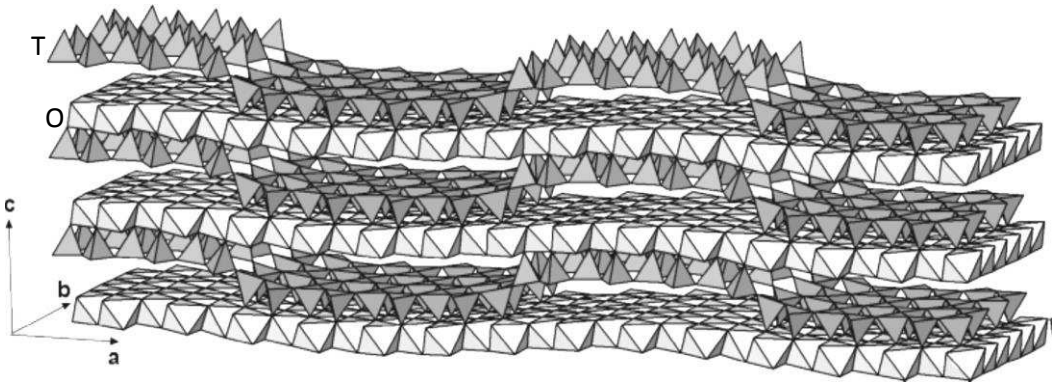


Figure 2.13 Longitudinal modulations of antigorite [Capitani and Mellini, 2004], T – tetrahedral layer, O – octahedral layer.

The stability of serpentine minerals is related also to crystal chemistry and substitutions of Al^{3+} for Si^{4+} in the tetrahedra (Figure 2.14). This type of substitution reduces the dimensional misfit between the layers, thus making the whole structure more stable. Accordingly, aluminous lizardite is more stable than non-aluminous antigorite [*Caruso and Chernosky*, 1979].

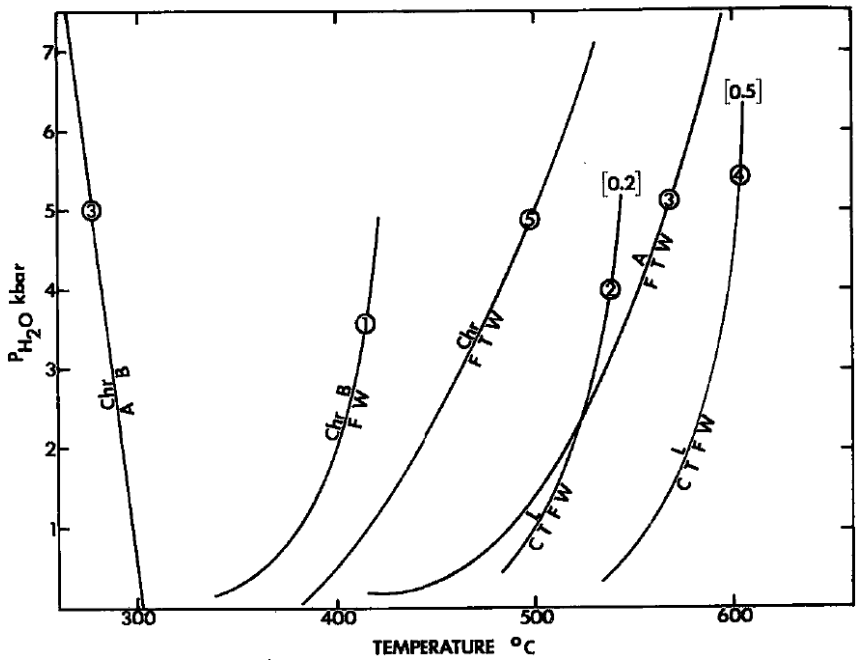


Figure 2.14 P-T diagram illustrating the relative stabilities of chrysotile (Chr), lizardite (L) and antigorite (A), clinochlore (C), talc (T) and forsterite (F) [Caruso and Chernosky, 1979]. Circled numbers relate to Al atoms per formula unit (apfu) in $Mg_6Si_4O_{10}(OH)_8$. For example, 0.2 apfu for lizardite equates to 3.7 wt% Al_2O_3.

2.3.2. Ultramafic rocks and their suitability for *in situ* CCSM

Several factors determine the reservoir suitability for *in situ* CCSM but one of the most important is its compositional / chemical affinity to CO_2, *i.e.* the presence of readily leachable divalent cations that will permanently bind the CO_2. Several candidate sites have been suggested globally, with Mg and Ca-rich silicate rocks dominating this research field [*Lackner et al.*, 1995]. In this study only the Mg-rich silicates are investigated, including ultramafic rocks and serpentinites, differing in wt% MgO, with dunite being the richest containing about 50 wt% of MgO.

Other rocks considered as a suitable injection reservoirs are mafic rocks, such as basalts *e.g.* Columbia River flood basalt in North America (a 200 000 km^2 sheet with average thickness of 1 km) [*McGrail et al.*, 2006; *Schaef et al.*, 2011].

The following Section focuses on classification and occurrence of ultramafic rocks only.

The reactivity of ultramafic rock is investigated in Chapter 5.

2.3.2. Classification of ultramafic rocks in the context of CCSM

Ultramafic rocks are originally igneous rocks, containing > 90% of mafic (etymology: MAgnesiumFerrumIC) and related minerals including: micas, amphibole, pyroxene, olivine, opaque minerals (magnetite, chromite), accessory minerals (zircon, apatite, titanite, etc), epidote, allanite, garnet, mellilite, *etc.* [*Gillespie and Styles*, 1999]. They may be classified according to their content of mafic minerals (M): olivine, orthopyroxene, clinopyroxene and hornblende (Figure 2.15) [*Gillespie and Styles*, 1999; *Le Maitre et al.*, 2002; *Streckeisen*, 1973].

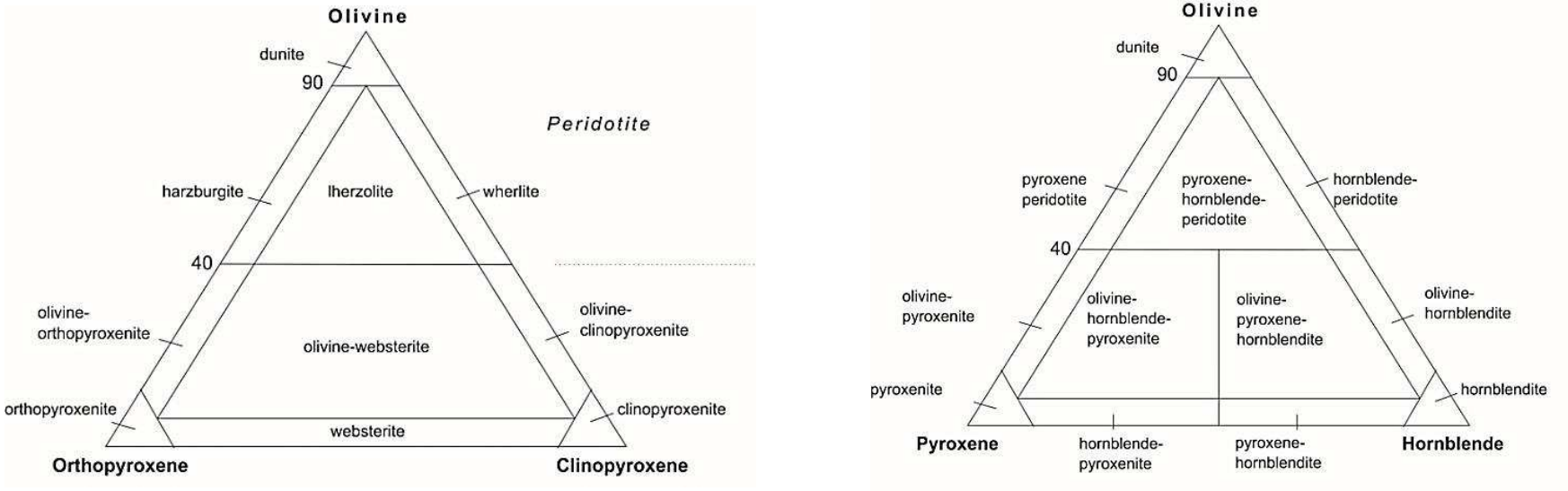


Figure 2.15 Classification of ultramafic rocks; (left) rocks containing olivine and pyroxene; (right) rocks containing olivine, pyroxene and hornblende [Gillespie and Styles, 1999].

In nature, the ultramafic rocks are invariably hydrated (with rocks up to 100% hydration being common) and otherwise altered, often constituting a complex mineral paragenesis [*Styles et al.*, 2014a]. In the CSSM system, the mineralogical/chemical diversity in the present state is more important than the rocks original petrogenesis as it determines their applicability for the technology. Styles *et al.* [*Styles et al.*, 2014b] proposed a new classification scheme of ultramafic rocks whereby the classical olivine / orthopyroxene / clinopyroxene triangular diagrams are modified to show the hydrated equivalents of the predominant mineral phases (Figure 2.16).

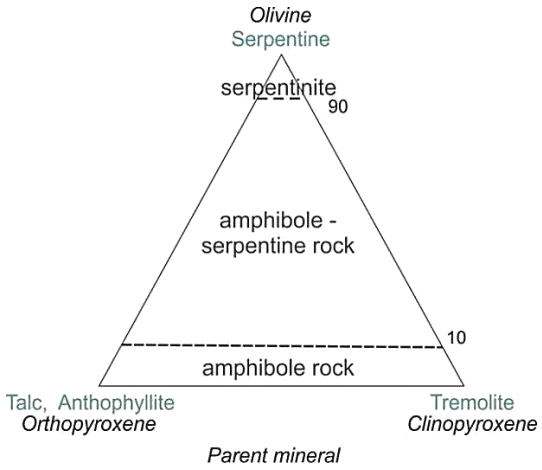
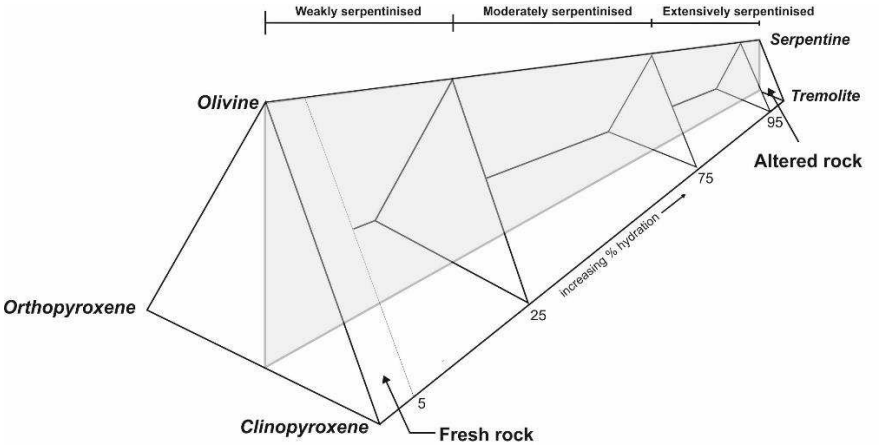


Figure 2.16 Classification of hydrated ultramafic rocks [Styles et al., 2014a]. The actual mineral is shown in green with the parent anhydrous mineral in black.

Based on the assumption that the pyroxenes and amphiboles behave similarly during CCSM, and that these phases are inferior to serpentine, Figure 2.17a was simplified and a vertical cross-section produced (Figure 2.17b) [*Styles et al.*, 2014a]. It shows the volume proportion of constituent minerals in un-hydrous (olivine and pyroxene) and hydrous (serpentine and tremolite) continuum (numbers in bold below the diagram). The Figure also indicates the proportion (area %) of the global abundance of these rocks. Four extremes are distinguished: serpentine-rich rocks, olivine-rich rocks, pyroxene-rich rocks and amphibole-rich rocks, with the largest proportion covered by variably serpentinised olivine-rich rocks (55% of global abundance).

A



B

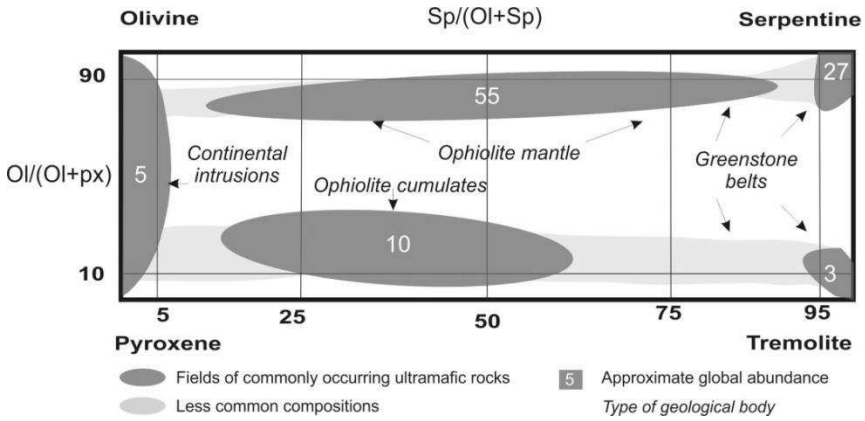


Figure 2.17 a) The range of mineralogical compositions of naturally occurring ultramafic rocks; b) classification diagram based on the plane through the apexes in (a) representing the proportions of constituent minerals [Styles et al., 2014b].

Weathering and low temperature alteration of ultramafic rocks often results in their significant carbonation (Figure 18). The newly formed complex paragenesis of dominantly Mg, ±Fe, Ca silicate – Mg, ±Fe, Ca carbonate frequently serves as natural analogue of the proposed CCSM technologies. Accordingly, the distribution, extent and rates of silicate to carbonate transformations as well as the source of the CO_2 have been studied widely (Kelemen and Matter, 2009; Stephen *et al*, 2013; Lacinska *et al*, 2014). Studies suggests that natural carbonation is spontaneous and rapid, as exemplified by ~10^4 - 10^5 tons of atmospheric CO_2 converted to solid carbonate via weathering of ultramafic rocks in Oman (Kelemen and Matter, 2009). It is also known that the hydrated form of ultramafic rocks – serpentinite undergoes a more extensive transformation than their unhydrous equivalents (Lacinska *et al,* 2014), perhaps being also related to the degree of element substitutions, in particular Al^{3+}, in the minerals of interest. The source of CO_2 for carbonation is still debatable, and it is possible that in many cases mixing the atmospheric CO_2 with CO_2 originating from dissolution of pre-existing carbonates will occur (Stephens *et al*, 2013).



Figure 2.18 White carbonate veins cross-cutting outcrop of weathered peridotite, Oman-UAE Ophiolite, United Arab Emirates. Image courtesy of Dr M Styles.

2.4. Summary

This literature review provides background information on several aspects of mineral carbonation with emphasis on processes involved in *in situ* and *ex situ* CCSM. The underlining chemistry, in terms of mineral dissolution and Mg-carbonates precipitation was presented. The feedstock and resource materials were described, with aspects given of serpentine crystal structure and chemistry, and the division of ultramafic rocks in the context of CCSM. The following Chapters will focus on the mineralogical and geochemical variation of serpentine minerals and their suitability for *ex situ* CCSM through detailed analysis of their reactivity in acid. Further, the ultramafic rocks will be investigated under conditions relevant for *in situ* CO_2 injection and the extent of *in situ* Mg-carbonate precipitation will be determined.

Chapter 3 Mineralogical and geochemical characterisation of serpentine minerals for CCSM

3.1. Introduction

Serpentine minerals are candidate feedstock materials for carbon capture and storage by mineralisation (CCSM). Their reaction with CO_2 to produce carbonate minerals offers a route towards permanent sequestration. Serpentine mineral chemistry and their worldwide occurrence make them applicable for both *in situ* and *ex situ* CCSM technologies.

In the context of CCSM, the serpentines serve primarily as donors of Mg^{2+} cations. The cations are extracted during accelerated dissolution, aided by thermo-mechanical activation. The extraction efficiency is defined by the mineral structure and chemistry, whilst the total amount of cations extracted defines the overall CCSM process efficiency.

Successful mineral identification is usually possible based on the results of X-ray diffraction analysis (XRD). However accurate XRD identification and quantification of serpentine mineral polymorphs, and polytypes in particular, is often obstructed by: poor crystallinity (in the context of crystal / amorphous content) giving rise to poor diffraction data [*Mellini*, 2013], strong superposition of the main diffraction peaks [*Cavallo and Rimoldi*, 2013], and high degree of sample heterogeneity [*Gualtieri et al.*, 2014; *Viti*, 2010]. The sample volume analysed is rarely monomineralic [*Viti and Mellini*, 1997], which makes it difficult to obtain reliable data from a pure mineral that could act subsequently as a reference for the analysis of unknown samples. All these challenges raise questions over the

accuracy of powder diffraction data within the Inorganic Crystal Structures Database (ICSD) of serpentine minerals, and a comprehensive appraisal of the quality of these PXRD patterns is given by Wicks [*Wicks*, 2000].

Thus, during this study a combination of techniques including PXRD, FTIR, TGA, XRF and SEM was used to allow for accurate identifications of samples prior and post experimental testing. This level of analysis is essential to elucidate the minerals effectiveness for use within CCSM technologies.

This Chapter, therefore presents the results from a detailed mineralogical and geochemical investigation of specific serpentine samples. It serves as background information for the following Chapter on accelerated Mg^{2+} leaching for *ex situ* CCSM.

PXRD, FTIR and TGA were used collectively for mineral identification. Chemistry was assessed using XRF and SEM-EDS quantitative analysis. SEM together with optical microscopy was used for the characterisation of rock texture.

3.2. Materials

Nine serpentine mineral samples were collected and used in the cation leaching study (Chapter 4), as detailed in Table 3.1: three were collected at the Lizard Peninsula, UK (summer 2012); one at Montecastelli Pisano, Tuscany, Italy (summer 2013); four were obtained from the British Geological Survey rock collection or from Dr M Styles previous studies; and one sample of a well characterised lizardite 1T was supplied by Prof. M. Mellini (2012).

Table 3.1 Samples used in this study, their locality and mode of occurrence.

Sample number	Specimen origin / Previous number		Locality	Coordinates * **BNG – British National Grid**	Serpentine type	Mode of occurrence
AML2	Collected by Dr MT Styles	SI2M	Pian del Re, Monviso Massif, Italy	Easting 44 00 59.8 Northing 07 06 06.2 Coordinate System WGS84 (º ' ")	**antigorite**	vein
AML59	Collected during PhD fieldwork	NA	Supplied by BGS shop, unknown locality	NA	**fibrous variety of antigorite, picrolite**	?vein
AML6	Collected by Dr MT Styles	SU5	Quarry NW of Bidya, UAE	UAE 433740 2814672	**chrysotile**	vein
AML60	Obtained from BGS collection	RC274/ 3	New Amianthus Asbestos Mine, Kaapsche Hoop, Transvaal region, South Africa	NA	**chrysotile**	?vein
AML4	Obtained from Prof. M Mellini	NA	Sample supplied by Mellini (2012), Elba, Italy	NA	**lizardite**	vein
AML46	Collected during PhD fieldwork	NA	Kennack Sands, Lizard Peninsula	SW73619 *BNG16568	**lizardite**	vein
AML53	Collected during PhD fieldwork	NA	Gwendreath Quarry, Lizard Peninsula, UK	SW73415 BNG16958	**lizardite**	vein
AML57	Collected during PhD fieldwork	NA	Gwendreath Quarry, Lizard Peninsula, UK	SW73415 BNG16958	**lizardite**	veins and nodules in serpentinised peridotite
AML62	Collected during PhD fieldwork	NA	Montecastelli, Tuscany, Italy, sample found at the same locality as hydromagnesite studied by Boschi *et al* (pers. comm. 2013)	Not recorded	**lizardite**	vein

Serpentinisation of ultramafic rocks usually results in the formation of finely intergrown serpentine-dominated paragenetic complexes, and it is practically impossible to separate out monomineralic sub-samples. Crystallisation in veins, on the other hand, increases the probability of finding monomineralic samples, hence field-sampling efforts were focused on those specific lithologies. The samples were photographed and assessed *in situ* as hand specimens. They were then brought to the laboratories at the British Geological Survey (BGS) and together with all other "inherited" samples, were split into sub-samples for mineralogical, chemical, textural and structural characterization. A reference sample was kept for every material type.

3.2.1. A brief description of the geological setting for samples collected at the Lizard Peninsula and Montecastelli Pisano.

3.2.1.1. Lizard Peninsula, UK.

The lithologies at the Lizard Peninsula, Cornwall belong to an ophiolite complex that was emplaced during the Variscan convergence [*Kirby*, 1979; *Styles and Kirby*, 1980]. The complex consists of peridotites, gabbros, hornblende schists, meta-sediments, dolerites, meta-dolerites and acid-basic banded gneisses (the Kennack gneisses) [*Kirby*, 1979; *Styles and Kirby*, 1980]. The peridotites have been extensively serpentinised [*Power et al.*, 1997] and contain numerous serpentine-filled fractures. These fractures post-date the main stage of peridotite serpentinisation (late Devonian / early Carboniferous) and represent the final, lowest temperature (< 250°C) stage of emplacement [*Power et al.*, 1997]. The

fractures were the main focus of source material for this study and three main lithological contacts between the fracture and host rock were identified and examined in the field:

- Fracture surface mineralisation in mylonitic amphibole peridotite.
- Fracture surface mineralisation in lherzolitic (`primary`) peridotite: **lizardite samples AML46, AML53 & AML57** (mineralisation from zones close to peridotite and Kennack Gneiss contact).
- Fracture surface mineralisation from serpentinised dunite.

The brief description below only includes the lithologies that were analysed subsequently in the laboratory, *i.e.* those originating from lherzolitic peridotite.

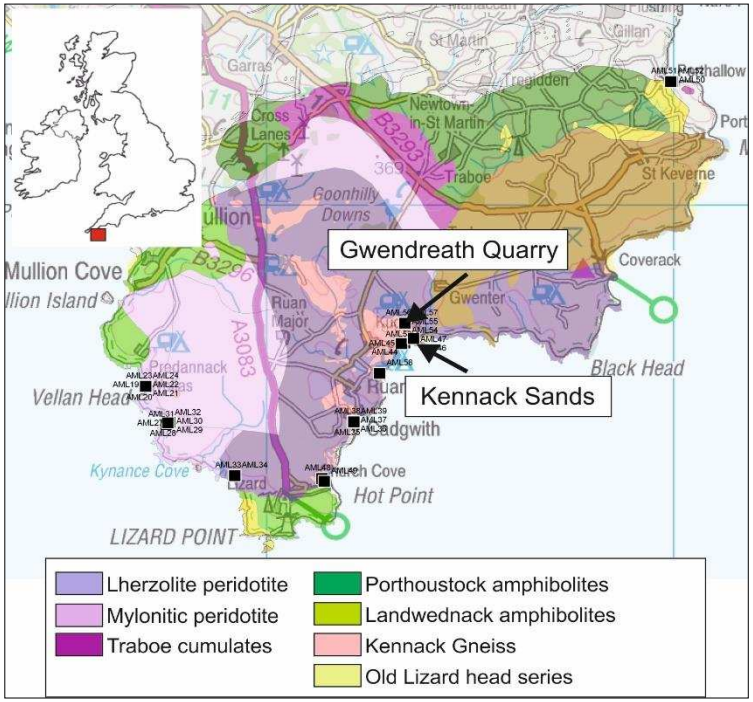


Figure 3.1 Simplified geological map of the study area around the two sampling locations of Kennack Sands and Gwendreath Quarry (exported from GIS, pers. comm. Dr. MT Styles).

Serpentine minerals at Kennack Sands.

These coastal outcrops (Figure 3.2a) displayed a wide range of veins, comprising not only serpentine minerals but also coarse (up to 10 cm long) crystals of fibrous amphibole (anthophyllite-ferrogedrite) and lesser amounts of willemseite and nimite (and possibly other chlorite-group minerals). The diverse mineralogy probably resulted from enhanced hydrothermal activity associated with syntectonic mafic and felsic intrusions of the Kennack Gneiss. The north-eastern extension of Kennack Sands was analysed previously by Midgley [*Midgley*, 1951] who reported a serpentine mineral with monoclinic symmetry (resembling antigorite). This was later verified by Whittaker & Zussman [*Whittaker and Zussman*, 1956] and calculation provided by Rucklidge & Zussman [*Rucklidge and Zussman*, 1965] showed the average crystal structure to be trigonal not monoclinic. They, however, noted that the layers may be rotated by ± 60° or 180° and displaced by ± b/3, which, based on Bailey`s polytype classification [*Bailey*, 1969], is not consistent with the trigonal system.

A sample of lizardite^{AML46} was collected from a fracture mineralisation hosted by the primary peridotite. The mineral was white, soft and greasy to soapy, almost talc-like; displaying similar appearance to that described by Midgley (1951). Randomly distributed platy, mica-like crystals were also observed.

Serpentine minerals at Gwendreath Quarry.

The quarry is set in the primary peridotite that is locally tectonised and cross-cut by mafic to felsic intrusions, probably belonging to the Kennack Gneiss intrusion. One wall of the quarry was examined in detail and two lizardite samples AML53 and AML57 were extracted (Figure 3.2b,c,d). Lizardite^{AML53} occurs as a dense mass

and displays a variety of (usually intermixed) green shades, with an apparent texture ranging from greasy creamy light to vitreous dark green and with a mineral hardness of *ca.* 3 (Mohs scale). Lizardite^{AML57} was collected from veins (< 50 mm wide) and nodules located a few cm to the left of lizardite^{AML53}. It exhibited epidote green colour, was semi-transparent, generally massive to locally sheared, with hardness ranging from ~ 2 – 3 (Mohs scale), and had a waxy to semi-vitreous lustre. The direction of crystal elongation or shearing was perpendicular to the host rock edge. This mineralisation appeared to be associated with a shear / fault zone and occurred in close vicinity to the mafic / felsic dyke. Slivers of host rock were found embedded within the green serpentine, possibly suggesting a dynamic mineralisation event with contemporaneous brecciation.



Figure 3.2 (a) Outcrop of lherzolite (primary) peridotite at Kennack Sands: sample locality for lizardite 1T AML46; (b, c, d) mineralisation at Gwendreath Quarry: sample locality for lizardite $2H_1$, AML53 and AML57.

3.2.1.2. Montecastelli Pisano, Italy.

A sample set of serpentine minerals and partially carbonated serpentinites were collected from Montecastelli (Pisano) and Malentrata (magnesite deposit), but only samples from Montecastelli were analysed in the current study (Figure 3.3). The samples originated from a serpentinite escarpment eroded by the Pavone River. The serpentinite is a multi-kilometric body, embedded in shales. The central part of the body hosted a small copper deposit that was intermittently exploited during the 19th century and closed in 1869. As a result, significant amounts of serpentinite-rich mine tailings were produced. The tailings were partially carbonated and the carbonation processes were studied by Boschi *et al* [*Boschi et al.*, 2013].

The samples chosen for the current study originated from a fracture surface of the host-serpentinite (Figure 3.4). The thickness of the fractures / veins varied, with ~ 1 - 2 cm being observed typically. At least two polymorphs of serpentine minerals were present at that locality: light creamy green, coarsely fibrous, locally distinctively - deformed antigorite (probably picrolite); and another light green, not fibrous, but with well-developed lineation and waxy lustre, confirmed to be lizardite. The latter was selected for further studies.



Figure 3.3 Locality of Montecastelli Pisano in Italy, a serpentinite region where AML62 was collected. Modified from map data © 2014 Basarsoft, GeoBasis-DE/BRG ©2009, Google.



Figure 3.4 (a) Serpentinite escarpment along the Pavone River, Montecastelli Pisano; (b) blocks of host serpentinite with serpentine mineralisation of the fracture surface.

3.2.2. Summary of the nine samples investigated - mode of occurrence and hand specimen descriptions

Corresponding images are presented in Figure 3.5.

(1) **Antigorite**^{AML2} – dark green and massive, collected by MT Styles and J Naden from Pian del Re, Monviso Massif, Italy.

(2) **Antigorite**^{AML59} – greasy green and fibrous (picrolite), obtained from the BGS shop. The origin and locality of the sample is unknown.

(3) **Chrysotile**^{AML6} – supplied by MT Styles (2012) and collected during BGS field seasons in the United Arab Emirates (original number SU5). The mineral was lineated and dull green, with local reddish discoloration, probably due to iron oxide / oxyhydroxide mineralisation.

(4) **Chrysotile**^{AML60} – extracted from a < 10 cm wide vein in a large block (up to 20 cm^3). It was distinctively fibrous and earthy olive green. RC274/3 (original number) was obtained from the BGS rock collection, with locality given as New Amianthus Asbestos Mine, Kaapsche Hoop, Transvaal region in South Africa.

(5) **Lizardite 1T**^{AML4} – supplied by M. Mellini (2012), originated from veins, several meters long and a few decimeters thick, along block joints of tectonised lherzolitic to harzburgitic serpentinite [*M. Mellini and Viti*, 1994b]. The serpentine was dark green and displayed a lineation. The sample also contained a trace of a white, flaky carbonate coating.

(6) **Lizardite 1T**^{AML46} – collected from veins cross-cutting peridotite at the NW side of the Kennack Sands, Lizard Peninsula. It was creamy to light green, and soft and greasy to touch. The sample contained a high content of non-serpentine minerals, mainly talc and chlorite.

(7) **Lizardite 2H1**^{AML53} – collected from fracture mineralization in primary peridotite, Gwendreath quarry, Lizard Peninsula. The mineral was light creamy green, with a greasy to waxy lustre.

(8) **Lizardite 2H1**^{AML57} – collected from fracture mineralization in primary peridotite, Gwendreath quarry, Lizard Peninsula. It was hard, light olive green, with vitreous to greasy lustre and occurred as < 5 cm veins and nodules.

(9) **Lizardite**^{AML62} polygonal with 1M sectors (tentative identification) – lizardite collected from fractures in serpentinite exposed along the Pavone River Valley, Montecastelli, Italy. The mineral was green to light-creamy green,

with a greasy to waxy lustre. It exhibited lineation, probably resulting from shearing along the fracture surface.



Figure 3.5 Hand specimen images of the serpentine minerals investigated in this study: a) massif antigorite; b) fibrous antigorite; c) lizardite 1T, trace carbonate is present as white patches; d) mixture of lizardite 1T, chlorite and talk; e&f) lizardite $2H_1$; g) felted chrysotile and g) fibrous chrysotile. Scale – each square on the scale bar represents 1 cm^2.

3.3. Methods

All samples obtained from the field were washed under running tap water, dried and then gently crushed to < 1 cm particles using a pestle and mortar. The resultant aggregates were then analysed under a binocular microscope and visually separated into host rock-free material for further analyses.

A detailed appraisal of the composition, *i.e.* structure, chemistry and texture of these serpentine minerals was made using a range of complementary analytical techniques (instrumental details are given in Appendix E). The techniques of XRD, FTIR and TGA were used collectively for mineral identification. The chemistry was assessed using XRF and SEM-EDS quantitative analysis. SEM together with optical microscopy was used for the characterisation of rock texture.

3.4. Results and Discussion

This section presents the results of a comparative textural, mineralogical and structural study of nine serpentine–rich specimens: two antigorite-rich, two chrysotile-rich and five lizardite-rich samples, as starting materials for the acid leaching experiments (Chapter 4). For clarity and to avoid back-referencing between the different analytical methods, a commentary is provided within an individual results section. The data is summarised in section 3.5.

3.4.1. Optical Microscopy

A petrographic polarising microscope was used for the textural assessment of minerals in thin section form, with emphasis on crystal sizes and spatial relationships. The thin sections were prepared from grain mounts of powder aggregates, rather than slivers of rock, as performed more usually.

The ***antigorite*** samples**, AML2** and **AML59**, showed distinctively different textural features in thin section. The crystals in sample AML2 were fine, predominantly < 50 µm in size and exhibited suture boundary contacts, giving rise to a massive, interlocking rock texture. The mineral was colourless and displayed grey shades 1st order interference colours (the interference colours aided mineral identification). A trace amount of a mineral exhibiting anomalous blue interference colours (probably chlorite) was observed also. The antigorite within sample AML59 (Figure 3.6a) was also colourless and again exhibited grey shades 1st order interference colours, with the crystals being elongated and near-fibrous. The length of the crystals was difficult to appraise due to the character of the thin section specimen, but their thickness did not usually exceed 10 µm. A trace amount of < 10 µm, roughly equant crystals with suture boundaries were observed to have inter-grown with the fibres. This sample also contained traces of carbonate and hematite.

The ***chrysotile*** samples**, AML6** and **AML60** exhibited similar optical features including fibrous morphologies, < 30 µm diameter in AML6, and < 5 µm diameter in AML60. The fibres in AML60 (from the New Amianthus asbestos mine) were longer and better-defined, while in AML6 the fibres were intimately inter-grown giving rise to “felted” texture. The serpentine minerals, in both samples, were colourless and displayed grey interference colours. Sample AML60 also contained a significant amount of calcite. Analysis of chrysotile samples proved difficult due

to their fine crystallinity and small particle size and thus no images are presented in Figure 3.6.

The ***lizardite*** samples, **AML4** (Figure 3.6b) and **AML46** (Figure 3.6c) displayed a wide textural diversity. The lizardite 1T in sample **AML4** was generally colourless, with some crystals displaying faint orange- to green-beige pleochroism. The interference colours were low to mid 1st order grey, and the extinction was uneven and mostly undulatory probably reflecting distortion or deformation of the crystal structure. Sample **AML46** was the most inhomogeneous of all analysed. Apart from lizardite, the other minerals identified optically and confirmed subsequently by XRD included talc, chlorite, halite and quartz. A mineral resembling muscovite was also observed, however, due to the character of the specimen (*i.e.* fine particles within a polished thin section (PTS), with aggregates causing possible distortion of optical properties) this identification was considered tentative. The lizardite mineral exhibited a plate-like morphology and very well-defined cleavage (Figure 3.6c). The sample also contained various composite particles containing inter-grown crystals of rosette-like, blocky and elongated morphologies with sutured boundaries and undulatory extinction. Some particles showed deformational textures, such as kink bands and broken laminae. The interference colours did not exceed usually greys of 1st order. There was also a small amount of iron oxide / hydroxide and carbonate minerals.

The ***lizardite*** sample **AML53** (Figure 3.6d) exhibited particles with composite / mosaic-like, elongated-laminate and uniform-blocky texture. All the particles represented fragments of finely ground vein material. Again, the nature of this PTS specimen, *i.e.* randomly distributed grains of milled powder acted to obscure the natural spatial relationships. The composite particles were complex and

comprised discretely inter-grown crystals and < 20 µm thick fibrous crystal veinlets. They displayed patchy extinction and grey interference colours. Uniform-blocky particles were the second most common feature. Some of them displayed strain texture reflected in uneven, undulatory extinction and sutured boundaries. Greys of low 1st order interference colours, rarely reaching faint yellows of mid-1st order were observed. The elongated particles were relatively scarce, and displayed slightly higher interference colours of yellows of mid-1st order, and sweeping extinction. Scarce rosette-like aggregates, approximately 150 µm in diameter, again with sweeping extinction were present in association with the above.

Lizardite sample **AML57** (Figure 3.6e) was prepared as both crushed material and as a thin section of rock sliver - both specimens displayed similar textural features. Despite the uniform character of the hand specimen sample, considerable textural diversity was observed in thin section with evidence for brittle deformation and possible recrystallization. Feather-like crystals with sutured boundaries, expanded ribbon-like (almost boudinage-like) large crystals, and relatively uniform “smooth” zones were observed in the rock sliver, in agreement with features seen in the powder PTS sample. Accordingly, the extinction was sweeping and irregular, confirming a high degree of deformation.

Sample **AML62,** tentatively identified as polygonal serpentine exhibited “felted” cross-hatched texture of intimately inter-grown crystals set in a fine matrix (Figure 3.6f).

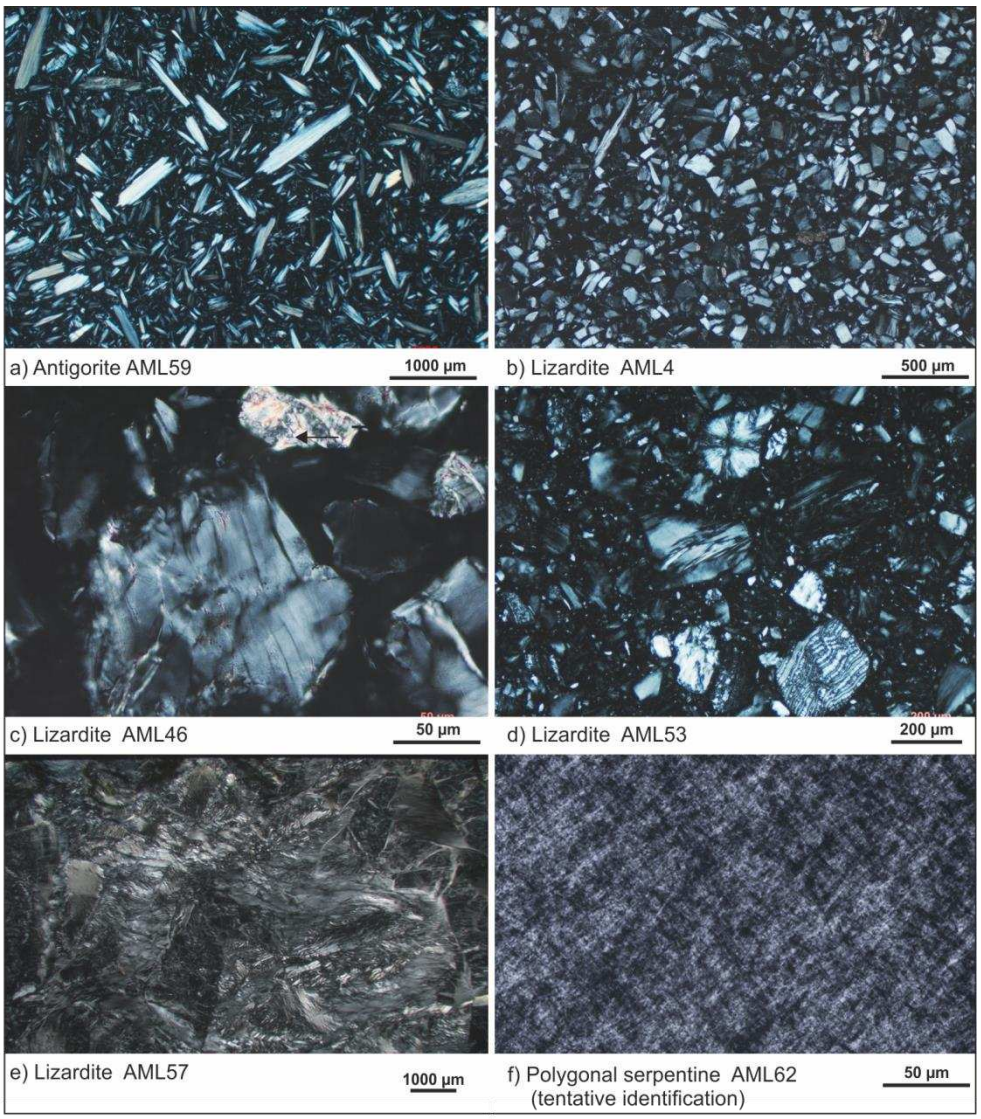


Figure 3.6 Crossed polarised light images of the serpentine samples used in this study: a) elongate particles of antigorite^{AML59}, no image is presented for antigorite^{AML2} due to optical similarity; b) equant particles of lizardite 1T^{AML4}; c) lizardite 1T^{AML46} with a well-developed cleavage; d) textural diversity in lizardite 2H$_1$^{AML53};, e) and f) prepared from fragments of rock not powders and show natural texture of lizardite 2H$_1$^{AML57} and polygonal serpentine^{AML62}, respectively. Due to analytical difficulties, no images are shown for chrysotile samples.

3.4.2. X-ray Diffraction

PXRD analysis was performed with reference to Powder Diffraction File (PDF) patterns, as recommended by Wicks [*Wicks*, 2000], or using well documented literature patterns, listed as "Indexed or Star Quality", *e.g.* 00-050-1625 [*M. Mellini and Viti*, 1994a] for lizardite 1T or 01-084-1391 [*M. Mellini and Zanazzi*, 1987] for lizardite $2H_1$.

Based on the comparison of a full experimental diffraction pattern with that calculated from ideal structural data of expected phases, the samples were identified as:

- **Antigorite** – samples **AML2** and **AML59**
- **Chrysotile** – samples **AML6** and **AML60**
- **Lizardite 1T** (1 layer trigonal polytype) – sample **AML4**
- **Polygonal lizardite** with 1M (1 layer monoclinic polytype) sectors – sample **AML62** (tentative identification)
- **Lizardite $2H_1$** (2 layer hexagonal polytype) – samples **AML53** and **AML57**

A summary of the XRD analyses, combining quantitative & semi-quantitative results, along with associated crystal structure references are presented in Table 3.2. A few minor, unexplained diffraction peaks, of low intensity, were not included in the quantification. However, where present, it is noted that the quantified results, as reported, might be slightly erroneous, *e.g.* samples AML57 and AML62.

Table 3.2 Summary of PXRD data (analyses performed in collaboration with Ms D. Wagner). Reference - provides detailed information on crystal structure.*

Sample	Reference *	Antigorite	Lizardite 1T	Polygonal serpentine	Lizardite $2H_1$	Chrysotile	Talc	Chlorite	Calcite	Dolomite	Magnetite	Hematite	Halite	Unidentified peaks
AML2 01-087-2096	NA	Major	-	-	-	-	-	-	-	-	Trace	-	-	
AML59 00-007-0417	[*Hess et al.*, 1952]	98.8	1.2	-	-	-	-	-	-	-	-	Trace	-	
AML4 01-082-1838	[*M. Mellini and Viti*, 1994b]	-	79.9	-	-	19.6	-	-	-	0.5	-	-	-	
AML46 01-080-4148	[*M. Mellini et al.*]	-	89	-	-	-	1.2	9.4	-	-	-	-	0.3	
AML62 00-050-1606	[*Krstanovic*, 1997]	-	5.9	94.1	-	-	-	-	-	-	-	-	-	4.52A, antigorite?
AML53 01-084-1391	[*M. Mellini and Zanazzi*, 1987]	-	-	-	99.1	0.9	-	-	-	-	-	-	-	
AML57 01-084-1391	[*M. Mellini and Zanazzi*, 1987]	-	-	-	98	2	-	-	-	-	-	-	-	4.24A, Na, Al silicate?
AML6 00-052-1562	[*Bailey*, 1988]	-	-	-	-	94.7	-	-	-	-	4.3	1	-	
AML60 00-010-0381	[*Whittaker and Zussman*, 1956]	-	-	-	-	87.7	1.4	-	11.1	-	-	-	-	

The analysis of PXRD patterns for ***antigorite samples*** (**AML2** and **AML59**) proved to be relatively straightforward, with good whole pattern fit being obtained using 01-087-2096 and 00-007-0417 [crystal structure, *Hess et al.*, 1952]. These samples were largely monomineralic with the presence of only minor amounts of magnetite in AML2 and a trace amount of hematite in AML59. These trace iron-rich phases were identified also within the ***chrysotile sample*** **AML6**, as identified using PDF 00-052-1562 [crystal structure, *Bailey*, 1988]. ***Chrysotile AML60***, indexed using PDF 00-010-0381 [crystal structure, *Whittaker and Zussman*, 1956], was found to contain significant amounts of calcite (~ 10%) as well as a trace amount of talc.

The analysis of ***lizardite samples*** proved to be much more challenging, and unequivocal results could be obtained only by using a combination of analysis techniques (see XRD challenges below, Section 3.4.2.1.)

All ***lizardite*** samples were spiked with quartz to assist with quantitative analysis. However, for samples containing significant amounts of chrysotile (*e.g.* AML4), qualitative analysis was performed also without quartz, due to the significant overlap of (202) at 2.45 Å in chrysotile with (110) in quartz.

Sample AML4 (Figure 3.7) was confirmed as ***lizardite 1T,*** based on a very good whole pattern fit with PDF 01-082-1838 [crystal structure, *M. Mellini and Viti*, 1994b], in agreement with a well-documented, refined structure for lizardite from the same locality [*Gregorkiewitz et al.*, 1996; *M. Mellini and Viti*, 1994b]. The PDF pattern also matched that recommended by Wicks [*Wicks*, 2000]. PDF 00-010-0381 [crystal structure, *Whittaker and Zussman*, 1956] for chrysotile was used to explain the diffraction peaks at 2.58, 2.54, 2.45, 2.27 and 2.09 Å, whilst an unassigned feature at ˜2.61 Å was attributed tentatively to lizardite $2H_1$.

Polygonal serpentine has been detected previously in samples from this locality [*M. Mellini and Viti*, 1994b] but no reference powder diffraction pattern was available in the ICSD PDF4 database.

Samples **AML53** and **AML57** (Figures 3.8) were identified as ***lizardite 2H$_1$*** using PDF 01-084-1391 (quality S-star structure, as determined by Mellini and Zanazzi [*M. Mellini and Zanazzi*, 1987]). A significant diffraction peak that appears to be diagnostic for that phase occurs at 2θ = 40.03° corresponding to (111), 2.61 Å (being absent from lizardite 1T). It is noted that a good initial whole pattern fit (including the peak at 2.61 Å) could be obtained for chrysotile-2Oc1 using PDF 00-052-1563, however this data set was not in agreement with the complementary FTIR and TGA data provided below (Sections 3.4.6 and 3.4.7). 2Oc1 was the only ortho-chrysotile pattern available in the ICSD database but was not recommended by Wicks (2000) [19]. The lizardite 6T polytype, PDF 00-046-1445, was also considered, but discarded as the full pattern fit was poorer than that for L2H$_1$, and the quality of this PDF reference data was questionable (marked as B-blank).

The PXRD patterns for **AML53** and **AML57** exhibited the same peak positions but slightly different relative intensities, with the latter exhibiting less intense, broader peaks. For example, two well-defined peaks in AML53 at (102) and (104), *d* spacings 3.89 Å and 2.86 Å, respectively, were only denoted by very low intensity, broad humps in AML57. This is attributable to a lower extent of crystallinity (*i.e.* less ordered crystal structure) in agreement with high degree of deformation within AML57 observed in thin section microscopy. A low intensity peak at 2.45 Å within both diffractograms was tentatively attributed to trace amounts of chrysotile, (202), which was observed also in the thin section veins.

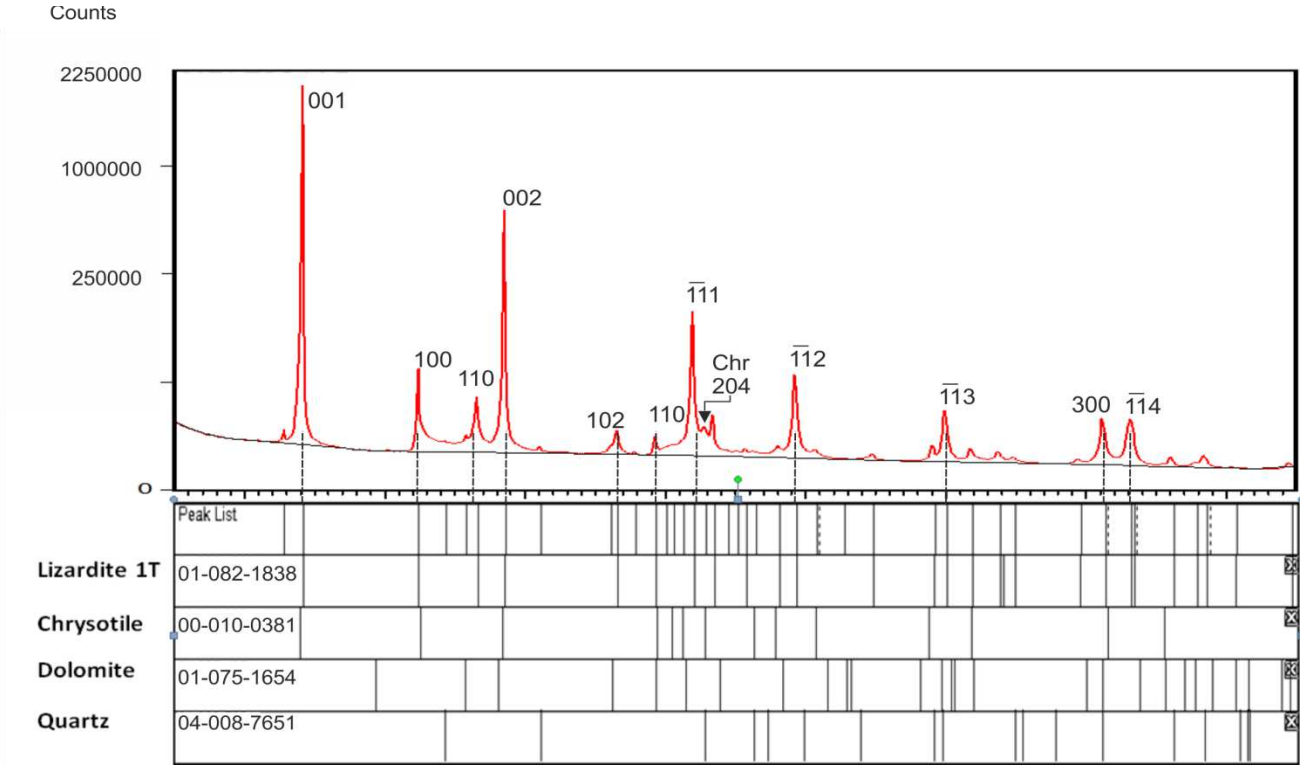


Figure 3.7 X-ray diffractogram for sample AML4 containing lizardite 1T and trace amounts of chrysotile, dolomite and quartz. Miller indices are shown for the dominant phase of lizardite 1T. The line figure shows the experimental pattern acquired at the top and calculated patterns extracted from PDF data corresponding to the candidate phases present.

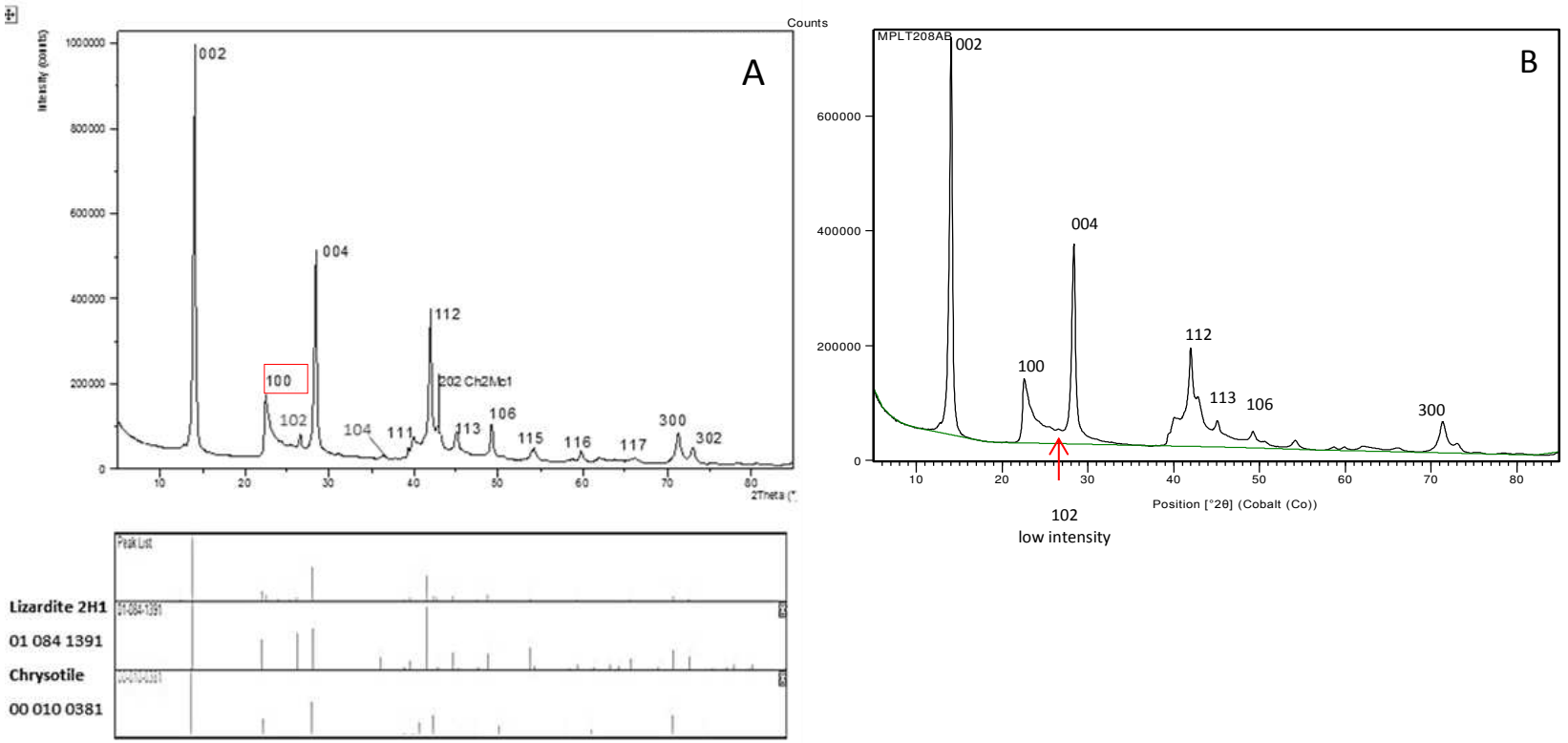


Figure 3.8 PXRD patterns for (a) AML53 and (b) AML57, assigned as lizardite $2H_1$. The differences in peak sharpness are attributed to differences in the crystallinity (degree of order within the crystal structure) with AML57 appearing to be less crystalline (less ordered crystal structure).

Sample **AML62** (from Montecastelli Pisano) was identified as being a mixture of ***lizardite 1M*** (86.6%) and ***lizardite 1T*** (5.4%) (Figure 3.9). This identification was based on a very good whole pattern fit with PDF 00-050-1606, produced by Krstanovic, from monoclinic lizardite from Crni Kamen, Serbia [*Krstanovic*, 1997]. Additional diffraction peaks at 3.89 Å, 2.50 Å, 2.42 Å and 2.14 Å corresponding to (010), ($\bar{1}\bar{1}1$), (003) and ($\bar{1}\bar{1}2$), respectively, were assigned to trigonal lizardite with reference to PDF 01-082-1838. An unassigned peak at 4.51 Å was tentatively attributed to antigorite (220).

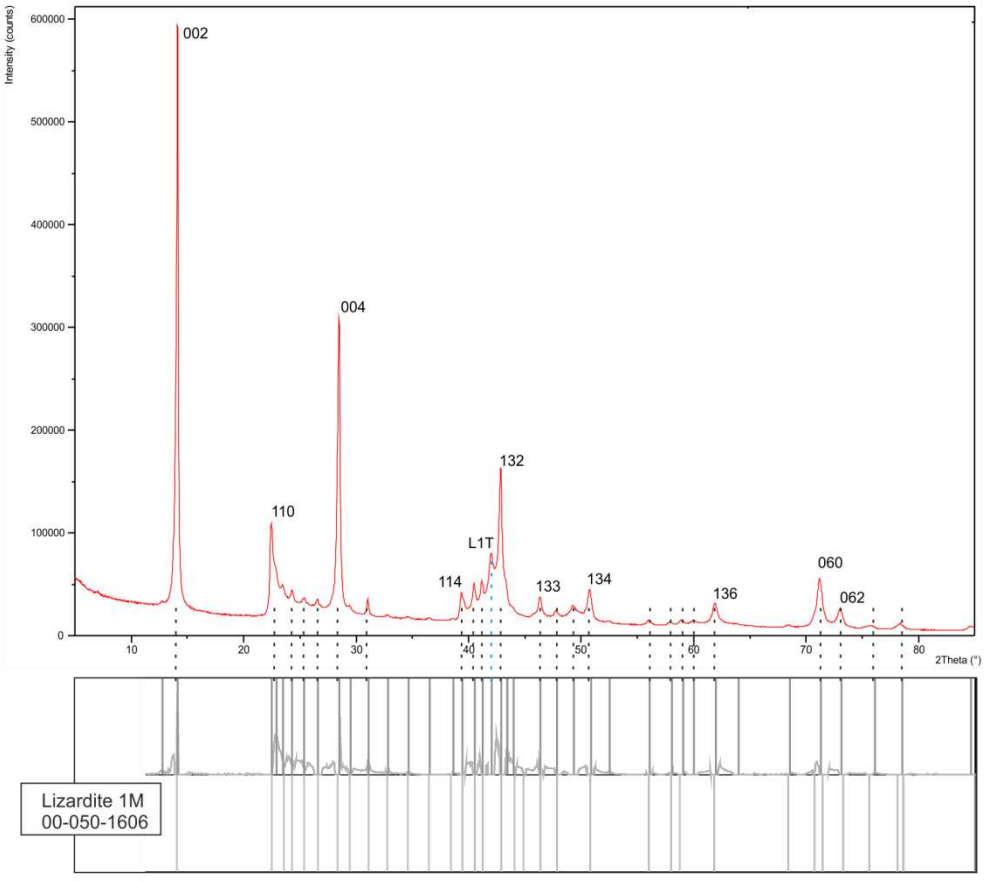


Figure 3.9 PXRD pattern for sample AML62, identified as being a mixture of lizardite 1M (dashed lines) and lizardite 1T (blue line) (01-082-1838).

The PXRD analysis of sample **AML46** (Kennack Cove, Cornwall) was largely ambiguous because good pattern fits were obtained for both monoclinic (PDF 04-013-7650) and trigonal (PDF 04-012-9602) symmetries. These reference patterns appeared to be nearly identical in terms of peak position, even though the unit cell parameters as stated in the PDF documents were dissimilar. It is noted that the 04-013-7650 PDF pattern (monoclinic) from a mineral sample obtained also from Kennack Cove, Lizard, with reference to crystal structure measurement by Rucklidge and Zussman [*Rucklidge and Zussman*, 1965], states that all crystallographic angles are 90° despite the fact that the β angle is ≠ 90° for a true monoclinic system. The reason for this discrepancy is unknown. Careful examination of the two reference patterns revealed subtle variations in peak intensities, although this parameter is strongly affected by preferred orientation and hence should not be regarded as a diagnostic tool.

Ultimately, based on comparison with a pattern obtained for a mineral that also originated from the Lizard Peninsula, at Gew Graze, *i.e.* lizardite 1T 01-080-4148 (structure reference [*M. Mellini et al.*, 2010]) and with lizardite $1T^{AML4}$, the sample ***lizardite***^{AML46} was identified as being a trigonal polytype, being slightly less crystalline (less ordered structure) than AML4. Other minerals identified within AML46 included talc, chlorite and halite. It is considered that halite originated from sea salt fines deposited in and around this coastally-located sample.

The number of peaks in an XRD scan provide information on the symmetry of the mineral, *i.e.* the lower the number of reflections, the larger the number of systematic extinctions, the higher the symmetry. This general trend was observed for lizardite samples analysed in this study, as illustrated in Figure 3.10. The number of distinct peaks decreases from lizardite $2H_1$ to lizardite 1T, being the

highest symmetry serpentine mineral. Lizardite 1M shown in Figure 3.9, being the lowest symmetry, contains noticeably more reflections.

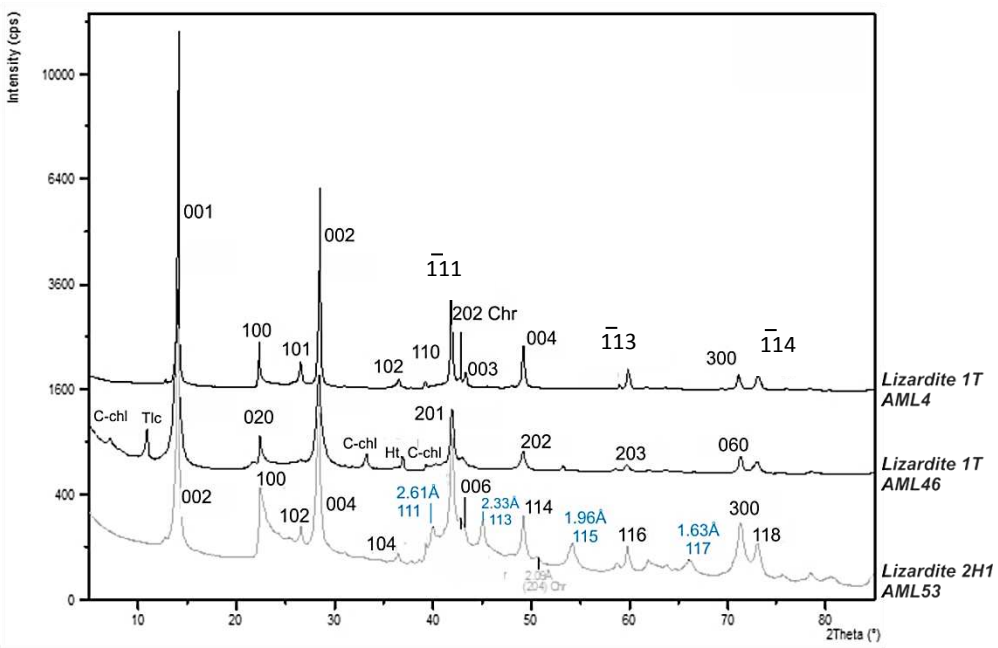


Figure 3.10 Comparison of XRD patterns for samples of lizardite 1T AML4, AML46 and lizardite $2H_1$ AML53. Sample AML46 contained impurities, in the form of clinochlore (C-chl), talc (Tlc) and halite (Ht). The peaks diagnostic for lizardite $2H_1$ are highlighted in blue.

3.4.2.1. XRD challenges

This crystallographic study highlighted previously made statements on the challenges and difficulties of powder XRD analyses of serpentine minerals. Accurate identification and quantification of serpentine mineral polymorphs, and polytypes in particular, is often obstructed by: poor crystallinity (in the context of crystal / amorphous content) giving rise to poor diffraction data [*Marcello Mellini*, 2013], strong superposition of the main diffraction peaks [*Cavallo and Rimoldi*, 2013], and high degree of sample heterogeneity [*Gualtieri et al.*, 2014; *Cecilia Viti*,

2010]. The sample volume analysed is rarely monomineralic [*Viti and Mellini*, 1997], which makes it difficult to obtain reliable data from a pure mineral that could act subsequently as a reference for the analysis of unknown samples. All these challenges raise questions over the accuracy of powder diffraction data within the Inorganic Crystal Structures Database (ICSD) of serpentine minerals, and a comprehensive appraisal of the quality of these PXRD patterns is given by Wicks [*Wicks*, 2000].

Quantitative analysis of powder diffraction data may be performed using Rietveld Refinement, the reference intensity ratio (RIR) technique, or a combination of both. The Rietveld Refinement technique involves comparison of a full experimental pattern with one calculated from ideal structural data of expected phases [*Giacomini et al.*, 2010]. Since the likelihood of stacking disorders in serpentine minerals is high, a straightforward application of the Rietveld method is not recommended [*Gualtieri and Artioli*, 1995]. Similarly, the RIR method may give erroneous results if applied on its own, as the preferred orientation of serpentine mineral crystals may not be taken properly into account [*idem*.]. However, a combination of Rietveld Refinment and the RIR technique has been applied previously to quantify the amount of chrysotile in bulk samples, and it was concluded that the methods applied together were successful for the appraisal of 1 – 50 wt% chrysotile [*Gualtieri and Artioli*, 1995]. This approach was used recently to assess the amount of chrysotile in highly contaminated mine tailings [*Gualtieri et al.*, 2014]. Gualtieri and Artioli [*Gualtieri and Artioli*, 1995] stated also that for mixed samples with severe peak overlaps, deconvolution is possible using robust fitting procedures and the application of crystallographic constraints, both provided by Rietveld fitting. It was suggested to focus on the analysis of serpentine minerals peaks with limited overlap, *e.g.* $(13\bar{1})$ for antigorite at 2.52 Å is well separated from $(\bar{2}02)$ at 2.45 Å and (202) at 2.55 Å for chrysotile.

As confirmed by this part of the study, the greatest difficulty in phase identification relates to the appraisal of mixed chrysotile and lizardite polytypic samples. Peak overlaps are severe and mineral differentiation becomes virtually impossible. Accordingly, FTIR and TGA were used in to aid qualitative analysis (Sections 3.4.6 and 3.4.7). Quantitative analysis using Rietveld Refinement was attempted also. Nevertheless, the results for some samples remained inconclusive and for those, only semi-quantitative data was presented (Table 3.2).

3.4.3. Scanning Electron Microscopy, including quantitative EDS analysis

SEM analyses were performed on grain mounts as well as carbon sputter coated polished thin sections. The results of the grain mount analyses, *i.e.* the morphological features of grains before and after the acid leaching experiments, are presented in Chapter 4. However, it was noted that almost every grain mount sample contained trace amount of fibres (probably chrysotile), confirming that natural serpentine samples are rarely monomineralic (mono-polymorphic), with direct implication for the quantitative and qualitative PXRD analyses.

The spatial relationships and morphologies of crystals were appraised from polished thin sections and exemplary images are shown in Figure 3.11. Antigorite sample **AML2** exhibited relatively uniform textures and composition with only minor impurity on magnetite (Figure 3.11a). The crystals were finely inter-grown, forming a dense mosaic.

Lizardite 1T and chrysotile from sample **AML4** (Monte Fico, Elba) appeared to be intimately inter-grown, with the latter filling the residual porosity between truncated prismatic lizardite crystals (Figure 3.11b). A similar crystal morphology was observed for lizardite $2H_1$ (**AML53** and **AML57**, *e.g.* Figure 3.11d) where the

prisms were embedded in a matrix of low BSE contrast (lower atomic number). In conjunction with the PXRD data, the matrix was attributed to a slightly more hydrous lizardite. The prisms were often distinctively trigonal and radially arranged around a specific point, suggesting that they constituted fragments of polygonal serpentine, similar to that previously observed in samples from Gew Graze, Lizard Peninsula [*Cressey et al.*, 2008]. The lizardite $2H_1$ samples also contained < 30 µm wide veins of fibrous serpentine, probably chrysotile.

The lizardite–rich sample **AML46** (Kennack Sands, Figure 3.11c) exhibited a wide morphological and compositional diversity, with the presence of talc and chlorite inferred from the BSE images and confirmed by XRD. The crystals were usually micro-porous and frequently cleaved.

Polygonal serpentine sample **AML62** exhibited "felted" micro-texture of elongate, often nano-tubular, and randomly oriented, <1 µm diameter crystals in a locally porous matrix of other, unidentified but likely less-hydrous, serpentine mineral (Figure 3.11d). The chrysotile sample **AML60** (Figure 3.11f) was dominated by long fibres, whilst **AML6** was dominated by elongate prisms.

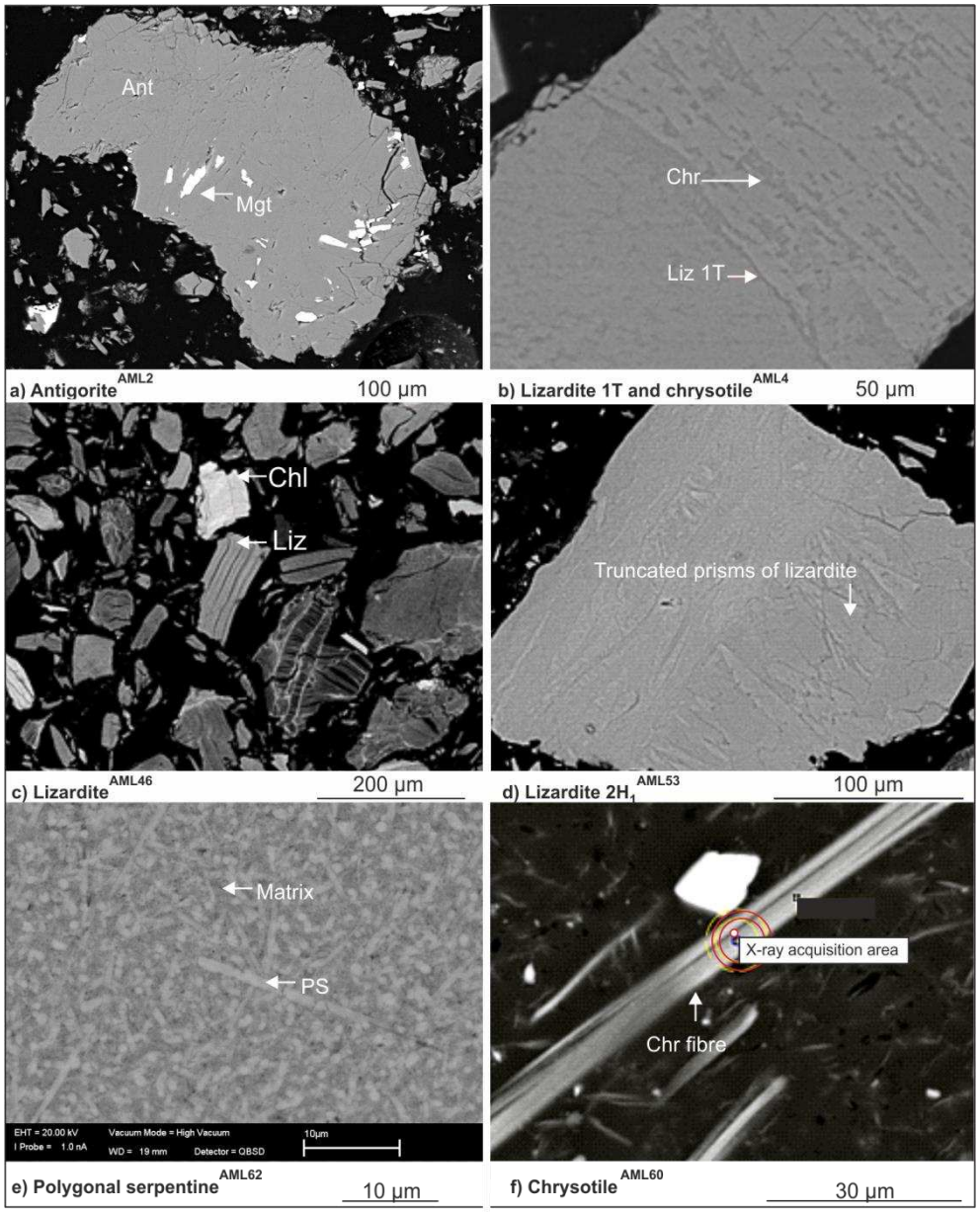


Figure 3.11 Exemplar BSE images of serpentine mineral polished thin sections showing: a) compositionally uniform antigorite[AML2], bright speckles within the grain correspond to magnetite (Mgt); Antigorite[AML59] exhibited similar features, b) lizardite (Liz) and chrysotile (Chr) from sample AML4; c) particles of lizardite (Liz) and chlorite (Chl) in AML46; d) a particle with prismatic crystals of lizardite $2H_1$ in sample AML57; e) polygonal serpentine (PS) in porous matrix of less-hydrous serpentine; f) a fibre of chrysotile from AML60 sample, also showing the site of SEM-EDS acquisition spot. Chrysotile AML6 exhibited similar features.

3.4.3.1. Quantitative SEM-EDS analysis

The aim of the SEM-EDS part of this study was to appraise the chemical composition of the minerals within these serpentine-rich samples on the fine scale. Quantitative compositional data is presented in terms of wt% oxide, with analytical totals and atoms per formula unit (apfu) values calculated on the basis of 7 oxygens (Table 3.3).

Table 3.3 Overview of quantitative SEM-EDS analyses of serpentine minerals. The data correspond to individual analysis, it is not a mean value.

	Antigorite AML2	Antigorite AML59	Lizardite 1T AML4	Chrysotile AMl4	Lizardite $2H_1$ AML53	Lizardite $2H_1$ AML57	Lizardite AMl62	Talc* AMl46
MgO	38.96	38.35	39.36	38.52	42.28	40.92	38.28	31.09
Al_2O_3	1.42	0.25	3.1	1.89	0.12	0.42	2.55	0.21
SiO_2	44.02	45.15	41.74	43.63	44.69	44.53	41.66	62.72
FeO	3.57	5.39	3.88	2.94	1.06	1.5	2.78	nd
Cr_2O_3	0.3	nd	nd	nd	nd	nd	nd	nd
NiO	0.13	nd	nd	nd	nd	0.28	nd	0.45
Total	**88.4**	**89.15**	**88.09**	**86.97**	**88.19**	**87.64**	**85.28***	**94.47**
Apfu values calculated on the basis of 7 oxygens								
Si	2.03	2.07	1.94	2.03	2.04	2.05	1.98	8
$^{[IV]}Al$	-	-	0.06	-	-	-	0.02	-
$^{[IV]}\Sigma$	2.03	2.07	2.0	2.03	2.04	2.05	2.0	-
Mg	2.67	2.66	2.72	2.67	2.87	2.8	2.71	5.91
Fe	0.14	0.17	0.15	0.11	0.04	0.06	0.11	-
Cr	0.01	-	-	-	-	-	-	-
Ni	0.01	-	-	-	-	0.01	-	0.05
$^{[VI]}Al$	0.08	0.02	0.11	0.1	0.01	0.02	0.12	0.03
$^{[VI]}\Sigma$	2.92	2.85	2. 98	2.89	2.93	2.89	2.95	5.99

**The low analytical totals (<87) was probably related to the fine crystallinity and mineral instability under the electron beam. "nd" - not detected. The data for talc present within AML46 is consistent with expectation and is included in Table 4.3.*

SEM-EDS quantitative analyses revealed minor compositional inhomogeneities in minerals within the same specimen, related mainly to the presence of variable, usually trace, amounts of Al, Fe, Mn and Cr, and the degree of hydration, in practice manifested as subtle contrast differences in the BSE images.

The presence of Al in the tetrahedral site of serpentine minerals affects their stability, further investigated in the context of acid-leaching experiments investigated in Chapter 4. Accordingly, based on quantitative analysis, the starting samples were classified into three groups (Figure 3.13):

(i) *low Fe and/or Al content;* FeO < 2 wt% and Al_2O_3 < 1 wt% - $L2H_1$

(ii) *moderate Fe and/or Al content;* FeO < 4 wt% and Al_2O_3 < 2 wt% - antigorite^{AML2} and chrysotile (from AML4 sample, Monte Fico, Elba)

(iii) *high Fe and/or Al content;* FeO < 5.5 wt% and Al_2O_3 < 3.5 wt% - antigorite-picrolite^{AML2}, lizardite 1T^{AML4} and polygonal serpentine^{AML62}

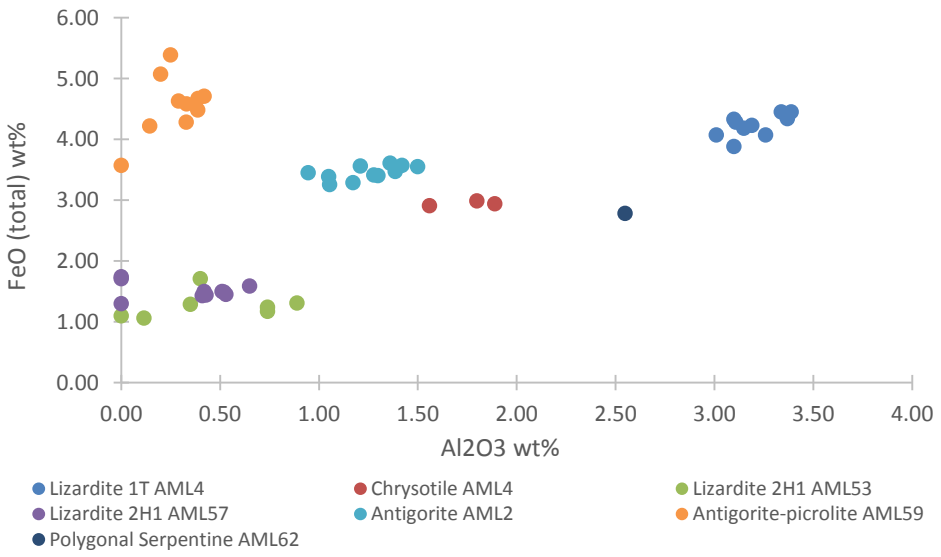


Figure 3.13 Variation in Al_2O_3 to Fe-O ratios for the serpentine minerals used in this study, from SEM-EDS quantitative analysis. Due to instability under electron beam, the data collection for chrysotile and lizardite AML46 was obscured and thus not included in the plot. The presence of Al in the serpentine crystal structure affects their stability, a parameter further discussed in the context of acid-leaching in Chapter 4.

Elemental substitutions varied from sample to sample, but the variations were generally insignificant for the tetrahedral positions, with the exception of lizardite $1T^{AML4}$ (Monte Fico), where Si^{4+} was substituted by Al^{3+}. For this sample the composition was in agreement with previous measurements [*M. Mellini and Viti*, 1994b] and determined as:

$$(Mg_{2.72}\,Fe^{total}_{0.15}\,Al_{0.11})_{\Sigma 2.98}\,(Si_{1.94}\,Al_{0.06})_{\Sigma 2}\,O_5(OH)_4$$

All the other minerals analysed in this study exhibited full (slightly overcharged) Si^{4+} occupancy of the tetrahedral sites and any substitutions, if present, were related to the octahedral positions. For example, composition for lizardite $2H_1^{AML57}$ was determined to be:

$$(Mg_{2.80}Fe_{0.06}Ni_{0.01}Al_{0.02})_{\Sigma 2.98}Si_{2.05}O_5(OH)_4$$

3.4.3.2. SEM-EDS challenges

The analytical totals for serpentine minerals from EDS analysis, where only elements with atomic number greater than 5 (Boron, thin Be-window) were analysed, should theoretically be 100% minus the amount of water in the crystal structure. The amount of water within antigorite is expected to be between 11.0 - 13.5 wt%; for lizardite 12 - 15 wt%; and a similar or slightly higher value for chrysotile [*Page*, 1968]. This gives rise to total values of ~ 87 - 89 wt% for antigorite, and correspondingly lower values for the other two polymorphs. However, a significant number of quantitative analyses in this study fell below these anticipated values, reflecting the challenges associated with data acquisition such as fine crystallinity of the minerals, inhomogeneity of the samples, serpentine beam sensitivity, as indicated above. Accordingly, only 'representative' analyses consistent with previous studies, and other results

obtained in this study, are presented in Table 3.3. The results obtained for fine-scale crystalline samples of chrysotile (AML60) and lizardite (AML46) were also found to be systematically lower than would be expected for serpentine minerals. A full set of analyses, ~ 10 per mineral, including lizardite 1T, lizardite $2H_1$, antigorite and chrysotile^{AML60} (shown only for comparison), is presented in Appendix A (Table A.3.).

The data was compared to analyses reported in "DHZ Rock Forming Minerals" [*Deer et al.*, 2009] and the analyses by Viti & Mellini [*C. Viti and Mellini*, 1997] for lizardite and chrysotile from Monte Fico, Italy. Although the analytical totals presented here were comparable to the previously published data, and corresponded to the anticipated values (100% - H_2O), small deficiency in octahedral site occupancy was observed for all of the other samples, and also corresponded to a small excess of Si. Whilst the origin of the discrepancy is uncertain, factors that made the SEM-EDS quantification process difficult included: the fine-scale crystallinity of the minerals (*e.g.* Figure 3.11d for a comparison of the X-ray acquisition spot and crystal size in chrysotile^{AML60}), inclined grain boundaries, sample inhomogeneity or material sensitivity to the electron beam.

3.4.4. Transmission Electron Microscopy

The TEM was used mainly for the bright field (BF) diffraction contrast imaging of crystal morphology. A few corresponding SAED patterns were also acquired.

Figure 3.15 presents an overview of the range of crystal morphologies of serpentine minerals encountered in this study. The crystals within the lizardite

samples were either platy or prismatic (Figures 3.15a-e). The lizardite samples also contained morphologies resembling nanotubes that could either reflect the presence of nanotubular serpentine or scrolls of lizardite platelets, as explained further in Section 3.4.4.1. Nanotubular morphologies were predominantly characteristic of chrysotile and for specific cross-sections of polygonal serpentine, but not for lizardite or antigorite. Indeed, a sample of chrysotile^{AML60} (Figure 3.15d) was characterised by long, narrow nanotubes with inner and outer diameters of 5 and 25 nm, respectively. Most of the grains analysed showed streaked SAED patterns (*e.g.* Figure 3.15a), indicative of the presence of thin planar defects, related to disorder in the stacking sequences of the layers.

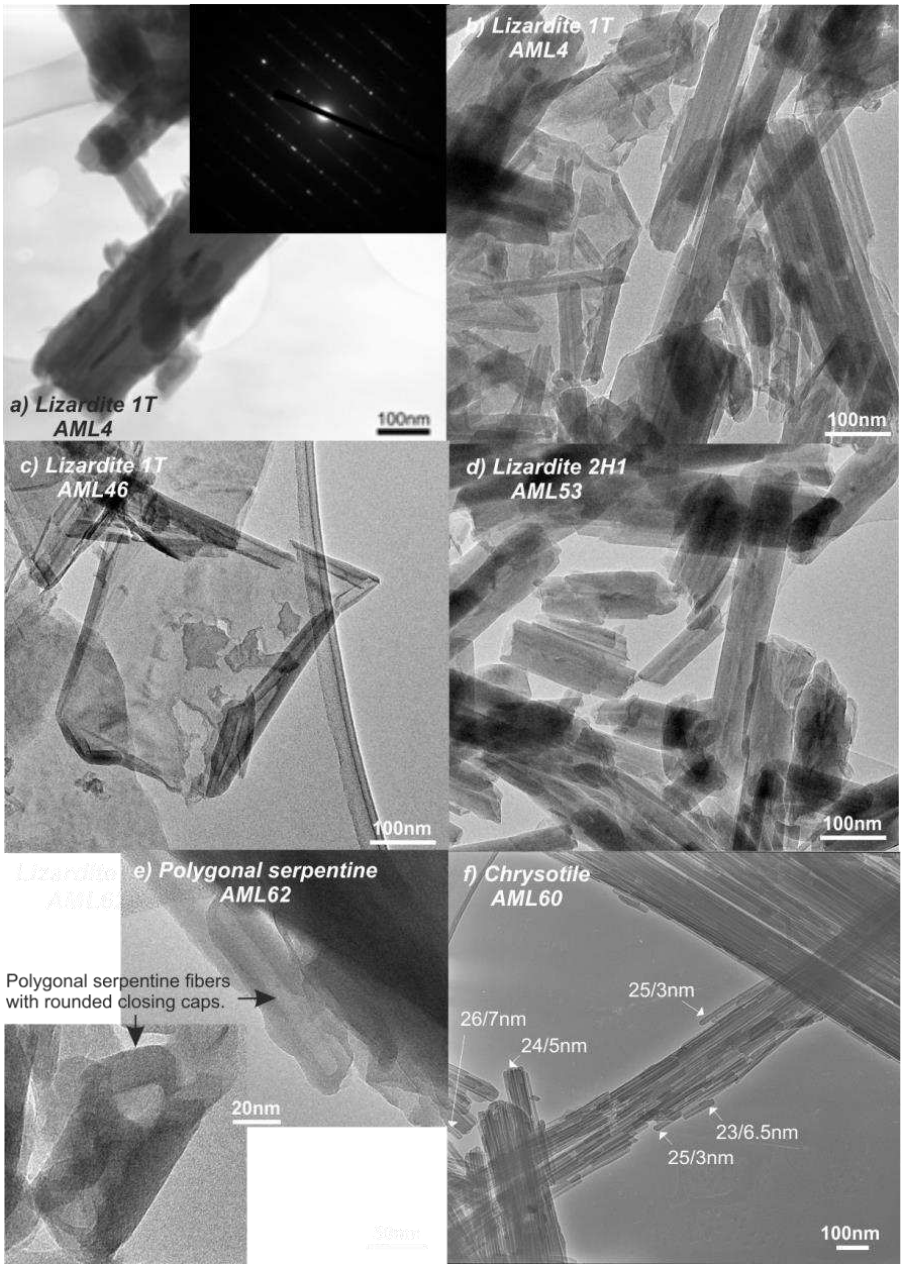


Figure 3.15 BF diffraction contrast TEM images of serpentine minerals analysed in this study: a) elongate crystal of lizardite $1T^{AML4}$ and as associated SAED pattern indicating presence of thin planar defects, related to disorder in the stacking sequences of the layers; b) elongate-tubular and platy particles originating from AML4 samples, probably representing chrysotile and lizardite crystals, respectively. The platy particle exhibits edge scrolling (see text for details); c) platy crystal of lizardite 1T from sample AML46, with a distinctive crystal edge scrolling, similar to that observed by Wicks and Chatfield [Wicks and Chatfield, 2005]; d) elongate crystals from lizardite $2H_1^{AML53}$; e) polygonal serpentine^{AML62} with rounded closing caps, similar to those previously observed by Baronnet et al [Baronnet et al., 2006] and f) nanotubular chrysotile from sample AML60.

3.4.4.1. TEM challenges

The primary aim of the TEM analyses was to provide additional information on the crystal structures of the serpentine minerals on the very fine scale. It, however, became apparent that the direct acquisition of SAED patterns and images of these minerals was not straightforward, due to problems related to the instability of these crystals under the high energy electron beam. The images shown in Figure 3.15 were acquired as quickly as practicable. However, dehydroxylation of the minerals was significant and in many cases occurred within a few seconds of exposure to the beam, leading to instantaneous amorphisation and prohibiting further analysis. A reduction of accelerating voltage from 200 kV to 100 kV and use of a TEM-cryo-stage didn't provide any significant improvement. Future investigations would require the use of low dose techniques, with a reduction of beam current density.

The dominance of nanotubular morphologies, as observed in TEM, was not consistent with the platelet morphologies expected for lizardite crystals, suggesting:

(i) The TEM samples examined contained a high proportion of chrysotile fibres, making the volume analysed not representative of the whole sample.

(ii) The presence of crystal scrolls. Wicks and Chatfield [*Wicks and Chatfield*, 2005] reported the tendency of thin, flat lizardite crystals to curl at their edges, in response to the relaxation of internal stresses. In some cases the scrolled edges detached from the crystals, or the whole lizardite crystal curled up, giving rise to morphologies that resembled chrysotile

nanotubes. Scrolls at crystal edges were observed in this study for lizardite $1T^{AML46}$ and lizardite $1M^{AML62}$ (Figure 3.15c,e). Detailed observations also revealed that some large diameter tubes, *e.g.* in lizardite $2H1^{AML53}$ (Figure 3.15d), were in fact half-tubes attached to fragments of diaphanous, flat-layer host particles. It is noted that scrolls could form also in response to exposure to the high energy electron beam.

3.4.5. X-ray Fluorescence

XRF analysis was performed for all samples and wt% oxide and loss of ignition values are given in Table 3.4.

Table 3.4 XRF compositional and loss of ignition data. The major components are in bold. The chemistry reflects the mineralogical heterogeneity of the samples. The Fe_2O_3 represents total iron

Sample name	*AML2*	*AML59*	*AML4*	*AML46*	*AML53*	*AML57*	*AML62*	*AML60*	*AML6*
Predominant mineral phase	**Antigorite**	**Antigorite**	**Lizardite 1T (+chrysotile)**	**Lizardite (+talc, chlorite)**	**Lizardite $2H_1$**	**Lizardite $2H_1$**	**Polygonal Serpentine**	**Chrysotile**	**Chrysotile**
SiO_2	**41.58**	**43.7**	**39.99**	**43.09**	**42.39**	**42.65**	**40.06**	**37.77**	**38.26**
TiO_2	<0.01	<0.01	<0.01	0.16	<0.01	<0.01	<0.01	<0.01	<0.01
Al_2O_3	**1.54**	**0.29**	**2.93**	**2.8**	**0.89**	**0.2**	**3.17**	**0.12**	**0.28**
Fe_2O_3 total	**6.63**	**4.15**	**4.28**	**1.36**	**1.85**	**1.04**	**3.29**	**1.82**	**11.19**
Mn_3O_4	0.09	0.13	0.04	0.12	0.03	0.03	0.04	0.26	0.08
MgO	**39.14**	**40.82**	**40.34**	**37.85**	**42.25**	**42.08**	**40.97**	**34.64**	**38.06**
CaO	<0.01	<0.01	0.14	0.05	0.01	0.02	0.02	7.96	0.13
Na_2O	<0.05	<0.05	<0.05	0.9	<0.05	<0.05	<0.05	<0.05	<0.05
Cr_2O_3	0.3	0.01	0.01	0.02	<0.01	0.01	<0.01	<0.01	<0.01
NiO	0.22	0.09	0.04	0.19	0.2	0.21	<0.01	<0.01	0.07
F	<0.1	<0.1	<0.1	<0.1	<0.1	<0.1	<0.1	<0.1	<0.1
Cl	<0.1	<0.1	<0.1	0.5	<0.1	<0.1	<0.1	<0.1	<0.1
Total	**89.51**	**89.19**	**87.77**	**87.18**	**87.62**	**86.24**	**87.55**	**82.58**	**88.07**
LOI	12.1	12.52	13.2	14.93	13.94	14.46	13.6	18.16	13.23

The XRF data confirmed that SiO_2 and MgO were the dominant components of all the samples, as expected. The chrysotile samples showed the lowest values for both oxides with ~ 38 wt% SiO_2 and 34-38 wt% MgO. The antigorites and lizardites showed consistently higher proportions of these oxides, with ~ 44 and 43 wt% SiO_2 and ~ 41 and 42 wt% MgO in antigorite and lizardite, respectively. The wt% oxides values for the lizardite-rich sample AML46 differed from the serpentine norm due to presence of talc and chlorite.

The Fe_2O_3 (representing total iron) identified in the samples could originate from more than one source but, as confirmed by SEM-EDS, most of the Fe was within the serpentine lattice itself. The increased Fe values in antigorite^{AML2} suggested the presence of magnetite, consistent with PXRD data.

CaO was generally attributed to (Ca/ ±Mg) carbonate impurities, whilst the ~ 8 wt% CaO value within chrysotile AML60 was attributed to calcite, consistent with the 11.1% value indicated by XRD.

For monomineralic serpentine samples, the LOI should be consistent with the crystal structure water content. Apart from samples AML60 and AML46 that contained other mineral phases, the values of LOI reported in Table 3.4 were in accordance with the values expected, suggesting that no carbonates or hydrous mineral phases were present in significant amounts.

3.4.6. Fourier Transform Infrared Analysis

The serpentine minerals can be successfully identified based on position of absorption bands in the infrared spectrum. Three well-defined spectral regions were observed for all the samples (Figure 3.16).

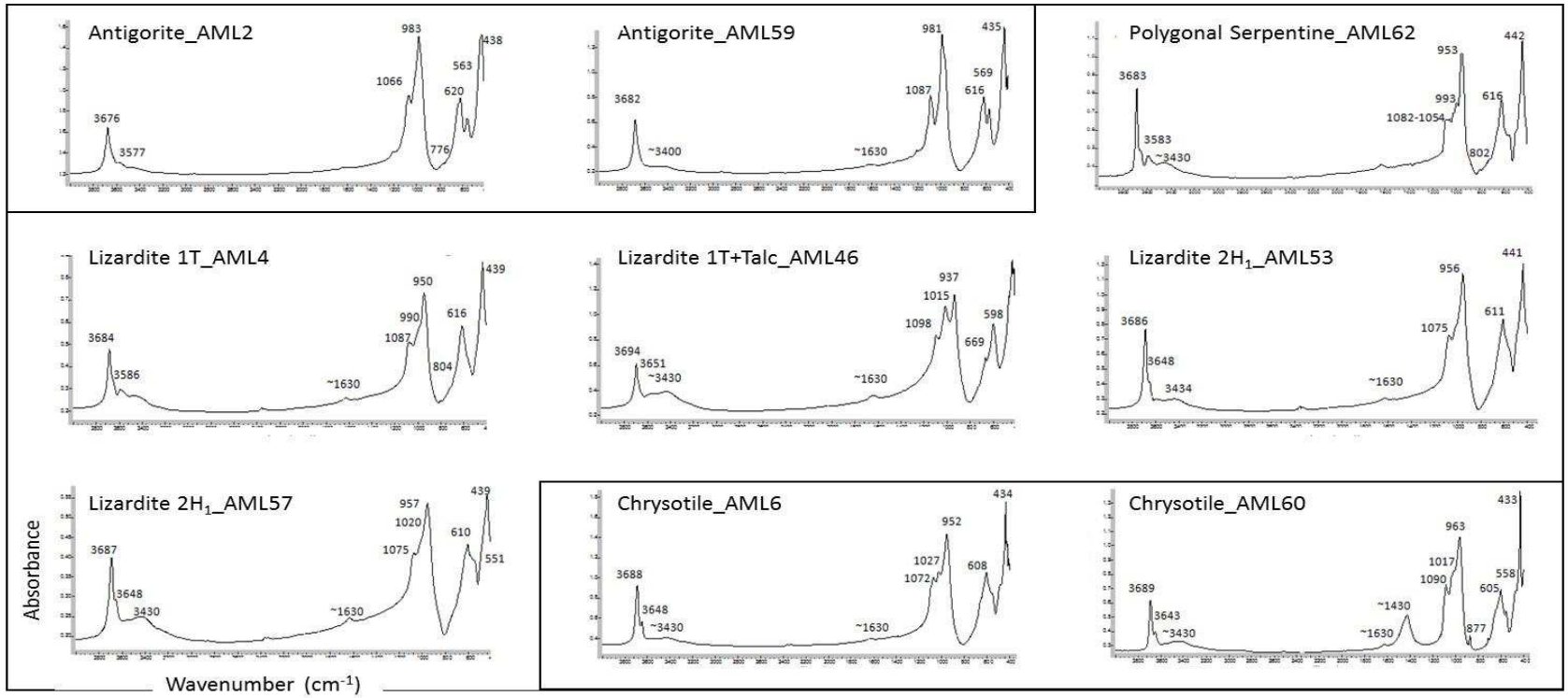


Figure 3.16 FTIR spectra of serpentine samples analysed in this study showing three main regions related to vibrations of OH-groups: 3400-3800 cm^{-1}, vibration of Si-O: 800-1200 cm^{-1} and a region below 800 cm^{-1} with bands of variable origin. The presence of chrysotile is manifested by a low intensity peak or hump at ca. 1030-1015 cm^{-1} as exemplified by AML6 and AML60. In antigorite a sharp diagnostic peak is present at ca. 560 cm^{-1}.

3.4.6.1. Stretching vibrations of hydroxyl groups (3400-3800 cm^{-1})

In this spectral region, the samples displayed a major peak, related to OH bonding with Mg cations in octahedral coordination, at wavenumber varying from 3676 cm^{-1} (antigorite^{AML2}) to 3694 cm^{-1} (lizardite-rich^{AML46}). This peak position depended on the type of octahedral cation and structural disorders [*Farmer*, 1974]. It was characterised by subtle asymmetry towards the lower energies with a distinctive shoulder occurring at ~ 3650 cm^{-1}. The asymmetry was attributed to a slight variation in O-H bond strength, possibly arising from heterogenic cation substitution in the predominantly Mg-dominated octahedral sites [*Fuchs et al.*, 1998; *M. Mellini et al.*, 2002]. In some samples, the asymmetry developed into a low intensity peak, particularly in lizardite-rich AML53, AML57 and chrysotile-rich AML6 and AML60. The peak position of stretching OH vibrations for the two antigorite samples differed slightly from 3676 cm^{-1} to 3682 cm^{-1} for antigorite^{AML2} and antigorite^{AML59}, respectively. The latter value was reported previously for fibrous antigorite (picrolite) [*Bishop et al.*, 2002], in agreement with our sample.

Two other lizardite-rich samples (AML4 and AML62) exhibited a low intensity absorption band at 3585 cm^{-1}. It is noted that a band at 3575 cm^{-1} in lizardite 1T from Monte Fico Elba (the same locality as AML4) was reported by Fuchs *et al.* and Balan [*Balan et al.*, 2002; *Fuchs et al.*, 1998] and attributed to hydroxyl bonded to ferrous Fe^{2+} atoms. The slight shift towards higher wavenumber, in our samples, suggests a stronger bond, and one possible way to strengthen the bond would be to permit trivalent rather than divalent substitution. This could correlate with the presence of significant levels of Al^{3+} in lizardite^{AML4}, lizardite^{AML62} and antigorite^{AML2}, as indicated by XRF. The two lizardite-rich samples also exhibited a band at ~ 805 cm^{-1} that was assigned previously to tetrahedrally-coordinated ferric (Fe^{3+}) iron [*Fuchs et al.*, 1998]. Antigorite^{AML2}, with above average aluminium

content (*ca.* 1.4 wt%), also exhibited a low intensity broad absorption band around 3580 cm^{-1}. All these findings pointed towards the coupled substitution of Fe^{3+} for Si^{4+} in tetrahedral (~800 cm^{-1}) and Al^{3+} for Mg^{2+} in octahedral coordination (~3583 cm^{-1}). The presence of Al^{3+} in the octahedral position compensates the charge imbalance resulting from trivalent substitution in the tetrahedral position. This type of substitution was used by Mellini [*M. Mellini*, 1982] to calculate the lizardite 1T formula on the basis of charge balance and five cations per unit cell [$(Mg_{2.79}Fe^{2+}_{0.04}Fe^{3+}_{0.10}Al_{0.07})(Si_{1.83}Al_{0.17})O_5(OH)_4$] and later modelled by Scholtzova [*Scholtzova and Smrcok*, 2005]. Balan *et al*. [*Balan et al.*, 2002] computed a theoretical infrared spectrum for lizardite 1T using first-principles quantum mechanical calculations and although they noted a low intensity band at 3584cm^{-1} in an experimental FTIR spectrum, they did not confirm it with the modelling. Balan (*ibid*.) assigned the experimental 3584 cm^{-1} band to a band at 3574 cm^{-1} reported by Fuchs *et al.* [*Fuchs et al.*, 1998] as Fe^{2+} for Mg^{2+} substitution at the octahedral site. The small discrepancy between peak positions may be due to analytical error or may indeed suggest additional trivalent cation substitution, and although inferences made here may be valid, they have to be cross-checked with a modelled spectrum. Modelling (using drift functional theory) of FTIR spectra for lizardite 1T, $2H_1$ and 1M is currently ongoing, in collaboration with Eva Scholtzova (Institute of Inorganic Chemistry, Slovak Academy of Sciences, Bratislava).

In addition, a wide, low intensity absorption band at approximately 3400 cm^{-1} was observed. The origin of this absorption band is equivocal and assigned to the vibrations of water molecules adsorbed to the minerals [*Anbalagan et al.*, 2010] or to interlayer hydrogen bonding, promoted by the substitution of trivalent cations, *i.e.* Al^{3+} or Fe^{3+}, in both tetrahedral and octahedral sites [*Fuchs et al.*, 1998; *Marcello Mellini et al.*, 2002; *Serna et al.*, 1979]. Serna [*Serna et al.*, 1979]

noted that with increasing Al^{3+} content the absorption shifts slightly to lower frequencies.

3.4.6.2. Stretching vibrations of the tetrahedral sheet (800-1200 cm^{-1})

Depending on the structure of the serpentine mineral, two or three main bands in the 800 - 1200 cm^{-1} spectral region could be distinguished. The highest energy band, for the samples analysed, ranging from 1066 - 1098 cm^{-1}, was attributed to the stretching of apical Si-O bonds. This peak was sharp and usually asymmetric. The lowest energy band, from 937 - 983 cm^{-1}, was attributed to the vibration of Si-O bonds in the basal plane. The wide range of values could have originated from subtle changes in bond length, reflecting the varying degrees of elemental substitution. This lower peak was usually sharp, mostly symmetric, with minor tilt towards the higher wavenumber (*e.g.* antigorite[AML59]). Chrysotile exhibited another absorption band at ~ 1025 cm^{-1} that was assigned to the second Si-O-Si vibration in the basal plane. This peak was characteristic for chrysotile and related to the electrostatic properties of nanotubes [*Balan et al.*, 2002]. Chrysotile[AML60] also exhibited a low intensity peak at *ca.* 1039 cm^{-1}. Some other samples analysed also displayed a minor shoulder in that area, and this was probably indicative of chrysotile and polygonal serpentine impurities, as observed previously (*ibid.*).

3.4.6.3. Vibrations in the low-wavenumber region (400-800 cm^{-1})

The interpretation of spectra at lower frequencies was problematic due to the overlap of different vibrational modes [*Marcello Mellini et al.*, 2002; *C. Viti and Mellini*, 1997]. The experimental spectra showed a few absorption bands, two of which were present in all the samples analysed. Sharp, symmetric to asymmetric

peaks in the range 598 - 615 cm^{-1} could correspond to the previously described 605 – 625 cm^{-1} region, attributed to the bending vibrations of the inner $^{VI}R^{2+}$ O-H bonds (R^{2+}= Mg). The external $^{VI}R^{2+}$ O-H bonds were usually seen at higher wavenumber of 640 – 650 cm^{-1} [*M. Mellini et al.*, 2002], but were not identified in the samples examined here. It is noted that Balan *et al.* [*Balan et al.*, 2002] reported also a band at 618 cm^{-1} and assigned it to the in-plane displacement of hydrogen atoms.

The antigorite samples exhibited an additional well-defined peak at ~ 565 cm^{-1} attributable to Mg-O out of plane vibrations [*Yariv and Heller-Kallai*, 1975]. This vibration was absent in the lizardites due to their higher symmetry and as explained by Mellini [*M. Mellini et al.*, 2002] it would otherwise destroy the local three fold symmetry of the Si sites.

The second most intense band in the 400 – 800 cm^{-1} region was found at ~ 433 - 443 cm^{-1} and tentatively attributed to in-plane Mg-OH vibrations (439 cm^{-1}, as reported by Balan *et al.[Balan et al., 2002])*. Additional, non-serpentine bands were identified in chrysotile^{AML60} and lizardite^{AML46}. The chrysotile-rich sample also contained calcite, and this was reflected in three main absorption bands at ~1426, ~876 and ~712 cm^{-1}. Lizardite^{AML46} exhibited two absorption bands at ~1015 and ~669 cm^{-1} due to the presence of talc.

3.4.7. Thermogravimetric Analysis

Serpentine minerals can be identified according to their dehydroxylation temperatures [*Cecilia Viti*, 2010], hence thermogravimetric analysis (TGA) was

used for the qualitative discrimination of the polymorphs and polytypes present in these serpentine samples.

Prior to analysis, all samples were dry-ground using a ball-mill and sieved to <250 µm particle size. 20-80 mg of each sample was heated in a 150 ml alumina crucible across a temperature range of 30-1000°C. Figure 3.17 presents the weight loss curve and its 1st derivative for lizardite[AML4] and is used for explanation of the general trends. Curves for the other serpentine samples are shown in Figure 4.18 and all are summarised in Table 3.5.

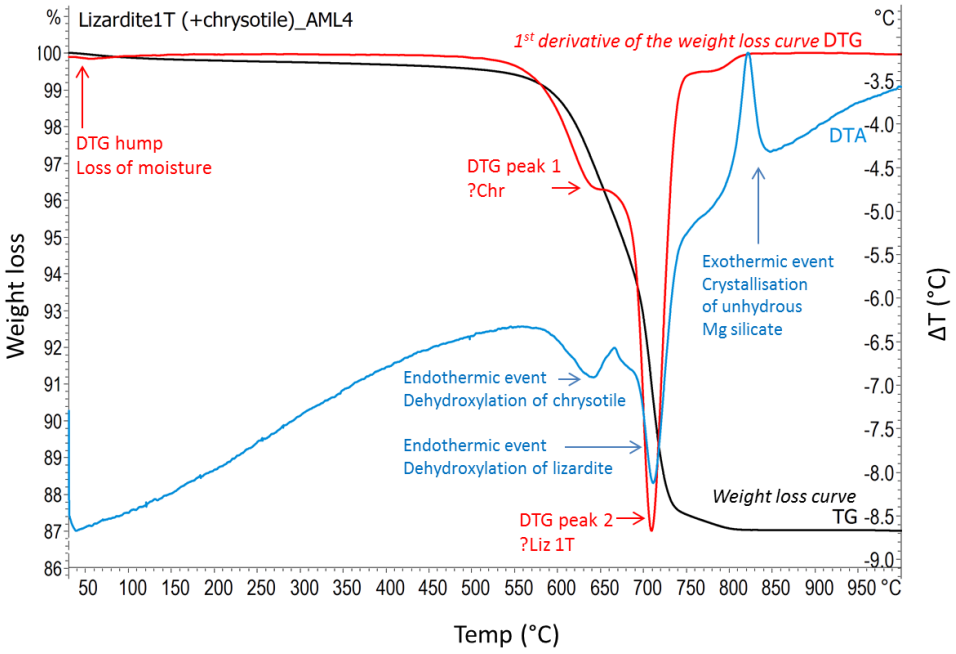


Figure 3.17 Graph showing curves for: weight loss (TG / black), its 1st derivative (DTG / red) and a 1st derivative of ΔT curve (DTA / blue) for Lizardite AML4, dominated by signatures due to lizardite 1T and chrysotile, indicated on the DTG curve by a weight loss at ca. 710°C and ca. 650°C, respectively.

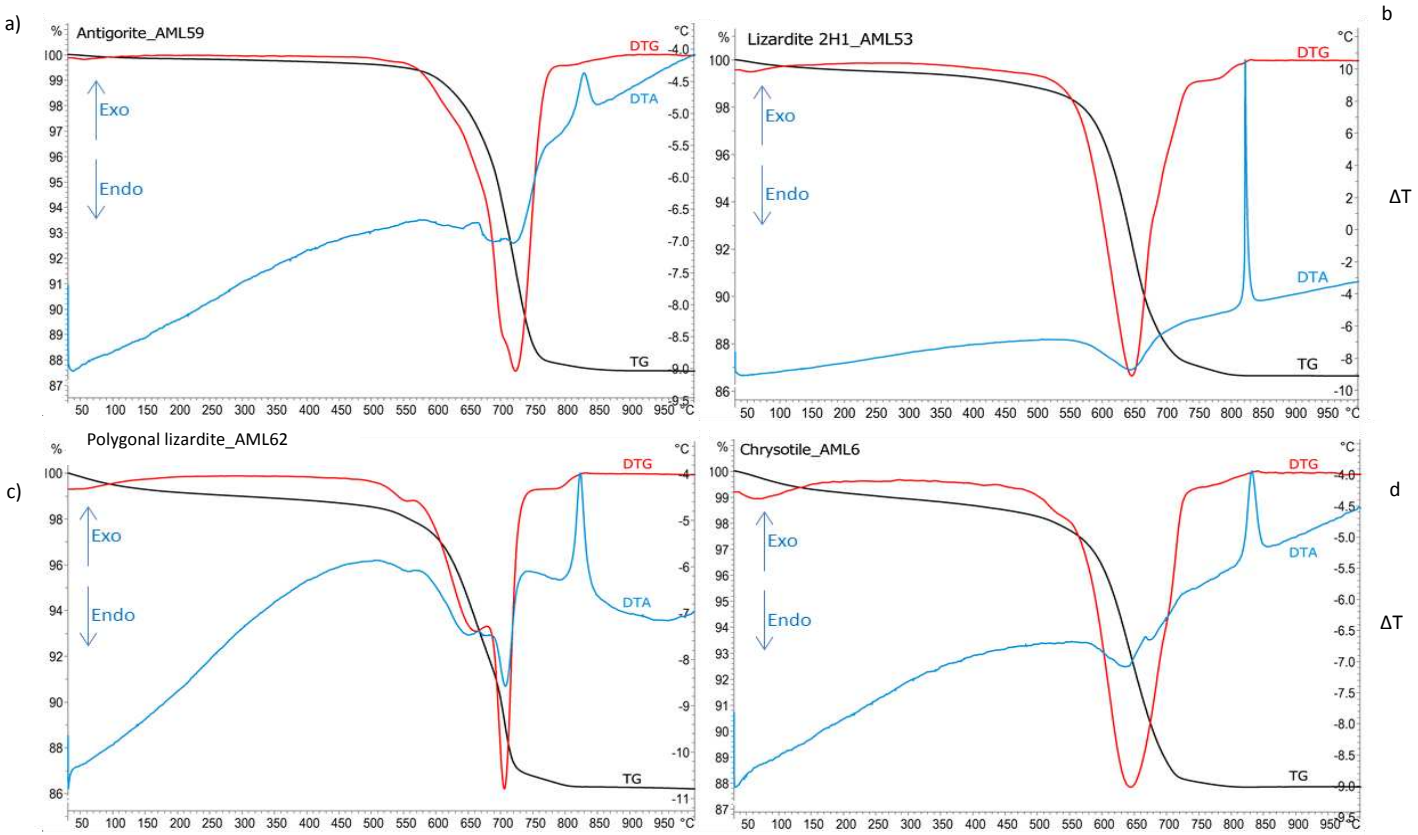


Figure 3.18 Example TG, TGA and DTA curves for a) antigorite AML59, b) lizardite $2H_1$ AML53, c) lizardite 1M AML62 and d) chrysotile AML6. The polygonal serpentine presents characteristics of chrysotile and lizardite, due to overall tubular morphology with planar lizardite 1M sectors, respectively.

Table 3.5 TG weight loss (%) data for all samples analysed (data obtained in collaboration with Ms D. Wagner 2011 - BGS)

		Weight loss 1			**Weight loss 2**			**Weight loss 3**			**Weight loss 4**			**Weight loss 5**			
		Temperature range T(°C)		**TG loss**	Temperature range T(°C)		**TG loss**	Temperature range T(°C)		**TG loss**	Temperature range T(°C)		**TG loss**	Temperature range T(°C)		**TG loss**	
Mineral name	Sample No	from	to	(%)	from	to	(%)	from	to	(%)	from	to	(%)	from	to	(%)	Total weight loss (%)
Antigorite	AML2	30	430	0.38	430	728	6.75	728	820	4.56	-	-	-	819	917	0.22	11.94
Antigorite	AML59	30	432	0.30	432	702	6.36	702	785	5.48	785	880	0.26	-	-	-	12.42
Lizardite 1T	AML4	30	454	0.36	454	649	3.51	649	753	8.78	753	830	0.35	-	-	-	12.96
Lizardite 1T	AML46	30	367	1.4	367	506	0.84	507	634	5.63	634	731	3.43	731	862	1.25	12.54
Lizardite 2H1	AML53	30	331	0.58	331	675	10.59	675	735	1.68	735	828	0.47	-	-	-	13.32
Lizardite 2H1	AML57	30	333	0.97	333	666	10.09	666	744	2.04	744	830	0.40	-	-	-	13.50
Lizardite PL 1M	AML62	30	429	1.19	429	565	0.93	565	674	5.92	674	742	5.11	772	853	0.24	13.90
Chrysotile	AML6	30	433	1.42	433	522	0.55	522	739	9.95	739	836	0.20	-	-	-	12.13
Chrysotile	AML60	30	433	1.71	433	641	10.43	641	860	5.84	-	-	-	-	-	-	17.98*

** high weight loss related to presence of serpentine and calcite*

The dehydroxylation-related weight loss for serpentine minerals was usually completed at 800°C, in agreement with data reported by Viti [*Cecilia Viti*, 2010]. Total weight loss varied from sample to sample, but correlated generally with the amount of structural water in the serpentine minerals, increasing from antigorite to chrysotile. Accordingly, antigorite samples and surprising one chrysotile sample (AML6) displayed the lowest weight loss, around 12 wt%. The lizardite-rich samples displayed a weight loss range from just below 13 to 13.5 wt%. The extremely high value of ~ 18 wt% measured for chrysotile-rich AML60 could be explained by the presence of calcite.

The weight loss was recorded as a function of temperature and four subtly different temperature regimes were distinguished, based on the main weight loss episodes (Table 3.5). Weight loss (1^{st} derivative) on the DTG curve usually corresponds to an **endo**thermic signal on the associated DTA curve (ΔT between the substance analysed and a reference) and can be explained by dehydroxylation events. General features observed in all the samples include:

- A low temperature endothermic signal < 100°C, assigned to the presence of adsorbed moisture.
- An **exo**thermic broad-band or a sharp peak > 800°C, most probably related to the re-crystallisation of dehydrated serpentine residuum into Mg silicate. The re-crystallised residuum in lizardite^{AML62} was identified by XRD as forsterite (Mg olivine), in agreement with previously published data [*Cecilia Viti*, 2010].

The ***antigorite*** samples (*e.g.* AML59, Figure 4.18a) displayed limited, < 1% weight loss below 430°C. The highest weight loss was observed between 430 and ˜800°C, with endothermic peaks present at 715°C and 738°C, and shoulders at 702°C and 720°C, for antigorite^{AML59} and antigorite^{AML2}, respectively. The subtle shift of the

dehydroxylation temperature towards a higher value, may reflect an increase in antigorite super-periodicity (large periodicity along x direction, alternating wave structure) [*Cecilia Viti*, 2010].

The DTG and DTA curves for ***lizardite* 1T^{AML4}** (Figure 3.17) were in good agreement with those observed for LIZ MNF 3 and LIZ MNF 4, as reported by Viti [*Cecilia Viti*, 2010]. The most prominent weight loss occurred in the 450 - 800°C temperature range, with a main DTG peak at~700°C and a shoulder at 649°C. The occurrence of the doublet has been previously reported for serpentine minerals but its origin is still debatable. As suggested by Viti [*Cecilia Viti*, 2010], it could be related to a combination of factors, including the presence of chrysotile impurities or the formation of intermediate phases during serpentine dehydroxylation. The lizardite 1T^{AML4} sample contained chrysotile and a shoulder on the TGA curve coupled with an endothermic trough at ˜640°C (Figure 3.17, peak 1) could have reflected its presence.

The ***lizardite* samples AML53** (Figure 3.18b) **and AML57**, identified by XRD as two layer hexagonal polytype $2H_1$, exhibited a broad but distinctive DTG peak at ˜630°C associated with a broad DTA trough. This temperature-related mineral dehydroxylation signature was amongst the lowest recorded for all the samples, including chrysotile; and was interpreted previously as reflecting a weakening of the interlayer bond strength (irrespective of chemistry) [*Cecilia Viti*, 2010]. This is consistent with the $2H_1$ structure, in that the expanded basal spacings and longer O2 - O3 distances resulted in weaker H-bonding [*M. Mellini and Zanazzi*, 1987]. Both lizardite^{AML53} and lizardite^{AML57} samples exhibited a very weak signal at 742°C and 747°C, respectively, potentially related to the presence of antigorite.

The DTG curve for ***lizardite***^{AML62} (Figure 3.18c) was characterised by four well defined weight loss events, with a low intensity broad peak at *ca.* 540°C, followed by a broad but higher intensity peak at *ca.* 660°C, a sharp, high intensity peak at *ca.* 710°C and low intensity broad hump at *ca.* 880°C. The origin of the lowest intensity peak is unknown, but may be related to impurities of antigorite at the higher end of temperature range and chrysotile at the lower end. The presence of two closely-spaced peaks, *i.e.* at 660 and 710°C make be significant of polygonal serpentine with the lower temperature peak reflecting the tubular (chrysotile-like) structural component, while the higher temperature being assigned to planar lizardite 1M in the sectors.

Lizardite^{AML46} showed noticeable weight loss across the temperature range 0 - 360°C, probably reflecting the presence of mineral phase impurities. The most significant loss, however, was observed in a range 500 - 730°C, with two "merged" broad TGA peaks at 615°C and 665°C, being lower than expected for 1 layer lizardite (*e.g.* lizardite 1T^{AML4}), perhaps suggesting lower structural ordering. The sample also contained significant amount of talc, confirmed by a TGA signal at 794°C.

The ***chrysotile*** samples (*e.g.* AML6, Figure 3.18d) showed a subtly different response to heating, with limited, but higher than average weight loss for serpentine minerals, at the low temperature end and a significant loss of ~10 % for AML60 across 433 - 640°C and for AML6 across 520-740°C. The weight losses corresponded to endothermic signals at 630 and 640°C, respectively, being lowest amongst serpentine minerals, a diagnostic tool for chrysotile. Sample AML60 contained a significant amount of calcite, as confirmed by a broad TGA signal at 651°C.

3.5. Summary

The aim of this part of the study was to appraise the composition and the structure of the nine serpentine mineral - rich samples, as starting materials for the studies on accelerated acid dissolution for *ex situ* CCSM (Chapter 4). The starting material correlates with the efficiency of CCSM technologies, and hence a full understanding of structure, chemistry and mineralogy is essential. In this study, structure and mineralogy were determined using a combination of XRD, FTIR and TGA, whilst mineral composition was appraised using XRF and SEM-EDS. SEM and TEM were used to assess sample texture and crystals morphology. The main conclusions are:

1. ***Antigorite*** can be identified unequivocally by the XRD, FTIR or TGA methods. The ease of qualitative analysis arose from the mineral's distinctive wavy crystal structure, giving a distinctive XRD pattern. On FTIR spectra, the presence and position of absorption bands at *ca.* 565 cm^{-1} differentiated monoclinic antigorite from trigonal lizardite. Furthermore, antigorite is generally the serpentine with the highest temperature of crystallisation and contains rarely any significant amounts of other low temperature serpentine impurities; hence any overlap of analytical signal was rarely an issue. The highest temperature of crystallisation was also reflected in the highest temperature of dehydroxylation and associated loss of weight, as indicated by the thermogravimetric study.

2. The analysis of ***chrysotile*** and ***lizardite*** proved to be more challenging, especially when the two minerals were finely inter-grown. Qualitatively, the minerals could be differentiated based on their FTIR spectra, specifically in a

region *ca.* 1025 cm^{-1} where the nanotubular structure of chrysotile produces a distinctive peak that is absent in the flat layered lizardite or indeed, in antigorite. In addition, the generally lower temperatures of dehydroxylation, as determined by TGA, in this study, aided chrysotile identification. The presence of chrysotile in polymorphic mixtures was also inferred from XRD, with d spacing of 2.02Å corresponding to (204). A peak at approximately the same position was previously reported as being diagnostic for chrysotile (202) [*Buttner and Saager*, 1982].

3. Unequivocal determination of ***lizardite*** polytypes was only possible using XRD data. Further studies will focus on obtaining electron diffraction data to aid definitive polytype identification. Subtle structural changes between polytypes were not distinguished within FTIR spectra, and TGA data only provided inferences on the resistance of a specific crystal structure to applied heat, from which a serpentine polytype could tentatively be assigned. The lower the temperature of dehydroxylation - the weaker the inter-layer bonds and hence the lower the crystal symmetry.

   Based on a very good XRD pattern fit, with reference to PDF documents derived from Inorganic Crystals Structure Database (ICSD), both trigonal lizardite (L1T) and two layers hexagonal lizardite ($L2H_1$) were identified unambiguously and this identification was consistent with the results obtained from TGA and FTIR. Indeed, the two lizardites could be differentiated by variable dehydroxylation temperatures, as observed on the DTG curves, *i.e. ca.* 700°C for trigonal polytype and *ca.* 645°C for two layers hexagonal. The difference in dehydroxylation temperature was related to the strength of the interlayer bonding ($L2H_1$ < L1T) and the ease of structural damage in response to heating. Furthermore, the results obtained for lizardite 1T corresponded well to those reported by Mellini [*M. Mellini and*

Viti, 1994a] and Gregorkiewicz & Viti [*Gregorkiewitz et al.*, 1996; *C. Viti and Mellini*, 1997] and gave confidence to the other analyses obtained in this study.

Sample AML62 was identified tentatively as polygonal lizardite with sectors occupied by monoclinic lizardite. The uncertainty of this identification was related to contradictory lines of evidence given by the different analytical techniques. SEM imaging suggested a two phase sample with the major being a hollow-core (tubular like chrysotile) with chunky, thick wall mineral (unlike chrysotile) set in an anhedral mass. The XRD data suggested that the major phase was monoclinic lizardite (1M based on a very good whole pattern fit with 00-050-1606), and the dehydroxylation temperature from the DTG curve pointed towards chrysotile and lizardite 1T (655°C and 700°C, respectively). The presence of chrysotile could also be inferred from the FTIR spectrum with a peak at ~ 993 cm^{-1}. However, in the light of the image analysis and combining all the evidence, it was inferred that the mineral was a polygonal serpentine with polygons probably occupied by monoclinic flat layered lizardite. This polytype is a "transitional" form [*Cecilia Viti*, 2010] between a flat layered lizardite and a rolled or tubular chrysotile with 15 or 30 sectors [*Baronnet et al.*, 1994], hence its FTIR and TGA signals fell in to the intermediate region of values.

4. This study has shown that care must be taken when analysing serpentine minerals. They are hydrous compounds with complex crystal structure. They are sensitive to high energy electron beams and usually occur as micron-scale intergrowths, making qualitative and quantitative analysis difficult. The structural polymorphic and polytypic complexity adds another challenge and apart from the polytypes encountered in this study, *i.e.* lizardite 1T or $2H_1$

belonging to the twelve standard polytypes distinguished by Bailey *et al.* [*Bailey*, 1969], another 32 non-standard theoretical polytypes are possible as proposed by Bailey *et al.* [*Bailey and Banfield*, 1995].

Chapter 4 Acid extraction of Mg^{2+} from serpentine minerals for *ex situ* CCSM

4.1. Introduction

Serpentine minerals have attracted considerable attention in recent years due to their potential application in carbon capture and storage by mineralisation (CCSM). They are a group of Mg-rich silicates that serve as cation, predominantly Mg^{2+}, donors for both *ex situ* and *in situ* CCSM. Cations are released from the mineral structure by a variety of pre-treatment processes, all of which ultimately lead to accelerated disintegration of the feedstock mineral. The degree of disintegration and hence the amount of Mg^{2+} released puts constraints on the subsequent carbonation process and the overall efficiency of the technology. For *in situ* CCSM to be implemented on an industrial scale, the pre-treatment process has to be efficient and relatively fast, providing a high percentage of cations at acceptable cost. Attempts to accelerate the reaction kinetics of Mg^{2+} extraction have included: heat treatment [*Maroto-Valer et al.*, 2004], reduction of particle size and the use of various organic or inorganic solvents [*Park and Fan*, 2004; *Pundsack and Somerville*, 1967; *Wang and Maroto-Valer*, 2011] and bacterial leaching [*Power et al.*, 2010].

Previous CCSM experimental studies have tended to utilize only one mineral, *e.g.* antigorite [*Krevor and Lackner*, 2011; *Maroto-Valer et al.*, 2004; *Park and Fan*, 2004 and references therein], lizardite [*Daval et al.*, 2013; *Sanna et al.*, 2013; *Schulze et al.*, 2004; *Wolf et al.*, 2004] or chrysotile [*Ryu et al.*, 2011], making it impossible to compare the effects of mineral structure and ease of cation release

for a given set of experimental conditions. Indeed, the available data about serpentines used in CCSM is far from comprehensive, reflecting a general lack of awareness of the complexity of serpentine mineral structures. For example, one of the most commonly used samples in CCSM studies, *i.e.* antigorite originating from the Cedar Hill quarry in Pennsylvania, has often been described as a serpentine from Cedar Hill [*Park and Fan*, 2004 and references therein; *Renforth*, 2012]. Where given, the data suggests that antigorite was the only serpentine phase present. However, Maroto-Valer *et al.* [*Maroto-Valer et al.*, 2005] reported on the presence of olivine within samples from Cedar Hill. Further, the BGS team has shown that crushed Cedar Hill rock samples contained antigorite and lizardite, with relicts of olivine and mafic rock fragments with feldspar and clinopyroxene [*Styles et al.*, 2014a]. PXRD has additionally revealed quartz, magnetite, smectite and trace amounts of pyroaurite [*Styles et al.*, 2014b]. The examples above suggest that: (i) the purity of "standard materials" used in CCSM studies to date, and described as monomineralic, might actually be quite low; and (ii) often the availability and comprehensiveness of starting mineral data in some published studies is lacking. This has a direct impact on the interpretation of experimental data, and makes the association of the results to CCSM technologies potentially misleading, particularly with regard to assumptions made on mineral reactivity under specific experimental conditions.

In this context, it should be emphasized that serpentines are a structurally complex mineral group and assuming they have identical functional properties in the context of CCSM is inappropriate. A systematic mineralogical and geochemical assessment of starting materials ideally should be a requirement for any experimental CCSM study, however no combined studies: *i.e.* including antigorite, chrysotile and lizardite with its polytypes and comparative reactiveness, exist in

the current literature. Only a few studies have reported on the use of more than one type of serpentine [*O'Connor et al.*, 2002; *Styles et al.*, 2014b], but investigations of three or more types under the same conditions have never been made, and hence meaningful assessments of relative reactivities was impossible.

O'Connor *et al* [*O'Connor et al.*, 2002] reported on the use of lizardite and antigorite in a parallel mineral carbonation experiment. The assigned the heat-activation induced changes of particles morphologies to the different crystal structures of the two minerals. The importance of crystal structure was also highlighted by Yoo *et al* [*Yoo et al.*, 2009] and Van Essendelft [*Van Essendelft*, 2008] who reported that further studies are required to elucidate fully the extraction of Mg^{2+} from serpentine using acids. Further, Wang and Maroto-Valer [*Wang and Maroto-Valer*, 2011], in their study on antigorite dissolution, noted that different polymorphic forms might exhibit different dissolution behaviours, but this aspect was not studied further.

Here we present the results of experimental investigation of Mg^{2+} leaching from a variety of serpentine minerals polymorphs and polytypes. In order to gain improved understanding of the functional properties of serpentine polymorphs and polytypes in the context of CCSM, a set of laboratory experiments, combined with a detailed mineralogical and geochemical study of the purest starting samples possible, has been devised and reported on here. Nine samples of fully characterised serpentine minerals (Chapter 3) were leached with 1.4 M ammonium bisulphate for a maximum of three hours at a constant temperature of 70°C. The experiment was designed specifically to appraise Mg^{2+} extraction efficiency from structurally different serpentine minerals. Solid and liquid reaction residues were collected systematically, at different time intervals, and analysed using a combination of complementary analytical techniques to appraise compositional and textural time-dependent transformations. This approach

provided means for unravelling the factors controlling the extraction efficiency of Mg^{2+} from the various polymorphs and polytypes of serpentine minerals.

This Chapter presents the results of experimental investigation of Mg^{2+} leaching from selected serpentine minerals polymorphs and polytypes. The leaching efficiency was assessed based on accelerated acid mineral dissolution and the controlling factors, including: crystal structure and chemistry, rock texture and particle size distribution are discussed and their influence evaluated.

4.2. Materials and methods

This Section presents a brief summary of the methods and materials used in the acid leaching experiments, with associated details and a description of all techniques used presented in Appendix A.

4.2.1. Materials

To enable determination of the structure-dependent efficiency of Mg^{2+} extraction, a number of specific serpentine minerals and their acid-treated residues were investigated. The starting materials included two antigorite, two chrysotile and five lizardite–rich specimens (Chapter 3). Even though attention had been given to sourcing mineralogically homogeneous samples, the specimens still exhibited some heterogeneity, containing minor amounts of other serpentine types, magnetite/hematite or carbonate minerals (Chapter 3). In particular, two samples were distinctively heterogeneous, *i.e.* lizardite AML46 (with 10 % of chlorite and 1 % of talc) and AML60 (with 10 % calcite in the chrysotile).

The rock samples were milled to pass through a 250 µm sieve. The morphologies, size distributions and the specific surface area (BET N_2) of the powders are summarised in Table 4.1. The samples were categorised based on the dominant particle shape, *i.e:*

- *Dominantly-elongate:*
  - antigorite$^{\mathbf{AML59}}$ with grains up to 300 µm long / 50 µm in diameter and numerous elongate fines (< 10 µm);
  - chrysotile$^{\mathbf{AML6}}$ with grains < 100 µm long / 20 µm in diameter, with < 5 µm sized tubular "off-shoots"; and
  - chrysotile$^{\mathbf{AML60}}$ with tubes up to 300 µm long / 10 µm in diameter
- *Dominantly-equant:*
  - most lizardite samples: AML4, AML53, AML57 and AML62 with grains reaching 300 µm diameter
- *Dominantly-platy:*
  - lizardite^{AML46} with grains up to 100 µm in diameter and < 10 µm thick.

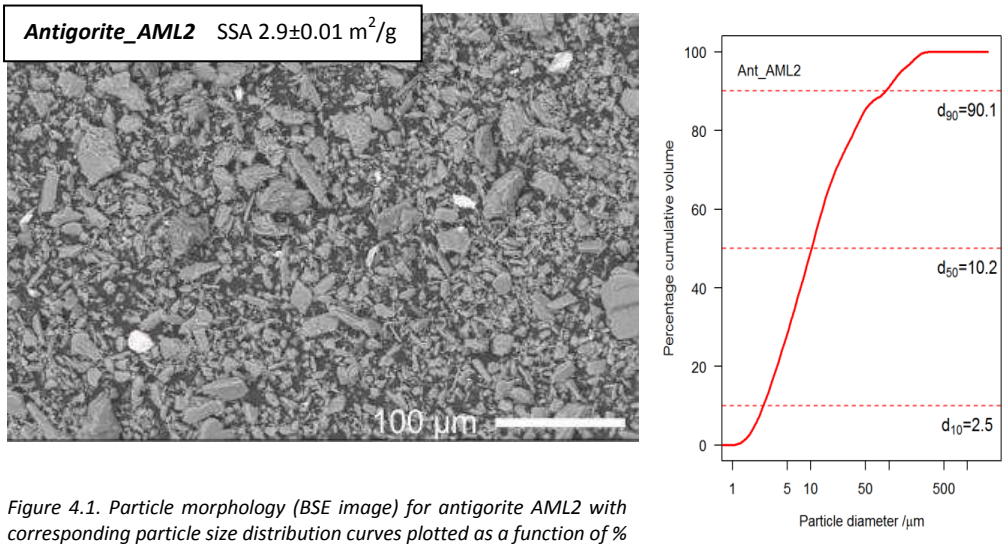


Figure 4.1. Particle morphology (BSE image) for antigorite AML2 with corresponding particle size distribution curves plotted as a function of % cumulative volume. SSA - in the table of each plate is the specific surface area.

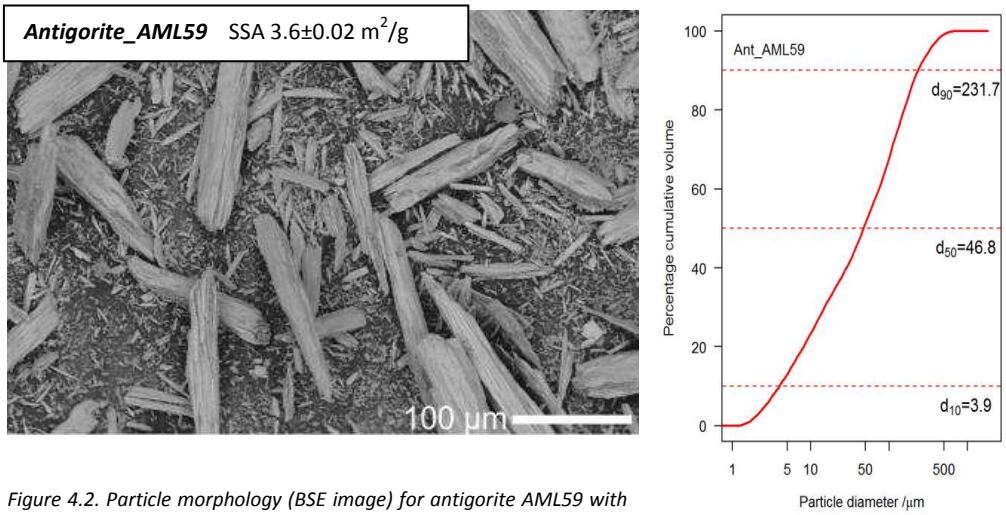


Figure 4.2. Particle morphology (BSE image) for antigorite AML59 with corresponding particle size distribution curves plotted as a function of % cumulative volume

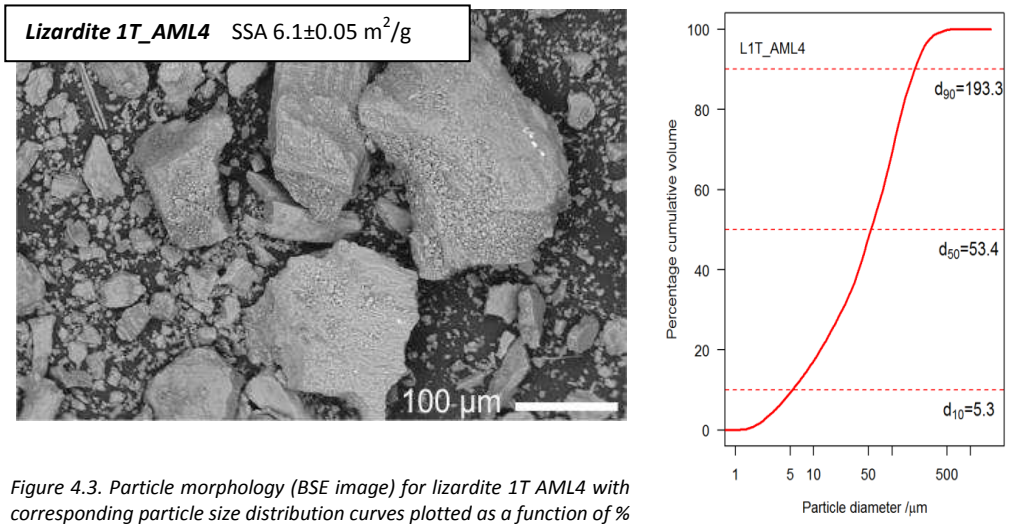


Figure 4.3. Particle morphology (BSE image) for lizardite 1T AML4 with corresponding particle size distribution curves plotted as a function of % cumulative volume.

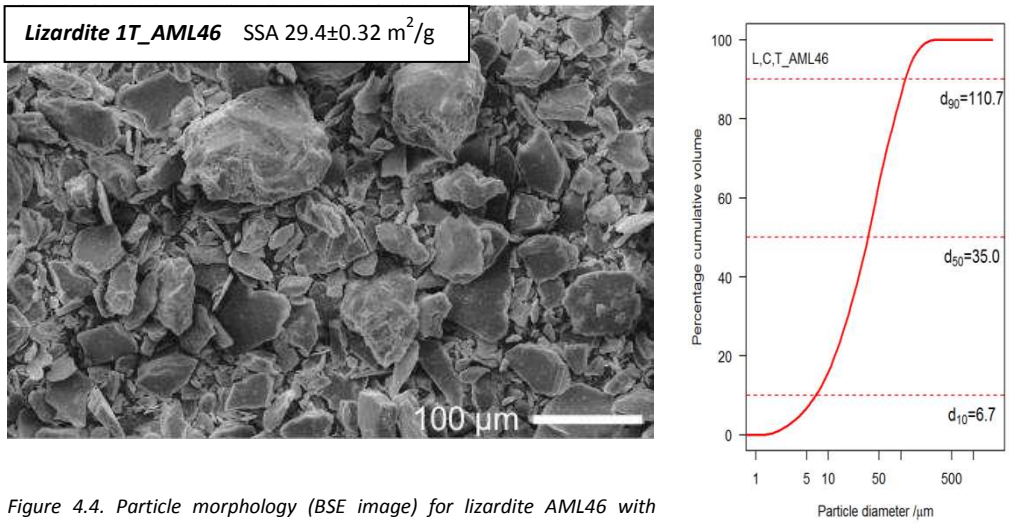


Figure 4.4. Particle morphology (BSE image) for lizardite AML46 with corresponding particle size distribution curves plotted as a function of % cumulative volume.

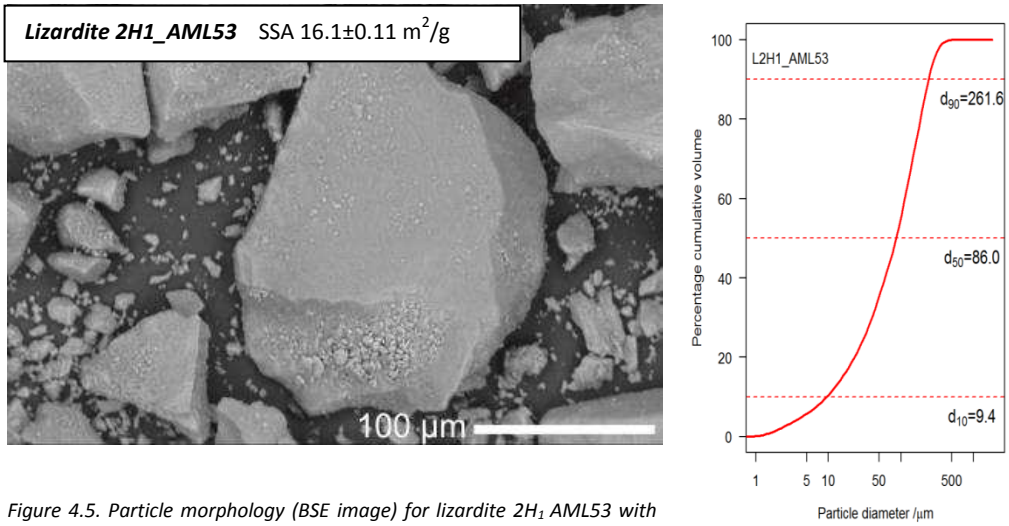


Figure 4.5. Particle morphology (BSE image) for lizardite $2H_1$ AML53 with corresponding particle size distribution curves plotted as a function of % cumulative volume.

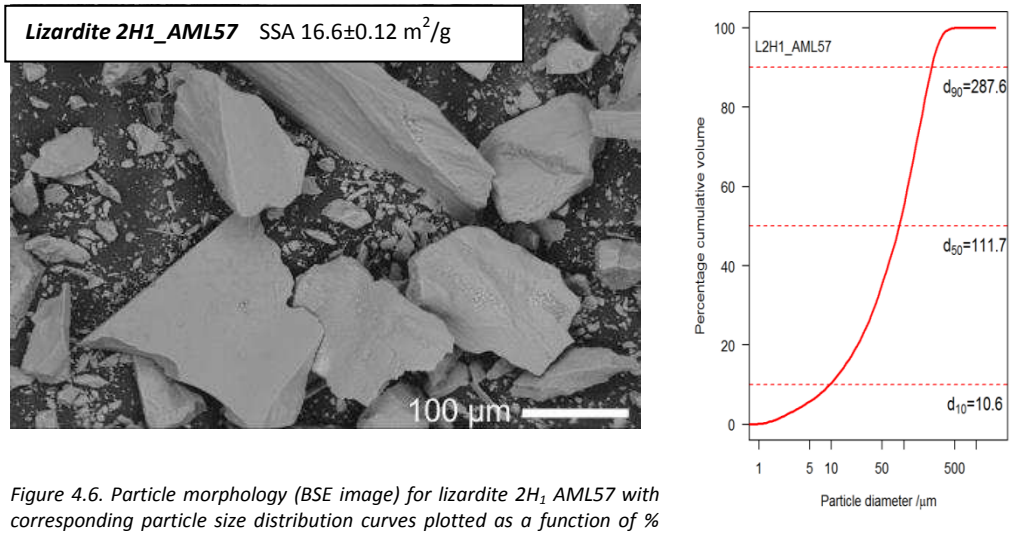


Figure 4.6. Particle morphology (BSE image) for lizardite $2H_1$ AML57 with corresponding particle size distribution curves plotted as a function of % cumulative volume.

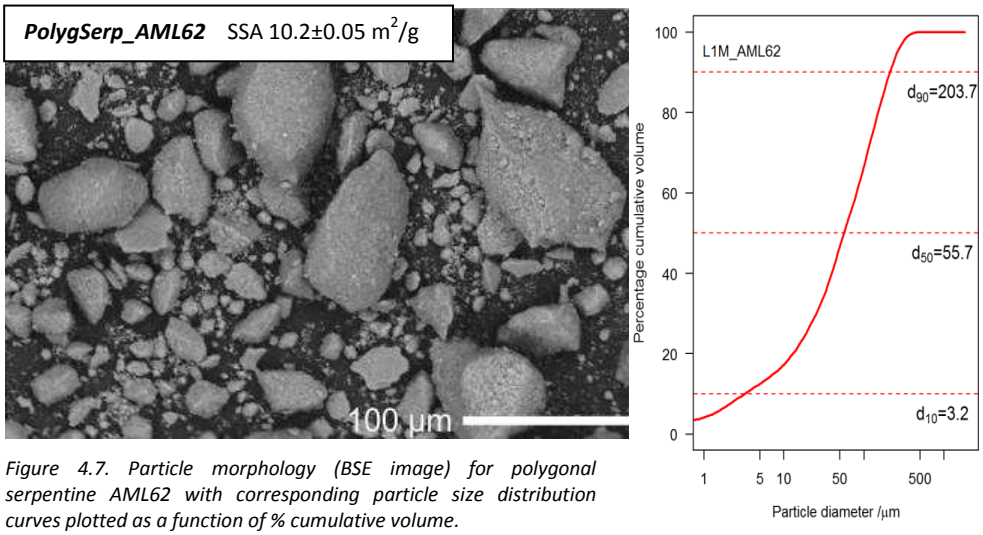


Figure 4.7. Particle morphology (BSE image) for polygonal serpentine AML62 with corresponding particle size distribution curves plotted as a function of % cumulative volume.

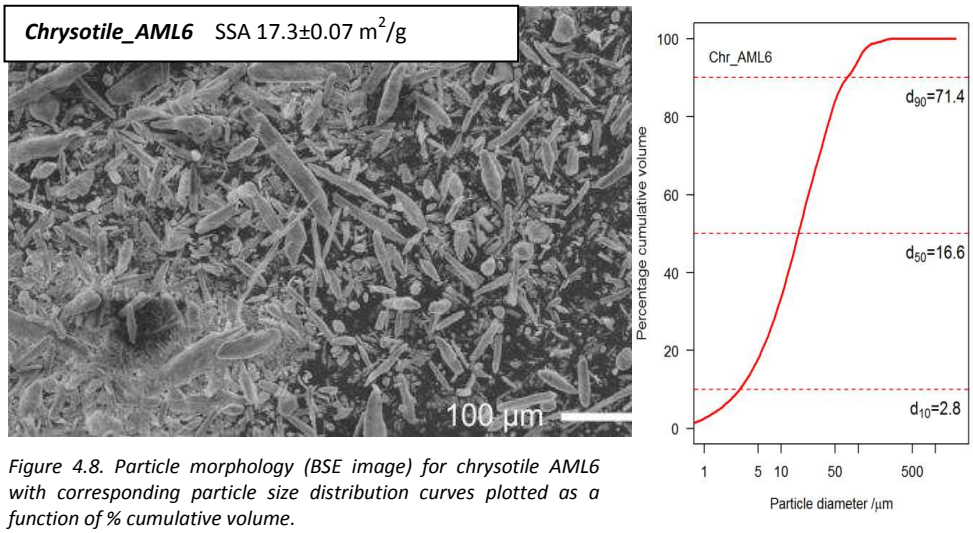


Figure 4.8. Particle morphology (BSE image) for chrysotile AML6 with corresponding particle size distribution curves plotted as a function of % cumulative volume.

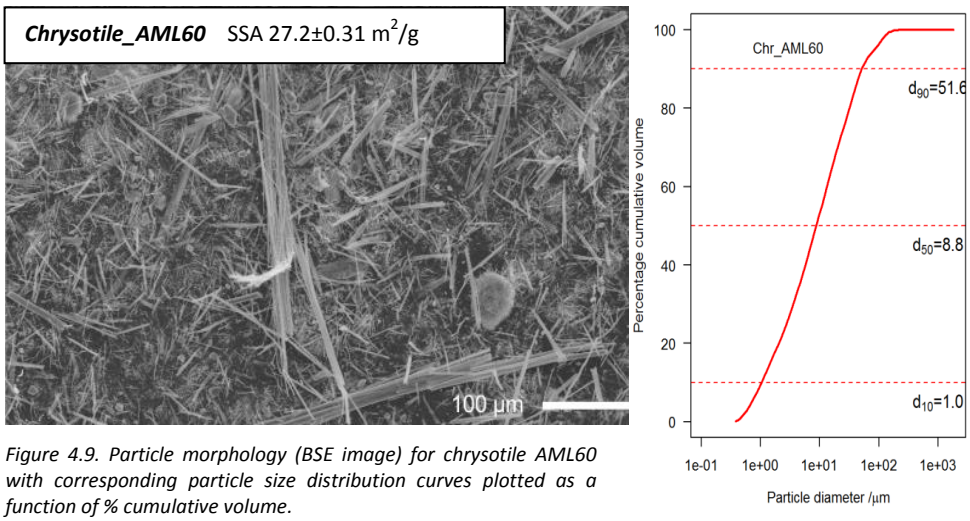


Figure 4.9. Particle morphology (BSE image) for chrysotile AML60 with corresponding particle size distribution curves plotted as a function of % cumulative volume.

The PSD plots were prepared in "R" using a code written by Dr B Rawlins (BGS), the logarithmic scale on x-axis of PSD plots was used for clarity of data presentation.

The particle distribution curves (plotted against % cumulative volume in Figures 4.1-4.9), and the spread of d_{90}, d_{50} (median) and d_{10} values, varied greatly between samples, providing valuable information on the amount of fines, an important parameter in calculating reaction rates. Low d_{90} values, as measured for the chrysotile samples and antigorite[AML2], suggested a significant proportion of fines. The PSD values were estimated using Mie Theory [*Beckman and Coulter*, 2011], based on the scattering of light from assumed spherical particles. However, it is noted that the probability of sheet silicate minerals, such as serpentine, forming spherical-like particles during grinding is low, with most powders being dominantly equant-angular, tubular or platy (Figure 4.1-4.9). Hence, the values for particle diameters, as obtained using laser diffraction and Mie theory, may only reflect the near "true dimensions" of equant particles, such as lizardite 1T[AML4] and lizardite $2H_1$[AML53], but are not realistic for elongate, fibrous or platy particles. The low d_{90} values returned for nanotubular chrysotile[AML60] are potentially misleading, and SEM or OM image analysis is required to provide more reliable data on particle dimensions. Further, a comparison of median values and true particle dimensions obtained from image analysis suggested that d_{50} values may correspond to the diameter of elongate particles, *e.g.* d_{50} for chrysotile[AML60] = 8.8 µm, consistent with the average diameter of clustered fibres (Figure 4.9).

Surface area

Surface area is important in quantifying mineral – water reaction rates [*Brantley and Mellott*, 2000]. The specific surface area was measured using N_2 BET and the values returned are shown in Table 4.1. The geometric surface area was calculated from the particle size distribution, applying a spherical approximation for antigorite[AML2], lizardite 1T[AML4 AML46], lizardite $2H_1$[AML53 AML57] and polygonal serpentine[AML62]; and a cylindrical approximation for chrysotile and the remaining antigorite samples.

A comparison of specific surface area (N_2-BET) and geometric surface area is presented in Table 4.1. It is clear that the values of specific surface area are up to 2 orders magnitude higher than that of geometric surface area, stemming from the fact that BET surface area is sensitive to microporosity. Brantley and Mellott [*Brantley and Mellott*, 2000] reported BET surface area to be 10-40 times greater than geometric surface area based on spherical approximation. It is noted that BET surface area do not often provide an ideal measure of the reactive surface area, in particular for the systems where the access of dissolved species to the surfaces of microspores is supposedly transport-limited [*Kaszuba et al.*, 2013]. However, in the system of sheet silicates such as serpentine minerals, with variable intrinsic intra-crystalline microporosity, the dissolution might not be transport limited. Further, this study shows that the biggest difference in the extent of dissolution correspond to the variation in the SSA, suggesting that intra-crystalline porosity did affect the dissolution significantly. It is thus that the rates of mineral dissolution are normalised to geometric rather than specific surface area, to account for differences in particle morphology, therefore allowing to highlight the importance of intra-crystalline microporosity.

Table 4.1. Comparison of specific (BET N_2) and geometric surface areas of particles investigated in this study. Geometric surface area values were calculated from particle size distribution data utilising spherical and cylindrical geometric approximations for the given samples.

The geometric figure best approximating the morphology of the studied particles: - Sphere, GSA calculated using $GA=4\cdot\pi\cdot r^2$ - Cylinder, GSA calculated using $2\cdot\pi\cdot r\cdot h$; where $h = 20\cdot r$ for chrysotile AML60	Antigorite AML2	Antigorite AML59	Lizardite 1T AML4	Lizardite 1T (+Chl+Tlc) AML46	Lizardite 2H1 AML53	Lizardite 2H1 AML57	Polygonal serpentine AML62	Chrysotile AML6	Chrysotile AML60
Geometric surface area (m^2/g)	0.352	0.143	0.142	0.137	0.106	0.097	0.574	0.256	0.492
Specific surface area BET N_2 (m^2/g)	2.9 ±0.01	3.6 ±0.02	6.1 ±0.05	29.4 ±0.32	16.1 ±0.11	16.6 ±0.12	10.2 ±0.05	17.3 ±0.07	27.2 ±0.31

4.2.2. Methods

This study was undertaken to appraise the relationship between efficiency of cation removal (predominantly Mg^{2+}) and serpentine mineral crystal structure, this being an important parameter in assessing the overall efficiency of *ex situ* CCSM.

To profile fully the structure-leaching interrelationship, ideally a mineralogically and structurally homogenous sample is required. However, in natural materials, serpentine polymorphs and polytypes are intimately inter-grown and their separation is effectively impossible. Accordingly, natural serpentine vein mineralisation was appraised in this study, which provided source material with less mineralogical and structural complexity than compositionally heterogeneous host rock.

Details on sample origin and collection are presented in Chapter 3. The initial reduction from hand specimens to gravel sized particles was performed using a metal pestle and mortar. The particles were then examined under binocular microscope to recover the purest possible sub-samples (Figure 4.10). This involved the visual separation of discrete impurities such as carbonates, fragments of host rock (usually serpentinised peridotite) and chromite-magnetite grains. A hand magnet was used to remove any magnetic minerals as well as any iron shards originating from the pestle and mortar.



Figure 4.10 Lizardite before and after separation under binocular microscope.

Approximately 70 g of sample was crushed using an agate ball-mill for approximately 5 min. The powders were then sieved to pass through a 250 µm mesh, a size applicable for industrial processing with no further milling or sieving required. Special attention was given to the preparation of chrysotile asbestos-rich samples, and a protocol was produced specifically, based on BGS procedures for preparing hazardous asbestos-bearing samples, and followed at all times.

The procedure used for ion leaching was based on that of Wang and Maroto-Valer [*Sanna et al.*, 2013; *Wang and Maroto-Valer*, 2011], modified slightly to accommodate the constraints of the experimental apparatus and summarized in Table 2.

1.4 M NH_4HSO_4 solution was prepared using Acros Organics extra pure ammonium hydrogen sulphate and ultrapure (Mili-Q) water (18.2 MΩ cm^{-1}). This provided an acidic solution, pH < 1. To appraise the time dependent structural and compositional modifications, leaching residues and leachates were collected at specific time intervals. Each serpentine powder sample was split into four 10 g sub-samples and poured into separate HDEP bottles filled with 200 ml of the acid pre-heated to 70°C. The bottles were placed on a rotation mixer at 6 rpm (Figures 4.11 a, b). For each sample set, the leaching experiments were stopped at 30, 60, 120 and 180 minute time points, whilst leachate and residuum were obtained.

Samples of leachate were extracted using a syringe with a 0.2 µm Nylon filter (Figure 4.11c). The filtered leachate was split into sub-samples for:

- pH (filtered)
- ICP-AES (4ml, filtered and acidified with 0.04 ml HNO_3)
- Ion chromatography (filtered, not acidified)

After sufficient leachate was extracted, the remaining solution was filtered using a Buchner Funnel in a fume cupboard. The solid residue was then collected and split

for further analyses. The residual fluid was disposed of in the fume cupboard sink and flushed with sufficient amount of water.

Table 4.2 Summary of experimental conditions used.

Serpentine polymorph/polytype	Powder sample	Sample mass (g)	Solution	Solution Volume (ml)	P	T°C	Duration
Antigorite x2 samples Lizardite x5 samples Chrysotile x2 samples	<250 µm	10	1.4 M NH_4HSO_4	200	Ambient	70	3 hours

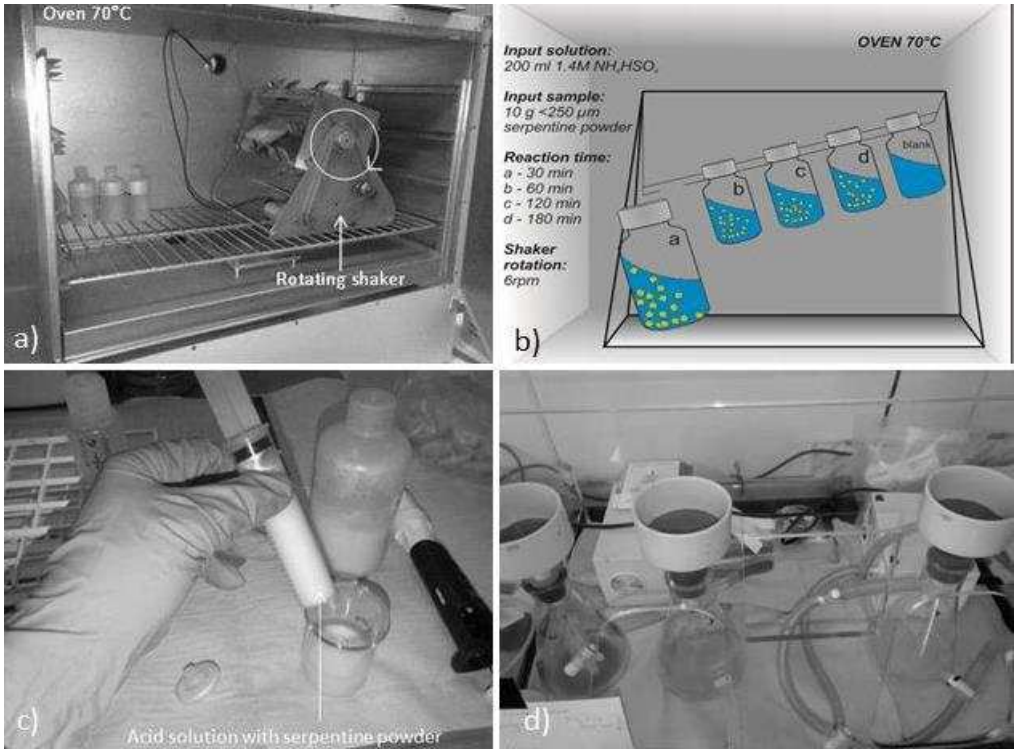


Figure 4.11. Apparatus for short-term acid leaching experiments. (a, b) Bottles of powdered samples in acid on a rotating shaker in an oven heated to 70°C, (c) Extracted leachate filtered using a Nylon syringe (0.2 µm filter), (d) Solids filtered using a Buchner Funnel.

The extraction of Mg^{2+} was appraised in parallel with the structural, chemical and textural transformations, as described below. The generalised reaction of serpentine dissolution in NH_4HSO_4 can be written as:

$$Mg_3Si_2O_5(OH)_4 + NH_4HSO_4 + 2H_2O \rightarrow 3Mg^{2+} + 2H_4SiO_4 + NH_4^+ + HSO_4^- + 3O_2$$

4.3. Results

In the following Sections, the process-induced changes in leachate chemistry, mineralogy and texture of the solid reaction residues are presented. Where appropriate, a short commentary is given, but a detailed discussion is provided in Section 4.4.

4.3.1. Leachate chemistry (ICP-AES)

4.3.1.1. Ionic concentration

Magnesium and silicon were the major elements in all the starting serpentine mineral samples (Chapter 3), followed by variable amounts of iron and aluminium, usually up to three orders of magnitude lower. The mineral elemental compositions were reflected in the concentration of aqueous species in the acid experiment-derived leachates, with the amount of Mg^{2+} in solution being two to three orders of magnitude higher than that of $Fe^{2+,3+}$ (*i.e.* Fe^{total}) and Al^{3+}, with values after 3 h of 0.1 – 0.5 mol/l Mg^{2+}; 0.004 – 0.01 mol/l Fe^{total} and < 0.002 mol/l Al^{3+}.

The dissolved concentration of Mg ions is most important factor for CCSM technology, thus the samples were classified into those with (Figure 4.12):

- low Mg^{2+} extraction ≤ 0.2 Mol/l (3 h): *i.e.* samples of antigorite and lizardite $1T^{AML4}$
- high Mg^{2+} extraction ≥ 0.4 Mol/l (3 h): *i.e.* lizardite $2H_1$ and chrysotile

The amount of Mg^{2+} released into the solution appears to be controlled (amongst other factors such as particle size, surface area and mineral chemistry) by the

polymorph and polytype of serpentine, and consequently by the minerals' structure, with the lizardites $2H_1$ and chrysotile providing higher concentrations than antigorite and lizardite $1T^{AML4}$. Sample AML62 contained polygonal serpentine and an interstitial matrix of proto-serpentine, in amounts approximating to 50% each and with the latter contributing mostly to the moderate amounts of Mg^{2+} in solution. If AML62 was made purely of polygonal serpentine (with aluminous lizardite 1M in the polygons) it would be classified as one with low Mg^{2+} extraction, as revealed by analysis of the solids and further discussed in Section 4.4.3. Similarly, the lizardite-dominated sample AML46 provided a relatively high Mg^{2+} concentration, but as explained further in Section 4.3.2, this might be related to the presence of heavily cleaved, *i.e.* prone to reaction, particles. The analytical uncertainties in the ICP-AES measurements, based on repeated analyses of standard solutions (Appendix C), were estimated to be around 5%.

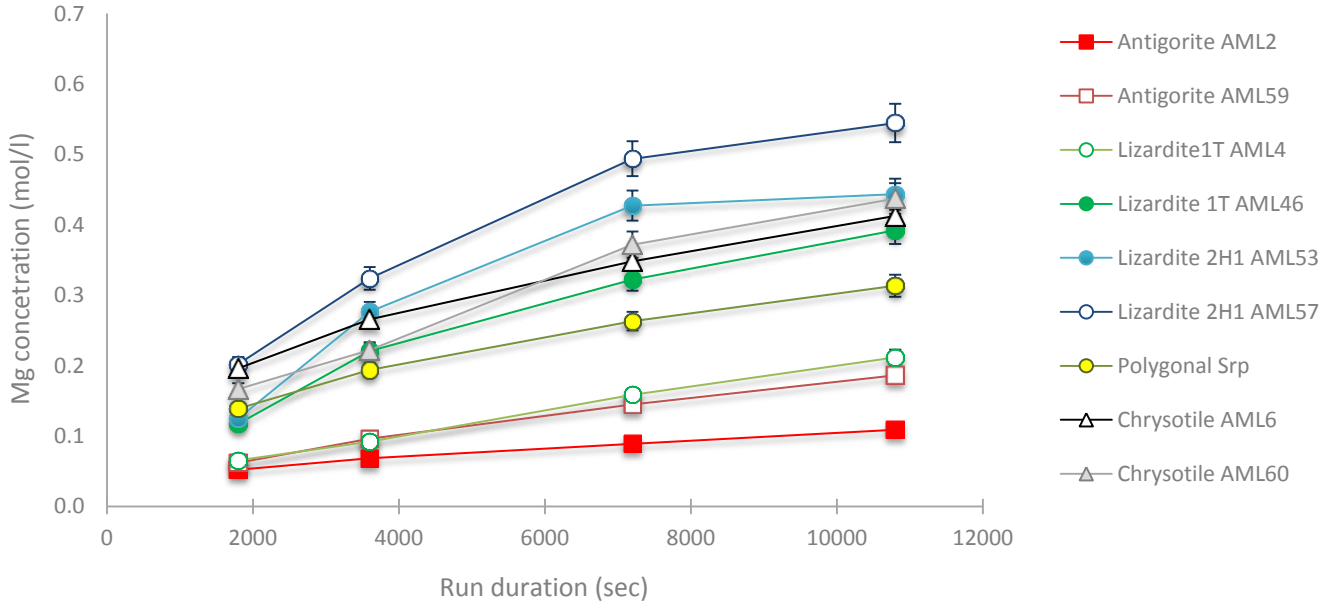


Figure 4.12 Concentration of Mg^{2+} in the leachates versus run duration. The amount of Mg^{2+} released into solution appears to be controlled (amongst other factors such as particle size, surface area and mineral chemistry) by the polymorph and polytype of serpentine, and consequently by the minerals' structure, with the lizardites $2H_1$ and chrysotile providing higher concentrations than antigorite and lizardite $1T^{AML4}$. 5% error bars applied.

4.3.1.2. Rate of mineral dissolution

The dissolution rates (R) of serpentine minerals were estimated using the following equation, based on the concentration of metal (i) in the leachate solution (*Brantley et al,* 2008):

$$Ri = (\frac{V}{GSA * m} * \frac{dC}{dt})/n$$

Where V is the volume of solution (l); GSA is the geometric surface area (m^2/g); m is the <*starting*> mass of the sample (g); dC/dt is the change of elemental concentration (mol) with time (s); and n is a coefficient determined from the mineral stoichiometry (XRF data). The material starting surface area only was taken into account for these calculations; however, it is recognised that the mineral surface area may undergo significant changes during the course of the experiments and hence some uncertainty may be associated with the rates presented here. Further, the dissolution rates were normalised to geometric surface area and not specific surface area (SSA BET N_2), to account for a significantly different particle shape and size distribution amongst the samples analysed.

The log rate values range from *ca.* -5 mol/m^2/g for lizardite $2H_1$[AML57] to *ca.* -6.1 mol/m^2/g for antigorite[AML2] over the first 30 minutes of reaction, with a generally decreasing trend over the further duration of individual experimental runs, apart from lizardite $2H_1$[AML57] and lizardite-dominated[AML46] that exhibited a subtle rate increase around the 60th minute mark of the experiment, followed by a decrease (Figure 4.13). Similarly lizardite 1T[AML4] and chrysotile[AML60] showed a dissolution

rate increase, but around the 120th minute of the reaction. Both cases are difficult to explain, but might have been related to a time-delay in the activation of reactive surfaces in the particles, possibly due to textural and/or structural obstructions. In addition, the faster initial dissolution rates of these samples may have been related to the preferential dissolution of fines, particularly for chrysotile^{AML60} with d_{50} of ~9 µm.

Generally, the dissolution rates obtained in this study were significantly higher (*i.e.* log rate of -6 to -5 mol/m^2/g) than those reported for antigorite [*Critelli et al.*, 2015], lizardite [*Daval et al.*, 2013] and chrysotile [*Thom et al.*, 2013] with associated log values *ca.* -11 mol/m^2/g each. This substantial difference might be related largely to the dissimilarity of the experimental conditions, *i.e.* these referenced experiments were conducted at the low temperatures of 25°C, 27°C and ~22°C, respectively, compared to the 70°C used in this study; combined with the use of different solutions resulting in an overall higher pH > 2, than the pH < 1 conditions used in this study. It is known that in many cases, the rate of reaction doubles for every 10°C rise in temperature.

Figure 4.13 demonstrates that the rates of dissolution:

- Vary significantly between the polymorphic and polytypic groups of serpentine, being the highest for lizardite $2H_1$ and chrysotile samples and lowest for antigorite^{AML2}, with intermediate values returned for aluminous lizardite, polygonal serpentine and antigorite^{AML59}
- Largely correspond to the amount of Mg^{2+} released, with relatively high rate and high Mg^{2+} release for lizardite $2H_1$ and chrysotile and a generally lower rate of Mg^{2+} release for antigorite and lizardite 1T, over the first 120

minutes of the experiment; after that, the rates for chrysotile [AML6] and lizardite $2H_1$ [AML53] slow down significantly

- Exhibit variable profiles when plotted against experiment duration; while some curves exhibit flattening, indicative of approach to steady state conditions, some curves (*e.g.* lizardite $2H_1$ AML53) show more variation in change of rate. These variations may be explained by textural (PSD, mineral intergrowths) and structural/chemical heterogeneity amongst the samples, with all of these affecting the reactivity of the minerals at different stages of the experiment (*e.g.* dissolution of fines, dissolution of structurally and chemically different polymorphs, formation of passivating layers, *etc*…).

Concluding, it is clear that the correlation between the polymorphic and polytypic variations and dissolution rate is related to a combination of crystal structure and chemistry of each mineral. For example, lizardite $2H_1$ and chrysotile exhibited regularly distributed intra-crystalline porosity (3.2.2.1) that provided additional conduits for surface protonation, thus resulting in significantly higher reaction rates as well as the actual amount of Mg^{2+} released. Crystal chemistry also plays and important role in mineral reactivity, as discussed in section 4.4.3.

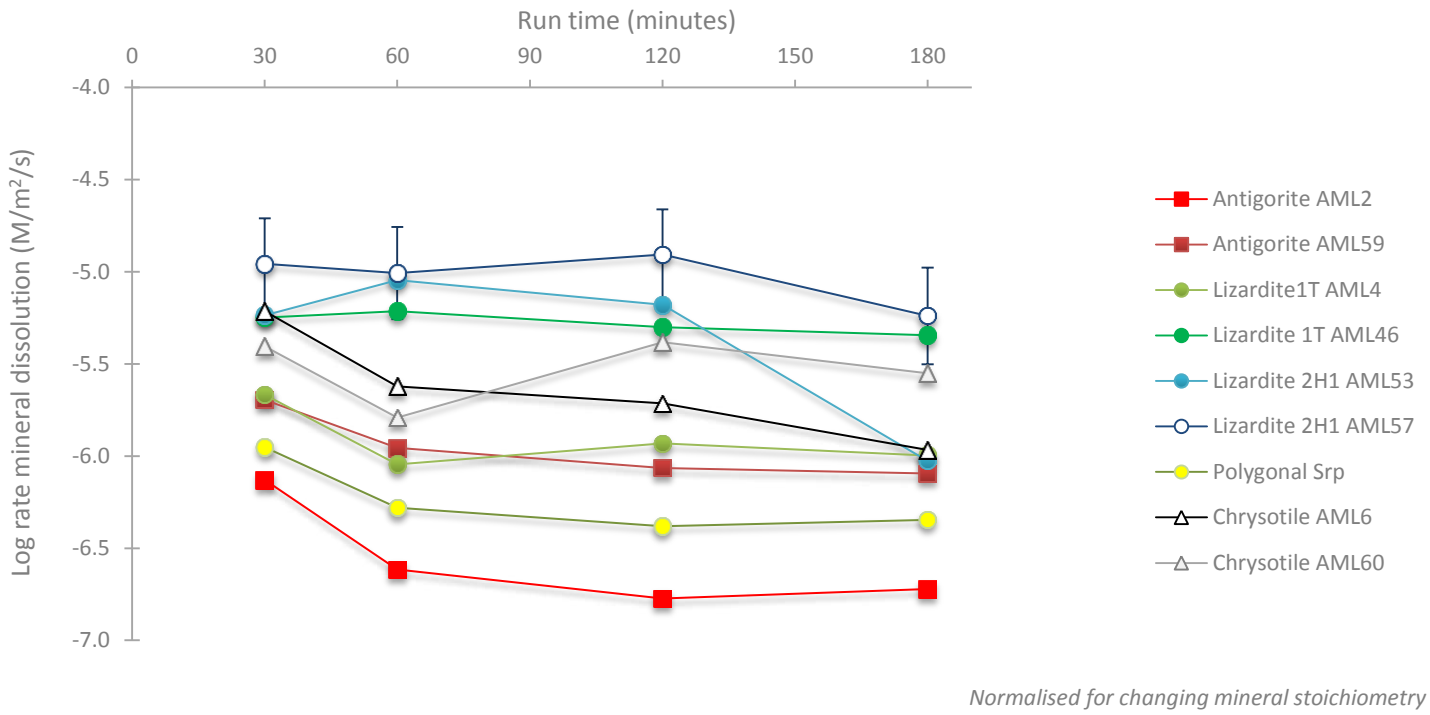


Figure 4.13. Logarithmic plot of mineral dissolution rate versus run time (s). The rates were calculated based on the concentration of Mg^{2+} and normalised for changing mineral stoichiometry. The plot shows a clear dependence of dissolution rate on crystal structure , with lizardite 2H1 and chrysotile plotting at higher values compared to antigorite and lizardite $1T^{AML4}$, $1M^{AML62}$.

4.3.1.3. Saturation Indices and Chemical Affinity

The ionic speciation of the experimental solutions was modelled using PHREEQC 3.2 [*Parkhurst and Appelo*, 1999], based on elemental concentrations measured in the liquid (ICP-AES) and the pH of solutions at a given reaction temperature (70°C) and time. This data, together with the BRGM database (Base de Donnee Thermoddem_V1.10) containing data for phases of interest, was used to calculate the saturation indices of potentially precipitating phases and the chemical affinities of serpentine minerals (antigorite, chrysotile and lizardite).

Saturation Indices – predicted *versus* present phases

Saturation index is a value used to determine whether the water is saturated, under-saturated or supersaturated with respect to a given mineral, and can be calculated from:

$$SI=\log_{10}(IAP/K_{sp})$$

Where IAP is ion activity product and Ksp is equilibrium constant. The solution is saturated with a respect to a mineral when SI=0, under-saturated when SI<0 and oversaturated when SI>0.

The geochemical modelling showed that the experimental solutions were far from equilibrium with respect to serpentine minerals, being manifested by low negative values of saturation indices (SI) as tabulated in Table 4.3. Values of SI for antigorite ranged from *ca.* -773 to -553, being the lowest of all samples modelled. All lizardite and chrysotile samples exhibited much higher Sis, varying from *ca*. -27

to -41. The general unification of SI values for the latter two mineral types is surprising, particularly in the light of their significantly different extent of dissolution. This might be related to the limited availability of thermodynamic data for serpentine minerals, and the values of Sis for lizardite samples are based on one set of lizardite data only, without accounting for structural, *i.e.* the polytypic complexity of this mineral. Hence, the data presented here have to be greatly generalised, with the potential for significant error.

Table 4.3 Saturation indices of serpentine minerals calculated using PHREEQC

	Saturation Index			
Sample and dominating serpentine mineral	**30 min leachate**	**60 min leachate**	**120 min leachate**	**180 min leachate**
Antigorite AML2	-657.76	-572.51	-558.83	-552.80
Antigorite AML59	-572.22	-556.86	-563.62	-772.71
Lizardite 1T AML4	-35.18	-34.41	-32.54	-32.06
Lizardite 1T AML46	-33.31	-31.10	-29.20	-28.24
Lizardite $2H_1$ AML53	-41.09	-30.37	-28.17	-27.49
Lizardite $2H_1$ AML57	-33.55	-31.87	-29.51	-28.95
Polygonal Srp. AML62	-33.62	-32.75	-31.83	-31.11
Chrysotile AML6	-33.65	-32.38	-32.18	-31.43
Chrysotile AML60	-32.82	-31.98	-30.26	-29.67

The incongruent dissolution of serpentine minerals in the presence of NH_4HSO_4 resulted in siliceous residuum, *i.e.* Mg-leached solid product and hydrated sulphate minerals, including boussingaultite ($(NH_4)_2Mg(SO_4)_2 \cdot 6H_2O$) and

hexahydrite ($MgSO_4 \cdot 6H_2O$), the latter being an arte-fact of ammonium bisulphate use. Figures 4.14-4.15 show the mineral saturation indices (SI) plotted as a function of time. Due to the lack of thermodynamic data for boussingaultite, this mineral could not be considered in the speciation-saturation modelling and hence is not included in these plots.

The PHREEQC modelling suggested that the solutions were oversaturated with respect to quartz, chalcedony and amorphous silica (positive values of SI in Figures 4.14 & 4.15); although quartz, due to sluggish precipitation kinetics at low temperatures, is considered unlikely as a precipitate for the P-T conditions and short experimental durations of this study. The presence of amorphous silica in the solid residues was confirmed by TEM / SAED and FTIR (Section 4.3.3.5), however, evidence for crystalline silica was found using FTIR for one sample only, *i.e.* antigorite^{AML2}; if crystalline silica had formed in other samples, it may have been at levels below the detection limits of the analytical technique used. A discrepancy was noted in relation to hexahydrate, with microanalysis confirming the presence of hexahydrite in the solid reaction residuum of lizardite^{AML4}, whilst the solutions remained under-saturated consistently with respect to this mineral. Further, the speciation-saturation calculations suggested the possibility of secondary pyrite (FeS_2) in solutions of lizardite $2H_1$^{AML57}, polygonal serpentine^{AML62} and chrysotile samples, and secondary eskolaite (Cr_2O_3) in the solution of antigorite^{AML2}; however it is anticipated that eskolaite would form at higher P-T conditions than those used and hence is not considered a realistic precipitate here [*Logvinova et al.*, 2008]. The high saturation index returned for pyrite also requires further investigation, since microanalysis of the solid residues did not reveal any evidence for its presence. These discrepancies are attributed to a lack of direct measurement of the redox potentials (with conditions based on the Fe^{2+}/Fe^{3+} redox couple), making the approximation of the experiments'

geochemical conditions possibly less accurate, consequently leading to spurious results. Therefore, care is needed with the interpretation of the PHREEQC modelling data. It also should be emphasised that PHREEQC modelling may provide less reliable results* for high ionic strength solutions, such as those used in this study (note the error bars on the plots), and hence, it is important to interpret the output data in conjunction with complementary information, *e.g.* the microanalysis data from the solid reaction residues as done in this study.

**PHREEQC uses ion-association and Debye Hückel expressions to account for the non-ideality of aqueous solutions. This type of aqueous model is adequate for low ionic strengths, but may break down for the higher ionic strengths associated with the sea water conditions used in this study.*)

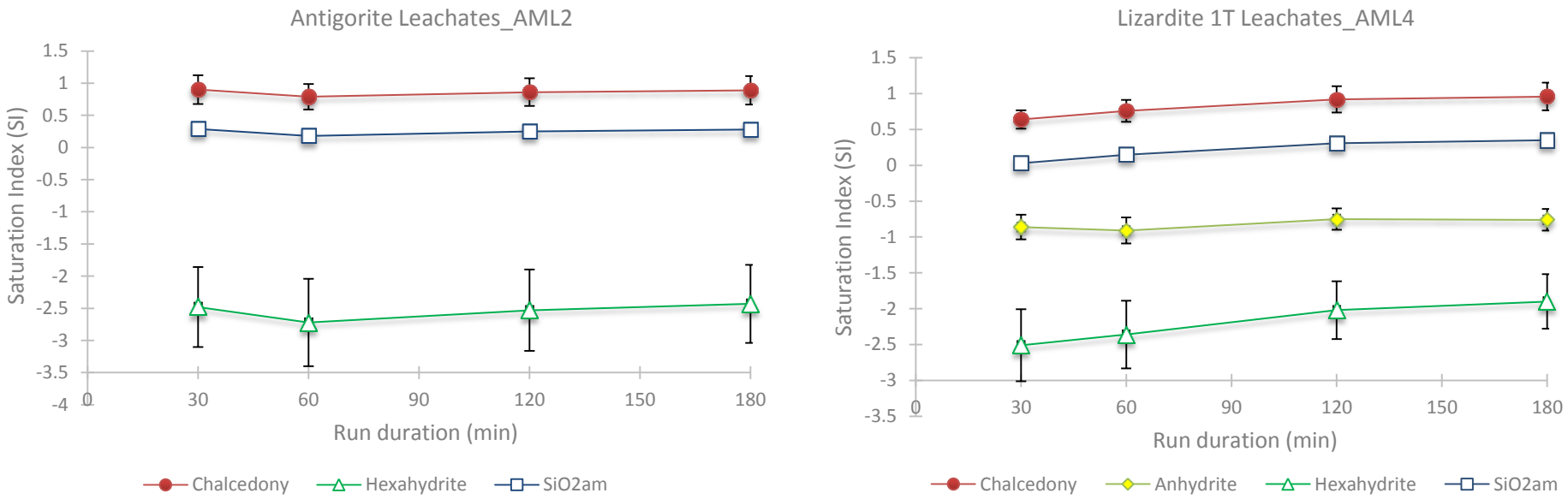


Figure 4.14. Saturation index values for selected phases as a function of run duration, for antigorite^{AML2} and lizardite 1T^{AML4} (70°C, 1.4M NH_4HSO_4). The data was modelled using PHREEQC 3.2; the error bars correspond to the percentage error: 100(Cat-|An|)/(Cat+|An|), as calculated by the program, varying from sample to sample depending on the input data.*

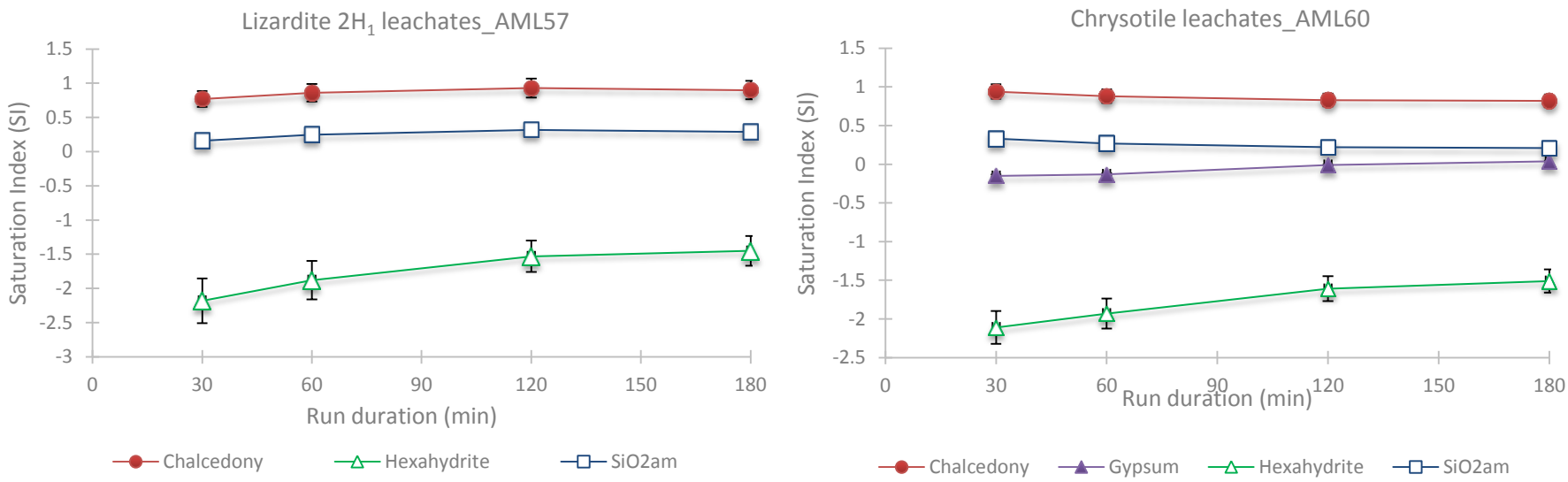


Figure 4.15. Saturation index values for selected phases as a function of run duration, for lizardite 2H1[AML57] and chrysotile[AML60] (70°C, 1.4M NH_4HSO_4). The data was modelled using PHREEQC 3.2; the error bars correspond to the percentage error: 100(Cat-|An|)/(Cat+|An|), as calculated by the program, varying from sample to sample and depending on input data. Both gypsum and anhydrite are likely secondary phases from the chrysotile [AML60] sample, as the original material contained < 10% calcite that upon dissolution would provide the necessary cations.*

Chemical Affinity

The driving force for a reaction, ΔG, controls whether a mineral dissolves or precipitates under a given set of conditions [*Brantley et al.*, 2008]. The chemical affinity A, where A=- ΔG, describes the distance from equilibrium (equilibrium with a particular mineral being manifested by A=0), and is a measure of the energy driving a particular reaction at specific temperature and pressure [*Brantley et al.*, 2008]. It is related to the saturation index (SI) of a given mineral, and can be calculated according to:

$$A = -R\ T\ \ln SI$$ [*Schott et al.*, 2009]

where R is the gas constant 8.3145 J/mol·K, and T is the temperature in K. Chemical affinity is positive when the reactants are under-saturated favouring dissolution; and negative when the reactants are super-saturated, favouring precipitation [*Schott et al.*, 2009].

Figures 4.16 – 4.19 show the calculated chemical affinities for the serpentine minerals plotted against the rate of their dissolution based on Mg and Si concentration in the leachates. It is evident that all experiments were performed under conditions far from equilibrium (high positive A values) and did not approach equilibrium with respect to serpentine minerals within the three hours of experimental duration. Accordingly, values of *ca.* 4000 kJ/mol for antigorite, and *ca.* 250 kJ/mol and 220 kJ/mol for lizardite and chrysotile, respectively, were obtained.

No clear and consistent relationship between the chemical affinity and dissolution rate was observed in this study, *e.g.* based on Mg concentration a number of samples exhibited a decrease in the rates of reaction with decreasing value of

chemical affinity, as would be expected if the system was approaching equilibrium; whilst others showed a flat or slightly increasing trend. It is however noted that the decreasing trend was distinctively more prominent for the rates based on Si concentration (also plotted in Figures 4.16-4.19), probably being related to progressive increase in the saturation index of silica phases in due course of the experiment, thus increasing its likelihood for precipitation. The analysis of solid reaction residues revealed the presence of siliceous layer, that might have formed via congruent dissolution of Mg silicate and re-precipitation of silica phases upon reaching saturation, as indeed indicated by the values of their SIs. This is further investigated in Section 4.4.4.3.1.

Although, the results presented here suggest that during the dissolution of serpentine minerals under far from equilibrium conditions the thermodynamic driving force, presented here as the chemical affinity of a reaction, is essentially constant and can potentially be eliminated, it must be stressed that (1) the experiments were carried out for a limited amount of time, whereupon little changes in chemical affinities were observed; and (2) the chemical affinities for lizardite samples in particular are based on one set of lizardite data only without accounting for structural, *i.e.* the polytypic complexity of this mineral, leading to generalisation of the results and a potential for significant error.

It might however stand that what is reported for kaolinite dissolution [*Schott and Oelkers*, 1995] (kaolinite being a dioctahedral Al-rich equivalent of lizardite), may also be true for serpentines in that, the rates become generally independent on chemical affinity at far from equilibrium conditions.

This study also shows that there are significant reaction rate variations between the different serpentine minerals, and putting lizardite polytypic complexity aside, it is clear that, the rate of antigorite dissolution was up to two orders of magnitude lower than that of lizardite group in general and/or chrysotile. These

minerals, despite belonging to the same mineral group and being compositionally alike, exhibit significantly different crystal structures. Surface reactions consist of successive elemental steps, each of which requires overcoming a potential energy barrier [*Schott and Oelkers*, 1995]. In the light of the transition state theory (TST), that focuses on the molecular configuration at the top of this barrier, the dissolving mineral-fluid interface can be viewed as a precursor of activated complexes* and the reaction rate is equal to the concentration of the activated complex and the frequency with which these complexes cross the energy barier [*Schott and Oelkers*, 1995]. The serpentine minerals will have at least two possible precursor complexes, *i.e.* Mg and Si sites; with their stoichiometry and "availability" depending strongly on the crystal structure, particularly the layer stacking, lateral arrangements and the strength of bonds. Antigorite exhibits localised stronger bonds and a much tighter intra-structural arrangements (primary due to layer modulations) in comparison to chrysotile and lizardite, meaning that the availability of its precursor complexes will be limited inevitably, probably to such extent that the rate and overall magnitude of mineral dissolution is affected greatly.

The TST may also be able to explain the variation in curves of chemical affinity *versus* rate, and the availability of different activated complexes as acid leaching progresses. This is however out of scope of this study.

**The precursor complex as is an activated compound of composition similar to the reacting material $\pm H^+$, OH^-, H_20, and being in equilibrium with the reactants [Schott and Oelkers, 1995].*

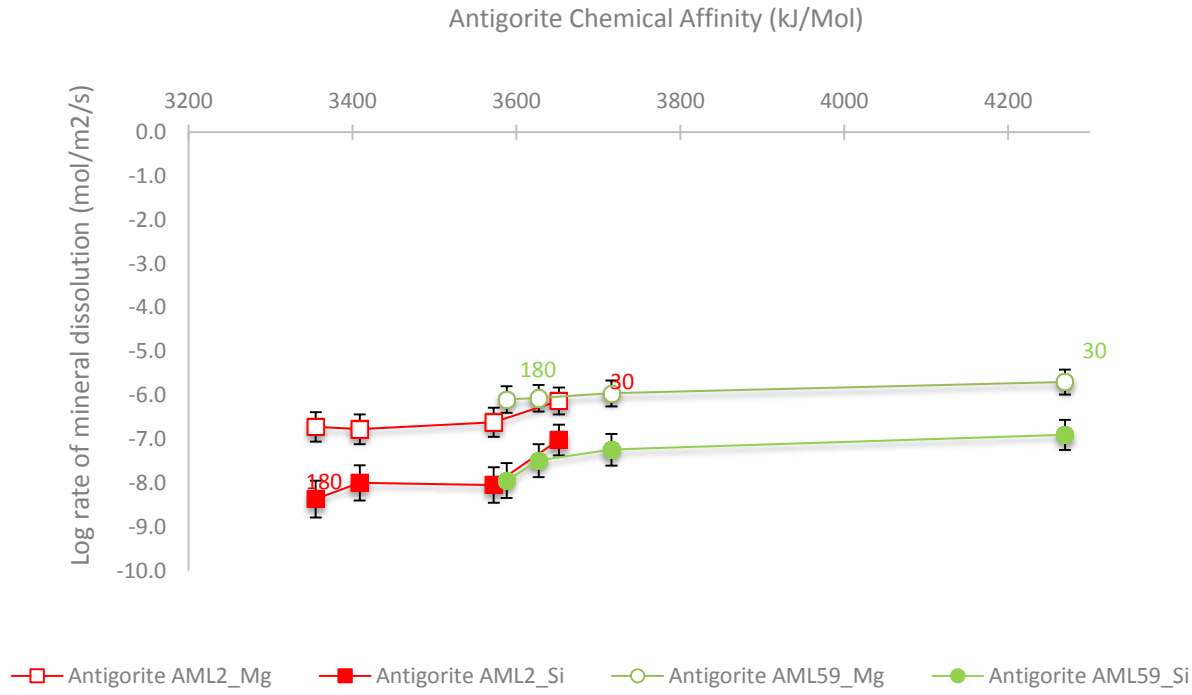


Figure 4.16. Log rate of antigorite dissolution, based on Mg^{2+} and Si^{4+} release from samples AML2 and AML59, as a function of the chemical affinity of antigorite. The values of log rate are normalised for mineral stoichiometry at a given reaction time (data derived from XRF analysis of the solid reaction residues). The 30 and 180 marks indicate half an hour and 3 hours experimental data points, with one and two hours data points found in between.

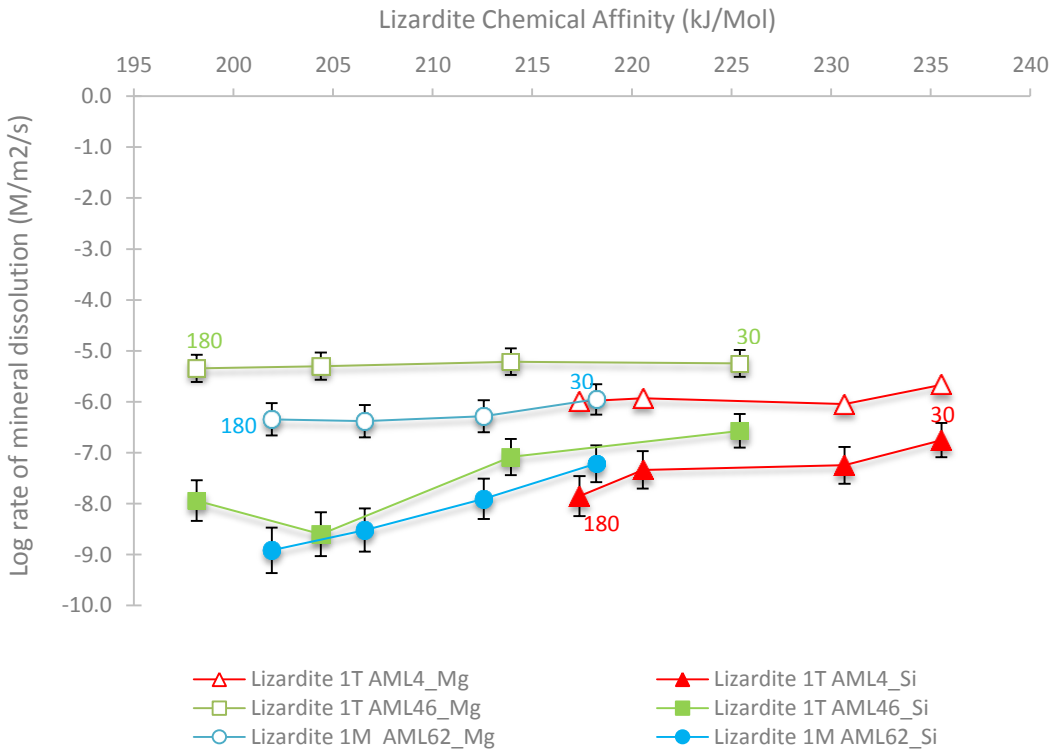


Figure 4.17. Log rate of lizardite dissolution based on Mg^{2+} and Si^{4+} release from samples AML4 (lizardite 1T), AML46 (lizardite 1T+chlorite+talc) and AML62 (lizardite 1M+protoserpentine), as a function of the chemical affinity of lizardite. The values of log rate are normalised for mineral stoichiometry at a given reaction time (data derived from XRF analysis of the solid reaction residues). The 30 and 180 marks indicate half an hour and 3 hours experimental data points, with one and two hours data points found in between.

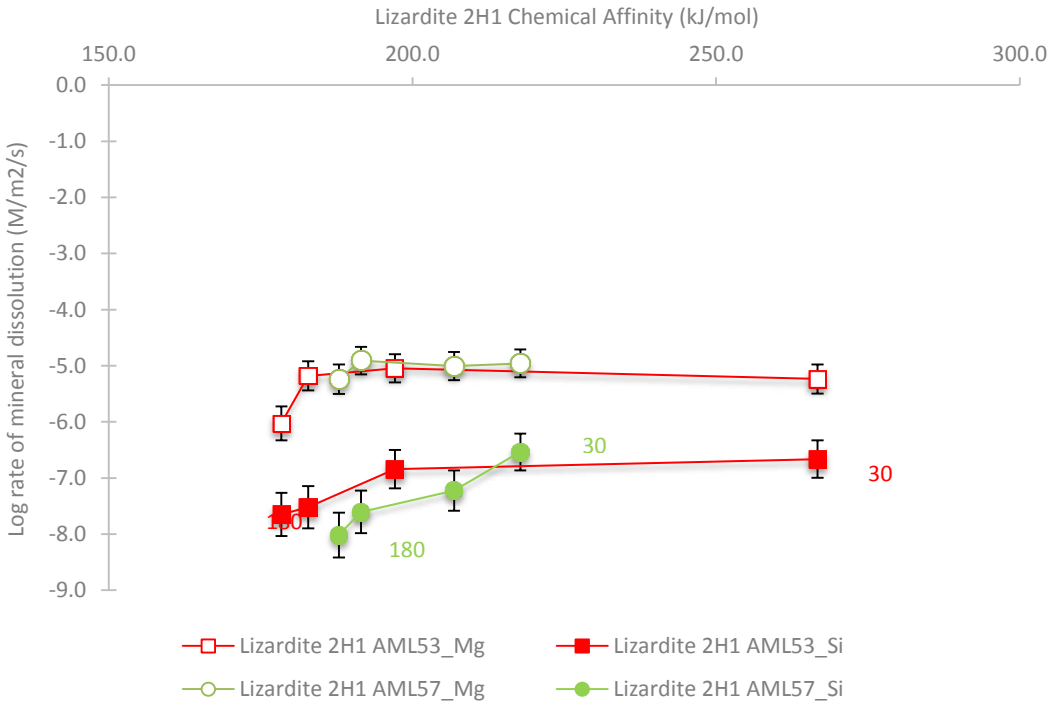


Figure 4.18. Log rate of dissolution of lizardite 2H1, based on Mg^{2+} and Si^{4+} release from samples AML53 and AML57 as a function of the chemical affinity of lizardite. The values of log rate are normalised for mineral stoichiometry at a given reaction time (data derived from XRF analysis of the solid reaction residues). Run durations: 30-180 minutes, right to left, as shown for sample AML53 (red). The 30 and 180 marks indicate half an hour and 3 hours experimental data points, with one and two hours data points found in between.

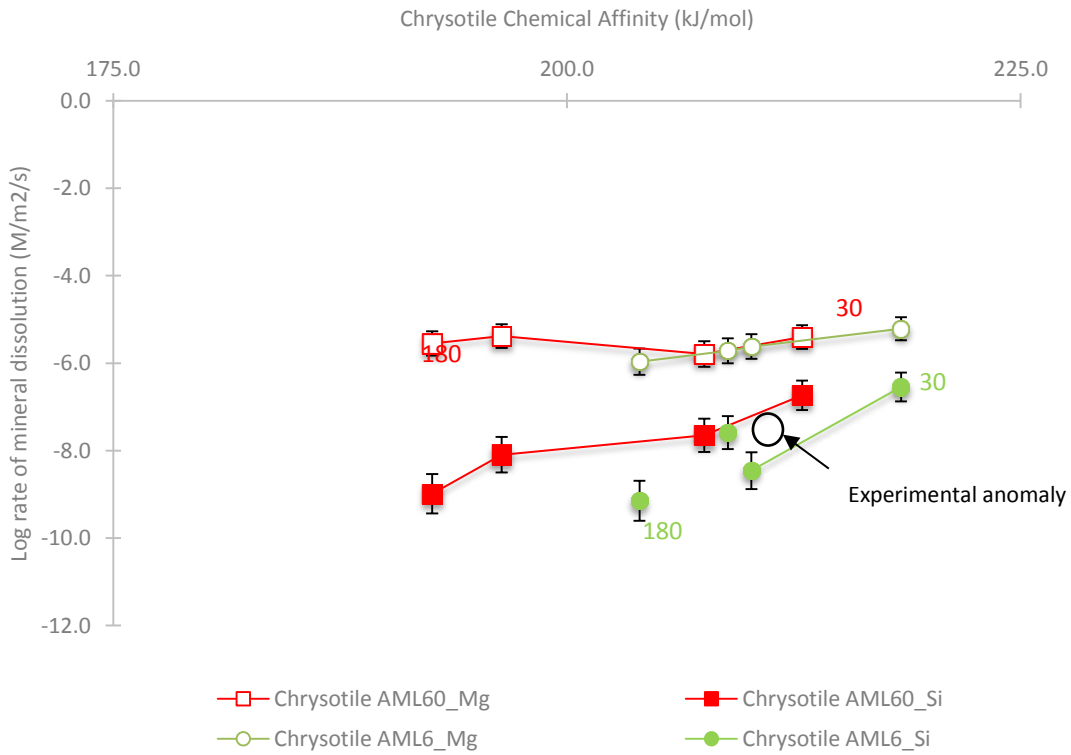


Figure 4.19. Log rate of chrysotile dissolution based on Mg^{2+} and Si^{4+} release from samples AML6 and AML60, as a function of the chemical affinity of chrysotile. The values of log rate are normalised for mineral stoichiometry at a given reaction time (data derived from XRF analysis of the solid reaction residues). Run durations: 30-180 minutes, right to left.

4.3.3. Mineralogy of solid reaction residues

In this Section the mineralogical and chemical transformations of bulk samples, as assessed using XRD, XRF and FTIR, are reported on. This is followed by an appraisal of the compositional and textural transformations of single particles, as observed using OM, SEM and EDS.

4.3.3.1. Mineralogical transformations – bulk samples

The mineralogical composition of the solid reaction residues was appraised using XRD. The quantitative analyses of the starting materials, and samples after ("b") 60 and ("d") 180 minutes of acid leaching are summarised in Table 4.4.

Table 4.4 Summary of XRD quantitative analyses using Rietveld Refinement. The results are tentative due to peak overlaps in serpentine minerals and the presence of poorly crystalline or amorphous material in the reaction residuum, and should only be used in combination with data from other techniques. Symbols: RR_b60 – Reaction residuum 60 min; NR-not refined; v – phase present but not quantified due to analytical difficulties. Major phases are highlighted in grey. (*) Boussingaultite in AML57 is probably overestimated.

Sample no	Dominant phase	Comments	Amor-phous	Lizardite 1T	Lizardite 1M	Lizardite 2H1	Chrysotile	Antigorite	Talc	Chlorite	Magnetite	Hematite	Calcite	Dolomite	Halite	Boussin-gaultite	Hexahydri-te	Gypsum	Retgersite
AML2	**Antigorite**	Not refined						> 85.2											
RR_b60								Major								Trace			
RR-d180								Major								Trace			
AML59	**Antigorite**			1.2				98.8											
RR-b60			8.1					90.6								1.3			
RR-d180			20.8					75.8								3.4			
AML4	**Lizardite 1T**			79.9			19.6							0.5					
RR-b60		Not refined		NR			NR												
RR-d180				88.2												8.2	3.6		
AML46	**Lizardite 1T**			89.0					1.2	9.4					0.3				
RR-b60				74.1					2.9	5.2						17.8			
RR-d180			6.2	50.1						8.6						35.1			
AML53	**Lizardite $2H_1$**					99.1	0.9												
RR-b60			36.7			56.9										6.4			
RR-d180			65.0			28.3										6.7			
AML57	**Lizardite $2H_1$**					98.0	2												
RR-b60			13.8			78.3										7.9			
RR-d180			43.5			13.0										43.5*			
AML62	**PLS-1M**			5.9	94.1														
RR-b60		Not refined		NR	v											v			
RR-d180		Not refined		NR	v											v			
AML6	**Chrysotile**						94.7				4.3	1.0							
RR-b60		+0.6 trevorite	16.7				71.3				1.8	0.3				9.9			
RR-d180			6.8				69.2									19.6			4
AML60	**Chrysotile**						87.7		1.4				11.1						
RR-b60							NR											v	
RR-d180							NR											v	

As expected, the most prominent transformations were observed for samples with the highest values of Mg^{2+} *EE,* with the amount of serpentine mineral decreasing rapidly with time (sample "b" to "d" (Table 4.4)). Accordingly, lizardite $2H_1$ and chrysotile showed the greatest transformation, with ~ 80 % of the lizardite destroyed after 3 h of acid-leaching. These samples were also characterised by the presence of amorphous material that correlated well with the presence of a siliceous reaction residuum, consistent with incongruent dissolution and structural damage to the serpentine minerals. The progression of structural damage during acid leaching is discussed further in Section 4.3.3.4 (FTIR).

A few minerals crystallised during the experiments, as a result of reaction between extracted Mg^{2+}, Ca^{2+} and Ni^{2+} ions, and the ammonium bisulphate solution:

- ***Boussingaultite*** $(NH_4)_2Mg(SO_4)_2{\cdot}6H_2O$ was identified in all but one reaction residue (lizardite $1T^{AML4}$). The amount of boussingaultite depended on (a) the length of post-experimental drying, with fluidic film retained on particle surfaces and (b) Mg^{2+}- saturation in solution, related to mineral EE.
- ***Gypsum*** $CaSO_4{\cdot}2H_2O$ was identified in the reaction residue of chrysotile^{AML60}, with Ca^{2+} originating from the dissolution of calcite.
- ***Hexahydrite*** $MgSO_4{\cdot}6H_2O$ was identified instead of boussingaultite in the reaction residue of lizardite $1T^{AML4}$.
- ***Retgersite*** $NiSO_4{\cdot}6H_2O$ was identified in the reaction residue of chrysotile^{AML6}. This mineral forms from solution between 31.5 and 53.3°C, above which it turns into nickelhexahydrite [*Frondel and Palache*]. This suggests that this mineral formed during the final cooling stages, since the experiment was run at a constant 70°C.

4.3.3.2. XRD challenges and data discrepancies

It should be noted that the XRD data may be associated with significant uncertainties. In many cases the interpretation was considered inconclusive due to severe peak overlaps between serpentine minerals, reaction products and quartz that was added as a secondary quantification standard. In addition, incongruent dissolution resulted in the development of a poorly crystalline or amorphous residuum that alleviated the problems of quantification. Accordingly, no quantitative data is provided for cases with poor whole pattern fits, *i.e.* lizardite $1M^{AML62}$ or chrysotile^{AML60}.

Further, the % value for lizardite 1T in the reaction residuum for sample AML4 "sample d 180 min" appeared to be higher than that of the starting material. However, it is noted that the original sample AML4 contained lizardite 1T and *ca.* 20% chrysotile. Chrysotile was completely dissolved during the experiment whilst lizardite was not, and as this data is normalised to 100%, it led to an apparent higher amount of lizardite 1T in the reaction residuum than the starting material.

Similarly, the data for lizardite^{AML46}, containing chlorite and talc, were not in agreement with other observations. These additional mineral phases did not dissolve and their amount in the residuum should reflect the starting material. However, as indicated in Table 4.2, the amount of chlorite appeared to decrease from 9.4% to 5.2% in the residuum after 60 minutes, but increase to 8.6% in the residuum after 180 minutes. This discrepancy was attributed to poor pattern fit and the heterogeneity of the analysed samples.

4.3.3.3. Chemical changes of the bulk solid residues

The chemical composition of the starting solids and corresponding reaction residues were appraised using XRF. The results were used as a means of unravelling the factors that affected Mg^{2+} extraction efficiency. The term ***extraction efficiency (EE)*** is used in this study to describe the percentage of cation extracted from a specific serpentine mineral normalised to the starting composition.

$$EE = (OC_x * 100)/OC_t$$

Where, OC_x is the oxide concentration measured in the reacted material and OC_t is the total oxide concentration in the starting material.

The full data set, reported as wt% metal oxide, is presented in Appendix D. Figures 4.20-4.22 illustrate the EE trends for Mg^{2+}, Fe^{total} and Al^{3+} as a function of time.

Chrysotile and lizardite $2H_1$ samples showed the highest EE, with nearly 85% and *ca.* 80 % Mg^{2+} extracted after 180 minutes, respectively. The extraction of Fe^{total} and Al^{3+} shown in Figures 4.21-4.22, was generally high for chrysotile and lizardite $2H_1$, reaching 80-90% of the starting elemental concentration. Three samples; two antigorites and lizardite 1T, showed low EE and the amount of Mg^{2+}, Fe^{2+} or Al^{3+} extracted after 180 minutes did not exceed 35%. A sample of polygonal serpentine with lizardite 1M in sectors ($PS1M^{AML62}$) fell between the two extremes with intermediate values for Mg^{2+}, Fe^{total} but high for Al^{3+} extraction, reflecting the aluminous composition of the starting serpentine. This sample was composed of two aluminous serpentine minerals: polygonal serpentine and proto-serpentine matrix, with the latter contributing most to the higher Al^{3+} extraction (Section 4.3.3.6)

The lizardite $1T^{AML4}$ sample contained *ca.* 20 % of chrysotile in the staring material. To obtain the Mg^{2+} EE from lizardite 1T only, an estimated EE value for chrysotile (based on sample AML60) was subtracted from the AML4 EE total. Accordingly, 20% of the 180 minute Mg^{2+} EE for $chrysotile^{AML60}$, *i.e.* 16.6%, was subtracted from the total Mg^{2+} EE for AML4, returning a residual value of *ca.* 5% - reflecting the Mg^{2+} EE for lizardite 1T only. Similarly, EE values from 30, 60 and 120 minute sample residues were estimated and plotted in Figure 4.20, confirming that the EE for AML4 was chiefly due to the presence of chrysotile, with only *ca.* 5% of Mg^{2+} extracted from lizardite 1T after 180 minutes. This preferential chrysotile leaching is further, very clearly shown by microanalysis of leached particles (Section 4.3.3.6). The original sample also contained *ca.* 0.5 % of dolomite that might have provided a trace (<0.5%) proportion of Mg^{2+}.

A few samples, *e.g.* $chrysotile^{AML60}$, showed fast initial dissolution and a subsequent, increasingly linear trend, resulting in an overall sub-parabolic to parabolic dissolution curve. The fast initial dissolution was attributed to the large number of very small particles (d_{50} = 8.8 µm) that would provide high surface area, enhancing fluid-rock interaction.

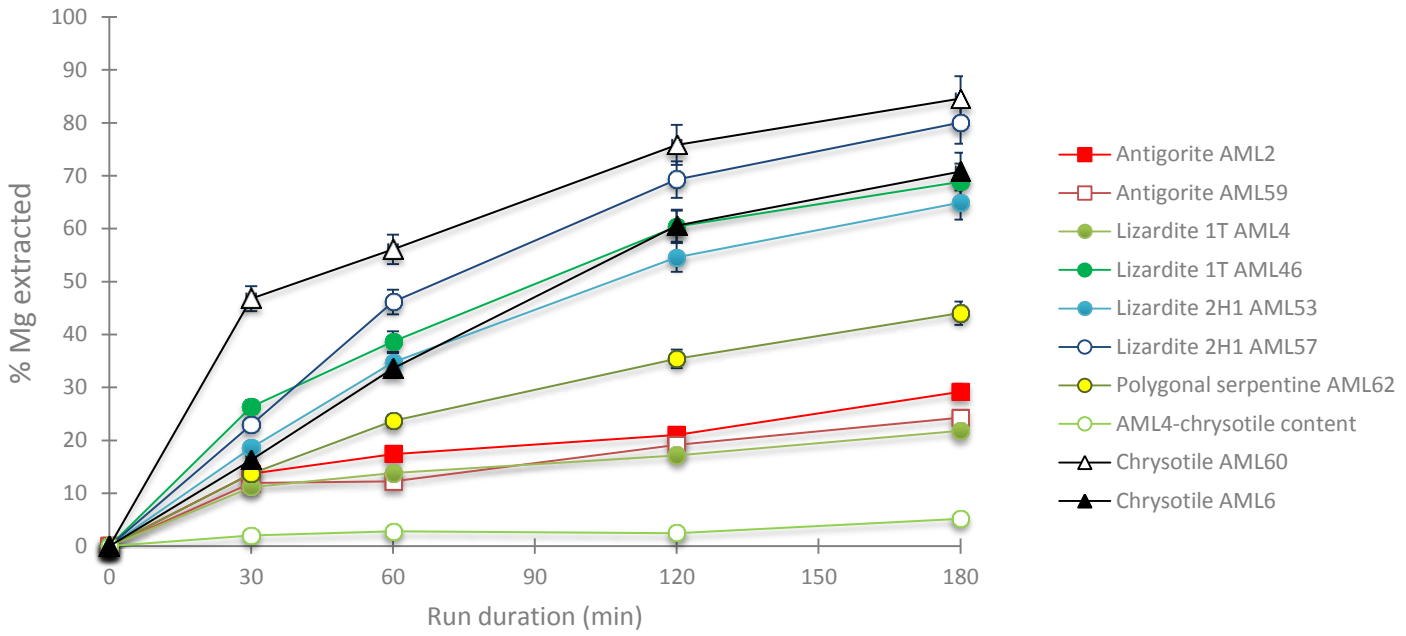


Figure 4.20. Percentage Mg extracted as a function of time based on solid residue XRF data, normalised to the composition of the starting material. 5% error bars are applied.

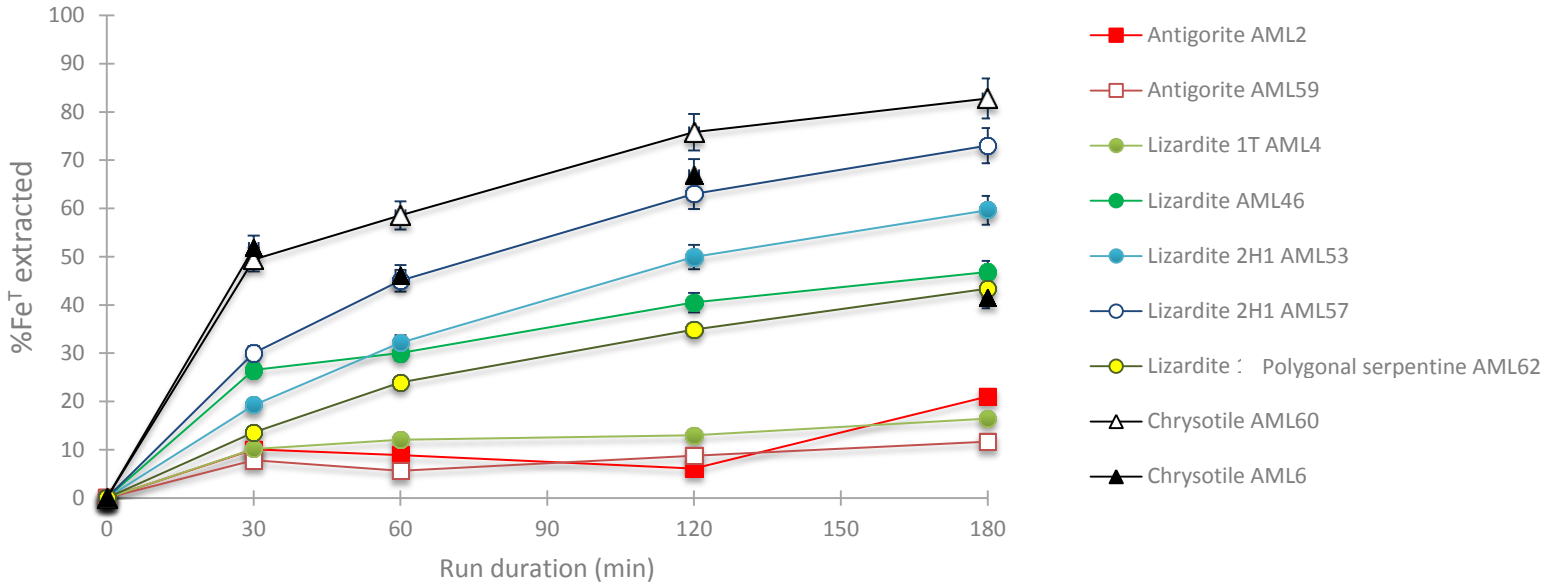


Figure 4.21 Percentage Fe extracted as a function of time based on solid residue XRF data, normalised to the composition of the starting material. 5% error bars are applied.

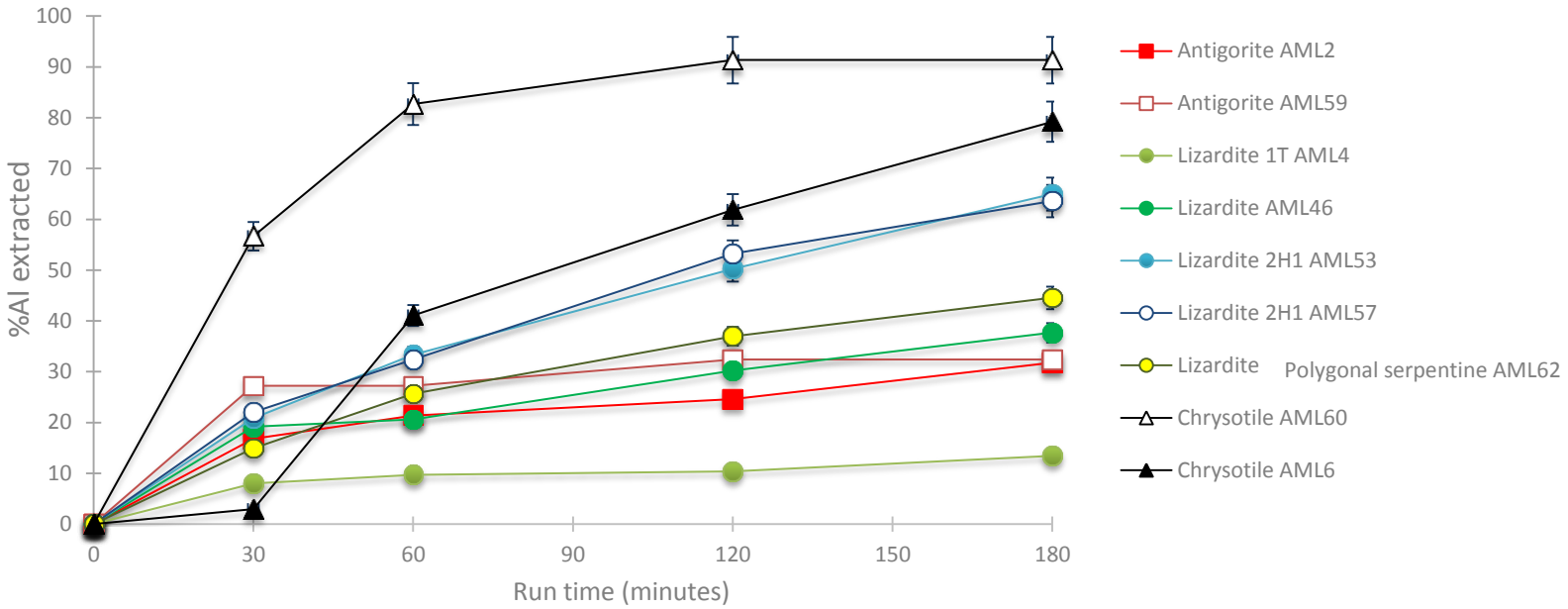


Figure 4.22 Percentage Al extracted as a function of time based on solid residue XRF data, normalised to the composition of the starting material. 5% error bars are applied.

4.3.3.4. Congruency of dissolution

Since most of the samples were largely monomineralic, the congruency of dissolution could be inferred from the amount of wt% MgO and SiO_2 remaining in the reaction residuum, again ascertained using XRF data.

During the congruent dissolution of a mineral, the elemental ratios in the leachate should be the same as in the mineral. Accordingly, the trend lines for MgO and SiO_2 dissolution, as plotted in Figure 4.23, would be expected to run parallel and with a small offset (related to the variable amounts of a given oxide in the starting material). However, this trend was shown only by antigorite^{AML2} (Figure 4.23b), reflecting the stoichiometric release of Mg^{2+} and Si^{4+}. The dissolution plots for all the other samples diverged, with line separations being particularly prominent for samples with high EE, *e.g.* chrysotile^{AML60} (a similar trend was observed for chrysotile^{AML6}) or lizardite $2H_1$^{AML57}, as shown in Figures 4.23c & d, respectively. This suggests that most of the minerals in this study dissolved incongruently, releasing variable amounts of Mg^{2+} (and Fe^{total} and Al^{3+}) into solution, whilst retaining most of the silica in the solid reaction residuum, consistent with the leachate chemistry data.

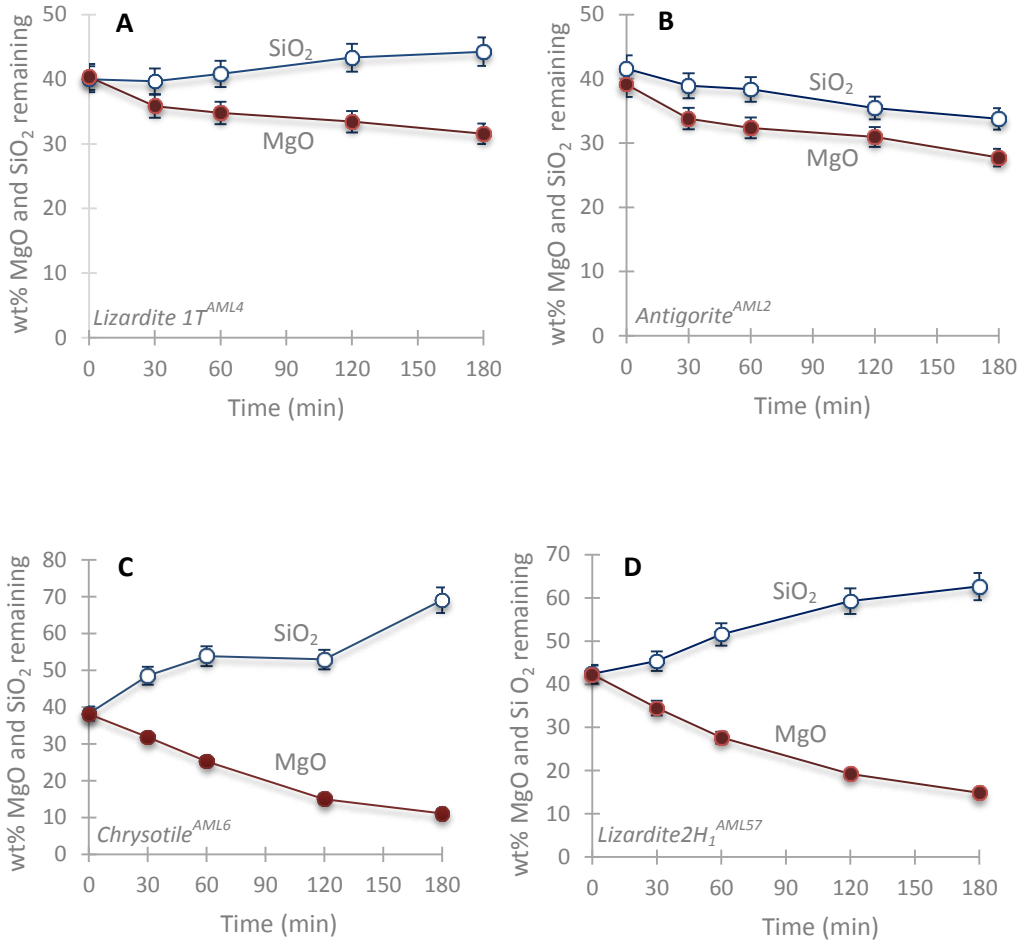


Figure 4.23 Concentration of MgO and SiO_2 (wt%) in the reaction residues as a function of time (XRF raw data) A) lizardite $1T^{AML4}$ showing non-stoichiometric dissolution; B) antigorite^{AML2} showing stoichiometric dissolution; C,D) chrysotile and lizardite $2H_1$ showing non-stoichiometric dissolution.

4.3.3.5. Chemical transformation as assessed by Fourier Transform Infrared Spectroscopy

All the starting serpentine samples and associated solid reaction residues were analysed, in the form of KBr discs, using FTIR spectroscopy. FTIR provided evidence for mineral transformations based on the observations of IR absorption bands, corresponding to molecular vibrations of specific functional groups within the crystal structures.

Figure 4.24 presents FTIR spectra of antigorite^{AML2}, lizardite1T^{AML4} and chrysotile^{AML60} starting materials and their associated reaction residues after 30, 60, 120 and 180 minutes of acid leaching. The structural transformations observed were similar for all these samples with the most prominent changes being associated with two spectral regions related to the lattice vibrations of:

- *Basal and apical Si-O bonds*: at 983 cm^{-1} and 1066 cm^{-1} in antigorite; 950 cm^{-1} and 1080 cm^{-1} in lizardite 1T; and 965 cm^{-1} to 1088 cm^{-1} in chrysotile. The main transformations related to these peaks included changes in relative intensity and the formation of new shoulders/peaks towards higher wavenumber. A general decrease in the "basal Si-O peak" intensity was observed, being attributable to a time-dependent transformation within SiO_4 tetrahedra and preferential breakage of weaker, basal Si-O bonds. The most prominent change of relative peak intensity was observed for chrysotile (Figure 4.24c), with near complete loss of the basal Si-O peak in the 180 minute residuum. This was attributed to the high degree of structural deformation, corresponding to high levels of Mg^{2+} release, during acid-leaching.

Structural modifications in the region of apical Si-O were related to: (i) general peak broadening and (ii) the presence of a new absorption band at *ca.* 1083cm^{-1}, previously attributed to amorphous silica [*Madejova*, 2003]. A low intensity peak at *ca.* 1143 cm^{-1} in antigorite (Figure 4.24, yellow arrow) and a distinctive shoulder in lizardite 1T were observed in the 120 and 180 minute residues. This peak/shoulder was previously observed at 1150 cm^{-1} ([*Farmer*, 1974] p. 369) and 1145 cm^{-1} [*Shoval et al.*, 1991], respectively, with the latter authors noting that this peak resolution appeared to be sensitive to the crystallinity of quartz within the sample, with well-crystalline quartz showing a well-defined peak or shoulder.

In the chrysotile sample, a quartz-related peak/shoulder at *ca.* 1145 cm^{-1} was not observed. The modified Si-O related peaks overlapped severely with bands corresponding to secondary gypsum and/or boussingaultite, and a distinctive peak at 1102 cm^{-1} (180 minutes residuum) probably related to either amorphous silica (opal in [*Farmer*, 1974] p. 369) or to stretching vibrations of SO_4 tetrahedra [*Liu et al.*, 2009], originating from secondary minerals. The presence of gypsum was also manifested by two peaks previously assigned to O-H bending vibration modes at *ca.* 1682 cm^{-1} and 1619 cm^{-1} [*Liu et al.*, 2009].

The presence of amorphous silica in the chrysotile residuum was confirmed by a peak at *ca.* 800 cm^{-1} [*Madejova*, 2003] that exhibited a subtle increase of intensity with time of reaction (orange arrow in Figure 4.24c)

- <u>*OH bonded to Mg cations*</u> in the octahedral position produced absorption bands at *ca.* 3676 cm^{-1} for antigorite, 3684 cm^{-1} for lizardite and 3690 cm^{-1} for chrysotile. The greatest decrease in relative intensity with time was observed for chrysotile (Figure 4.24c), in agreement with previous observations of high Mg^{2+}

EE. Equally, the low EE in antigorite and lizardite 1T was represented by the presence of a residual, but still well-defined peak in this spectral region.

Low dissolution-related structural deformation of lizardite 1T was also inferred from the presence of a low intensity peak at *ca.* 801 cm^{-1} in all the lizardite 1T reaction residues. This band was previously assigned to tetrahedrally-coordinated ferric iron [*Fuchs et al.*, 1998] and its persistence, even after 180 minutes of acid leaching, suggested none or a low degree of modification of the tetrahedral sites. This was in agreement with other data showing a low degree of dissolution for lizardite $1T^{AML4}$.

Other changes observed in the reaction residues were related to the formation of boussingaultite $(NH_4)_2Mg(SO_4)_2 \cdot 6H_2O$, whilst a series of low intensity peaks observed between 1435 cm^{-1} and 1470 cm^{-1} were attributed to bending vibrations of NH_4 bonds [*Culka et al.*, 2009]. The SO_4 stretching vibrations in boussingaultite occurred at *ca.* 980 cm^{-1} to 1133 cm^{-1} and overlapped with Si-O vibrations from serpentine minerals. Broad bands at *ca.* 1630 cm^{-1} and 3300 - 3440 cm^{-1} were probably related to H_2O, either in the crystal structure or in form of moisture adsorbed onto the particles [*Farmer*, 1974; *Madejova*, 2003]. Peaks at *ca.* 1430 cm^{-1} and 887 cm^{-1} in the chrysotile starting material were attributed to the presence of calcite [*Adler and Kerr*, 1963].

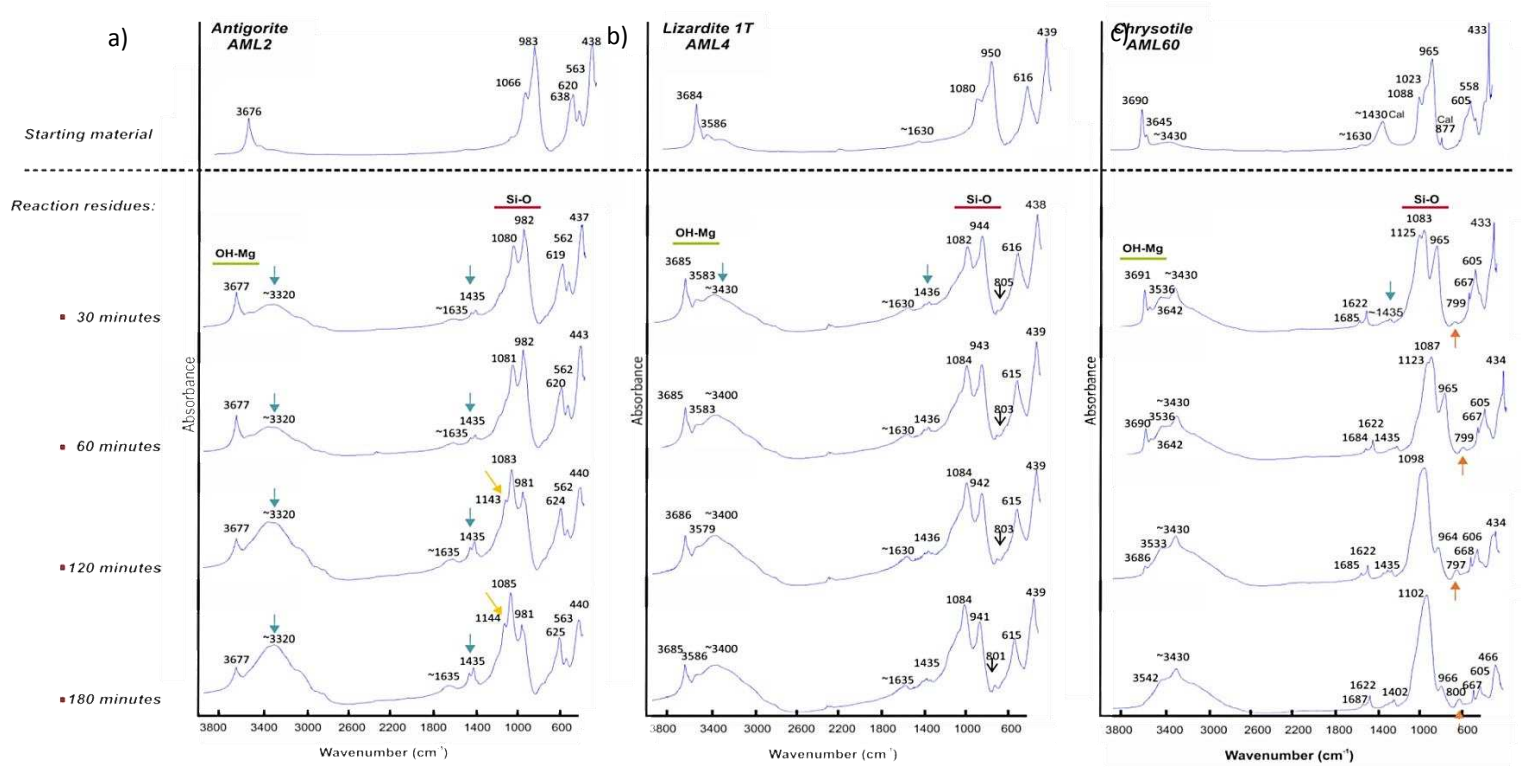


Figure 4.24 FTIR spectra of (a) antigorite^{AML2} (b) lizardite 1T^{AML4} and (c) chrysotile^{AML60} and associated reaction residues; reflecting the time dependent structural modifications that occurred during acid leaching. The blue arrows correspond to secondary boussingaultite, the yellow arrows indicate a low intensity peak attributable to quartz, and the orange arrows indicate a peak corresponding to amorphous silica.

4.3.3.6. Mineralogical and textural transformations of single particles

To observe the time-dependent mineralogical and textural changes, the reacted powders (60 and 180 minute residues) were prepared as polished thin sections and analysed by petrographic microscopy and SEM. The SEM observations have been summarised as composite figures with images presented alongside associated X-ray spectra and elemental distribution maps.

The ***antigorite*** samples displayed similar compositional and textural transformation features (*e.g.* Figure 4.25, AML2). The mineral fines commonly amassed into large, ~ 1 mm clusters, most likely being a consequence of drying of the solid residuum post-processing. The clusters contained a random selection of compositionally and texturally variable fines, including larger (up to 150 µm) unreacted antigorite particles cemented with siliceous matrix and/or boussingaultite.

The reacted particles retained the morphologies of the starting material. Their composition varied slightly, but the majority of particles showed serpentine composition, with only subtle changes in elemental Mg to Si peak ratios (Figure 4.25, Spectrum 1). A significant decrease of Mg was noted, however, in the very fine fraction of residual powder, indicating the preferential dissolution of fines.

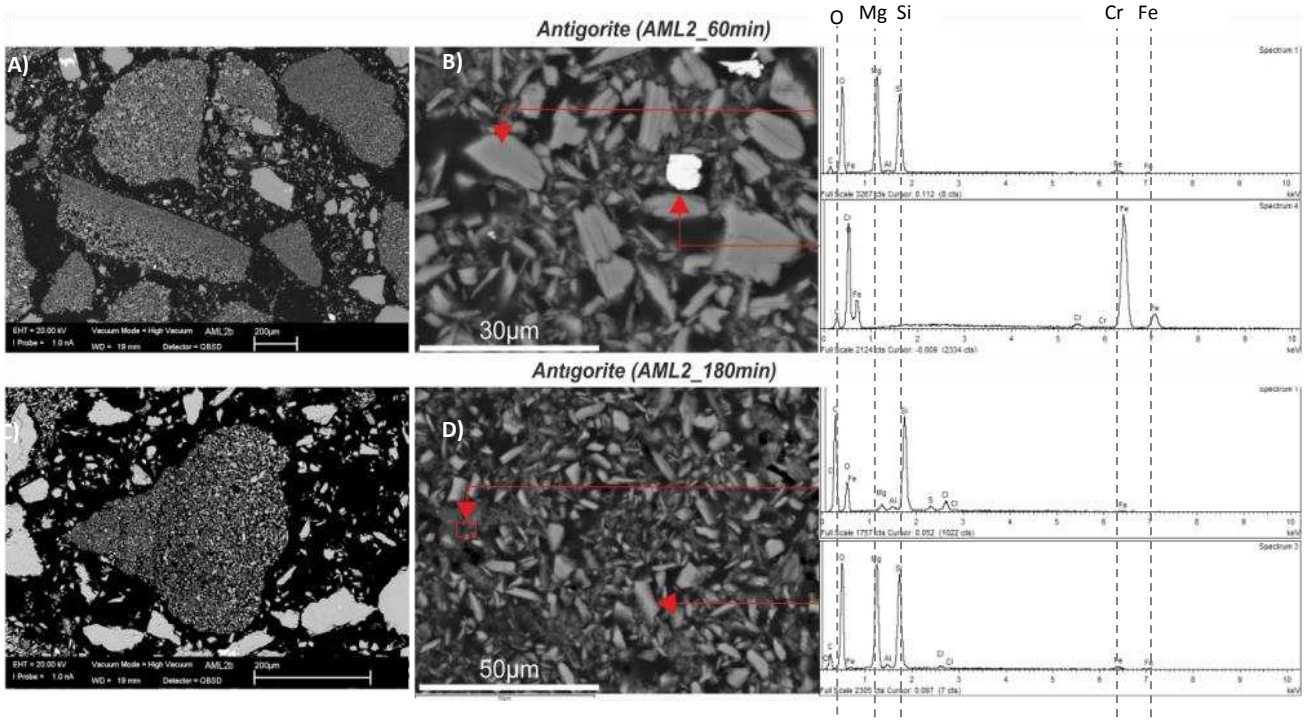


Figure 4.25 Textural and compositional time-dependent particle transformation in antigorite (example from AML2): a) 60 minute residuum with clusters of antigorite and leached, siliceous residuum; b) high magnification image of residual antigorite particles with composition approximating the starting material; scattered particles of magnesite were also observed; c) low magnification of 180 minute residuum cluster and d) high magnification image detailing the cluster with siliceous matrix and unreacted antigorite fines.

The reaction residues of the ***lizardite samples*** displayed a much wider textural and compositional diversity. Five samples of this polymorph group were analysed. The lizardites' EE ranged from the lowest amongst all the samples studied, *i.e.* lizardite $1T^{AML4}$ with only *ca.* 5% Mg-extracted after 180 minutes, to one of the highest, *i.e.* lizardite $2H_1^{AML57}$ with *ca.* 80 % Mg-extracted. The differences were clearly demonstrated in the texture and composition of the reaction residues.

The composite figure for lizardite $1T^{AML4}$ (Figure 4.26) illustrates the clusters of fines, similar to those seen in antigorite, along with partially leached individual particles. In particular, several compositionally and texturally varied particles with deeply leached zones embedded within slightly leached lizardite 1T were observed. The Mg-depleted zones probably corresponded to vein and interstitial chrysotile, a characteristic feature of the starting material and common in many serpentinites. These zones were usually fractured, and the fractures, when seen within a vein, were perpendicular to vein - host rock contact. Their origin was not clear but could be related to stresses induced by volume changes during Mg-leaching and / or dehydration during drying post-reaction (*i.e.* desiccation cracks). The preferential alteration of chrysotile-rich zones, which constituted approximately 20 % of AML4, dominated the EE of Mg^{2+} from lizardite $1T^{AML4}$.

The degree of mineral dissolution was time dependent and as expected, prolonged, 180 minutes exposure to acid resulted in a higher degree of mineral (chiefly chrysotile) transformation (Figure 4.26, EDS spectra from lizardite $1T^{AML4}$ after 60 and 180 minutes).

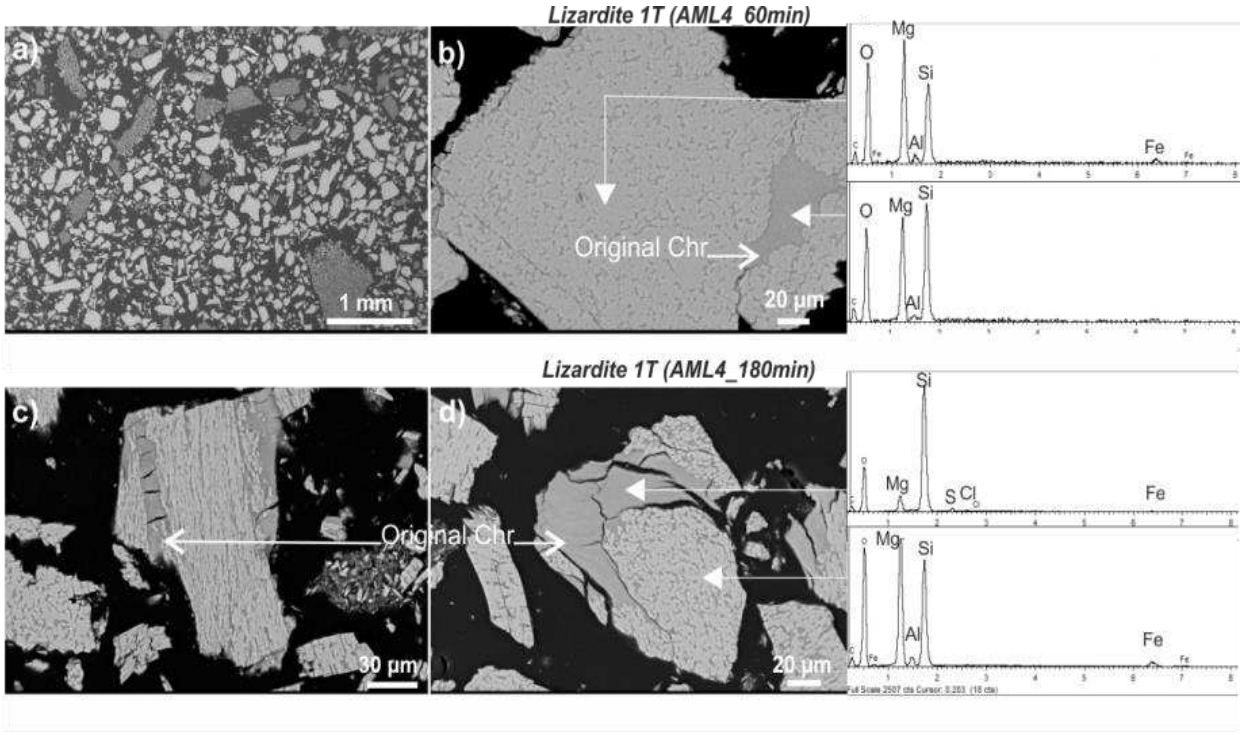


Figure 4.26 Textural and compositional time-dependent particle transformation in lizardite 1T (Monte Fico, Elba, AML4): a) low magnification BSE image of composite and partially-leached particles encountered in the 60 minute residuum; b) high magnification BSE image showing a partially Mg-leached zone corresponding to original chrysotile and virtually, intact lizardite 1T; c) and d) representative 180 minute leached particles with a pronounced siliceous residuum matching the distribution of original chrysotile; the lizardite 1T, manifested here by higher Z-contrast, remained un-leached.

The EE for the two ***lizardite $2H_1^{AML53,\ AML57}$*** samples (Gwendreath Quarry (UK)) were the highest amongst the lizardites analysed (up to 80% Mg-extracted in 180 minutes). The two samples varied initially in terms of degree of deformation and associated mineral crystallinity, and these features appear to have defined the transformation and reaction residue formation, and thus the EE (Figure 4.27).

As illustrated by BSE images of the reaction residues after 60 and 180 minutes of acid leaching (Figure 4.27), the particles exhibited two types of leaching-related transformation textures:

- ***Textures corresponding to features observed in the starting material***, *i.e.* the spatial distribution of co-existing minerals and the degree of sample deformation. This texture was manifested by the development of two variably-leached zones: *i.e.* (a) a heavily-leached, micro-fractured dense mass with low physical relief, exhibiting low BSE contrast, dominant in both samples; and (b) partially-leached euhedral to subhedral (locally truncated prisms), with embedded high relief crystals, dominant in the $L2H_1^{AML53}$. This transformational diversity was consistent with the starting lizardite samples being heterogeneous, reflecting a variable degree of crystallinity of lizardite $2H_1$ rather than a different type of serpentine.
- ***Leached layer textures,*** manifested by well-defined Mg-depleted reaction zones at particle edges and partially-reacted particle cores. The interfaces between these core/shell zones generally were chemically abrupt, whilst some particles exhibited tapered micro-cracks within the Mg-depleted zones. Residue particles, after 60 and 180 minutes of acid leaching, were chemically mapped and compositionally analysed using EDS. The leached zones were concentric for a large number of particles, following a shrinking core model for dissolution with an outer product layer (*i.e.* depleted reaction shell) surrounding each particle [*Teir et al.*, 2007]. This is illustrated by Figure

4.27a, with line profiles of Mg and Si wt% for a representative residue particle (60 minutes of leaching), along with corresponding elemental distribution maps, highlighting the compositional differences of these two distinctive zones.

This 'leached-layer texture' was observed predominantly within the less well-ordered lizardite $2H_1^{AML57}$. This sample was mineralogically homogeneous (composed of lizardite $2H_1$ predominantly) but exhibited significant textural heterogeneity, manifested by strong shearing. It is considered that the high degree of micro-deformation (inherited from the original rock) associated with this sample, resulting ultimately in low mineral crystallinity, was the main factor affecting the higher reactivity of this sample.

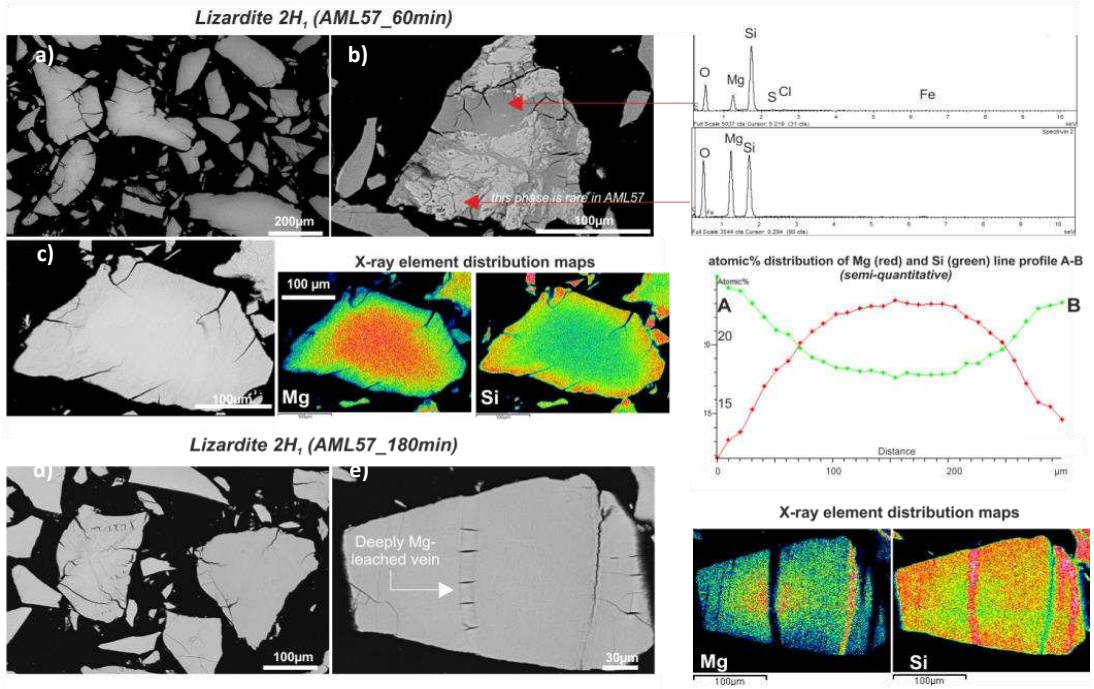


Figure 4.27 Textural and compositional time-dependent particle transformation in lizardite $2H_1$ from Gwendreath Quarry, Lizard Peninsula (AML57): a) low magnification image of 60 minute-leached particles showing a roughly even distribution of leached and fractured shells; b) high magnification image showing texture-controlled preferential leaching; c) high magnification image of a concentrically leached particle, with elemental distribution shown on the associated maps and line profiles; d) exemplary image of the 180 minute-leached particles and e) high magnification image and associated elemental distribution maps showing a deeply-Mg-leached shell and a deeply-leached vein, probably originally composed of chrysotile. For comparison, a representative image of the original, unreacted particle is given in Chapter 3, Figure 3.11.

4.3.3.7. Quantitative EDS analysis of reaction residues within lizardite $2H_1^{AML57}$

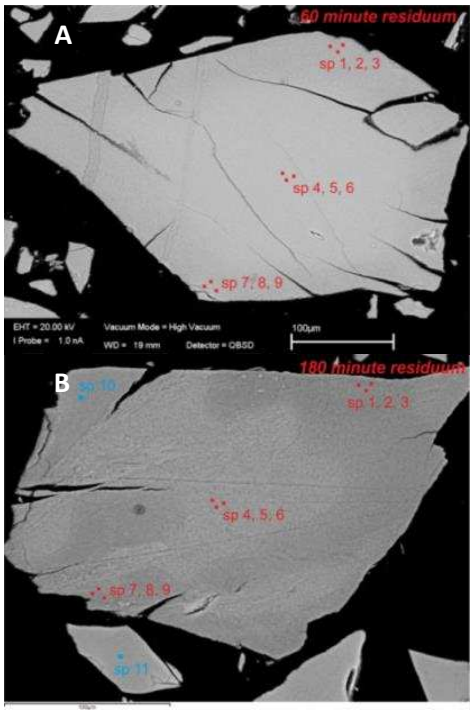
Quantitative analyses were performed on carbon coated thin sections of lizardite $2H_1^{AML57}$ using SEM-EDS. The analyses revealed that residue cores after 60 minutes of leaching contained *ca*. 38 wt% MgO (Table 4.5), *i.e.* only a few wt% lower than in unreacted lizardite (*ca*. 40.9 wt% MgO). The amount of MgO in the reacted particle shells, on the other hand, was much lower, with values of *ca*. 16 – 25 wt% MgO detected (Table 4.5).

The amount of MgO in residue particle cores after 180 minutes of leaching was noticeably lower, at ~ 33 wt%, but was only subtly lower in the residue particle shells, at 17 – 24 wt% than in the shells after 60 minutes. These chemical differences between residuum particles after 60 and 180 minutes demonstrates fast initial dissolution, then stabilisation of the shell material which suggests an associated process of passivation.

It is noted that the shell / core boundaries in residue particles after both 60 and 180 minutes were very well-defined, suggesting the progression of a well-defined reaction front as dissolution occurred.

A - Reaction residue / 60 minutes / Lizardite $2H_1$ AML57

	Particle shell			Particle core			Particle shell		
Spot	**1**	**2**	**3**	**4**	**5**	**6**	**7**	**8**	**9**
					wt% oxide				
MgO	15.8	17.3	16.4	**38.4**	**38.7**	**38.3**	25.6	24.4	25.7
Al_2O_3	nd	nd	nd	nd	0.3	0.4	0.2	0.2	0.2
SiO_2	61.8	60.0	61.8	43.2	43.9	43.1	61.5	62.4	61.4
SO_3^*	0.8	0.7	0.8	nd	nd	nd	0.5	0.6	0.7
FeO	0.5	0.4	0.4	0.8	0.8	0.6	0.6	0.6	0.6
NiO	nd	nd	nd	0.3	nd	nd	nd	nd	0.2
Totals	**78.8**	**78.4**	**79.4**	**82.7**	**83.7**	**82.5**	**88.3**	**88.1**	**89.3**



B- Reaction residue / 180 minutes / Lizardite $2H_1$ AML57

	Particle's rim			Particle's core			Particle's rim		
Spot	**1**	**2**	**3**	**4**	**5**	**6**	**7**	**8**	**9**
					wt% oxide				
MgO	20.0	20.1	17.6	**33.3**	**32.2**	**33.6**	22.6	24.4	21.7
Al_2O_3	0.6	0.7	0.5	0.9	0.9	1.0	0.7	0.6	0.5
SiO_2	60.1	57.9	60.0	47.4	46.6	46.9	59.8	56.4	59.8
SO_3^*	0.6	0.6	0.6	nd	nd	nd	0.5	0.4	0.6
FeO	0.8	0.9	0.9	1.4	1.4	1.3	0.9	0.9	0.8
Totals	**82.1**	**80.2**	**79.9**	**83.0**	**81.0**	**82.7**	**84.7**	**82.7**	**83.5**

Table 4.5 Quantitative SEM-EDS analyses of lizardite $2H_1$ reaction residues, after a) 60 and b) 180 minutes of acid leaching. The starting material contained ~ 40.9 wt% MgO, 44.5 wt% SiO_2, 1.5 wt% FeO, 0.4 wt% Al_2O_3 and 0.3 wt% NiO. The brighter irregular patches in Figure B were attributed to the

presence of Fe, in subtly higher amounts than in adjacent zones. The relatively high totals in spectra 7, 8 & 9 of particle A suggest a slightly less hydrous region of material.

**The presence of low levels of sulphur in the above analyses was attributed to the ingress of ammonium bisulphate solution into the intra-particulate porosity of the leached material.*

4.3.3.8. Quantitative EDS analysis of reaction residues within lizardite ^{AML62}.

The Mg^{2+} EE for AML62, identified tentatively as ***polygonal serpentine with lizardite 1M sectors PS1M*** (Chapter 3), was one of the lowest measured for the entire sample set, with only *ca.* 40% extracted after 180 minutes of acid leaching. One of the most immediately apparent changes in the reaction residuum was the formation of boussingaultite, in amounts greatly exceeding that of any other sample, occurring as elongate, prismatic crystals as well as a cementing mass for composite particles (Figure 4.28a).

The leached particles in PS1M retained the morphologies of the starting material and although subtle concentric leaching was observed, it was not concomitant with concentric fracturing, as observed for the case of lizardite $2H_1$.

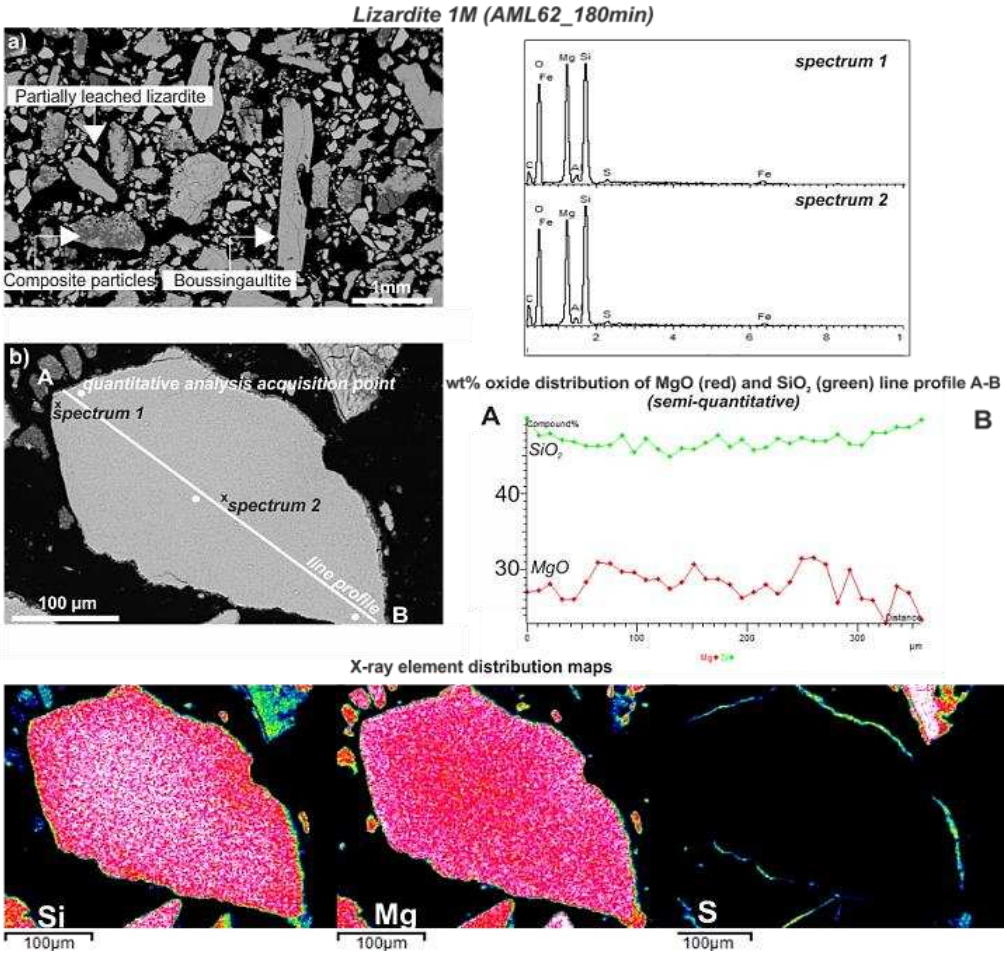


Figure 4.28 Textural and compositional time-dependent particle transformation in polygonal lizardite 1M (AML62): a) low magnification image showing a range of particles encountered in the 180 minute leaching residuum; b) image and X-ray elemental distribution maps of a representative particle showing subtle Mg-depletion of the outer shell and a general uniform chemical transformation. The scatter of data points on the MgO line profiles (line A-B), in particular, is related to sample heterogeneity.

Quantitative SEM-EDS analysis was performed on the same particle after 180 minutes of leaching (Figure 4.28) based on nine acquisition points, with six at the particle edge (three on opposite sides) and three at the core (Table 4.6). Collectively, the data showed that the core / shell boundary was diffuse and not as well-defined as in lizardite $2H_1$. The MgO-line profile (Figure 4.28) and associated quantitative analyses showed that the amount of Mg changed from ~ 40 wt% in the unreacted mineral to ~ 25 wt% in the shell and ~ 28 wt% in the

core, with the transformation appearing to be more uniform, affecting the whole particle.

The elemental distribution map for sulphur (Figure 4.30) and associated values of SO_3 in the EDS data (Table 4.6) suggested significant enrichment within a < 10 µm zone at the particle edge, and a roughly uniform, low distribution throughout the whole particle. Sulphur originated from the solution of ammonium bisulphate. This is similar to the distribution of Cl^- and Ba^{2+} reported by Hellmann *et al* [*Hellmann et al.*, 1990] and attributed to leaching-induced generation of a porous and open structure allowing for the large-scale influx of solvent molecules.

The levels of Al and Fe were almost constant throughout the reacted particle, with values measured comparable to those in the starting material, *i.e.* 2.2 and 2.8 wt% oxide, respectively.

Table 4.6 Quantitative SEM-EDS analyses of a reacted particle of polygonal serpentine with lizardite 1M in sectors (AML62) after 180 minutes of acid leaching. The analyses corresponded to six acquisition spots on two opposite edges and three analyses from the particle core. The acquisition spots are denoted as white dots on the associated BSE image (Figure 4.28).

	Particle rim			Particle core			Particle rim		
Sp No	1	2	3	4	5	6	7	8	9
					wt% oxide				
MgO	25.19	25.73	25.79	28.88	28.24	27.08	27.41	25.73	23.85
Al_2O_3	1.94	1.95	2.12	2.25	2.04	1.93	2.14	2.11	2.01
SiO_2	47.52	48.75	50.14	45.12	45.61	46.68	48.14	48.58	47.31
SO_3	2.02	1.81	1.33	1.44	1.44	1.63	0.96	1.24	0.97
FeO	2.27	2.1	2.08	2.38	2.33	2.28	2.29	2.13	2.11
Totals	**78.94**	**80.35**	**81.47**	**80.08**	**79.65**	**79.6**	**80.94**	**79.8**	**76.26**

The lack of concentric edge-fractures, the presence of faint core/shell boundaries, a more uniform elemental distribution and the presence of sulphur in the deepest parts of the particle suggest the action of a more gradual leaching rather than step-like dissolution/leaching process (with well-defined core/shell boundaries),

as observed for lizardite $2H_1$. This type of gradual leaching might be related to the micro-texture observed for particles in PS1M that included numerous randomly oriented fine (< 1 µm diameter), nanotubular crystals in a dense "anhedral" matrix of other, unidentified, serpentine mineral (Figure 4.29). Positive identification was hindered due to the fine nature of the mineral; however, it is likely to constitute a poorly-crystalline phase.

Figure 4.30 shows high magnification elemental distribution maps illustrating the preferential leaching of the serpentine matrix (dark grey contrast, BSE image, Figure 4.29) and the relative un-reactiveness of the nanotubular crystals. The progressive dissolution of the highly reactive matrix provided micro-permeable pathways for fluid ingress into deeper zones of the particles. The even distribution of sulphur within the particles was again in agreement with gradual fluid movement through zones of higher, well-interconnected micro-permeability.

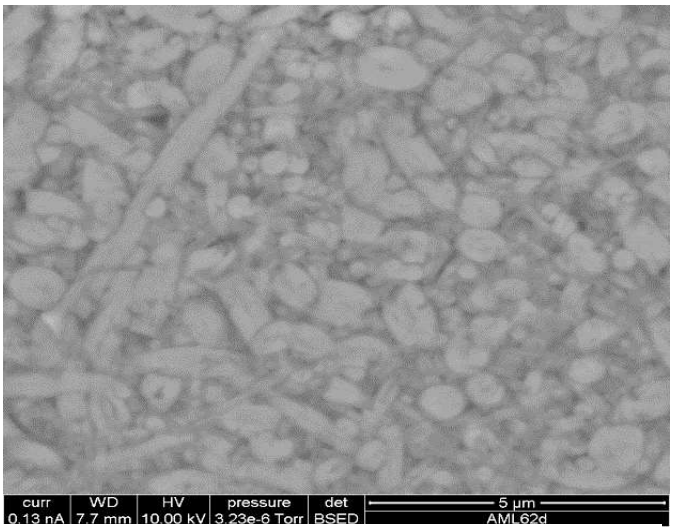


Figure 4.29 Reaction residuum in AML62 after 180 minutes, showing partially leached elongate and rounded crystals of lizardite within a deeply leached anhedral mass.

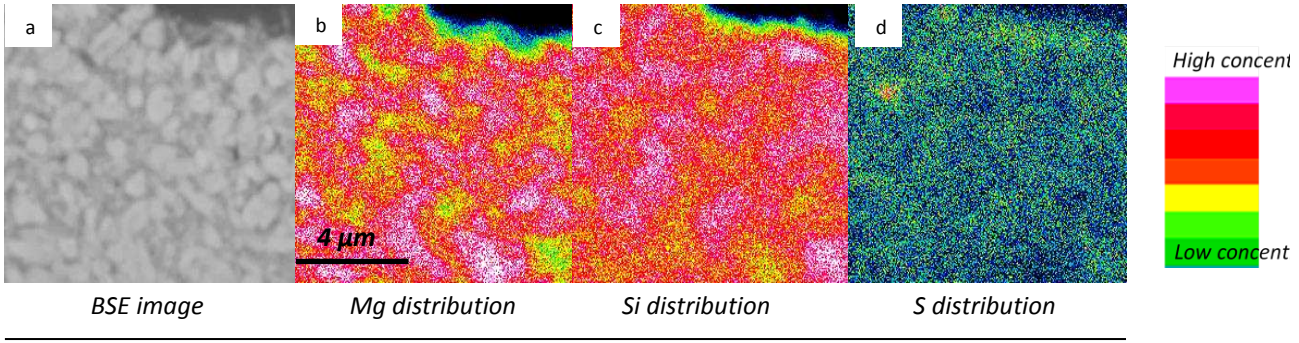


Figure 4.29 Elemental distribution maps for a particle fragment of PS1M after 180 minutes of acid leaching: a) BSE image; b) Mg-distribution map showing Mg-depletion in the low Z contrast regions of the corresponding BSE image; c) Si-distribution map with Si-enrichment in the low Z contrast region of the BSE image; and d) S-distribution map showing enrichment within the deeply Mg-rich zones.

The EE of the mineralogically heterogeneous ***lizardite 1T^{AML46}*** dominated sample from Kennack Sands (UK) was moderate with *ca.* 60 wt% MgO extracted after 180 minutes of leaching. Apart from lizardite, the original sample contained significant amounts of talc (< 2%) and chlorite (*ca*. 10%).

Neither talc, nor chlorite showed any significant evidence for dissolution and almost intact crystals of both were found within the leached residuum (Figure 4.31a,c). The lizardite-dominated particles displayed a wide range of textural and chemical transformations that were similar to those observed in lizardite $2H_1$. The spatial distribution of crystals and internal textures served as pathways for fluid penetration. The preferential leaching of an unidentified serpentine species present in AML46 resulted in the enhancement of texture, whilst minerals that proved leaching-resistant appeared prominent in the residuum. Consequently, un-reacted truncated prisms up to 10 µm long, concentrically arranged around a leached centre (possibly a polygonal serpentine), or aligned sub-parallel along vein walls, were observed. The leached residuum contained a large number of composite particles along with < 20 µm, platy almost shard-like Si-rich fines.

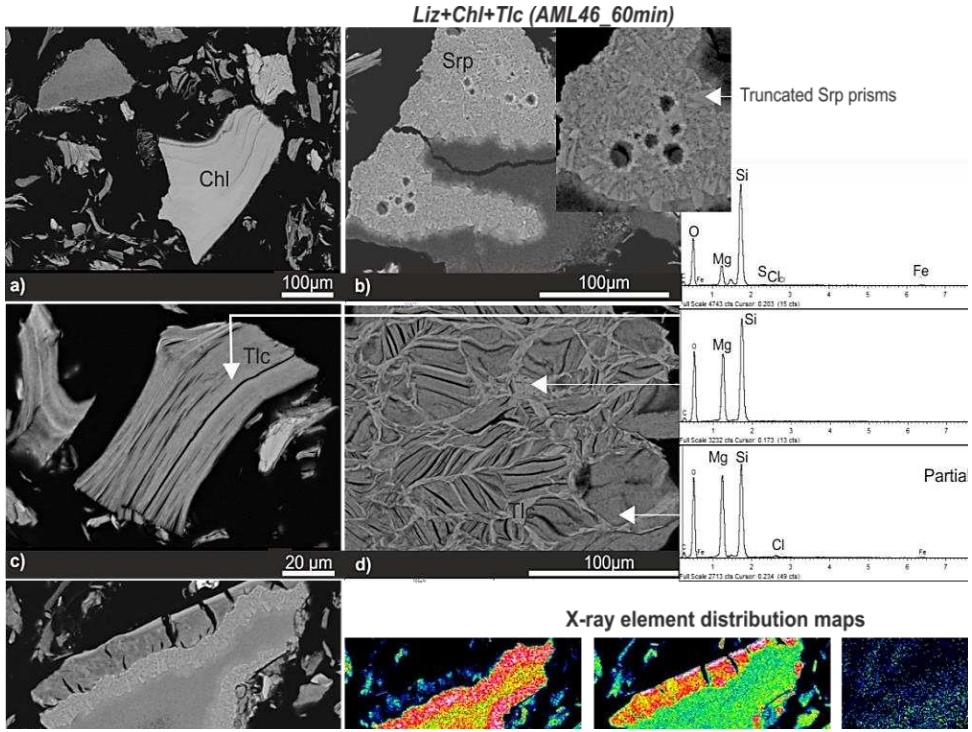


Figure 4.31 Textural and compositional features of a lizardite dominated sample from Kennack Sands (AML46) observed in the 60 minute leaching residuum, with similar features observed in the 180 minute residuum. The images and associated EDS spectra illustrate the sample's heterogeneity, i.e. the presence of talc and chlorite, and their transformation textures: a) unreacted particle of chlorite; b) Mg-leached matrix and unreacted lizardite; c) unreacted, opened along cleavage, talc with corresponding X-ray EDS spectrum; d) a composite particle of partially leached serpentine inter-grown with unreacted talc; e) a serpentine particle with corresponding elemental distribution maps as an example of sample heterogeneity-driven leaching, with deeply Mg-depleted zones and unreacted euhedral-prismatic crystals of lizardite (bright Z contrast on the associated BSE image).

4.3.3.10. Analysis of reaction residues within chrysotile

The ***chrysotile*** samples showed the highest EE amongst all the samples analysed with *ca.* 70% MgO extracted from AML6 (UAE) and *ca.* 85% from AML60 (RSA) after 180 minutes of acid leaching. The leaching features were, as expected, very different from those observed in the lizardite samples but again reflected the characteristics of the starting material (*e.g.* Figure 4.32, AML60). The clustering of fines was much more prominent and the dissolution was much more pervasive, resulting in a dense mass of siliceous fibres. The chrysotile ^{AML6} sample from the UAE displayed textural similarities but contained many more partially-leached, elongated prisms. No sharp interfacial contrast between particle shell and core was observed, again suggesting dissolution via a more uniform solution transfer process throughout the particle.

The starting chrysotile^{AML60} material contained *ca.* 10 % of calcite. Upon reaction with acid, the calcite dissolved readily and provided Ca cations into solution. These, in turn, reacted with sulphur from the dissociation of the ammonium bisulphate to produce gypsum. Accordingly, numerous laths of gypsum were observed within the siliceous mass of the dissolved chrysotile reaction residuum (Figures 4.32b & d).

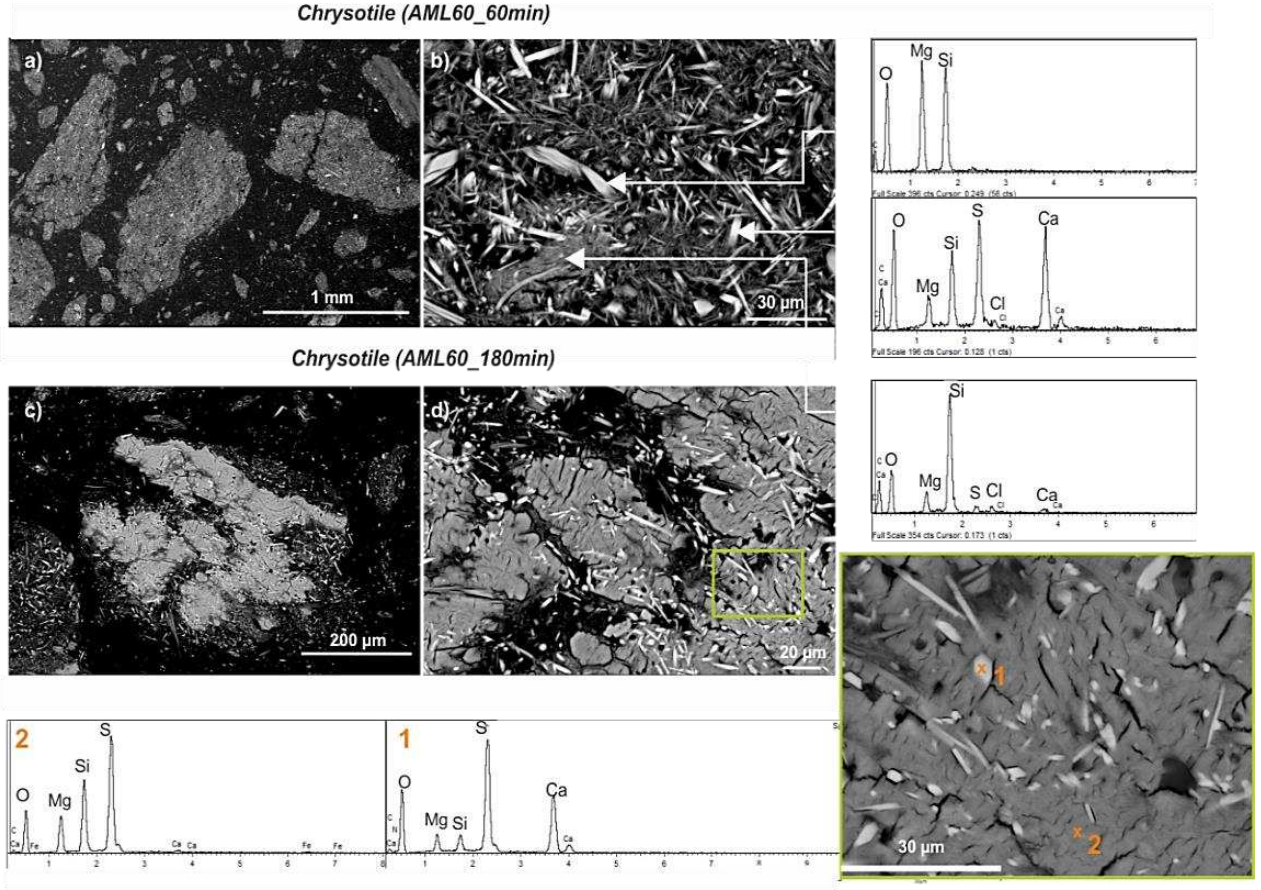


Figure 4.32. Textural and compositional features of chrysotile AML60 from the New Amianthus Asbestos Mine, RSA: a) composite particles containing deeply-leached siliceous residuum and crystals of gypsum; b) high magnification image of the internal textures observed within the composite particles and associated EDS spectra; c) a composite particle of a 180 minute residuum; and d) high magnification image showing the siliceous residuum engulfing prismatic crystals of gypsum – a by-product of the experiment.

4.3.3.11. Dissolution of rock samples

The dunite, harzburgite and serpentinite samples that were used in the mineral carbonation experiments (Chapter 5) were leached also with ammonium bisulphate. The composition of the starting material is summarised in Section 4.2.1, whilst the Mg^{2+} EE is illustrated by Figure 4.33, in a decreasing order from: serpentinite to dunite to harzburgite, of *ca.* 80%, 73% and 61%, after 180 minutes, respectively. The initial steep part of the curve is attributed to fast dissolution of fines present in the reacted powder.

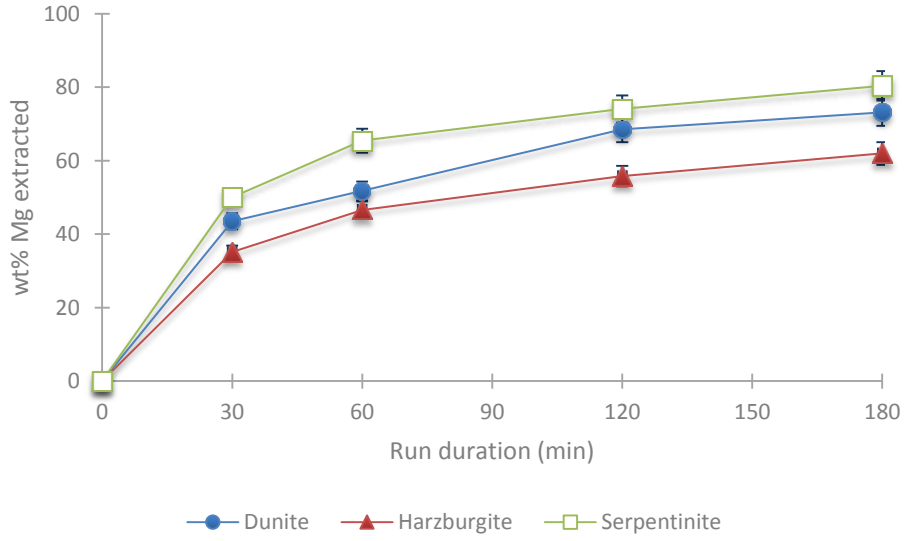


Figure 4.33 Time-dependent extraction efficiency of Mg (normalised XRF data) for serpentinite, dunite and harzburgite. 5% error is applied.

The reaction residues for all three samples displayed similar textural features (Figure 4.34). All contained a significant number of composite particles with partially dissolved silicate minerals. These particles were usually cemented with boussingaultite and a siliceous mass, and were probably an artefact of sample drying post-processing.

The textures observed in the partially-leached silicate particles suggested that leaching proceeded along preferential pathways, *i.e.* fractures, broken crystals and mineral cleavage, and was not concentric or uniform throughout the particles. Some minerals, *e.g.* clinopyroxene in harzburgite showed only little evidence for acid-related corrosion. Opaque minerals, *i.e.* magnetite and chromite, remained intact.

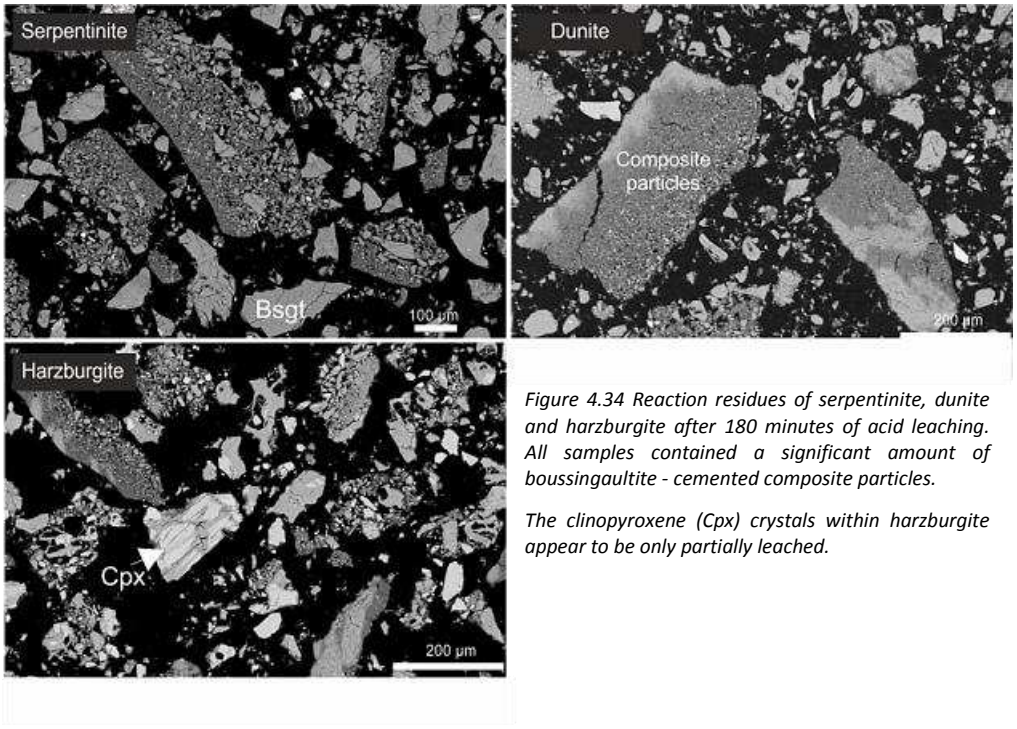


Figure 4.34 Reaction residues of serpentinite, dunite and harzburgite after 180 minutes of acid leaching. All samples contained a significant amount of boussingaultite - cemented composite particles.

The clinopyroxene (Cpx) crystals within harzburgite appear to be only partially leached.

4.3.3.12. Textural transformations of acid-treated particles

The textural transformations of particles were assessed based on SEM observations of powder grain mounts before and after the experiments, along with OM of polished thin sections. Both methods confirmed that the particle morphologies, apart from chrysotile[AML60], didn't undergo any significant changes during the experiments, with reaction residues resembling the starting material.

The OM images of Figure 4.35 illustrate the time-dependent (unreacted, and 60 and 180 minute residues) textural modifications in lizardite $2H_1$[AML57] thin sections,

manifested by fracturing at the edges of the reacted particles, *i.e.* "transformation cracks". These fractures were distinctively truncated and corresponded to those observed within the deeply Mg-leached siliceous shells ($L2H_1$, Figure 4.35c). It is noted that not all the reaction residues displayed reaction-related fracturing, *e.g.* $PS1M^{AML62}$ or antigorite. The lizardite 1T-dominated^{AML4} sample showed preferential fracturing only within deeply leached zones of former chrysotile. This fracturing was attributed to volume changes during Mg-silicate to siliceous residuum transformation.

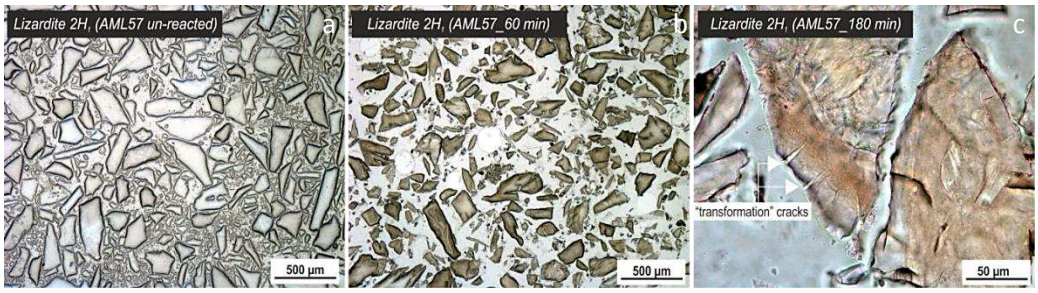


Figure 4.35 The morphologies of particles in lizardite $2H_1$, (a) before leaching and (b,c) after 60 and 180 minutes of acid leaching, respectively. a,b) reflected light petrographic microscope images and c) transmitted light petrographic microscope image.

The current texture of most of the reaction residues resulted from sample drying post-processing, giving rise to the formation of composite particles containing fines of variably-transformed serpentine particles, siliceous residuum and boussingaultite. The latter acted frequently as a cementing phase.

4.3.3.13. Boussingaultite as an experimental sink for magnesium

Boussingaultite, $(NH_4)_2Mg(SO_4)_2{\cdot}6H_2O$, is a rare type of sulphate mineral in nature, formed under fumarolic conditions. Fumaroles are vents found in regions of volcanic activity, through which steam and volcanic gases escape at elevated temperature.

In this study, boussingaultite formed as a by-product of reaction between extracted Mg^{2+} and dissociated ammonium bisulphate. The amounts of boussingaultite varied from sample to sample, with no clear trend in its distribution. For example, it was common in all the reacted rock samples and polygonal serpentine $PS1M^{AML62}$, but occurred only in small amounts in antigorite or chrysotile.

Figure 4.36 illustrates the distribution of boussingaultite in $PS1M^{AML62}$ along with associated X-ray elemental distribution maps. The mineral was found as either an anhedral cementing phase or as euhedral (prismatic) to subhedral crystals (up to 3 mm long). The cementing boussingaultite exhibited locally dendritic morphologies, suggesting rapid growth. It is inferred that the large euhedral crystals resulted from relatively slow growth from solution during the experiment, whilst the dense, locally dendritic mass crystallised during rapid drying of the solid reaction residuum post-processing. In either case, the boussingaultite acted as an elemental sink, capturing Mg^{2+} from the partially dissolved serpentine. This process would act to lower the EE, as determined from the experimental leachate concentrations.

Based on a modal analysis of $PS1M^{AML62}$ using X-ray elemental mapping data, it was estimated that ~ 40% by volume of all particles present in the reaction residuum were boussingaultite. This suggests that a value of *ca.* 40 % for Mg^{2+} EE was an underestimate for this sample.

Due to lacking thermodynamic data for boussingaultite, the thermodynamic modelling using PHREEQC was impossible. The closest, compositionally and paragenetically similar phase that could be modelled using PHREEQC was hexahydrate ($MgSO_4 \cdot 6H_20$), however it exhibited a saturation index of *ca.* -2, making the solutions under-saturated with its respect.

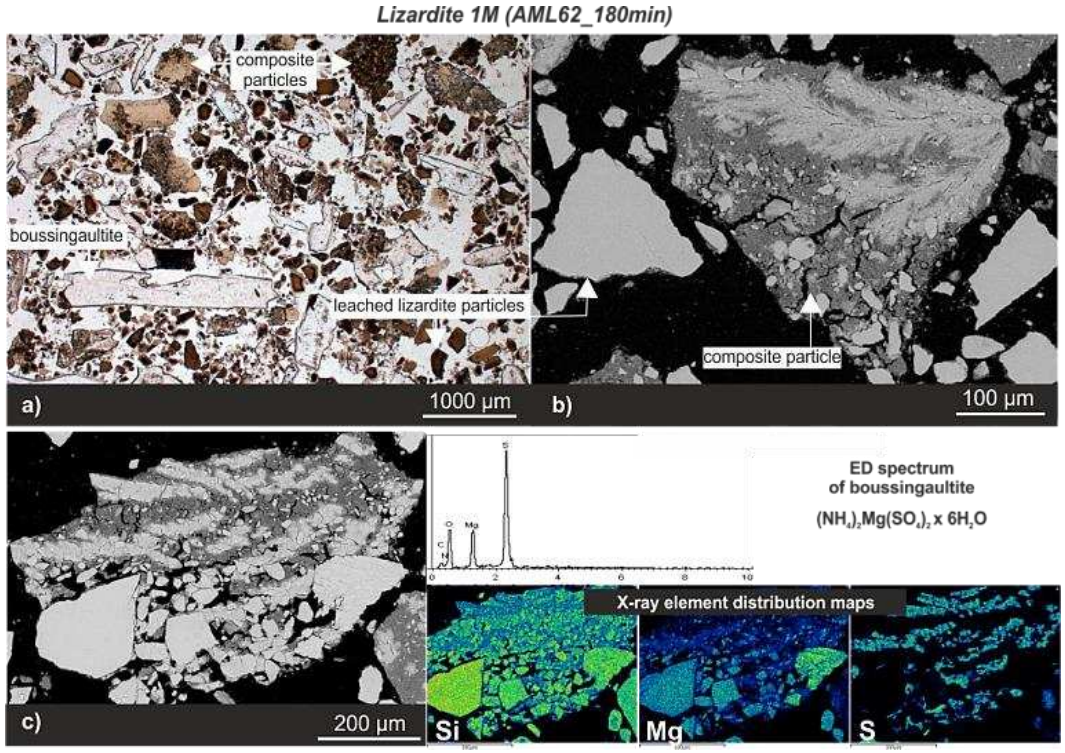


Figure 4.36 Mode of occurrence of boussingaultite in a 180 minute reaction residuum of polygonal serpentine PS1M: a) OM plane polarised light image of composite particles of reacted PS1M with scattered elongate boussingaultite crystals; b, c) BSE images of boussingaultite cement (bright backscattered contrast) and associated X-ray elemental distribution maps and EDS spectra.

4.4. Discussion

Serpentine minerals belong to a group of sheet silicates containing one tetrahedral layer occupied by Si^{4+} (± Al^{3+}, Fe^{3+}) and one octahedral layer occupied by Mg^{2+} (Fe^{2+}, Ni^{2+}, Al^{3+}, Fe^{3+}). The large number of possible arrangements of layers in a crystal leads to significant structural complexity of this mineral group (as detailed in Section 2.3.1.2). The three main serpentine species are lizardite with flat layers, antigorite with a wavy layer structure, and chrysotile forming cylindrical tubes. In addition, each of these species can be structurally modified further, giving rise to mineral polytypes.

Our previous research [*Styles et al.*, 2014b] highlighted that the polymorphic and polytypic complexity of serpentines controls the minerals' reactivity, but the underpinning reaction mechanisms remain poorly understood. Accordingly, to develop improved understanding of the reaction processes, a systematic set of laboratory controlled acid-leaching experiments was performed, using the purest possible serpentine mineral samples that could be obtained. Here, a discussion on the factors that affected the extraction efficiencies of cations from the different polymorphs and polytypes of serpentine minerals is presented.

4.4.1. Reaction rates and chemical affinity

The rates of mineral dissolution obtained in this study were significantly higher than those previously published for serpentine minerals under acid leaching conditions; *i.e.* values between -5 and -6 mol/m^2/g vs *ca.* -11 mol/m^2/g were observed, respectively. This might have been largely related to the variability of

experimental conditions (pH, T, particle size distribution, homogeneity of the input samples) used.

The geochemical modelling indicated that all experiments did not approach equilibrium with respect to serpentine minerals within the three hours of the experiment. Secondly, a poor correlation between the rates of reaction and chemical affinity of specific minerals was observed, except for antigorite that exhibited the slowest reaction rates and the highest values of chemical affinity. It is emphasised, however, that due to the limited availability of thermodynamic data for serpentine minerals; the affinities for lizardite samples, in particular, are based on one set of lizardite data only, without accounting for the structural, *i.e.* polytypic, complexity of this mineral. Therefore, the results presented here are greatly generalised and significant errors might be present due to the lack of appropriate input data.

4.4.2. The effects of rock texture on the EE

In an ideal scenario, dissolution experiments should be performed on single, homogeneous mineral phases. However, some minerals, such as serpentine, occur as finely crystalline aggregates, usually with minor impurities of other minerals, and they have to be regarded as fragments of rock with a specific, inherited microtexture.

The rock textures provide fine-scale (micro- to nano-scale depending on the size of the original features) porosity that serves as pathways for the ingress of reactive fluids, and hence texture is an important parameter when assessing rock-fluid interactions.

The rock texture encompasses: (i) the spatial distribution of morphologically and compositionally varied crystals; (ii) the number and dimension of veins and fractures; and (iii) the extent of brittle and/or ductile deformation. A combination of these features has been used to classify the samples studied here, with antigorite and chrysotile being texturally homogeneous on the scale of observation (*i.e.* 10's of microns), whilst the lizardite-dominated samples are texturally heterogeneous.

The image analyses of the acid-leached residues demonstrated that the reaction-induced transformations of serpentine particles are texturally controlled. This allowed division of the transformation patterns into:

4.4.2.1. Homogeneous patterns. As observed in samples with uniform crystal morphologies and spatial relationships, with insignificant numbers of veins and no clear evidence for preferential leaching. Samples belonging to this group were amongst the best (chrysotile) and worst (antigorite) in terms of Mg^{2+} EE.

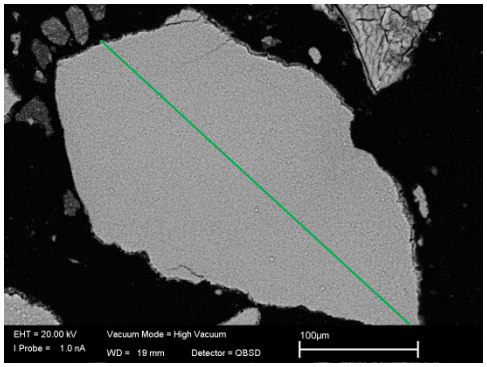
4.4.2.2. Heterogeneous patterns. As observed in samples with a high degree of inherited textural heterogeneity. Cation extraction was preferential in these cases and generally involved the initial dissolution of chrysotile and poorly crystalline lizardite (tentatively identified), followed by the dissolution of lizardite. In particular, for lizardite $1T^{AML4}$ that originally contained *ca.* 20% of chrysotile, XRD and SEM observations demonstrated that all the chrysotile was dissolved incongruently, leaving a siliceous residue behind, the location of which corresponded to veins and interstices between lizardite crystals and matched exactly with the original rock texture.

The leaching patterns for the lizardite $1T^{AML46}$ sample that contained chlorite and talc were more complex. Firstly, neither chlorite nor talc appeared to have corroded, and secondly, when intimately inter-grown with lizardite, the particles seemed to have formed a passivating shell preventing further lizardite alteration.

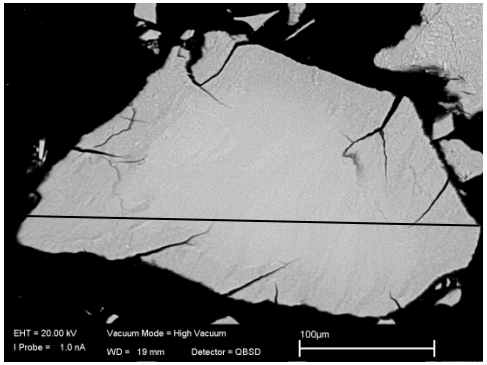
It was apparent also that this sample contained another serpentine phase that was more prone to leaching, probably in a less-crystalline form, in comparison with the unaltered protuberant truncated prisms of lizardite. Similar leaching patterns were observed for lizardite $2H_1$[AML53].

4.4.4.3. Leached layer texture. This distinctive type of particle transformation texture was manifested by a roughly concentric cation depletion zone, termed a "leached layer" or "leached shell", surrounding a partially altered or intact core.

Amongst all the serpentine minerals investigated in this study, only two samples showed the development of roughly concentric leached layers: *i.e.* polygonal serpentine PS1M[AML62] and lizardite $2H_1$[AML57]. The chemical gradients, illustrated by MgO and SiO_2 distribution line profiles for these two samples (Figure 4.37) varied from (i) roughly even throughout the grain for PS1M to (ii) sharp, with well-defined reaction front, for lizardite $2H_1$. The symmetric parabolic curve of Figure 4.38 (lizardite $2H_1$, black lines) is symptomatic of a sharp chemical gradient, with a deeply leached shell and a less-reacted particle core. The roughly straight line profile of polygonal lizardite (green lines), is more consistent with an even dissolution process and more uniform elemental distribution. The scatter of data points in the profiles for the PS1M sample was a consequence of this being a two-phase system.



Polygonal serpentine



Lizardite $2H_1$

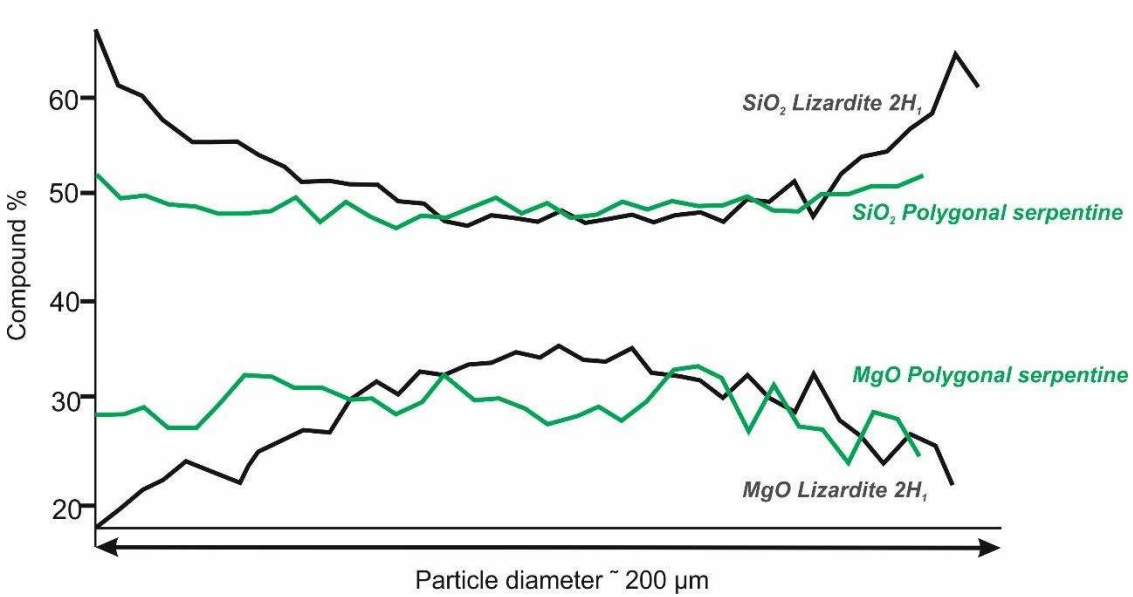


Figure 4.37 Comparison of wt% MgO and SiO_2 distribution profiles (SEM-EDS) across particles of lizardite $2H_1$ and polygonal serpentine PS1M (reaction residuum after 180 minutes of acid leaching) and corresponding BSE images. The shapes of these profiles reflect: a sharp chemical gradient between the Mg-leached shell and less leached core of lizardite $2H_1$ and a more gradual chemical gradient across polygonal serpentine, for both MgO and SiO_2. The x-axis is particle longer diameter.

This appears to be consistent with the rate of Mg extraction calculated from the solution chemistry. The rate plotted in Figure 4.38 against the minerals' chemical affinity drops suddenly at the late stage of the reaction for lizardite $2H_1$ whereas for polygonal serpentine, it drops initially and then remains roughly constant throughout the experiment. This suggests that the developing siliceous shell in lizardite $2H_1$ might have restricted (passivated) the conduits and limited the amount of Mg extracted towards the end of the experiment.

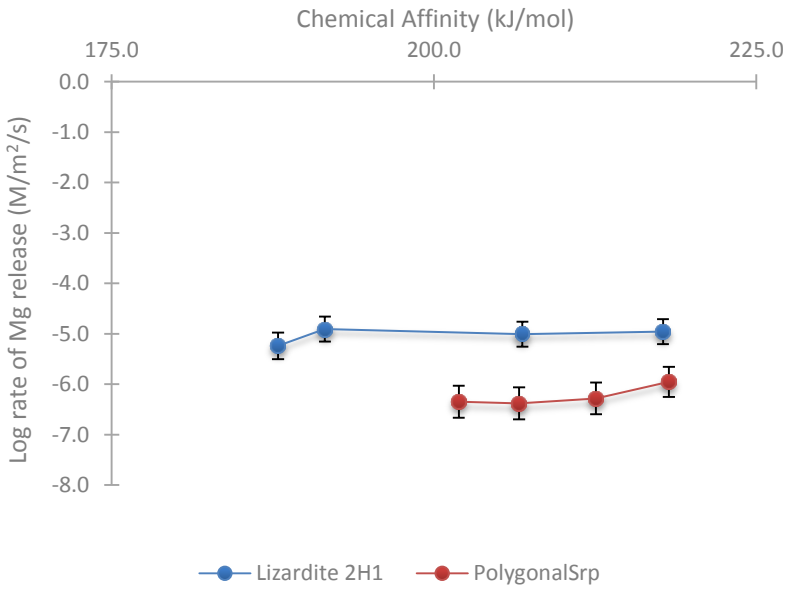


Figure 4.38 Rate of Mg release for lizardite $2H_1$ (red) and polygonal serpentine (green) vs chemical affinity and time of reaction, 30-180 minutes, right to left data points. The two different trends, i.e. roughly constant followed by a sudden drop in $L2H_1$ and initial drop followed by levelling may be indicative of: a) the formation of a passivating layer with time in $L2H_1$, causing drop in the rates; and b) the initial fast dissolution of fines in polygonal serpentine followed by continuous "diffusional" transport through micro-porous particles, facilitating a roughly constant rate of element release.

The residue particles of PS1M comprised very fine (< 1 μm), randomly oriented, occasionally hollow, lath-like crystals (< 1 μm diameter) of polygonal serpentine within a dense anhedral matrix of proto-serpentine, *i.e.* a less-well developed and thus less-crystalline type; both present in roughly equal amount. The combination of less-crystalline proto-serpentine, *being* more prone to leaching, and the hollow crystals of polygonal serpentine provided for high micro-permeability and well inter-connected pathways for reactive fluid ingress, promoting uniform transport of H^+ - in and Mg^{2+} - out of each particle (Figure 4.39a). Dissolution in this texturally-heterogeneous system was preferential, affecting the proto-serpentine matrix first (despite it being an Al-rich serpentine). The presence of sulphur, a component of the acid, in the centre of the leached particle was consistent with the presence of inherited or reaction-induced micro-porosity, providing the micro- or nano-conduits for the pervasive influx of solution into the core of the particles. The precise nature of these conduits requires further investigation; however, their action was in agreement with the previous observations of Hellman *et al.* [*Hellmann et al.*, 1990] and Kosuge *et al.* [*Kosuge et al.*, 1995]. Thus, it is considered that very fine-scale compositional heterogeneity and the presence of a less-crystalline micro-permeable matrix is essential for the transport of acid into the particle cores, resulting in uniform particle leaching.

Conversely, the original micro-texture in lizardite $2H_1$ residuum particles was characterised by distinctive shearing, reorganisation and phase re-crystallisation. Such deformation-induced texture seemed not to promote actively reaction pathways into particles with crystallographic and compositional uniformity. Consequently, chemical and textural transformations were accentuated within the outermost zones of these particles, where exposure to reactive fluid was prolonged. This resulted in a well-defined reaction front and a marked chemical gradient between the outermost leached-layer and the moderately affected core

(Figure 4.39b). The deeply leached siliceous outer layer was distinctively cracked. These transformation cracks tapered towards the particle core, but terminated at the core/shell boundary between the two variably leached zones. The origin of the cracks was attributed to a combination of:

- Volume change-induced strain, arising from Mg-dominated silicate to siliceous residuum transformation
- Preferential loss of cations, leading to transition from crystalline to a hydrated, amorphous solid [*Hellmann et al.*, 1990] that in turn may have undergone dehydration and fracturing. Dehydroxylation might have occurred also during powder drying.
- Mechanical fracturing of brittle siliceous residue due to particle-particle collisions and attrition during stirring in the reaction vessel

Deformation–induced texture in the starting lizardite $2H_1$ may have provided defects, *i.e.* sites of high surface strain energy, susceptible to preferential acidic attack during dissolution [*Hellmann et al.*, 1990]. This could also explain why samples of this type exhibited the highest EE.

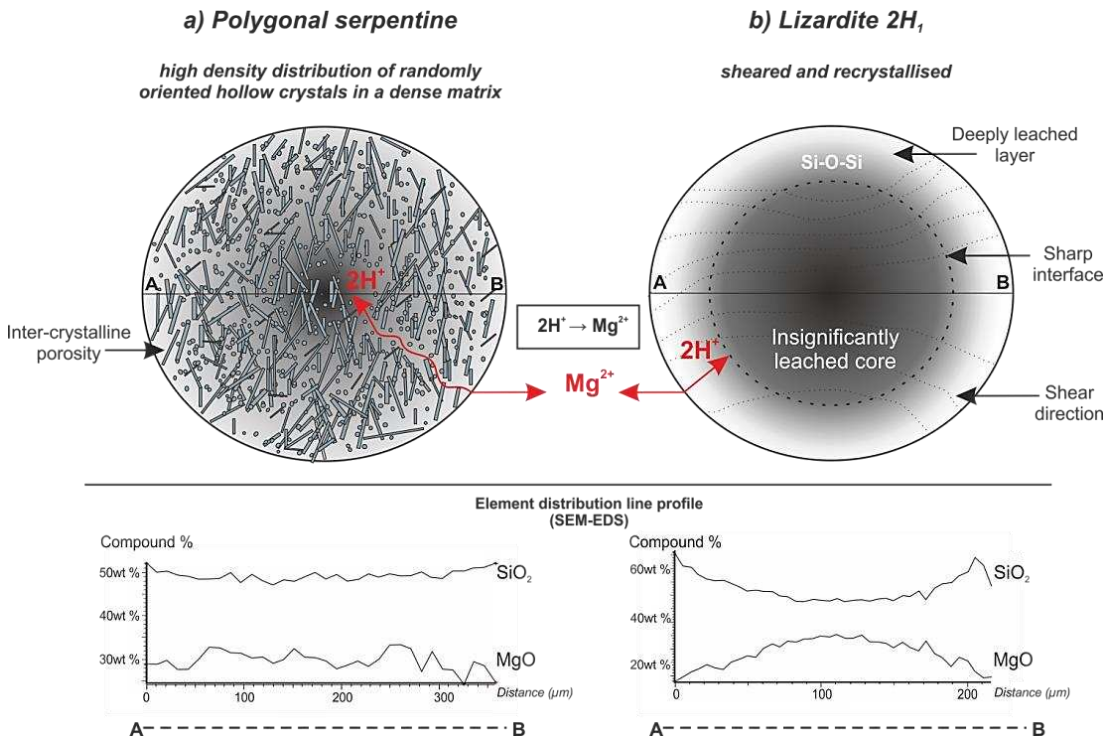


Figure 4.39 Model of leached layer formation through $2H^+$ - Mg^{2+} exchange in to particles of lizardite; a) polygonal serpentine - with significant amounts of inter-crystalline porosity, crystallographically heterogeneous with crystalline lizardite in a mass of "poorly crystalline" serpentine; and b) 2H1 - distinctively sheared but crystallographically uniform (poorly crystalline).

4.4.4.3.1. Generation of leached siliceous layers through an incongruent dissolution or a dissolution-re-precipitation mechanism

Two models for leached layer formation have been proposed, involving: (i) ***incongruent dissolution*** and exchange of cations in the outermost zone of minerals with hydrogen from solution, leading to the preferential removal of cations that exhibited weaker bonding with oxygen [e.g. *Weissbart and Rimstidt*, 2000]; and (ii) ***interface coupled dissolution/precipitation***, with bond-breaking, element release and re-precipitation occurring at the advancing fluid-mineral interface [*Hellmann et al.*, 2003; *Putnis*, 2009; *Ruiz-Agudo et al.*, 2012].

Whether the leached layer in lizardite $2H_1$ and polygonal serpentine formed through incongruent dissolution or an interface coupled mechanism, as suggested by Hellmann *et al* [*Hellmann et al.*, 2003], is debatable. The facts favouring non-stoichiometric dissolution through proton-cation exchange are:

a- Incomplete leaching of the outermost zone, with as much as 50% Mg remaining in the leached zone (from quantitative SEM-EDS analysis): no new Mg-silicate precipitated in the pore spaces, thus all that Mg was assigned to the original serpentine.
b- The leached particles largely retained the size and shape of the starting material.
c- The absence of clear growth patterns, *i.e.* tens of microns thick (siliceous shell).

However, the results of thermodynamic calculations performed using PHREEQC suggest that all solutions were saturated with respect to silica phases, with

saturation indices of *ca.* 0.3 for amorphous silica and *ca.* 1 for chalcedony and quartz in both samples discussed here (Figure 4.40). This advocates the possibility of silica dissolution and re-precipitation in the leached layer, as proposed by others [*Hellmann et al.*, 2003; *Putnis*, 2009; *Ruiz-Agudo et al.*, 2012]. In line with this theory, Hellman [*Hellmann et al.*, 2003] reported an abrupt amorphous-crystalline structural transition (0.5-2Å) associated with the re-precipitation of an amorphous secondary phase at the dissolving mineral interface, whilst Ruiz-Agudo [*Ruiz-Agudo et al.*, 2012] noted the presence of retreat steps on the mineral surface. None of these features were observed on the scale of tens of microns, as investigated in this study, and further nanoscale investigation is required. Depending on the rate of re-precipitation, this process may lead to preservation of the morphology of the starting material. In addition, the altered siliceous zones are porous [*Casey et al.*, 1989], thus, as suggested by Hellmann *et al* [*Hellmann et al.*, 2003], its presence should not affect the rate of intrinsic dissolution.

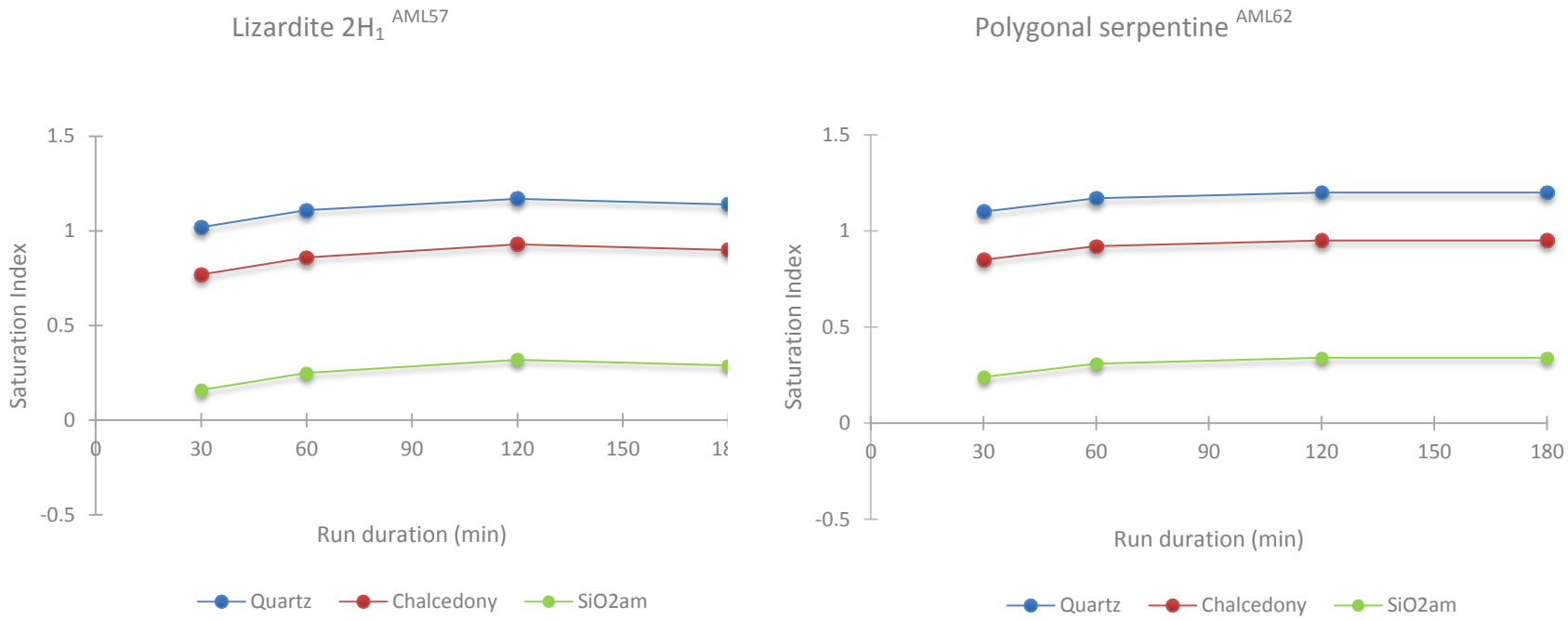


Figure 4.40 Saturation indices of silica phases for lizardite $2H_1$ and polygonal serpentine. The plots show that the experimental solutions were saturated with respect to quartz, chalcedony and amorphous silica at all points of the experiment, making them likely precipitates. This advocates an interfacial dissolution-re-precipitation process in the leached zone. Although, the curves look very similar for both examples, it is noted that the input fluid chemistry data was different.

It is apparent that irrespective of the mechanism of leached layer formation the two particle leaching examples given here are consistent with the operation of two distinct, fundamental processes at the mineral-fluid interface: *i.e. molecular diffusion and surface reaction* [*Murphy et al.*, 1989]. Fast reactions at the surface resulted in a depletion zone into the solid, as observed for lizardite $2H_1$; whilst molecular diffusion within the solid led to the lack of a depletion zone and more uniform dissolution of the entire particle [*Schott et al.*, 2009], as observed for the PS1M-dominated sample.

4.4.3. The effect of particle size and surface area on the EE

As opposed to the general consensus that the finer the powder the higher the surface area and the faster the dissolution rate, this study has shown that in a < 250 µm system of serpentine minerals the particle size distribution (PSD) may not be of great importance. For instance, antigorite^{AML2}, containing a significant amount of fines, with d_{90} = 90.1 µm and median d_{50} = 10.2 µm, exhibited the lowest SSA of 2.9 m^2/g and also one of the lowest EE. On the other hand, lizardite $2H_1{}^{AML57}$, with a high percentage of large particles and comparatively high SSA of16.6 m^2/g, dissolved readily, with a high Mg^{2+} EE of 80%. This is further shown for the remaining samples on the plot of Mg^{2+} EE as a function of SSA (Figure 4.42). It is evident that the EE depends on the SSA but typically not on the PSD, for the experimental system investigated here. The deviation of data points from a linear trend is probably related to a combination of PSD and compositional heterogeneity, well exemplified by lizardite1T^{AML46} containing an unreactive clinochlore and a moderate (d_{50} = 35 µm) PSD.

In general, the values of N_2-BET SSA were low for antigorites, moderate for lizardites and high for chrysotiles. It is apparent that these differences may actually indicate the differences in the amount of intra-crystalline microporosity, as expected for the structurally different serpentine minerals. The BET SSA was thus a reflection of both, the PSD and crystal structure, and generally the higher the BET SSA value the higher the EE (Figure 4.41). In this context, it is noted that the size distribution for < 250 µm sieved particles appeared not to have a significant effect on the reaction kinetics.

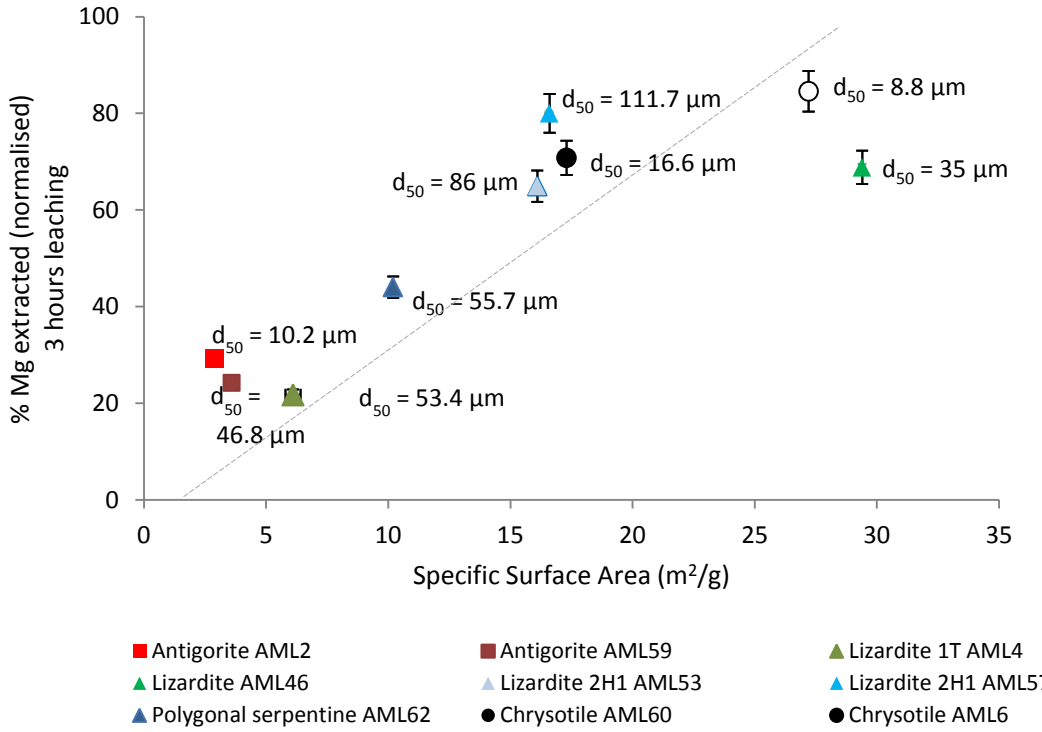


Figure 4.41 Mg-EE (normalised XRF data) as a function of specific surface area (BET N_2) with PSD mean values d_{50} given for each sample. The plot shows a general linear relationship between the two plotted variables, with discrepancies relating mainly to sample heterogeneity. The data suggests that EE depends on the SSA, but less strongly on the PSD for < 250 µm systems of serpentine minerals, as used in this study.

It is recognised that the mechanism for producing powder is of high importance for CCSM technologies and identifying an optimal speed and time for mechanical attrition may affect significantly the associated cost. This study suggests that milling to a very fine grain sizes may not be necessary if the best feedstock material is chosen. Indeed, if the feedstock material is mesoporous (2 - 50 nm pores) with high SSA, then grinding < 500μm powder is unlikely to make much difference to the leaching efficiency, presuming sufficient wt% of the target mineral species is present in the starting material.

Further, excessive grinding may damage the crystalline structure of the starting material, in turn lowering the activation energy and accelerating dissolution [*Fabian et al.*, 2010; *Sandvik et al.*, 2011; *Sanna et al.*, 2013]. For example, the leaching of fine antigorite powder (average particle size 37 μm) with 1.4 M ammonium bisulphate under continuous internal grinding (2 mm glass beads) resulted in the leaching of 42% Mg^{2+} after 1 h [*Park and Fan*, 2004], a value 3-4 times higher than the Mg^{2+} EE for antigorites determined in this study. This difference in EE is most likely related to a finer particle size combined with the continuous grinding process used in the study reported by Park and Fan (*idem.*).

4.4.4. The effect of mineral chemistry on the EE

This study provided evidence that the substitution of $Al^{3+} \rightarrow Si^{4+}$ in the tetrahedral position of the serpentine minerals investigated, increased the stability of crystal structure and thus its acid-resistance. Figure 4.42 illustrates the 180 minute Mg^{2+} EE as a function of Al content in the starting material.

The data suggests a near inverse linear trend for chrysotile and lizardite samples, *i.e.* with EE being inversely proportional to the amount of Al_2O_3 in the crystal structure. The scatter of the data, however, reflects the influence of other

parameters, *e.g.* the presence of aluminous clinochlore within lizardite[AML46] and the particularly stable crystal structures for antigorite.

For the case of the aluminous system of polygonal serpentine[AML62], the Mg^{2+} EE of *ca.* 40% was largely related to preferential leaching of a less-crystalline aluminous-proto-serpentine (elsewhere referred to as matrix), making probably up to 50% of the sample. This suggests that the degree of structure-ordering overrides the effect of Al acting to stabilize the mineral and thus increase its acid-resistance.

It appears that for the antigorite samples, the variable amount of Al did not affect its reactivity, resulting overall in similar Mg^{2+} EE for the two samples investigated.

The samples with the highest amount of Al were the serpentine only minerals, *i.e.* lizardite 1T[AML4] and polygonal serpentine[AML62] which exhibited tetrahedron substitutions. For example, the lizardite 1T [AML4] contained a total of 0.17 Al *apfu*, a portion of which balanced the slightly undercharged Si^{4+} tetrahedron (1.94 *apfu*), with the remaining Al positioned in octahedron positions, along with Mg and Fe, giving a formula unit of $(Mg_{2.72}Fe^{total}_{0.15}Al_{0.11})_{\Sigma 2.98}(Si_{1.94}\ Al_{0.06})_{\Sigma 2}O_5(OH)_4$. The tetrahedron substitutions of this well-ordered lizardite increased the thickness of the tetrahedral sheet and consequently reduced interlayer misfit and interlayer strain, thereby enhancing the mineral's stability [*Caruso and Chernosky*, 1979; *Mellini and Zanazzi*, 1987; *Ohanley et al.*, 1989].

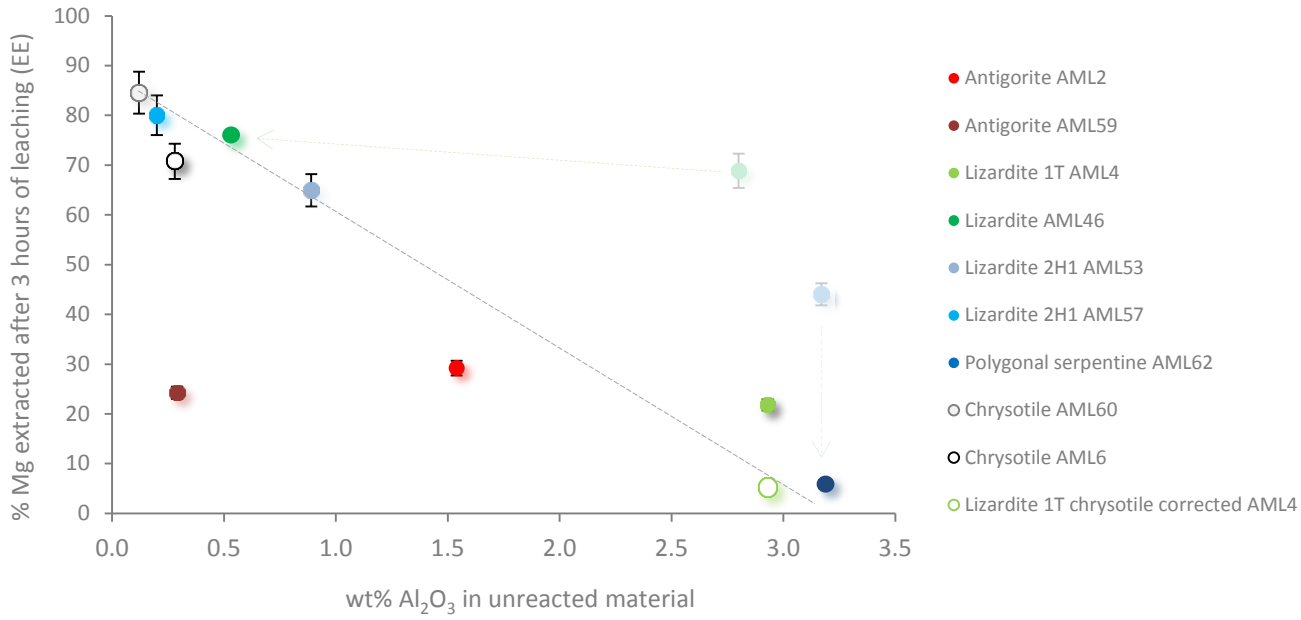


Figure 4.42 180 minute EE of Mg as a function of Al_2O_3 content (in the serpentine mineral starting material). The lizardite 1T AML4 data point was also plotted after correction for chrysotile content. The two data points in rectangles correspond to lizardite AML46 (green) and polygonal serpentinite AML62 after correction for non-reactive aluminous chlorite/talc content and highly reactive proto-serpentine in AML46 and AML62 respectively. The position data points corrected, i.e. in the rectangles, are more realistic as they represent the leaching efficiency of the mineral of interest and not bulk rock sample. After appropriate correction, a clear inversely proportional relationship between the extraction efficiency and Al_2O_3 content is clearly apparent. The straight line was only put there to help visualise the linear trend.

4.4.5. The effect of mineral structure on the EE

The irregularities in crystal structure and layer arrangements expose substantial amounts of potentially active interlayer surfaces to the presence of acid [*Kline and Fogler*, 1981]. Statements about the importance of serpentine structure on dissolution kinetics have been made [*Wang and Maroto-Valer*, 2011] but to date there has been no systematic studies comparing the reactivity of different serpentine polymorphs and polytypes under the same CCSM-related experimental conditions.

Data on reaction kinetics as a function of serpentine structure is required for the selection of the most suitable feedstock material for CCSM and this study has provided strong evidence for a relationship between crystal structure and reactivity of the feedstock material. The different inter-crystalline nature of antigorite, lizardite and chrysotile had a significant effect on the physical behaviour (*i.e.* the degree of strucutr break-up during leaching) of these minerals, as previously suggested by Capitani & Mellini [*Capitani and Mellini*, 2004], leading to substantial differences in Mg^{2+} EE, following the order:

Al-lizardite 1T (ca. 5%) < antigorite (24-29%) < polygonal serpentine 1M (ca. 43%) < lizardite $2H_1$ well-crystalline (ca. 65%) < "felted"chrysotile (ca. 70%) < lizardite $2H_1$ poorly crystalline (ca. 80%) < nanotubular chrysotile (ca. 85%)

4.4.5.1. Structural strenght of antigorite

As a means to accommodate dimensional misfit, antigorite exhibits a wave-like modulation with periodically inverted tetrahedral sheets attached to the concave side of the octahedral sheet [*Capitani and Mellini*, 2004 and references therein]. This effect is attributed to repulsion between adjacent apical oxygens and tetrahedral cations, with movement of the oxygens so that curvature arises [*Capitani and Mellini*, 2004]. The arrangement of tetrahedra results in a complex three-dimensional network of chemical bonds, that extend through the entire crystal *(idem.)* forming a highly stable "chemical cement". The lengths of the metal-oxygen bonds in antigorite are comparable to those in lizardite (Figure 4.43). However, subtle differences were reported for apical and basal bonding in the tetrahedra, with the former being shorter in the "long" half-wave of antigorite, *i.e.* 1.596 and 1.640 Å for apical and basal bonds, as opposed to 1.615 Å and 1.645 Å in lizardite, respectively [*Capitani and Mellini*, 2004]. The shortening of apical bonds may have contributed further to the structure stability. As pointed by Smyth [*Smyth*, 1913] "*…the solubility of an oxide varies greatly with the compound in which it occurs…*". This was later reiterated, recognising that the composition and structure of a multi-oxide mineral affects the extent of non-stoichiometric cation release [*Schott et al.*, 2009], and hence may be used to explain the variations in Mg^{2+} EE between antigorite and other serpentine polymorphs.

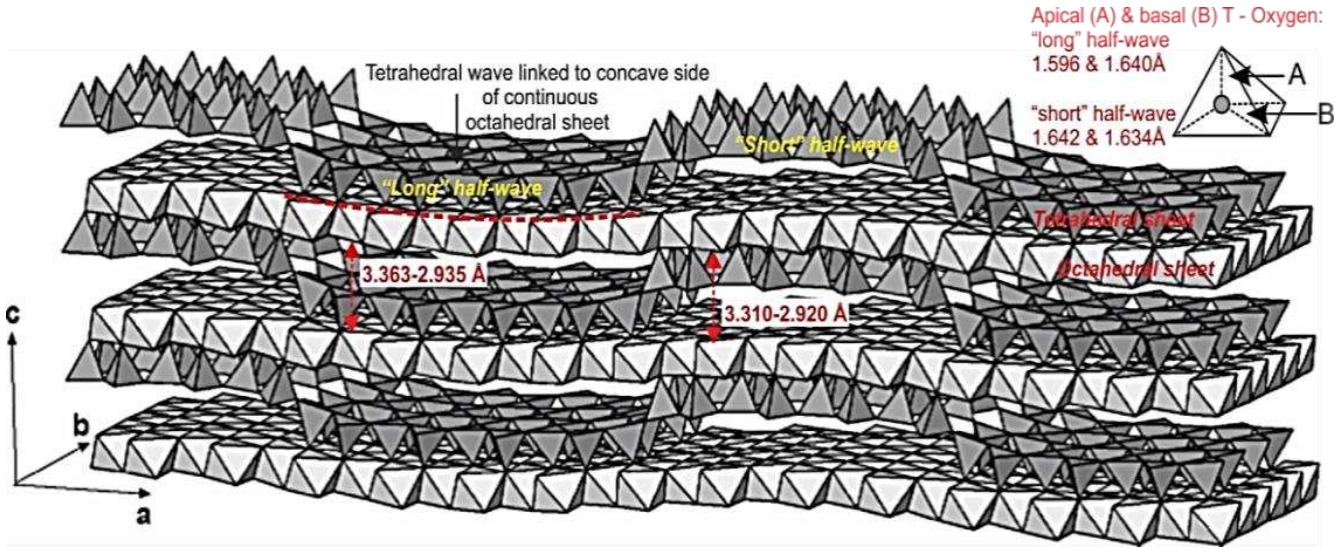


Figure 4.43Crystal structure of antigorite [Capitani and Mellini, 2004]. The reversal of tetrahedral sheets results in a strong three-dimensional structure that proved to be stable in the highly acidic conditions used in the present study.

4.4.5.2. Structural strength of lizardite

Flat layered lizardite can exhibit a wide range of stacking arrangements, manifested by subtle layer shifts and rotations giving rise to polytypes. Three lizardite polytypes were investigated in this study and the experimental data suggested that even subtle structural modifications in the flat layer serpentine, along with crystal chemistry, have an important effect on the kinetics of dissolution and, consequently, on cation EE. Two polytypes were identified unambiguously, *i.e.* lizardite 1T and lizardite $2H_1$. The third polytype was tentatively identified as lizardite 1M forming sectors in polygonal serpentine PS1M.

The trigonal polytype 1T exhibited parallel superpositions of adjacent layers (Figure 4.44), whilst layers in hexagonal lizardite $2H_1$ were rotated by 60°, best observed along the c-axis [*Mellini and Zanazzi*, 1987]. The main structural differences between lizardite 1T and lizardite $2H_1$ that affected EE**,** include:

- ***Interlayer distance***

The distance between the first layer octahedral sheet and the adjacent layer tetrahedral sheet, O3···O2 (Figure 4.44), is longer in lizardite $2H_1$ at 3.09 Å, compared to 3.03 Å in lizardite 1T. The layers are joined by H-bonding and the variable inter-layer distance affects the strength of the bond [*Mellini and Zanazzi*, 1987]. The higher the separation, *i.e.* in $L2H_1$, the weaker the H-bonding, the less stable the serpentine structure.

The increased basal spacing in the $2H_1$ polytype allowed for greater ingress of reactive fluid, resulting ultimately in higher Mg^{2+} EE, *i.e. ca.* 65% and 80% for the $2H_1$ polytypes, as opposed to *ca.* 5% for the one layer polytype 1T. Hence, it is recognised that the very low Mg^{2+} EE for lizardite 1T stems from a combination of

crystal structure and crystal chemistry (high Al content), as discussed in Section 4.5.3.

- ***Alternation of octahedral cations***

Lizardite $2H_1$ differs from 1T in the octahedral cation position [*Bailey*, 1969]. For the 1T polytype, the cations occupy exactly the same positions in the adjacent layers, whilst in the two layer polytypes, the cation positions alternate between position I and II (Figure 4.44, yellow and green Mg atoms, respectively). This lower structural order could have exposed potentially more Mg cations along the basal planes to ingressing acid, thus resulting in higher Mg^{2+} EE, with structural disorder activating the normally less active basal planes [*Kaviratna and Pinnavaia*, 1994; *Wieland and Stumm*, 1992].

- ***Effect of mineral crystallinity***

The comparison of EE for the two lizardite $2H_1$ samples from Gwendreath Quarry, UK, suggested that lower mineral crystallinity promotes faster dissolution, *i.e.* $L2H_1^{AML57}$ (*ca.* 65%) as compared with $L2H_1^{AML53}$ (*ca.* 80 %). This is also in consistent with dissolution in the aluminous system of polygonal serpentine^{AML62}, with preferential Mg-release from the less-crystalline matrix over the well-crystalline nanotubular crystals.

It is considered that poor crystallinity, *i.e.* distortion in the geometric ordering of atom positions in the crystal structure, results in localised high energy strain sites that would seek energy equilibration through structure relaxation, thus leading to faster reaction rates.

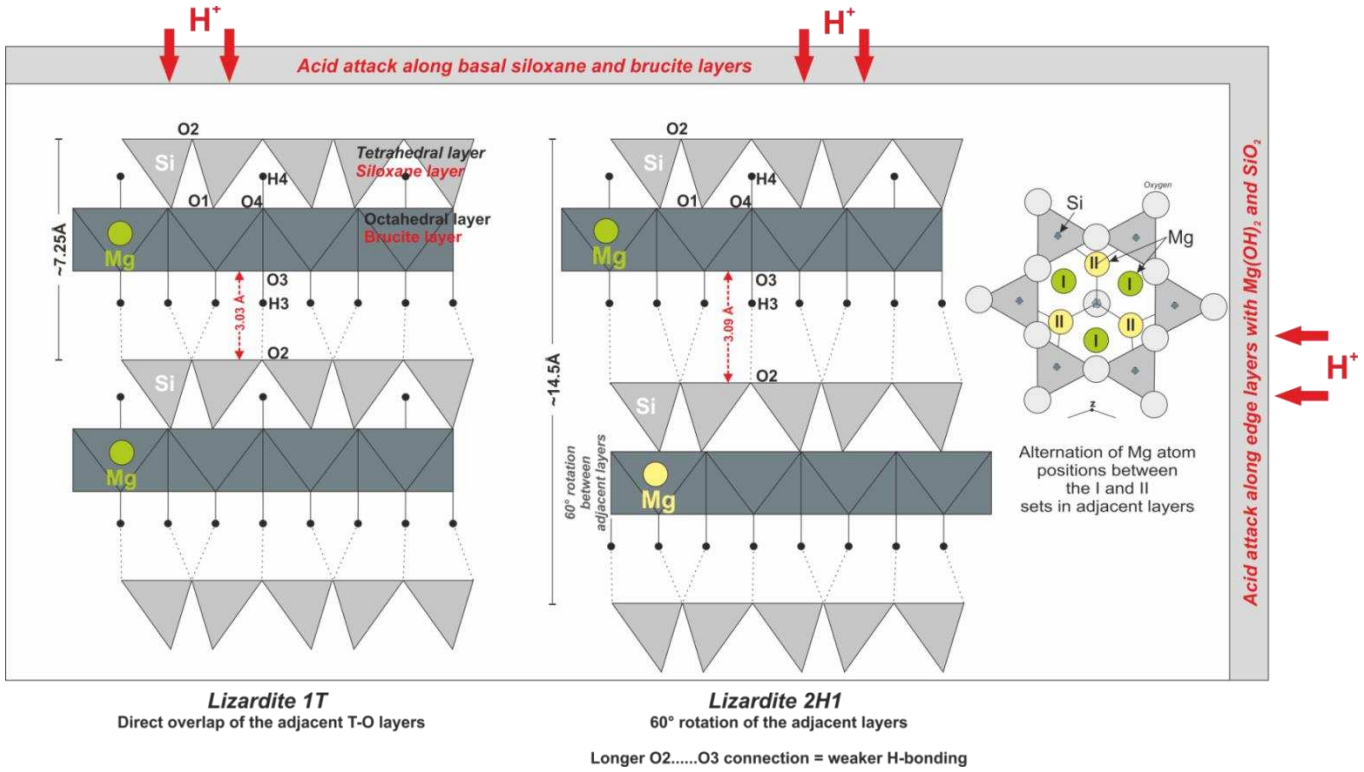


Figure 4.44 Comparison of crystal structures of lizardite 1T and $2H_1$ [modified from Bailey, 1969; Mellini and Zanazzi, 1987] and pathways for reactive fluid migration.

4.4.5.3. Structural strength of chrysotile

The chrysotile samples displayed variable Mg^{2+} EE, with *ca.* 70% for AML6 and *ca.* 85% for AML60. The difference in EE is attributed to the texture of the samples analysed. Chrysotile^{AML6} was characterised by dense "felted" aggregates of short nanotubular crystals, whilst chrysotile^{AML60} exhibited long, well-defined, separated nanotubes. This affected the reactive surface area and hence the resultant Mg^{2+} EE for these two minerals.

The high reactivity of chrysotile^{AML60}, in particular, resulting in high Mg^{2+} EE (85% after 180 minutes of leaching), was attributed to a specific type of interlayer misfit compensation and the formation of a continuous curvature resulting in a tubular crystal morphology with tetrahedral layer on the outside and octahedral layer on the inside of the tube [*Capitani and Mellini*, 2004]. The consequence of such tubular morphology is high strain and a defective lattice, which encourage faster bond breaking and dehydroxylation [*Gualtieri et al.*, 2012]. In addition, the resultant nano-tubular morphologies of these crystals provided additional reactive surfaces inside the nano-tubes, effectively increasing the surface area and thus enhancing the overall reaction rates.

4.4.6. Comparison with other studies using ammonium bisulphate

Previous experiments using ammonia-based processes were performed on antigorite from Cedar Hill [*Wang and Maroto-Valer*, 2011] and (low Al) lizardite-dominated serpentinised lherzolite from Gwendreath Quarry, Cornwall, UK (ET16) [*Sanna et al.*, 2013]. Figure 4.45 presents a comparison of the data from this thesis with that of [*Sanna et al.*, 2013; *Wang and Maroto-Valer*, 2011]. The extraction trend for the lizardite-dominated sample (ET 16, [*Sanna et al.*, 2013])

almost mimics the behaviour of $PS1M^{AML62}$. The extraction trend for antigorite [*Wang and Maroto-Valer*, 2011] on the other hand, plots significantly higher than the antigorites investigated in the present study. Wang and Maroto-Valer *(ibid.)* used a sieved 75-150 µm sample that could be responsible for the observed increase in sample reactivity. Further, the Cedar Hill antigorite may have contained significant amounts of other minerals, such as lizardite and olivine that would beneficially affect the rock's reactivity in acid. Hence, it is vital to analyse the starting material comprehensively before undertaking any process modelling and drawing conclusions about mineral reactivity for a given system. Otherwise, the data reported may be highly misleading, leading to mis-representation of the effectiveness of CCSM technology.

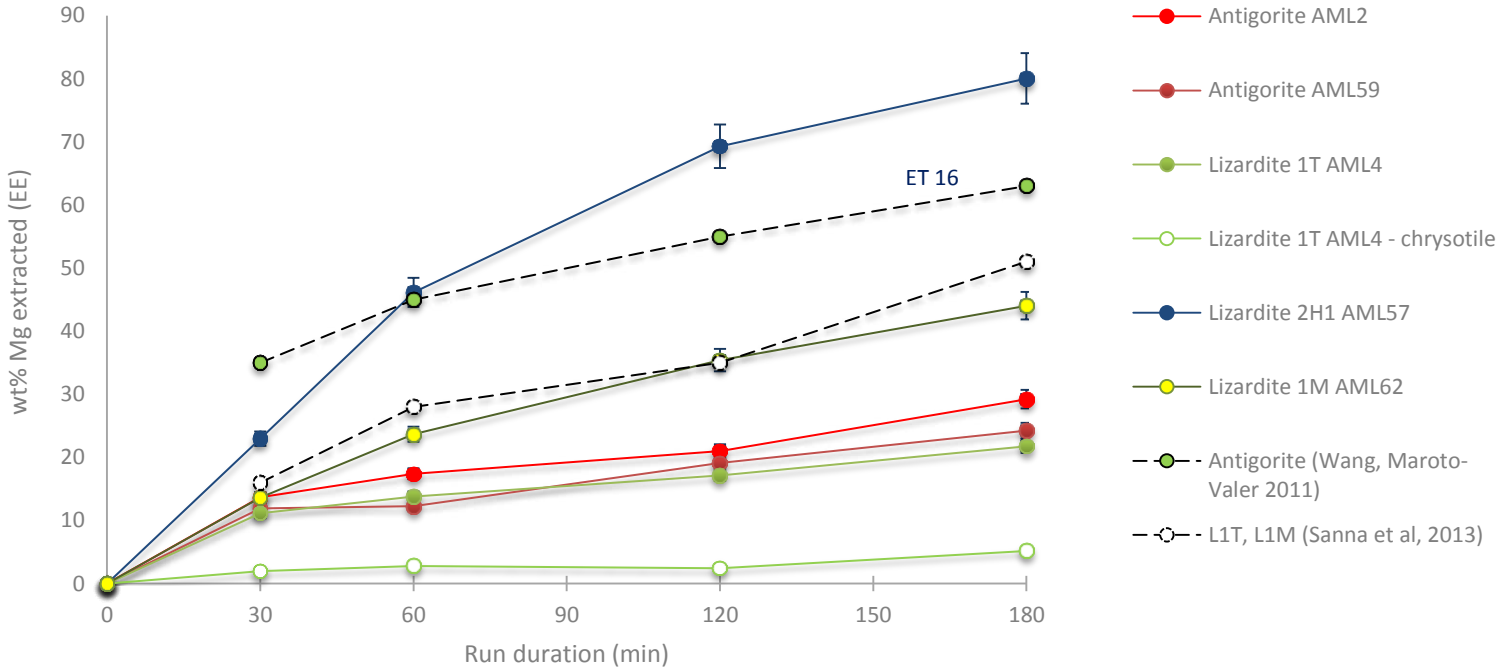


Figure 4.45. Comparison of Mg^{2+} extraction efficiencies (EE) from the present study with data reported by Wang & Maroto-Valer [Wang and Maroto-Valer, 2011] and Sanna et al. [Sanna et al., 2013]. The apparent high EE of antigorite from sample ET 16 (Wang and Maroto-Valer, 2011) in comparison with antigorite samples studied here may largely be related to a finer (75-150 µm) size fraction of the referenced data.

4.5. Summary

The reactivity of serpentine minerals in acid, at 70°C, was evaluated based on the extraction efficiency of Mg^{2+} as a function of time, from structurally and compositionally different polymorphs and polytypes.

This study has shown that the reactivity of a serpentine mineral for CCSM is a function of a ***complex interplay*** between the starting material texture (compositional homogeneity of the sample and the spatial distribution of the mineral components), crystal chemistry and the structure of all the mineral species present in the sample. The reactivity of serpentine mineral polymorphs and polytypes tested in this study, *i.e.* the Mg^{2+} EE***,*** increased from Al-lizardite 1T to chrysotile following the order of:

Al-lizardite 1T (ca. 5%) < antigorite (24-29%) < polygonal serpentine 1M (ca. 43%) < lizardite $2H_1$ well-crystalline (ca. 65%) < "felted"chrysotile (ca. 70%) < lizardite $2H_1$ poorly crystalline (ca. 80%) < nanotubular chrysotile (ca. 85%)

Although the selection of a single parameter most affecting the reaction kinetics is not advisable in any system containing natural materials (rocks and minerals), it is noted that a mineral phase with a "disorder-rich" structure, such as nanotubular chrysotile or multilayer lizardite polytype, leading to greater intra-crystalline porosity, may provide the best resource material. In particular, attention has to be given to crystal chemistry and a selection of a phase with the lowest possible

amount of aluminium may give a positive feedback on the overall kinetics of the mineral dissolution.

In addition, it was confirmed that materials with lower crystallinity undergo faster structure deterioration and thus dissolve faster. This was previously exploited during the thermal pre-treatment (630°C) of serpentine minerals for *ex situ* CCSM [*Werner et al.*, 2011].

The rates of mineral dissolution obtained in this study were significantly higher than those previously published for serpentine minerals under acid leaching conditions; with values between -5 and -6 mol/m^2/g vs *ca.* -11 mol/m^2/g being observed, respectively; being largely attributed to the variability of experimental conditions used.

This study showed that selection of a suitable feedstock material for CCSM is essential and if chosen correctly, it may significantly reduce the costs of an engineered CCSM process (*e.g.* through less grinding). In this context, it should be emphasized that serpentines are a structurally complex mineral group and unifying their functional properties in the CCSM system is inappropriate. Due to this complexity, it is critical to analyse the starting material comprehensively before undertaking process modelling and making conclusions about the minerals' potential reactivity in the given system.

It is noted that amongst those minerals that provided the best leaching efficiencies, the most suitable for CCSM technology will be one that is relatively ubiquitous and easily accessible. In this context, chrysotile serpentine seems the best feedstock material for CCSM, and the efficiency of natural carbonation of

chrysotile in mine tailings has been investigated previously [*Bodenan et al.*, 2014; *Jacobs and Hitch*, 2011; *Thom et al.*, 2013; *Wilson et al.*, 2006 and references therein]. Using the already finely ground tailings could help to offset costs associated with mine remediation and emission penalties (Wilson 2009). Due to their high surface areas, CCSM in mine tailings could sequester CO_2 at a rate ~ 50-100 times faster than *in situ* reaction in reservoir rock (*e.g. in situ* CCSM in peridotite) [*Thom et al.*, 2013]. Further, the end-products of such reaction are easily accessible and can be monitored at low cost (*idem.*). Thom *et al*. (*idem.*) also reported that ~2-6 Gt of tailings are present worldwide with a maximum sequestration capacity of ~0.5-2.5 Gt of CO_2.

Although chrysotile seems the best feed material, it must be stressed that some studies suggest it being the most hazardous of all serpentine minerals as it poses asbestos-related health risk of mesothelioma. On the other hand, if the feedstock material is mobilised in a controlled and safe manner, the carbonation of chrysotile asbestos may provide another way of mitigating health risks. All these aspects lead to a conclusion that *ex situ* CCSM using chrysotile may be a viable option, especially for areas in the vicinity of natural chrysotile deposits or mine tailings, but a detailed socio-techno-economic study combined with mineralogical and geochemical appraisal of the materials is essential prior to any engineered venture.

Chapter 5 Dissolution and carbonation of ultramafic rocks and serpentinite for *in situ* CO_2 sequestration

5.1. Introduction

This chapter focuses on ***in situ* carbon capture and storage by mineralization** (**CCSM**) in ultramafic rocks and serpentinites. Studies on *in situ* CCSM have received considerable interest from research organizations and industry to date, especially now that the mitigation of the effects of greenhouse gases has become an obligation for major fossil fuel suppliers and developed countries. Although *in situ* CCSM in principle provides for the long-term integrity of CO_2 and safe sequestration, it has yet to be implemented on an industrial scale, with barriers to large-scale deployment including concerns about process and operational technology costs [*Greenpeace*, 2014].

The fundamental process of *in situ* CCSM involves injection of CO_2 into suitable geologic formations, defined previously as a *carbon repository* [*Kaszuba et al.*, 2005], where it reacts with host rock to form mineral carbonates. Inevitably, the repository constitutes a complex structural and stratigraphic package, containing diverse geochemical environments, brine and groundwater chemistries, ***host rock***

compositions, lateral facies transitions, *etc.* [*Kaszuba et al.*, 2005]. Mafic and ultramafic rocks have been proposed as the main *host rocks* for CCSM [*Gislason et al.*, 2010; *Kelemen and Matter*, 2008; *Kelemen et al.*, 2011 and references therein]. These rocks are largely composed of Mg (plus Ca and Fe, in mafic rocks) silicate minerals that exhibit relatively high reactivities (and prone to dissolution) in acidic and neutral environments [*van Noort et al.*, 2013], providing divalent cations (predominantly Mg^{2+}) that are utilized in the precipitation of carbonate minerals for the permanent "crystallographic" sequestration of CO_2 in the mineral structure.

Over the past couple of decades, studies on CCSM have focused largely on isolated mineral grains such as olivine and their interaction with CO_2 under conditions relevant for *in situ* injection [*Giammar et al.*, 2005; *Johnson et al.*, 2014; *Olsson et al.*, 2012]. Whilst such studies are essential to allow for the determination of reaction kinetics and the factors that control mineral dissolution under hydrothermal conditions, it is also important to perform experiments within a system that, in terms of the repository characteristics, closely approximate the subsurface environment, *i.e.* the host rock. The reactivity of a mineral within a complex rock will not be the same as that of an isolated mineral grain, being influenced by the rock texture and compositional heterogeneity. Hence, the choice of host rock is critical [*Oelkers et al.*, 2008].

To appraise the reactivity of different Mg-dominated host rocks, batch experiments have been devised using ***dunite***, ***harzburgite*** and ***serpentine***, under conditions relevant for the injection of CO_2 at ~ 1 km depth, *i.e.* 70°C and 100 bar (10 MPa) CO_2 pressure. The experiments were run continuously for eight months (246 days) under supercritical (sc) CO_2 and in CO_2 – saturated brine (synthetic sea water), as well as

under an N_2-controlled atmosphere. The temperature selected was a compromise between that expected at the relevant injection depth (*ca*. 40-50°C) and the probability of reaction within a time-constrained experiment.

This Chapter presents the results of the analyses of solid and liquid reaction residues from these long-term, accelerated experiments, and provides information on:

- The variable reactivity of compositionally different host rocks: *i.e.* dunite, harzburgite and serpentinite, with emphasis on rock dissolution and carbonation.
- Rock transformations within CO_2-saturated brine and wet $scCO_2$.
- The degree of carbonation and carbonate recycling, and the implications for long-term system stability.

5.2. Materials and methods

5.2.1. Materials

Three types of candidate rocks for *in situ* CCSM were tested: *i.e.* ***dunite*** (UAE 5772), ***harzburgite*** (SU 15) and ***serpentinite*** (SU 20). All samples originated from the Oman - United Arab Emirates (UAE) ophiolite and were collected by Dr M. Styles during fieldwork in the UAE. They are thought to be typical of the rocks that might be encountered in an ophiolite mantle injection site.

The composition of the starting material is summarised in Tables 5.1 & 5.2. Briefly:

- ***Dunite*** was predominantly composed of olivine (forsterite Fo_{87}) with a trace amount of interstitial pyroxene. The rock was partially serpentinised.

- ***Harzburgite*** contained orthopyroxene (enstatite), olivine (forsterite) and trace amounts of amphibole, brucite and iron sulphide (pyrrhotite, as detected by XRD). The rock was partially serpentinised.
- ***Serpentinite*** was almost entirely composed of serpentine minerals. Trace amounts of carbonate (dolomite and pyroaurite), magnetite, chromite and halite (costal localisation) were detected. SEM investigations also revealed traces of partially amphibolitised, interstitial clinopyroxene (diopside $CaMgSi_2O_6$).

The whole rock chemistry was appraised using XRF (Table 5.2). As expected, Mg and Si were the dominant elements in all samples. The increased amount of Ca in harzburgite was related to the presence of diopside. Loss of ignition (LOI) values were related to the amount of volatile components in the samples, corresponding to H_2O and CO_2 in serpentinite minerals and carbonates, respectively; and as expected, the LOI for serpentinite was the highest for the three samples. Subtle discrepancies between the amount of serpentine (tentatively quantified by XRD) and the LOI for dunite and harzburgite were noted and may be related to sample heterogeneity.

Table 5.1 Composition of the starting materials. The results are based on a combination of XRD (semi-quantitative analysis), OPM and SEM analyses. For harzburgite, the data was obtained from a previous BGS study (BGS report).

	Forsterite	Enstatite	Diopside	Lizardite	Amphibole	Magnetite	Chromite	Chlorite	Dolomite	Pyroaurite	Magnesite
Dunite	50	trace	2	45	trace	-	2	-	trace	-	-
Harzburgite	40.5	17	5.5	30.5	2.5	-	-	3.6	trace	-	-
Serpentinite	-	-	trace	95	-	trace	trace	-	1	trace	trace

Table 5.2 Whole rock chemistry, as determined by XRF (Ti, Na, K, P, Sr, Zr, Ba, Cu, Zn, Pb, V, Hf, F and Cl were below detection).

	SiO_2	MgO	Al_2O_3	Fe_2O_{3t}	Mn_3O_4	CaO	Cr_2O_3	NiO	*Total*	*LOI*
	wt%									
Serpentinised Dunite	34.88	43.65	0.17	7.3	0.1	0.14	0.7	0.25	88.7	12.2*
Serpentinised Harzburgite	40.8	38.2	2.1	8.4	0.1	2.0	0.4	0.3	92.4	8.2
Serpentinite	34.1	39.6	0.3	8.3	0.1	0.2	0.5	0.2	83.3	17.9

*Note: The LOI of dunite is high and suggests nearly 100% serpentinisation. This is inconsistent with other observation (15% serpentine content as determined by XRD), and may be related to sample inhomogeneity.

5.2.1.1 Fracture mineralisation

Four cores were cut from each sample for use in the fluid-rock interaction experiments. Prior to experimentation, the cores were appraised under an optical microscope. The investigation focused on natural (n) and "induced" (i) fracture surfaces and the outer surface of the cores; *i.e.* material in direct contact with the reacting fluid. Figure 5.1 illustrates the main features observed in these starting materials. Briefly:

The ***dunite*** cores did not contain any natural fractures and those that were induced (i) for the purpose of these experiments were not mineralised with secondary phases.

Harzburgite contained natural, mineralised fractures, distributed in a sub-parallel to diagonal array. The fractures were covered by a white crust of dolomite, along with trace amounts of Fe oxy/hydroxide. Optical microscopy also revealed fractures filled with serpentine minerals and other finely-crystalline Mg silicates. The thickness of the fractures, as revealed by thin-section, varied from ≤ 30 μm for carbonates to ≤ 200 μm for silicates.

The ***serpentinite*** was cross-cut by an irregular array of veins of serpentine with minor amounts of pyroaurite-, dolomite- and Mg-carbonate (possibly hydrated). In addition, veinlets of magnetite, or lines of magnetite crystals were observed.

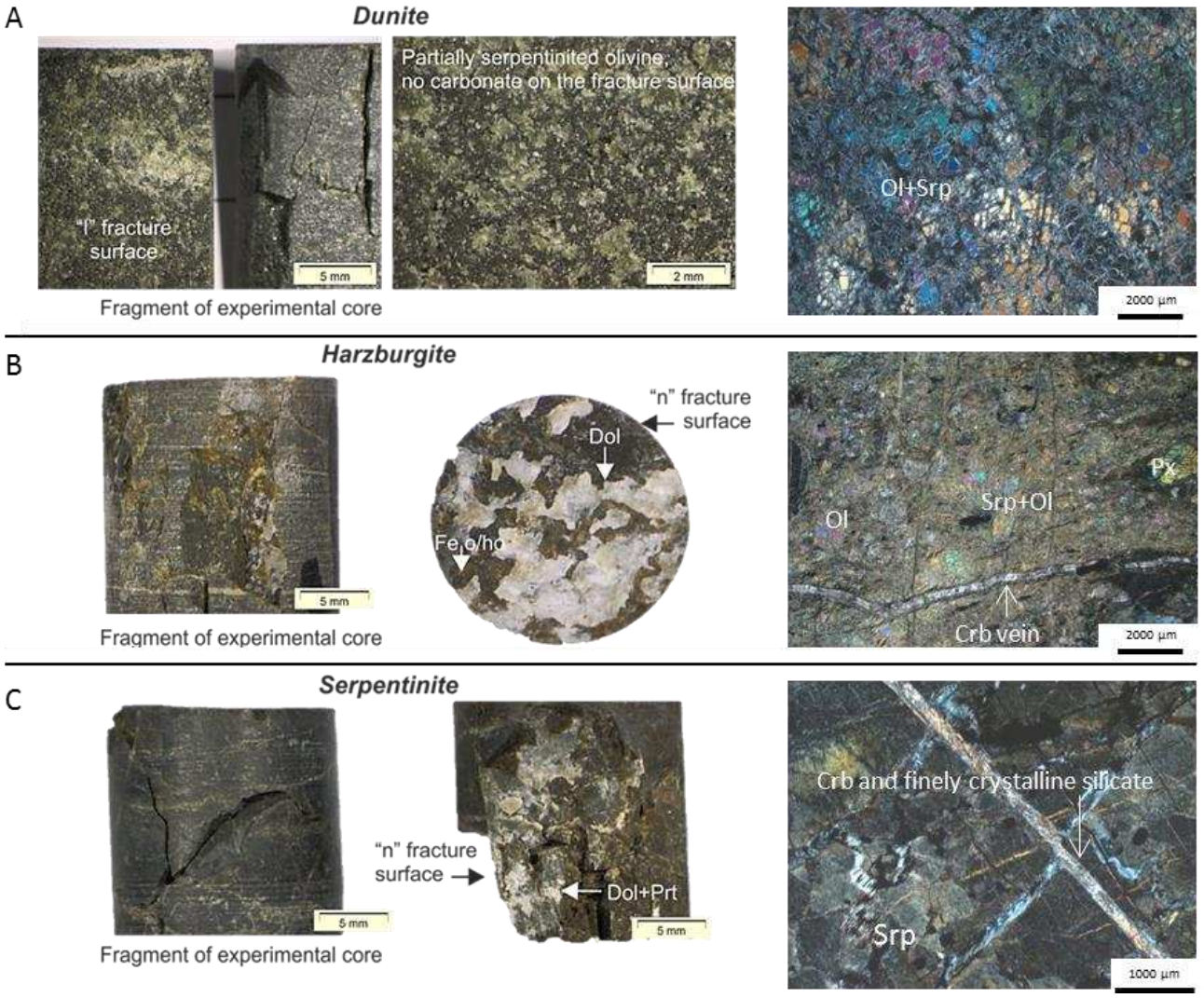


Figure 5.1 Hand specimen and crossed-polarised light optical microscope images of the A) dunite, B) harzburgite and C) serpentinite rock samples investigated in this study. The dunite sample was virtually natural "n" fracture-free and containing unmineralised induced "i" fractures only, whereas both the harzburgite and serpentinite samples contained mineralised "n" fractures filled with dolomite (Dol), pyroaurite (Prt) and Fe oxy/hydroxides (i.e. hematite and goethite).

5.2.1.2. Surface area

The surface area of each core was calculated from X-ray Computed Tomography (XRCT) data of the starting material. The area includes both the external cylindrical core surface and the surface of any open (induced or natural) fractures present in the core.

Examples of XRCT data reconstruction for cores investigated under a CO_2-atmosphere are shown in Figures 5.2 – 5.4, whilst surface areas are presented in Table 5.3. The surface area values were used in the rate calculations for net Mg^{2+} release (section 5.3.1.4)

Table 5.3 Surface areas of the rock cores used in the CO_2 pressurised experiments. Reconstructions and measurements of the surface areas were performed using Avizo Fire 8.2 software.

	CO_2 vessels / m^2
Serpentinite	0.0027
Dunite	0.0022
Harzburgite	0.0018



Figure 5.3 XRCT reconstruction of the Serpentinite core (starting material) used in the CO_2-pressurised vessel experiment. Sub-horizontal cross-cutting fractures were induced prior to the experiment to increase the reactive surface area. This core fell apart after pre-experimental fracturing and was used in the form shown in the image. The core was ca. 27 mm long and ca. 17 mm in diameter.

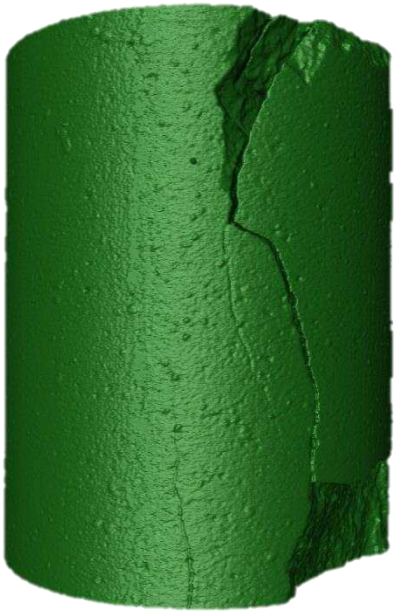


Figure 5.4 XRCT reconstruction of the Dunite core (starting material) used in the CO_2-pressurised vessel experiment. Sub-vertical cross-cutting fractures were induced prior to the experiment to increase the reactive surface area. Small fragments of the core fell apart after pre-experimental fracturing and the core was used in the form shown in the image. The core was ca. 27 mm long and ca. 17 mm in diameter.



Figure 5.5 XRCT reconstruction of the Harzburgite core (starting material) used in the CO_2-pressurised vessel. Sub-diagonal cross-cutting fractures were induced prior the experiment to increase the reactive surface area. Small fragments of the core fell apart after the pre-experimental fracturing and the core was used in the form shown in the image. The core was ca. 27 mm long and ca. 17 mm in diameter.

5.2.2. Methods

A detailed presentation of the Methodology is given in Appendix A. Briefly:

the three selected rock types were cut into ~ 27 mm long cores of *ca.* 17 mm diameter and allowed to react with wet supercritical CO_2 ($scCO_2$) and CO_2 saturated brine for 8 months (246 days), at 70°C (±5°C) and 100 bar (±5 bar) CO_2. Two pressure vessels were used for each rock type, one pressurised with CO_2 and the other with N_2, serving as a control experiment. Each vessel contained two cores, one immersed in CO_2-saturated saline solution and the other suspended above the liquid, in the headspace within the gaseous phase of wet $scCO_2$. A similar arrangement was utilised for the N_2-pressurised vessels. A magnetic stirrer was used to stir the solution every 4 days.

Table 5.4 Summary of samples and conditions for the CO_2 pressurised experiments.

Rock type	Core length (mm)	Core diameter (mm)	Geometric surface area (mm^2)	T (°C)	CO_2 P (bar)	Duration (days)	Experimental fluid	Starting fluid volume (ml)	Final fluid volume (ml)
Serpentinite	27.8	17.9	2700						
Dunite	27.6	17.3	2200	70	100	246	Saline solution	200	~110
Harzburgite	27.2	17.5	1800						

5.3. Results

5.3.1. Leachate chemistry

Eleven fluid samples (5-10 ml) were collected during each experiment. The samples were stored in a fridge and collectively analysed by ICP-AES and IC at the end of the experiment. Here, the temporal evolution of Mg^{2+}, Si^{4+}, Ca^{2+}, Fe^{total}, Na^{+}, Ba^{2+}, Ni^{2+} and Sr^{2+} is presented, whilst the full data set is tabulated in Appendix D.

5.3.1.1. Temporal evolution of Mg^{2+} concentration, $[Mg^{2+}]$

Mg is the main divalent cation expected to bind (sequester) CO_2 into carbonates in mantle rocks, thus particular emphasis was given to its temporal evolution during this study.

Figure 5.6, shows the change of $[Mg^{2+}]$ as a function of volume corrected time. The volume corrected time accounts for progressive decrease of fluid in the experimental vessel, calculated after Bevan and Savage [*Bevan and Savage*, 1989].

It is clear that samples from the CO_2- pressurised vessel exhibited a more apparent evolution of $[Mg^{2+}]$ with time than those from N_2–pressurised vessels. In serpentinite, a sudden increase of $[Mg^{2+}]$ during the initial two weeks of the experiment was observed, followed by a gradual increase over the next seven weeks, where the concentration peaked at just over 0.2 mol/l. From that point, a steady decrease in $[Mg^{2+}]$ occurred until the end of the experiment. This trend was attributed to the rapid dissolution of Mg-bearing phases, probably a combination of less stable Mg-

silicate and Mg-carbonate minerals, during the initial stages of the experiment. The progression to slower dissolution, expressed by the flattening of the slope, could reflect the equilibration of dissolution and precipitation rates. The decrease of [Mg^{2+}], from the seventh week onwards, was attributed to the precipitation of authigenic phases, and as described later in this Chapter, these phases were Mg-carbonates, primarily ferroan magnesite and magnesite.

The temporal variation of [Mg^{2+}] within the remaining samples was less pronounced, with a general steady increase observed for dunite under CO_2 conditions with maximum concentration of ~0.14 mol/l in the leachate after 246 days. The harzburgite leachate showed the lowest [Mg^{2+}], with ~0.08 mol/l at the end of the experiment, and although this curve displayed several discreet fluctuations, it generally maintained a flat trend.

As expected, solutions extracted from the N_2 pressurised control experiments did not show any significant changes in Mg^{2+} concentration over time.

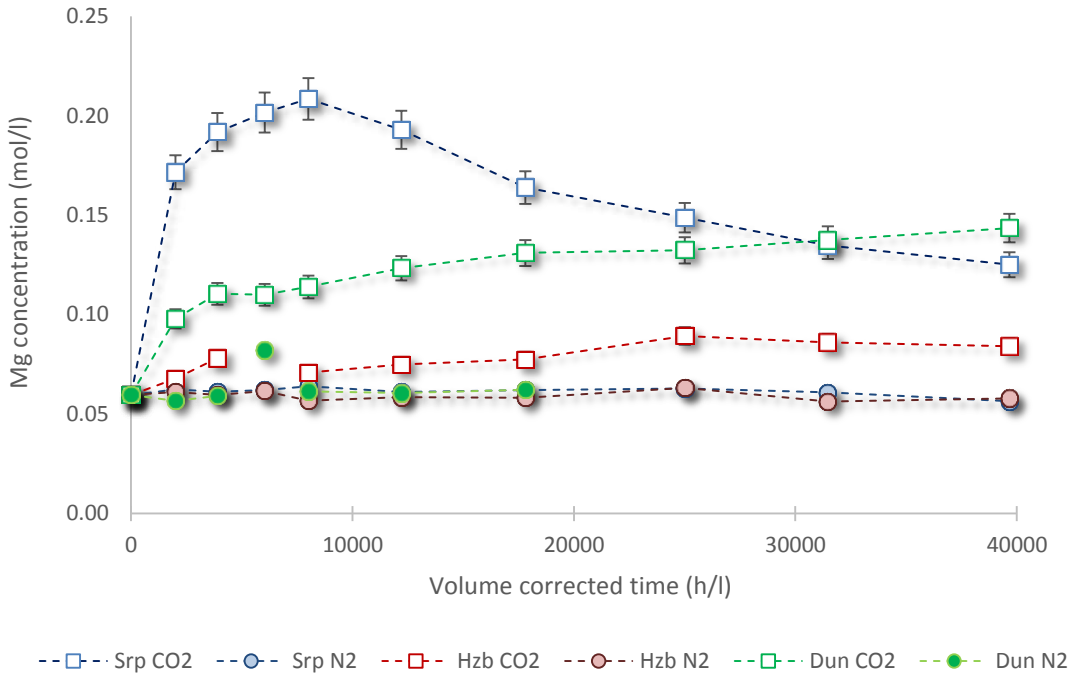


Figure 5.6 Mg concentration in the experimental leachates as a function of time for dunite, harzburgite and serpentinite, investigated under 100 bar CO_2 or 100 bar N_2-pressurised atmospheres. The most prominent temporal evolution of ions was observed for CO_2-reacted samples, in particular the Mg^{2+} concentration curve for serpentininte shows the prevailence of Mg-rich phases dissolution in the first 63 days, followed by the prevailence of precipitation over dissolution until the cessation of the experiment. (lacking 4th data point for HzbCO_2 due to major fluid leak)

5.3.1.2. Temporal evolution of Si^{4+} concentration, $[Si^{4+}]$

The temporal evolution of $[Si^{4+}]$ (Figure 5.7) exhibited general similarities for dunite and harzburgite, whilst showing significant differences for serpentinite. The trends for dunite and harzburgite showed a rapid increase of $[Si^{4+}]$ during the first 17 days up to ~ 0.004 – 0.005 mol/l, after which several fluctuations were observed, although the concentration rarely fell below 0.004 mol/l. Conversely, the $[Si^{4+}]$ within serpentinite leachates showed a more distinct trend, with three intervals being distinguished, *i.e:*

(i) 0 – 17 days - a rapid increase in $[Si^{4+}]$ up to ~ 0.0018 mol/l

(ii) 17 – 170 days - a subtle decrease in $[Si^{4+}]$, followed by an almost a steady state

(iii) > 170 days – a rapid increase to the highest $[Si^{4+}]$ measured during this experiment, of ~ 0.005 mol/l.

The starting dunite and serpentinite material contained similar amounts of magnesium and silicon and comparison of their ionic concentrations within the leachates allowed the congruency of rock dissolution to be appraised. As illustrated by Figures 5.6 and 5.7, the $[Mg^{2+}]$ established was up to two orders of magnitude higher than that of $[Si^{4+}]$, demonstrating that the dissolution of Mg-silicates under conditions of 70°C and 100 bar in saline solution was incongruent over the course of these eight month experiments.

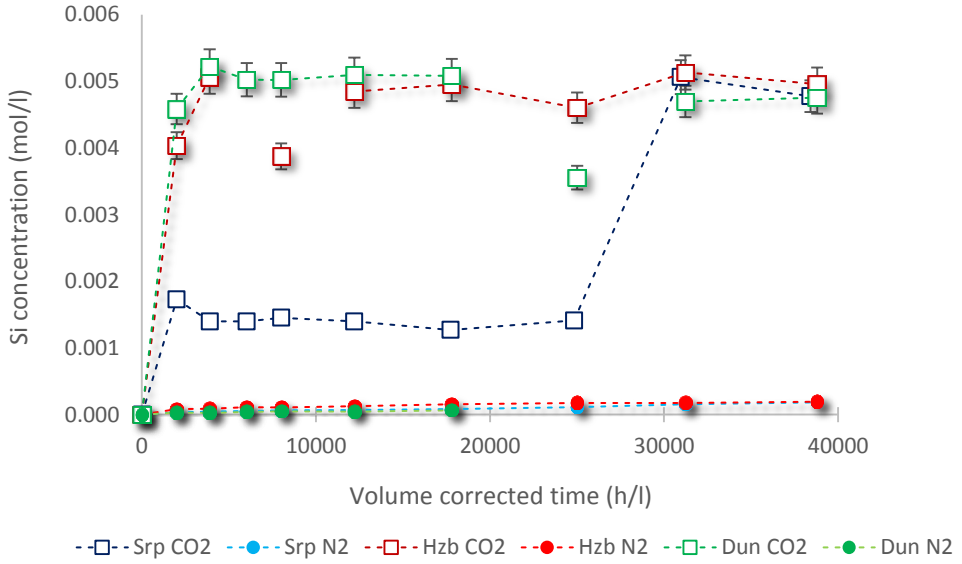


Figure 5.7 Si concentration in the experimental leachates as a function of time for dunite, harzburgite and serpentinite, investigated under 100 bar CO_2 or 100 bar N_2-pressurised atmospheres. Most prominent changes in the Si concentration were observed in the CO2-pressurised vessels, with dunite and harzburgite following similar trends of fast concentration rise with subtle fluctuations in the course of the experiments, whereas serpentinite exhibiting two notable concentration levels, i.e. initial moderate rise level throughout the experiment up until the 7th month when a significant increase in concentration occurred. In serpentinite, these fluctuations may be related to initial incongruent dissolution of serpentine minerals with preferential leaching of Mg and retention of Si in the solid residuum. (no 4th data point for HzbCO2 due to major fluid leak).

5.3.1.3. Temporal evolution of $[Ca^{2+}]$, $[Fe^{total}]$, $[Na^{+}]$, $[Ni^{2+}]$ and $[Sr^{2+}]$

The plots in Figures 5.8 – 5.11 illustrate the trends for $[Ca^{2+}]$, $[Fe^{total}]$, $[Na^{+}]$, $[Ni^{2+}]$ and $[Sr^{2+}]$, with key points being:

(i) A decrease of $[Ca^{2+}]$ and $[Sr^{2+}]$, as observed for leachates from serpentinite under CO_2, being attributable to the precipitation of a secondary Ca-carbonate with trace Sr and Ba content. A very good match was observed for $[Sr^{2+}]$ and $[Ca^{2+}]$ concentration profiles within serpentinite leachates under N_2 conditions, being attributable to the precipitation of aragonite, further evidence for which is presented later in this Chapter.

(ii) A rapid increase of the $[Fe^{total}]$ followed by a rapid decrease, was observed for dunite under CO_2 conditions, and slightly less prominently for harzburgite under N_2 conditions.

(iii) $[Ni^{2+}]$ exhibited a rapid initial increase for all rock samples under CO_2 conditions, followed by a decrease of concentration for the case of serpentinite and dunite, and fluctuating values for the case of harzburgite.

(iv) The rapid increase in concentration of most ionic species within the leachate collected on the 49^{th} day of experimentation for dunite under N_2 conditions could not be explained, and hence was attributed to analytical anomaly.

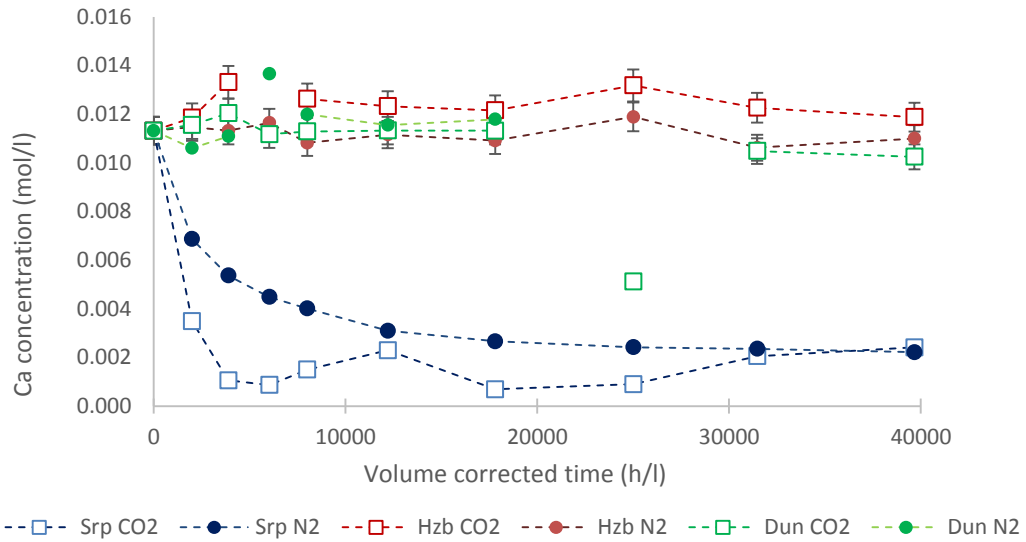


Figure 5.8 Ca concentrations in the experimental leachates as a function of time for dunite, harzburgite and serpentinite processed under 100 bar CO2 or 100 bar N2-pressurised atmosphere. The most prominent temporal evolution of ions was observed for the CO_2-reacted sample. The initial decrease in [Ca^{2+}], in agreement with [Ba^{2+}] and [Sr^{2+}], in the CO_2-pressurised serpentinite vessels was attributed to the precipitation of calcite; while gradual [Ca^{2+}] and [Sr^{2+}] decrease in the N_2-pressurised serpentinite vessel corresponded to the precipitation of Sr-aragonite. (no 4th data point for HzbCO_2 is missing due to fluid leak). The sudden drop in [Ca^{2+}] at ~ 25,000 h/l, in agreement with [Sr^{2+}], and [Si^{4+}], in the CO^2-pressurised dunite vessel was probably related to an analytical anomaly.

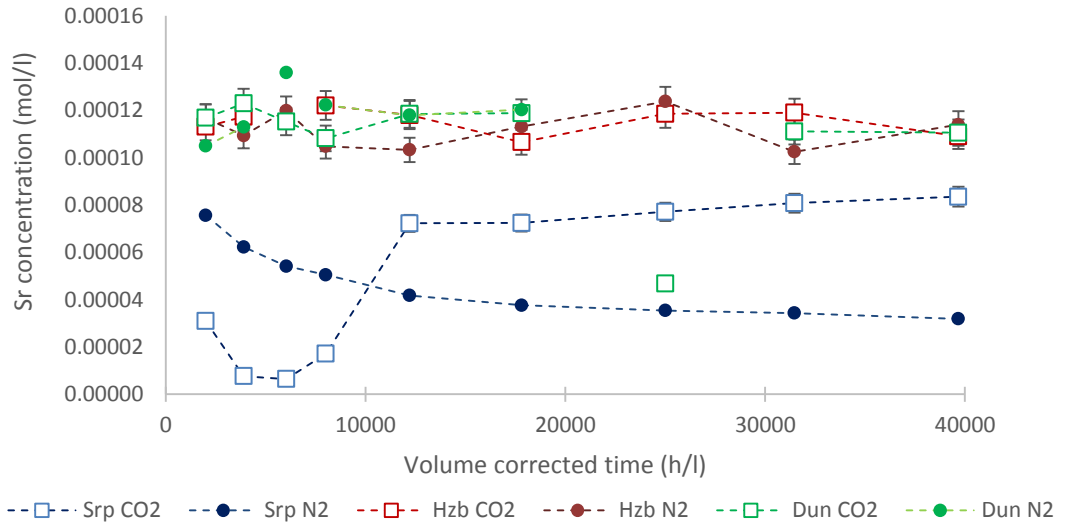


Figure 5.9 Sr concentration in the experimental leachates as a function of time for dunite, harzburgite and serpentinite processed under 100 bar CO_2 or 100 bar N_2-pressurised atmosphere. The most prominent temporal evolution of ions was observed for two serpentinite samples. The initial decrease in $[Sr^{2+}]$, in agreement with $[Ca^{2+}]$, in the CO_2-pressurised serpentinite vessels was attributed to the precipitaton of calcite; while the gradual $[Ca^{2+}]$ and $[Sr^{2+}]$ decrease in the N_2-pressurised serpentinite vessel corresponded to the precipitation of Sr-aragonite . (no 4^{th} data point for $HzbCO_2$ is missing due to fluid leak). The sudden drop in $[Sr^{2+}]$, in agreement with $[Ba^{2+}]$, $[Ca^{2+}]$ and $[Si^{4+}]$ in the CO2-pressurised dunite vessel was probably related to analytical anomally.

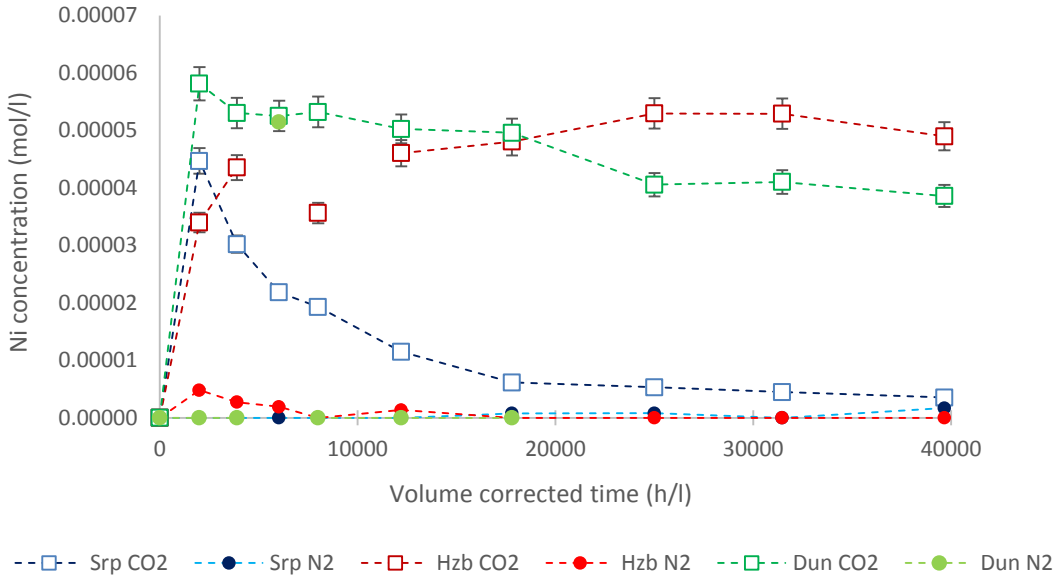


Figure 5.10 Ni concentration in the experimental leachates as a function of time for dunite, harzburgite and serpentinite processed under 100 bar CO2 or 100 bar N2-pressurised atmosphere. All CO2-pressurised samples show an initial increase in Ni concentration followed by a gradual decrease for serpentinite and dunite, and a continuous gentle increase for harzburgite. The sharp early spike for Dun N2, in agreement with other elements, is probably an experimental anomaly. (no 4th data point for HzbCO2 is missing due to fluid leak).

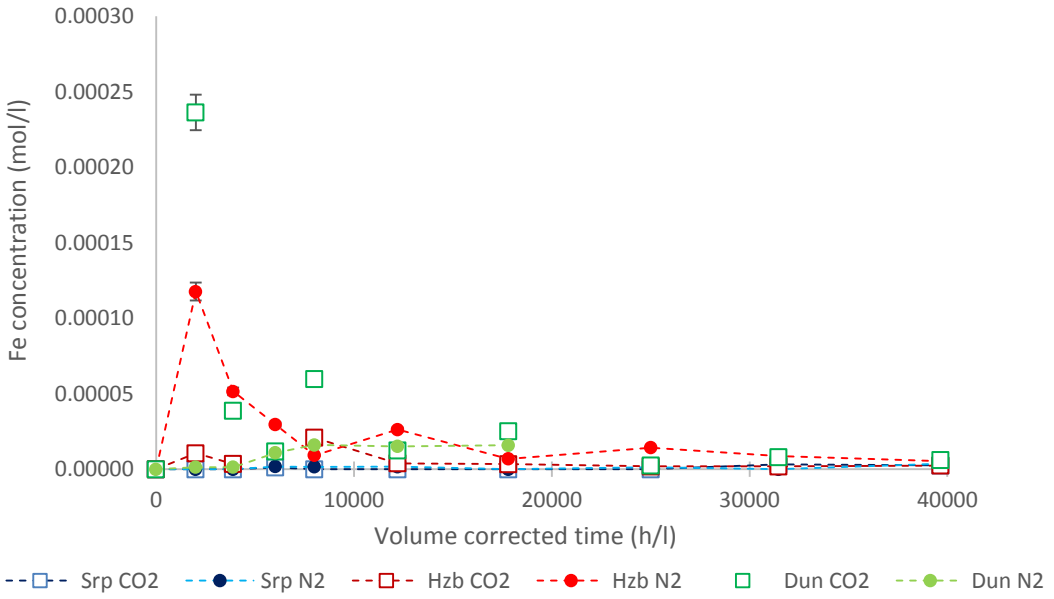


Figure 5.11 Fe concentration in the experimental leachates as a function of time for dunite, harzburgite and serpentinite processed under 100 bar CO_2 or 100 bar N_2-pressurised atmosphere. Apart from an initial positive spike in the Fe concentration in sample of $HzbN_2$ and a couple of spikes in $DunCO_2$, the temporal evolution of this element is not significant. These spikes may represent the dissolution of Fe-bearing minerals and relatively fast precipitation of Fe-bearing phases, likely to be Fe-O/OH, as confimerd by analysis of the solid reaction residues.

5.3.1.4. Rate of net Mg^{2+} release

Since Mg^{2+} was the most significant divalent cation in the rock - fluid system investigated here, both in terms of concentration and the capacity to bind CO_2, the net ionic release rate calculations were focused on this element only.

The rate (R) of net release of metal (i) from serpentinite, dunite and harzburgite was calculated from the following equation [*Brantley et al*, 2008]:

$$Ri = \left(\frac{V}{GSA} * \frac{dC}{dt}\right)$$

Where V is volume of the solution (l); GSA is the geometric surface area (m^2/g); and dC/dt – change of element concentration (mol) with time (s). The volume of solution was corrected for the volume of leachate sampled (Bevan and Savage, 1989).

Table 5.5 provides a summary of conditions and samples used, and the rates of net Mg^{2+} release. The rates are plotted further, as a function of volume corrected time in Figure 5.12. The Table also lists values of pH, corresponding to *in situ* conditions at 70°C and 100 bar in the CO_2 – pressurised experiments, as calculated using PHREEQC, as well as values obtained from measurements at ambient P and T. Values of pH 3.1 - 3.6 and pH 6 - 7 are shown, with the latter being higher due to CO_2 degassing under ambient conditions. For comparison, the modelling of pH *in situ* in the N_2 - pressurised vessels returned values of pH 6 - 8, being in close agreement with values measured in the solutions post-sampling.

Table 5.5 Summary of carbonation experiments, showing experimental conditions and net rates R of Mg released, for the CO_2 pressurised samples. Negative values of R indicate a rate of Mg uptake exceeded its release. In situ pH was modelled using PHREEQC 3.2 [Parkhurst and Appelo, 1999], and the measured pH corresponds to values returned during sampling at ambient P and T. The lack of a 3rd fluid sample from the harzburgite experiment was due to a major vessel leak.

Rock sample	T (°C)	P (bar)	Duration (days)	Length (mm)	Diameter (mm)	Area (GSA, mm^2)	Fluid	Start fluid volume (ml)	Final fluid volume (ml)	Rate of net Mg release ($mol/m^2/s$) at elapsed time point (days)								
										17 days	33	49	63	92	127	169	204	246 days
Serpentinite	70	100	246	27.8	17.9	2700	Brine	200	~110	1.29 x10^{-08}	4.78 x10^{-10}	1.07 x10^{-10}	4.17 x10^{-11}	-5.40 x10^{-11}	-6.11 x10^{-11}	-1.98 x10^{-11}	-1.23 x10^{-11}	-5.9 x10^{-12}
									PHREEQC calculated pH	3.3	3.2	3.2	3.3	3.1	3.1	3.2	3.6	3.1
									Measured pH (ambient P&T)	7.6	7.7	7.6	7.5	7.6	7.6	7.7	7.5	7.4
Dunite	70	100	246	27.6	17.3	2200	Brine	200	~110	6.07 x10^{-09}	2.47 x10^{-10}	-4.56 x10^{-12}	2.00 x10^{-11}	2.69 x10^{-11}	1.31 x10^{-11}	1.41 x10^{-12}	3.60 x10^{-12}	2.95 x10^{-12}
									PHREEQC calculated pH	3.3	3.3	3.2	3.2	3.2	3.2	3.2	3.2	3.1
									Measured pH (ambient P&T)	7.3	7.4	7.1	7.4	7.3	7.5	7.8	7.6	7.6
Harzburgite	70	100	246	27.2	17.5	1800	Brine	200	~110	3.56 x10^{-09}	1.72 x10^{-10}	No fluid sample	3.01 x10^{-10}	9.87 x10^{-12}	3.59 x10^{-12}	1.05 x10^{-11}	-1.94 x10^{-12}	-8.15 x10^{-13}
									PHREEQC calculated pH	3.1	3.1		3.1	3.1	3.1	3.1	3.1	3.1
									Measured pH (ambient P&T)	7.0	6.8		6.6	6.8	7.1	7.5	7.2	7.2

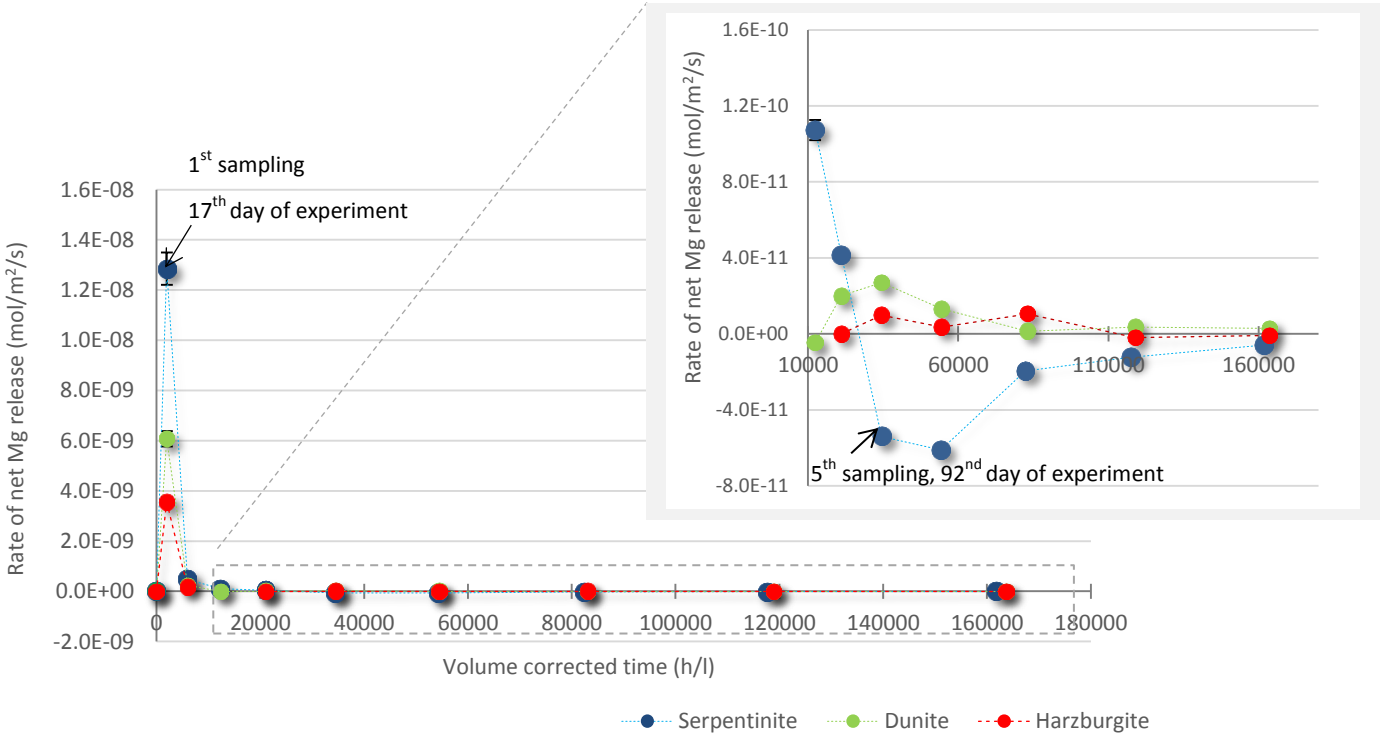


Figure 5.12. Net Mg release rate for serpentinite, dunite and harzburgite processed in the CO_2-pressurised vessels. The graph shows that the initial net release rate was the highest for the serpentinite, followed by dunite and harzburgite. A significant drop was noted for all samples, from the 17th day data point to the 33rd day of experiment. From that point onwards, the net rate of Mg release remained at a roughly even level for dunite and harzburgite, with most data points above the zero-line suggesting higher Mg release than uptake. The inset shows clearly that for serpentinite, the Mg uptake exceeded its release from ca. 70th day of experiment (between 4th and 5th data point), being most likely associated with the main peak of magnesite precipitation.

The value of the rate of net Mg^{2+} release gives an indication of two counter-balancing processes, *i.e.* values > 0 indicate that Mg release dominates; whilst values < 0 suggest that Mg uptake, *i.e.* mineral precipitation, prevails.

Figure 5.12 shows that the initial net Mg release rate was high, with respect to the overall rate measured throughout the experiment, reaching ~ $1.3 \cdot 10^{-8}$ mol/m^2/s, ~ $6 \cdot 10^{-9}$ mol/m^2/s and ~ $2 \cdot 10^{-9}$ mol/m^2/s for serpentinite, dunite and harzburgite, respectively. It is clear that the initial rate was approximately an order of magnitude higher for serpentinite than for the two remaining samples. A sudden drop in rate values was observed after the *ca.* 17th day (*i.e.* the 1st fluid sample data point) of the experiment, whereupon it remained at roughly the same level until the cessation of the dunite and harzburgite experiment, whilst exhibiting significant variation for serpentinite.

Further, the inset in Figure 5.12 shows that for both dunite and harzburgite, the rate value rarely dropped < 0, meaning that the release exceeded uptake at most time points of the experiment. For serpentinite, however, it is clear that around the 70th day of the experiment, *i.e.* between the 4th and 5th sampling points, the net Mg release rate fell below zero, and with subtle fluctuations, it remained in the negative field until the cessation of the experiment. This suggests that Mg^{2+} uptake surpassed its release, being related to the precipitation of magnesite, as confirmed by microanalysis of the post-run solids (Figure 5.35).

The initial rate peak may be associated with: a) fast dissolution of the surface immediately exposed to reactive fluid, *i.e*. the surface layer of the cores and inner open fractures; and b) fast dissolution of carbonate minerals present in serpentinite and harzburgite.

5.3.2.5. Predicted Phases and Chemical Affinity

The definitions of saturation index and chemical affinity have been presented in Chapter 4**.**

The ionic speciation of the experimental solutions was modelled using PHREEQC 3.2 [*Parkhurst and Appelo*, 1999], based on the ionic concentrations measured in the liquids extracted at different time points, and the pH of solution at 70°C and 100 bar, with the redox conditions controlled HS^-/SO_4^{2-} redox couple. This data, together with the Bureau de Recherches Géologiques et Minières (BRGM) database version, Base de Donnee Thermoddem_V1.10, containing data for phases of interest was used to calculate the saturation indices (SI) of potentially precipitating phases.

Figures 5.13 – 5.18 show the evolution of SI for selected phases, as a function of time, for all six samples investigated in this study, including three experiments pressurised with CO_2 and three with N_2. The plots show only those phases that exhibit SI > -3, *i.e.* indicating close to saturation and saturation conditions (SI = 0), with respect to a given mineral. Accordingly, quartz ± amorphous silica, hematite ± goethite and magnesite were included.

The modelling of predicted phases in the CO_2-pressurised experiments showed that the SI of magnesite ranged from SI = - 3.1 to -1.2, with the lowest values for harzburgite and the highest for serpentinite, respectively; suggesting overall, that the solutions, although being close to saturation with respect to magnesite, never

reached it. Previous studies showed that magnesite requires a critical SI between 0.25 and 1.14 to precipitate at 95°C and 100 bar pCO_2 (*i.e*. temperature conditions slightly higher than used in this study) [*Giammar et al.*, 2005]. However, analysis of post-experiment cores revealed the presence of magnesite in both dunite and serpentinite experiments. To verify the level of this discrepancy, PHREEQC Equilibrium_Phases code was run, selecting magnesite in equilibrium with the experimental solutions, *i.e.* SI = 0 as plotted in Figure 5.13. It must be noted that during this process, the measured ionic concentrations had to be fit in to those supposedly in equilibrium with magnesite, in other words, to achieve a shift from SI = -2.08 to -1.2 to SI = 0. In doing so the amount of the measured Mg increased by ~ 5%, highlighting a potential systematic error of the ICP-AES analysis (Table 5.6). This, however means that mineral phases with SI = -2 could exhibit actual SI = 0 and precipitate. It is also noted that during PHREEQC Equilibrium_Phases run the *in situ* pH of the fluid was also adjusted, from values close to 3 to pH values closer to 4.

The magnesite precipitation, in the supposedly under-saturated solution, could have been triggered also by the pre-existence of carbonate minerals in the starting material, potentially allowing the initial critical nucleation energy barrier to be overcome.

Table 5.6 Comparison of modelled Mg concentrations in solutions at 100 CO_2 pressure and 70°C (SI_{mag} = < -2.08 to -1.2 >), under the same P-T conditions but in equilibrium with magnesite (SI_{mag} = 0)

Serpentinite_CO_2 experiment	Mg (mol) concentration in initial solution	Mg (mol) concentration in the solution calculated to be in equilibrium with magnesite	% change in Mg concentration	pH at equilibrium with magnesite
Sample 1	1.717E-01	1.793E-01	4.43	4.1
Sample 2	1.918E-01	1.993E-01	3.91	4.1
Sample 3	2.016E-01	2.092E-01	3.77	4.1
Sample 4	2.085E-01	2.158E-01	3.50	4.1
Sample 5	1.930E-01	2.009E-01	4.09	4.1
Sample 6	1.639E-01	1.721E-01	5.00	4.1
Sample 7	1.488E-01	1.567E-01	5.31	4.1
Sample 8	1.348E-01	1.415E-01	4.97	4.1
Sample 9	1.251E-01	1.340E-01	7.11	4.1

Figure 5.13 Saturation indices for magnesite, amorphous silica and quartz, as a function of time for serpentinite under CO_2 - pressurised atmosphere.

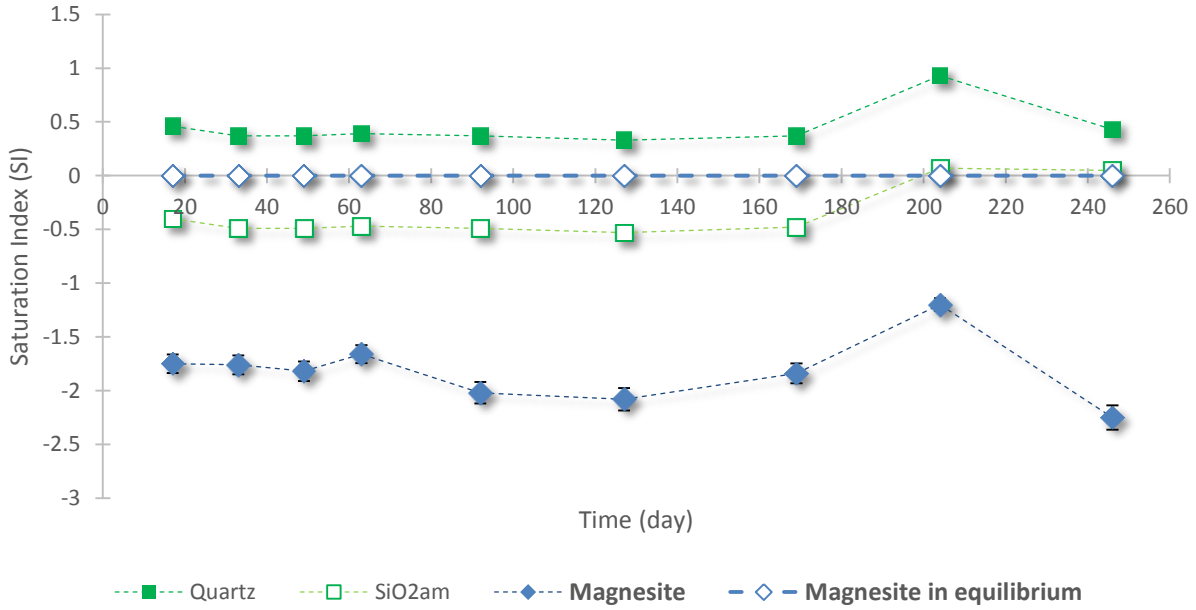


Figure 5.14 Saturation indices of magnesite, amorphous silica and quartz, as a function of time for dunite under CO_2 - pressurised atmosphere.

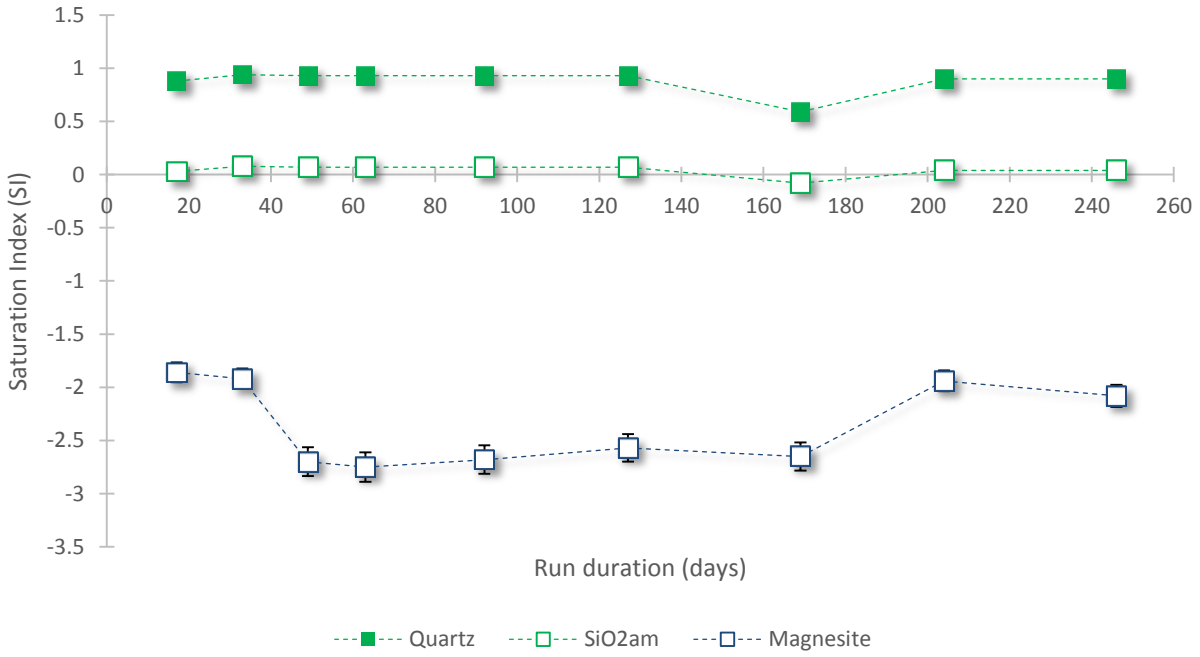
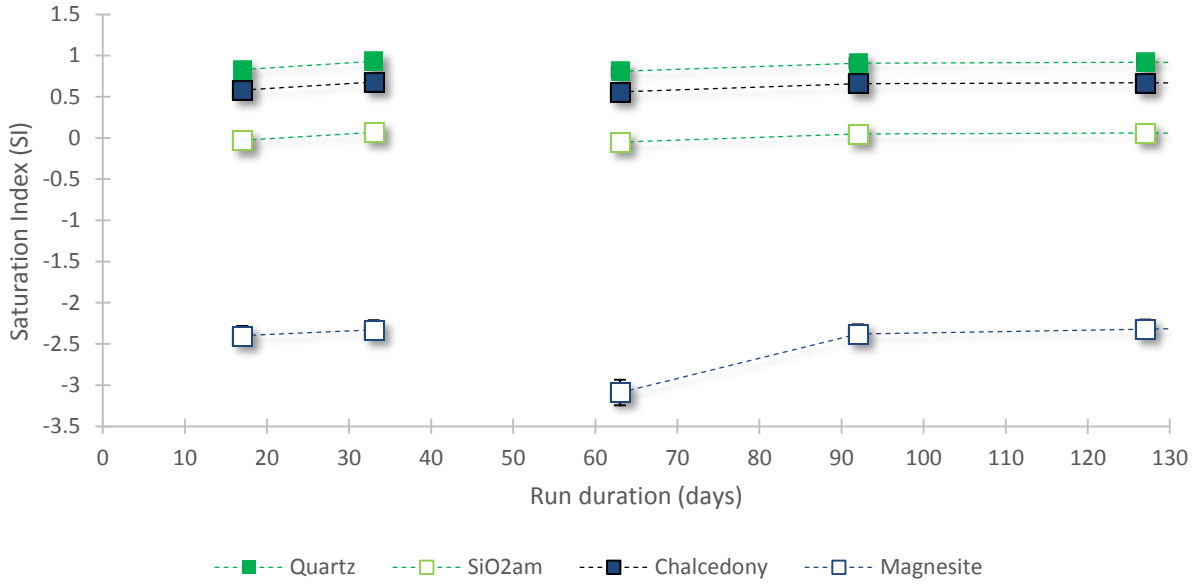


Figure 5.15 Saturation indices of chalcedony, magnesite, amorphous silica and quartz, as a function of time for harzburgite, under CO_2 - pressurised atmosphere.



Solutions in the N_2-pressurised experiments were not saturated with respect to any carbonate mineral. However, microanalysis of the serpentinite core after the cessation of the experiment revealed that it was covered by acicular crystals of aragonite. Similarly, to the serpentinite in the CO_2 pressurised experiment, this discrepancy was verified using PHREEQC Equilibrium_Phases code, selecting aragonite in equilibrium with the experimental solutions, *i.e.* SI = 0 as plotted in Figure 5.16. This modelling shifted the Ca concentrations by ~ 5%, being assigned to analytical error. Further, during this modelling, the pH was adjusted from ~ 7.9 to 8.3.

The modelling also revealed that in the experiments pressurised with N_2, the solutions were saturated with respect to serpentine minerals, as indicated by SI > 1, making lizardite and chrysotile likely phases to form. This correlates well with the evidence for serpentinisation along fractures, provided by microanalysis of harzburgite sample, in particular.

Figure 5.16 Saturation indices of aragonite at equilibrium, and amorphous silica and quartz, as a function of time for serpentinite under N_2 - pressurised atmosphere.

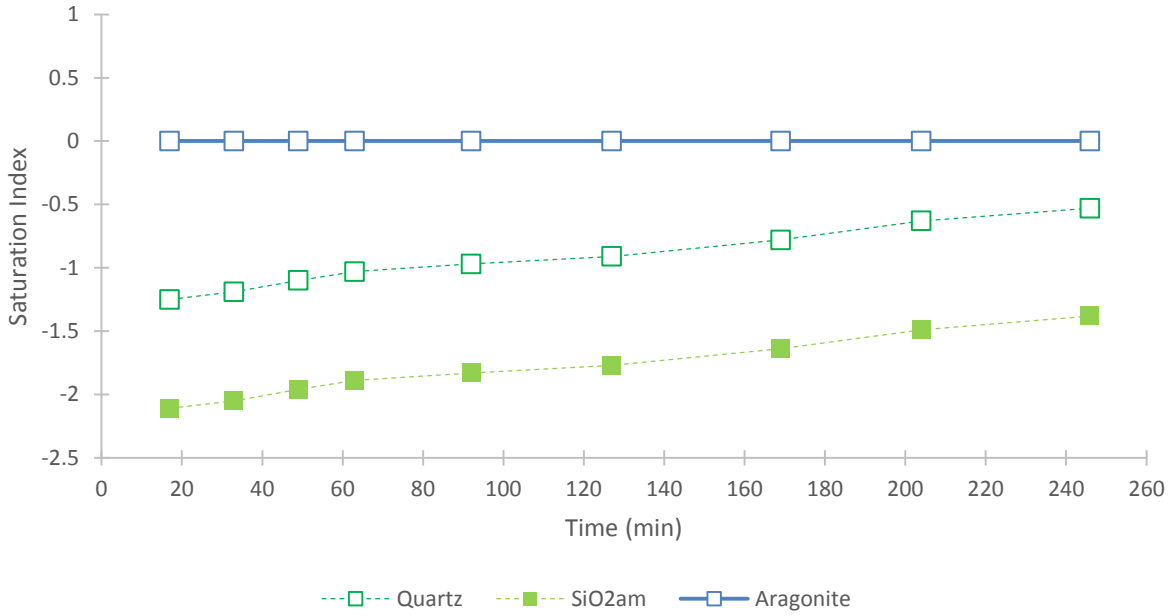


Figure 5.17 Saturation indices of hematite, goethite and quartz, as a function of time for dunite, under N_2 - pressurised atmosphere.

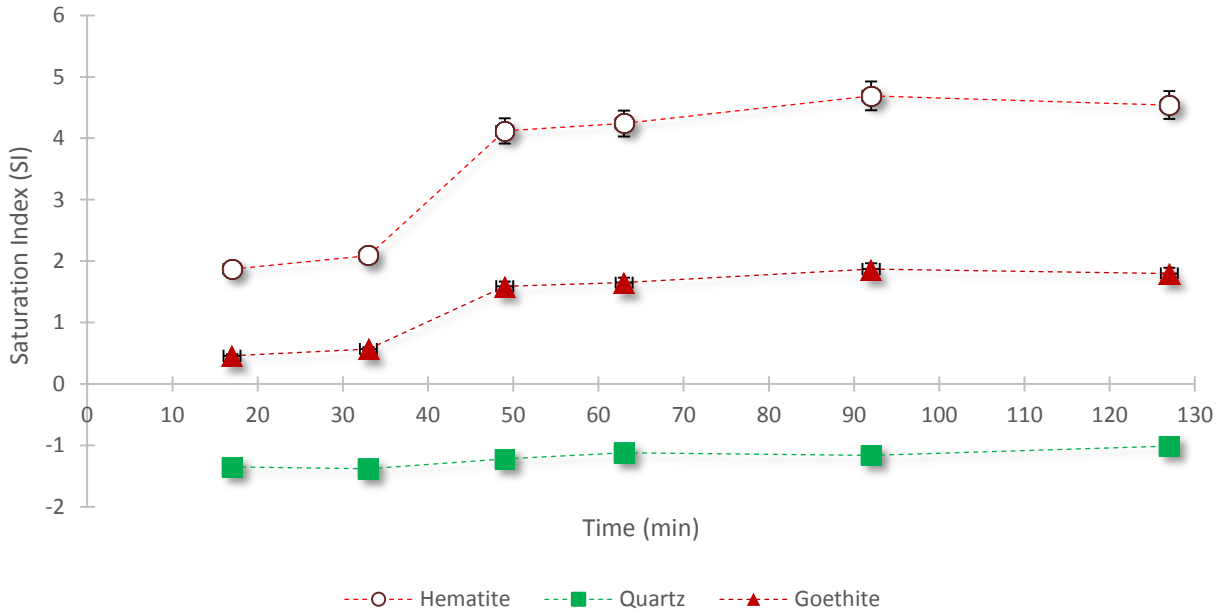
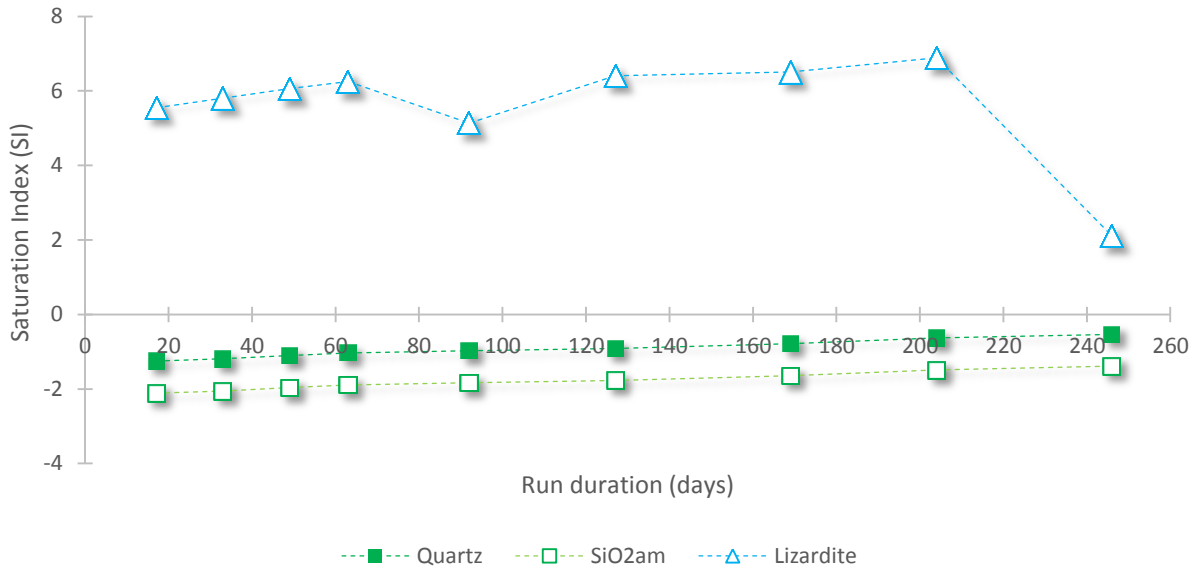


Figure 5.18 Saturation indices of chalcedony, amorphous silica and quartz, as a function of time for harzburgite, under N_2 - pressurised atmosphere.



5.3.2.6. Chemical affinity of mineral phases in the CO_2-pressurised serpentinite experiment

The CO_2-pressurised serpentinite experiment served as an example of extreme mineral transformation, *i.e.* with the most significant degree of mineral dissolution and precipitation. It is known that rate of the reaction commonly slows down towards equilibrium and this section shows the changes in the rate of net Mg release as a function of chemical affinity, as an indicator of distance from equilibrium with respect to specific Mg-bearing phases.

The chemical affinity (A) was calculated according to:

$$A = - R T \ln SI \text{ [*Schott et al.*, 2009]}$$

where R is the gas constant 8.3145 J/mol·K; T is the temperature in K; and SI is mineral saturation index. A positive value of chemical affinity relates to under-saturated reactants, *i.e.* likely to dissolve; zero equates to equilibrium, and a negative value relates to super-saturated reactants, *i.e.* likely to precipitate [*Schott et al.*, 2009].

The chemical affinity was calculated for six mineral phases, amongst which two were Mg^{2+} - bearing primary phases, *i.e.* silicate minerals present in the serpentinite starting rock, including lizardite and chrysotile $Mg_3Si_2O_5(OH)_4$; whilst four represented potential Mg^{2+}-secondary phases, *i.e.* carbonate minerals, including: magnesite ($MgCO_3$), hydromagnesite ($Mg_5(CO_3)_4(OH)_2x4H_2O$), nesquehonite ($MgCO_3$ x $3H_2O$) and lansfordite ($MgCO_3$ x $5H_2O$).

Figure 5.19 shows the rate of net Mg release, as a function of chemical affinity, for all the phases of interest. The time scale, *i.e.* run duration, is shown on the second vertical axis. The separation of the first data point from the remaining data set corresponds to a significantly higher initial rate of net Mg release, and details of the

remaining data points are shown in Figure 5.20. It is evident that lizardite and chrysotile remain far out of equilibrium throughout the whole experiment, with values of chemical affinity ranging from *ca.* 75 kJ/mol to 85 kJ/mol, and hence these phases are dissolving. Amongst the secondary Mg-bearing carbonates, it is clear that hydromagnesite is unlikely to form, being even further out of equilibrium (*ca*. 105 kJ/mol) than the serpentine minerals; whilst nesquehonite (*ca*. 25 kJ/mol) and lansfordite (*ca*. 30 kJ/mol) are potential secondary phases; and magnesite (0 kJ/mol) and quartz (ca. -3 kJ/mol) in particular, are definite secondary phases. These results are in a general agreement with the observations of the solid residues, where magnesite was the only carbonate mineral and quartz the only silicate mineral formed in the serpentinite pressurised with CO_2 experiment. The amount of magnesite calculated from changes in Mg^{2+} concentration in the leachate solutions is presented in the following section.

Overall, the data plotted indicate that, at conditions far from equilibrium, the rate of net Mg^{2+} release remained independent of chemical affinity.

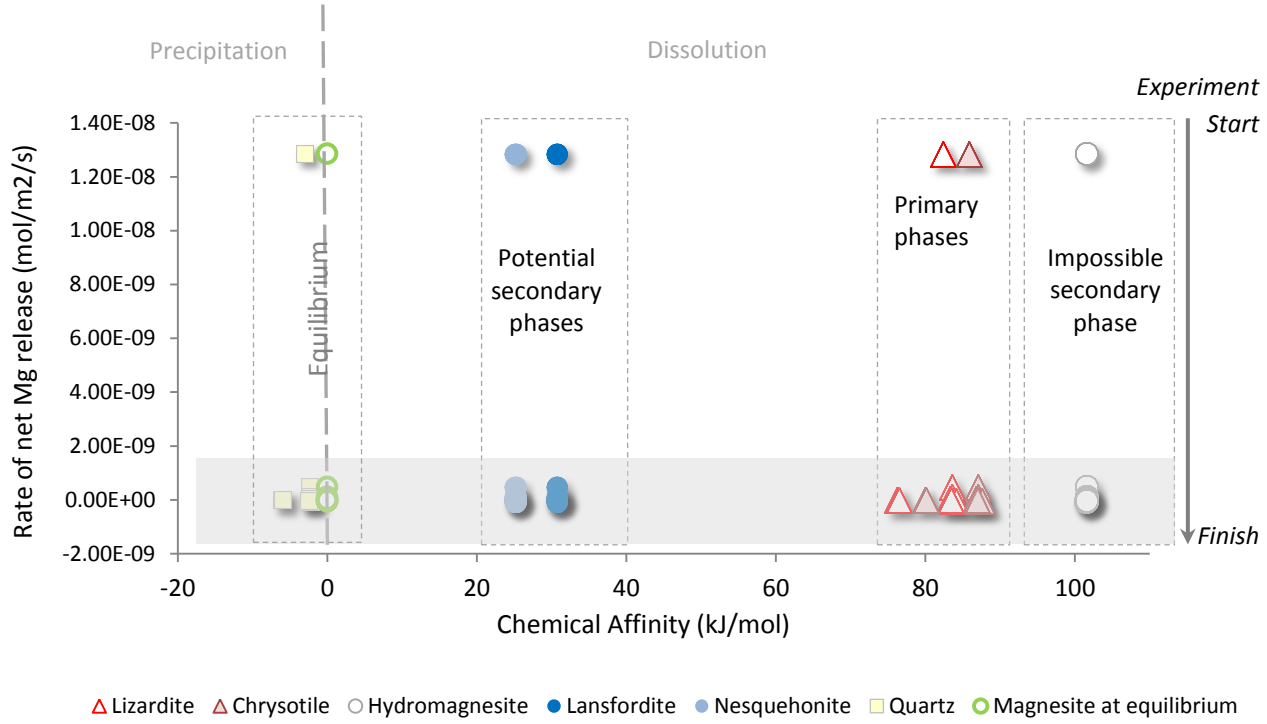


Figure 5.19 Rate of net Mg release versus chemical affinity. Nine data points are plotted per each phase, representing the nine sampling points during the experiments, with the shaded rectangle expanded in Figure 5.20 to show changes in samples 3-9. Hydromagnesite has been classified as an impossible secondary phase, due to its high affinity value, being higher than that of the primary phases that remain far from equilibrium throughout the whole experiment. Magnesite and quartz are the most likely secondary phases, with values of chemical affinity ≤ 0.

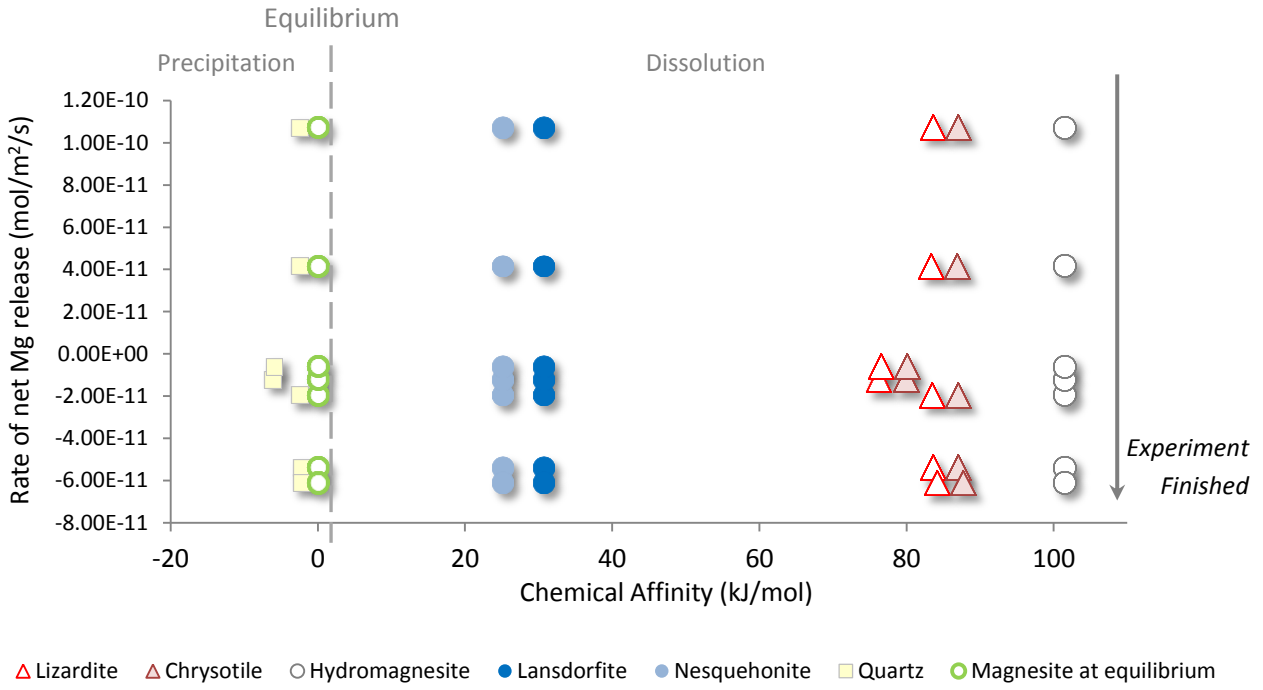


Figure 5.20. Rate of net Mg release versus chemical affinity for samples 3-9 (details of shaded section from Figure 5.19). It is clear that, except for magnesite, all the phases of interest in the Mg silicate – Mg carbonate system considered here remained out of equilibrium throughout the 8 months of experiment duration, and at those conditions, the rate appears to be largely independent of the chemical affinity.

5.3.1.7. The amount of magnesite formed in the CO_2-pressurised experiment of serpentinite

The plot of rate of net Mg release from the CO_2-pressurised serpentinite (Figure 5.20) suggests that, from ~ 70th day of experiment, the Mg uptake exceeds that of release. The calculation of the chemical affinities of potential phases and the analysis of post-experimental solids (presented below) confirmed that magnesite is the only Mg-bearing secondary phase formed in the serpentinite. The amount formed can be calculated from the change in Mg concentration between the 63rd day (nearest fluid measurement) until the cessation of the experiment (Figure 5.21).

$$\Delta C = C^1 - C^2 = 0.084 \text{ (mol} Mg^{2+}/l)$$

Thus, 0.084 M Mg^{2+} was likely utilised in the precipitation of magnesite. The weight of magnesite, as calculated from stoichiometry and adjusted to the volume of solution used in this study (*i.e.* 200 ml), was 1.4 g**.** By mass, this constitutes ~ 8% of the ~ 17.3 g starting serpentinite core.

Caveats to the calculation

Due to the complexity of this fluid-rock system, there are a number of caveats that limit the accuracy of this calculation:

- *A lack of data on the temporal evolution of bicarbonate ions in solution.*
- *The presence of chlorine in the original fluid composition, given that chlorine could act as another sink for magnesium, forming $MgCl_2$. Although, this highlights the assumption that magnesite was the only authigenic magnesium sink, which could lead potentially to an overestimation of the amount of CO_2 captured, no evidence for extensive $MgCl_2$ precipitation was found.*
- *Possible contamination of the fluid with precipitates and fragments of host rock from the core in the headspace that fell in to solution. It is not known at what stage of the experiment this occurred, nor the effect it might have had on solution chemistry.*

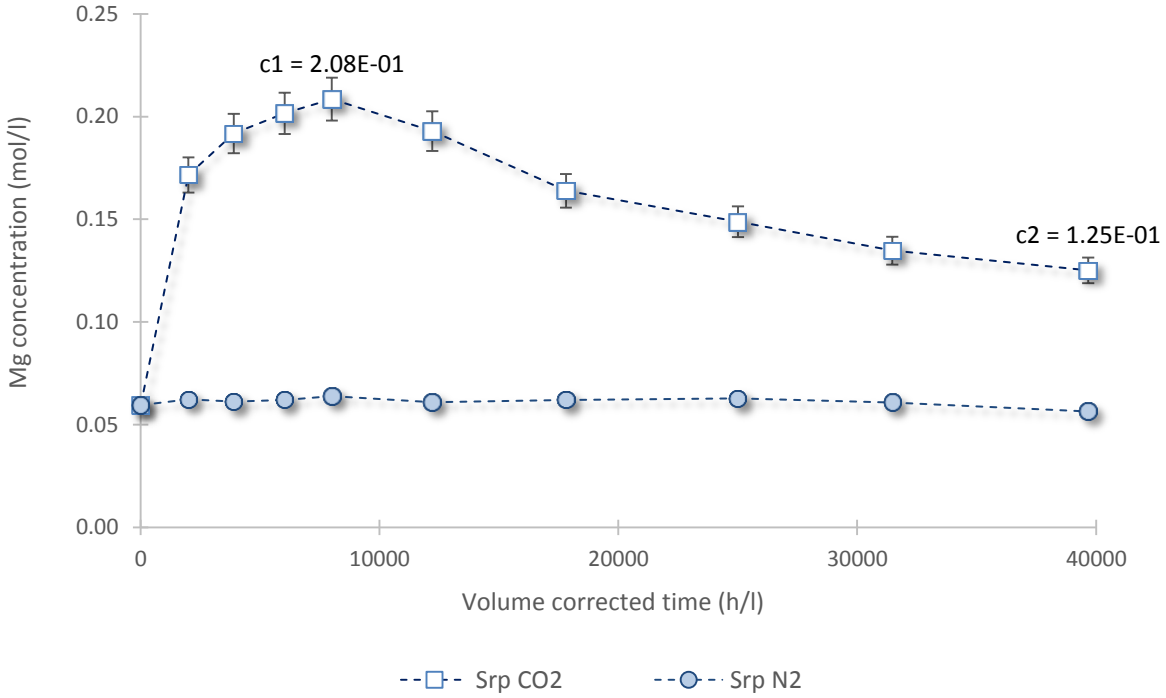


Figure 5.21 Mg^{2+} concentration in the solution of the CO_2-pressurised vessel of serpentinite as a function of time. The value of ΔC, i.e. the difference in concentration of Mg^{2+} between the 63rd and 246th day of the experiment may be used to calculate the amount of magnesite formed and hence the amount of CO_2 captured.

5.3.2. Mineralogy and geochemistry of solid residues

This Section provides a description of the experimental transformations of the cores, on the macro and microscopic-scales, as observed in hand-specimen, thin-section or in rock core fragments. Collectively, 12 cores were examined, four for each rock type, as extracted from the experimental vessels, pressurised with CO_2 and N_2 as a control. The rocks from the control vessel exhibited minimal transformation and thus their description is kept short. Samples marked T and B are from top ($scCO_2$) and bottom (CO_2-saturated brine) of the vessels, respectively.

The most prominent experimental transformations were observed for samples that reacted strongly with CO_2, and the degree of rock transformation varied between the type of original sample and the reactive fluid, *i.e.* CO_2-saturated brine (bottom of the vessel) or wet $scCO_2$ (top of the vessel). The serpentinite cores were most reactive in both environments and on cessation of the experiments; both cores were covered with a crust of magnesite. Dunite and harzburgite displayed moderate to little transformation, and both contained trace amounts of magnesite on the core following reaction with wet $scCO_2$. All the cores that reacted with CO_2-saturated brine were covered by a thin veneer of iron oxy/hydroxide. As expected, under pressurised N_2 control conditions, the cores did not show any significant changes.

Dunite under pressurized N_2 conditions.

Core samples of dunite, before and after the experiment, are shown in Figure 5.22. Apart from a very fine white coating of halite (NaCl) on the surface of the bottom, reacted core, no other evidence for transformation was apparent.

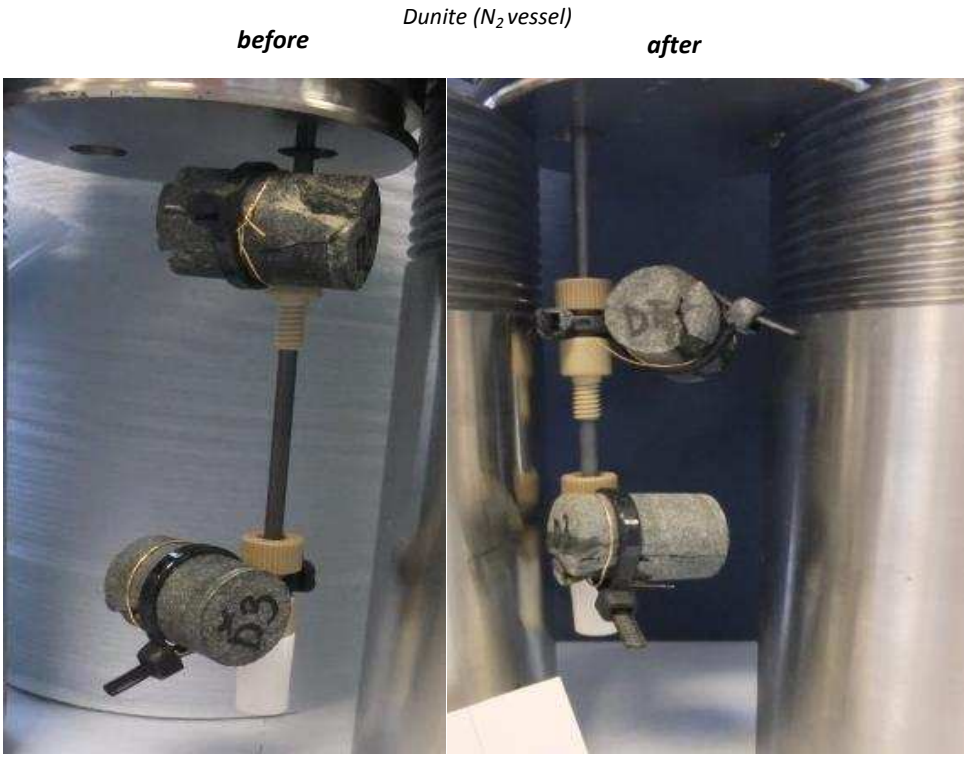


Figure 5.22 Dunite cores, before and after the experiment, in the N_2-pressurised vessel

Dunite under pressurised CO_2 conditions.

The two dunite samples that reacted under pressurised CO_2 conditions showed more prominent transformations, *i.e.* the core from the headspace (wet $scCO_2$) was

covered with a thin, uneven veneer of white magnesite precipitate that in places appeared to have effloresced from pre-existing fractures. The precipitate crystals amassed into round, unevenly spread patches on the core's surface.

The bottom core that reacted with CO_2-saturated brine exhibited significant colour changes, from dark green for the starting material to orange-brown for the reacted core. This colour change was attributed to the precipitation of a thin layer (< 1 mm) of iron oxy/hydroxides. A small amount of white crust on top of this core, as illustrated by Figure 5.20, had fallen from the sample above.

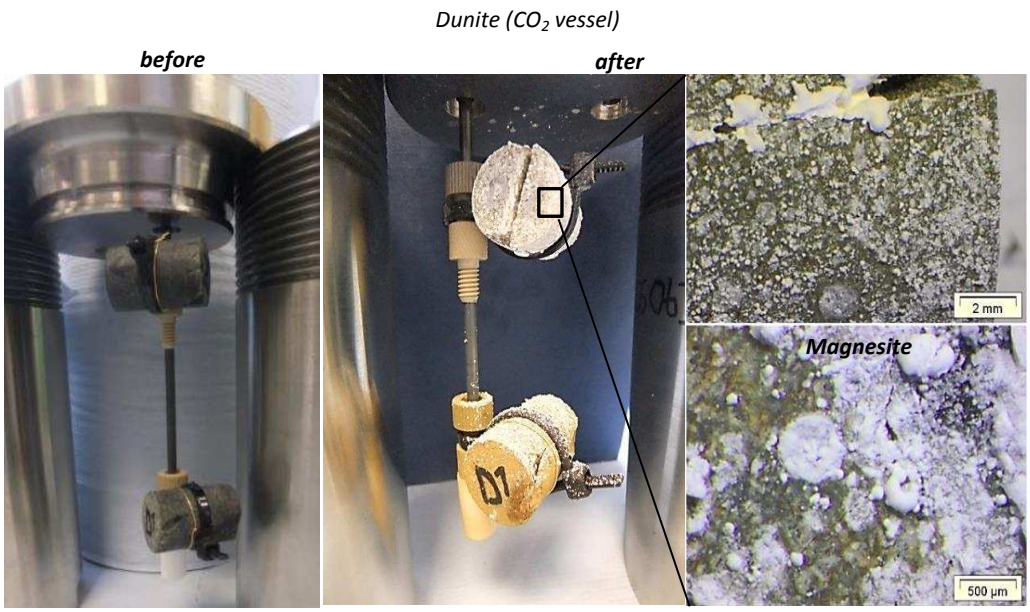


Figure 5.23 Cores of dunite before and after the experiment in the CO_2-pressurised vessel.

Microanalysis of dunite core from the wet $scCO_2$

Figure 5.24 Post-experiment core partially covered by magnesite and core-cross section



Figure 5.25 shows representative areas of the outer surface and inside zones of the top reacted core of dunite. The outer surface was covered by irregularly distributed, < 0.5 mm clusters of fine, < 1 µm approximately equant, locally rhombic crystals of magnesite (Figures 5.25a,b). The surface was also locally corroded, particularly in zones associated with olivine rather than the surrounding serpentine minerals (Figures 5.25c,d). The corroded olivine displayed cleavage planes along with numerous etch pits.

Thin section analysis of the reacted core inner zones revealed at least three morphologically-different types of Mg-carbonate: some Fe-rich, others probably hydrated. The carbonates were randomly distributed along induced fractures, but their small abundance and fine crystallinity compromised quantitative analysis. Recurrent distribution patterns suggested original intimate inter-growths of crystals and multiple stages of dissolution and re-precipitation during processing. Zoned nodular forms (< 5 µm) were observed also.

Thin section analysis also provided further evidence for the preferential dissolution of olivine in this mineralogically heterogeneous serpentinised dunite. For example, Figure 5.25j shows parallel, < 0.5 µm up to 10 µm deep, etch pits located at the edge of the olivine crystals. The pits showed distinctive branching at their base and some were filled partially with magnesite crystals.

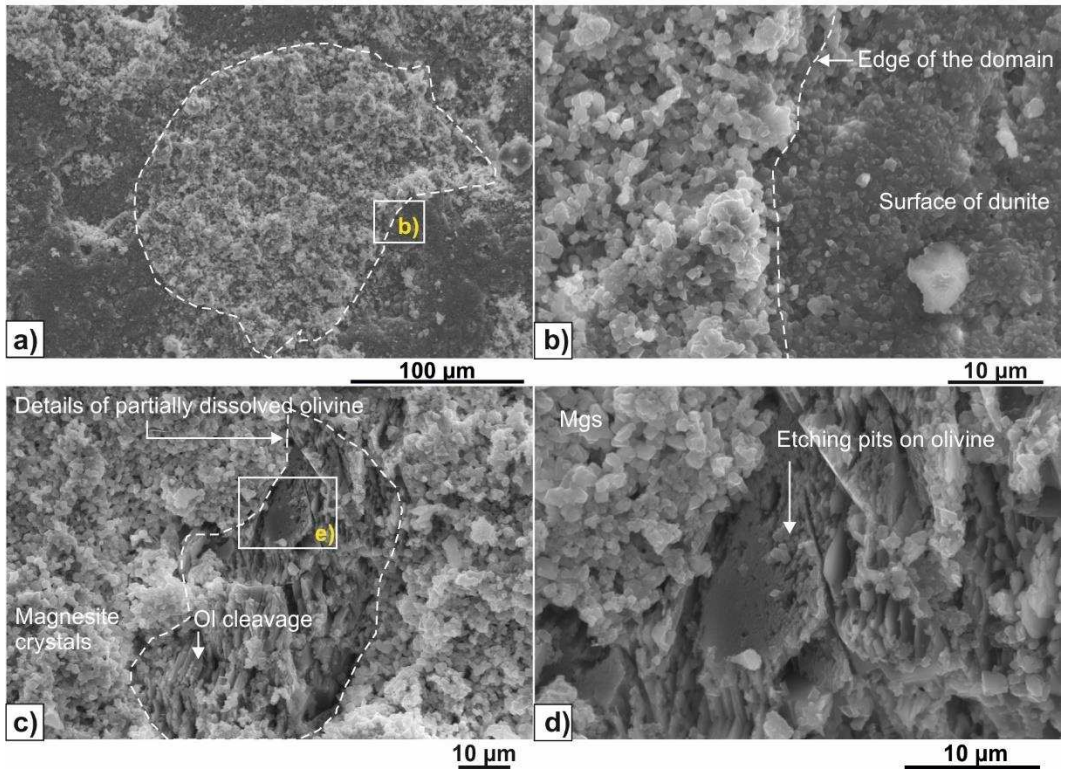


Figure 5.25A SEM (SEI or BSE) images of partially serpentinised dunite following reacting with wet $scCO_2$, showing: a,b) a cluster of finely crystalline magnesite on the outside part of the core; c,d) corroded olivine on the outside part of the core.

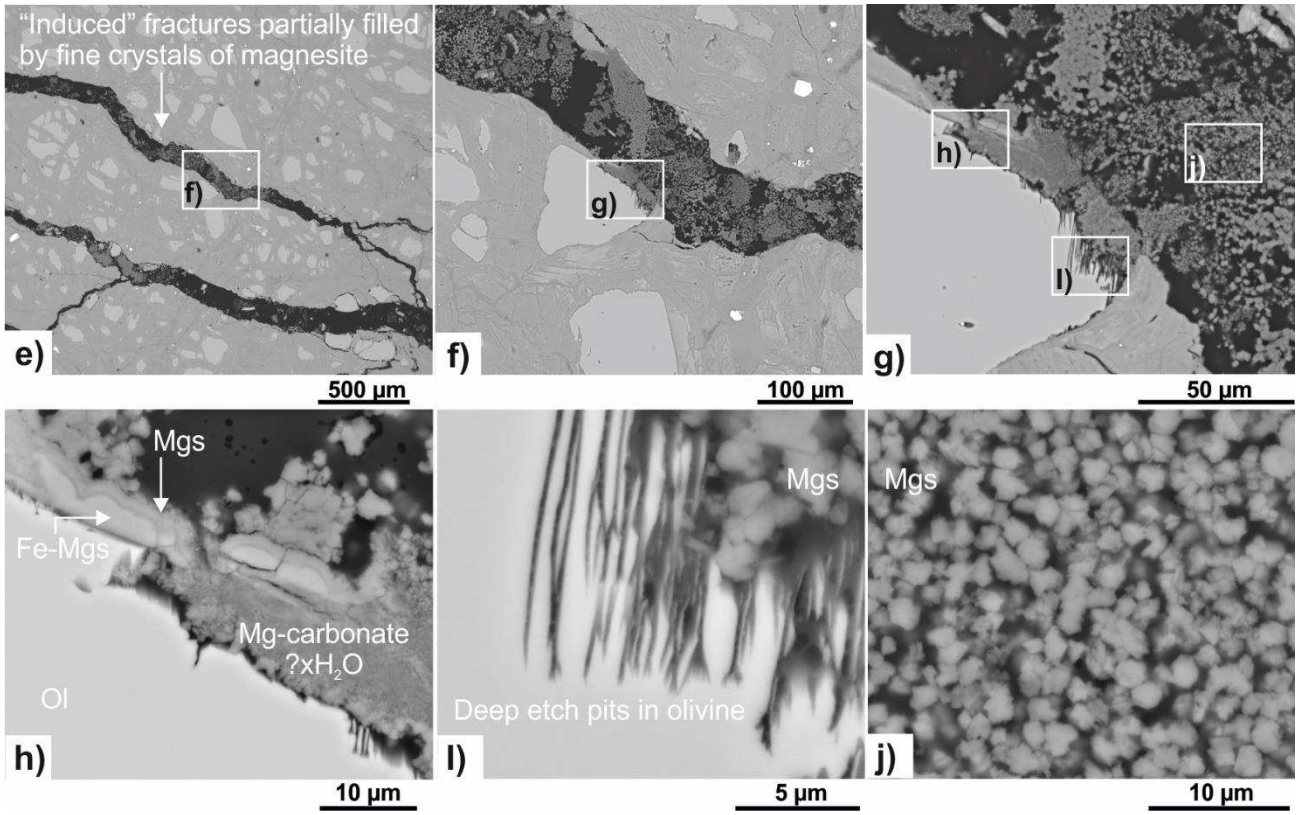


Figure 5.25B SEM (SEI or BSE) images of partially serpentinised dunite following reacting with wet scCO_2, showing e-h) Mg-carbonate mineralisation along an induced fracture; i) etch pits within partially dissolved olivine; and j) fine-scale characteristics of magnesium carbonate crystals.

Microanalysis of dunite core from the CO_2-saturate brine

Figure 5.26 Post-experiment core covered by Fe oxide/oxyhydroxides and core-cross section



The dunite core that was immersed in CO_2 / saturated brine exhibited a distinctively different mode of transformation, with three types of authigenic (secondary) minerals being observed:

1) Fe-rich oxide and/or oxyhydroxide, hematite and goethite respectively, formed an orange to brown stained veneer on the core surface. Detailed microanalysis of a fragment of the core opened along an induced fracture revealed that secondary Fe-mineralisation was present up to ~ 3 mm along the fracture (Figures 5.27b,c). In thin-section, the Fe-mineralisation was delineated by a narrow (< 5 µm), unevenly distributed coating with several distinctive < 2 µm nodules attached to the edge of the core (Figure 5.27a).

2) Mg-rich carbonates were relatively scarce and mainly present within the inner parts of the reacted core, where no evidence for secondary hematite/goethite formation was observed. The separation between the Fe-rich phases and the carbonates was graded, but generally coincided with a red, stained boundary ~ 3 mm from the edge of the core (Figures 5.27b,c).

The Mg-carbonate exhibited a wide variety of forms; dominated by 5 - 10 µm round aggregates / nodules, and 2 – 20 µm angular aggregates, both composed of amalgamated euhedral to subhedral < 1 µm crystals. A close examination of several discreet zones along the induced fracture surface revealed a close mineral association between the host olivine, the Mg-carbonate and ***3) < 1 µm nodules of silica***. Authigenic carbonate and silica were crystallographically aligned to olivine cleavage planes (Figures 5.27e,f). The congruent dissolution of olivine resulted in a mouldic cavity (resembling the shape of original phase) between serpentinite matrix and the corroded crystal; commonly termed secondary porosity.

The fluid-rock interaction also resulted in the formation of a delicate, nanotubular (< 2 µm long) phase (Figure 5.27g, inset), which could not be identified due to its relative scarcity and delicate structure. This phase formed a fine coating on the surface of the serpentine matrix, surrounding the olivine crystals, and hence was probably an alteration product of the serpentine minerals.

Mineral paragenesis along the induced fracture was complex and although it provided evidence for olivine dissolution and *in situ* precipitation of Mg-carbonate and silica, it is noted that the overall amount of authigenic minerals in dunite was very small, probably < 1 % of the original rock volume. Further, the analysis of the core in thin-section (cut perpendicular to the core length) did not confirm the observations from the fracture surface. The most prominent dissolution of olivine was within the first 200 µm from the core edge (Figures 5.27h,l), and dissolution was most pervasive in close proximity to other induced fractures. The olivine relics displayed euhedral to subhedral etch pits, suggesting that dissolution was crystallographically controlled.

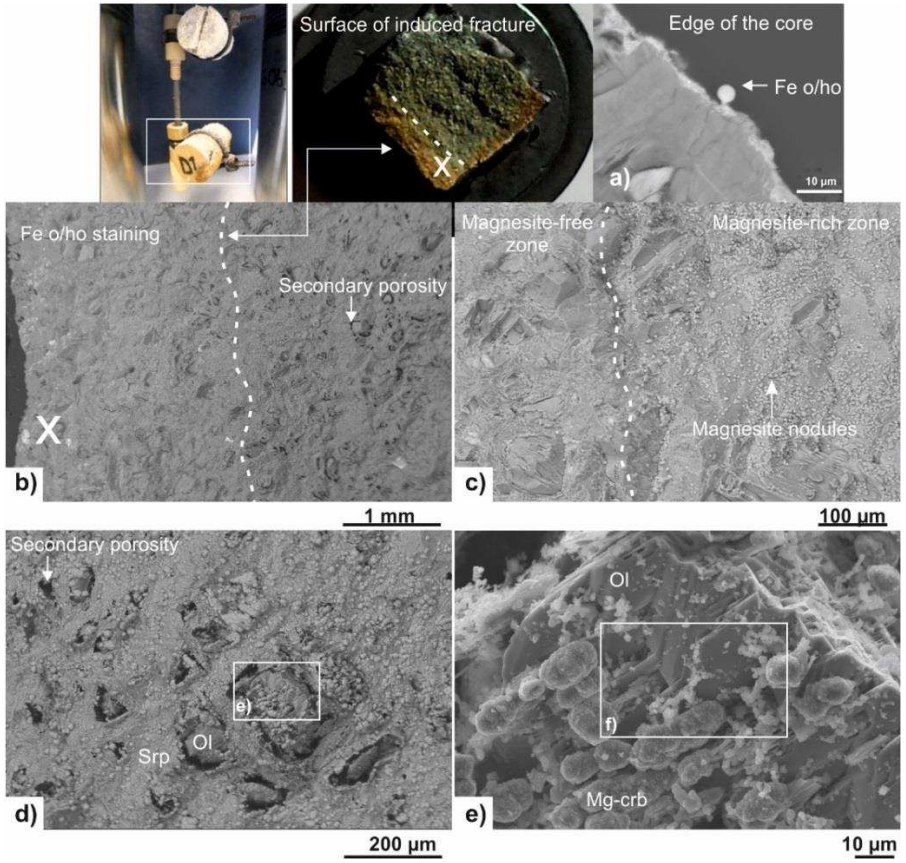


Figure 5.27A. BSE and SE images of dunite following reaction with CO_2 saturated brine. b-e) recorded along an induced fracture surface, showing complex authigenic mineralisation dominated by Fe oxide/oxyhydroxide in the first few milimeters from the core surface, followed by the coexistence of partially dissolved olivine, and authigenic Mg-carbonate, silica and an unidentified nanotubular phase.

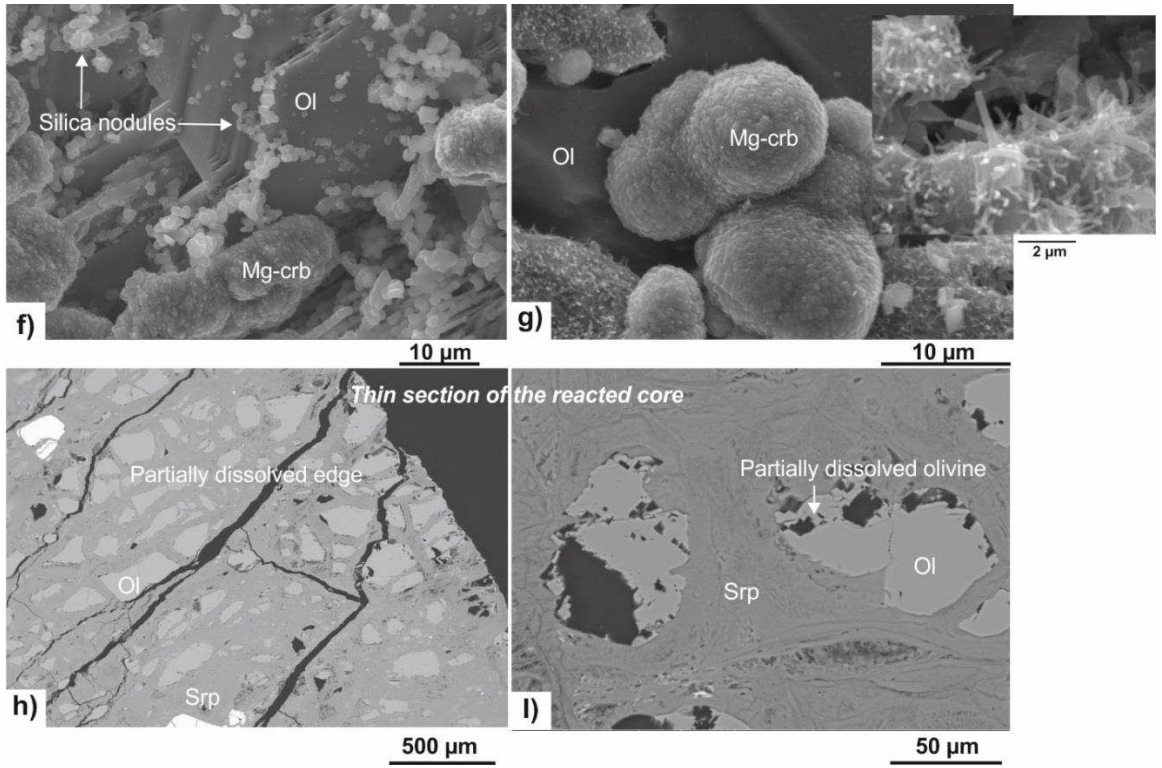


Figure 5.27B. BSE and SE images of dunite following reaction with CO_2 saturated brine. f-g) recorded along an induced fracture surface, showing complex authigenic mineralisation dominated by Fe oxide/oxyhydroxide in the first few milimeters from the core surface, followed by the coexistence of partially dissolved olivine, and authigenic Mg-carbonate, silica and an unidentified nanotubular phase. h,I) were acquired from a thin-section cut perpendicular to the length of the core.

Harzburgite under pressurised N_2 conditions

The degree of experimental transformation in the reacted cores of harzburgite, under pressurised N_2 conditions, was negligible and only related to localised darkening of the lower core (Figure 5.28). Although, its origin remained unclear, the darkening correlated with pre-existing fractures and hence may signify localised hydration, *i.e.* serpentinisation along open fractures

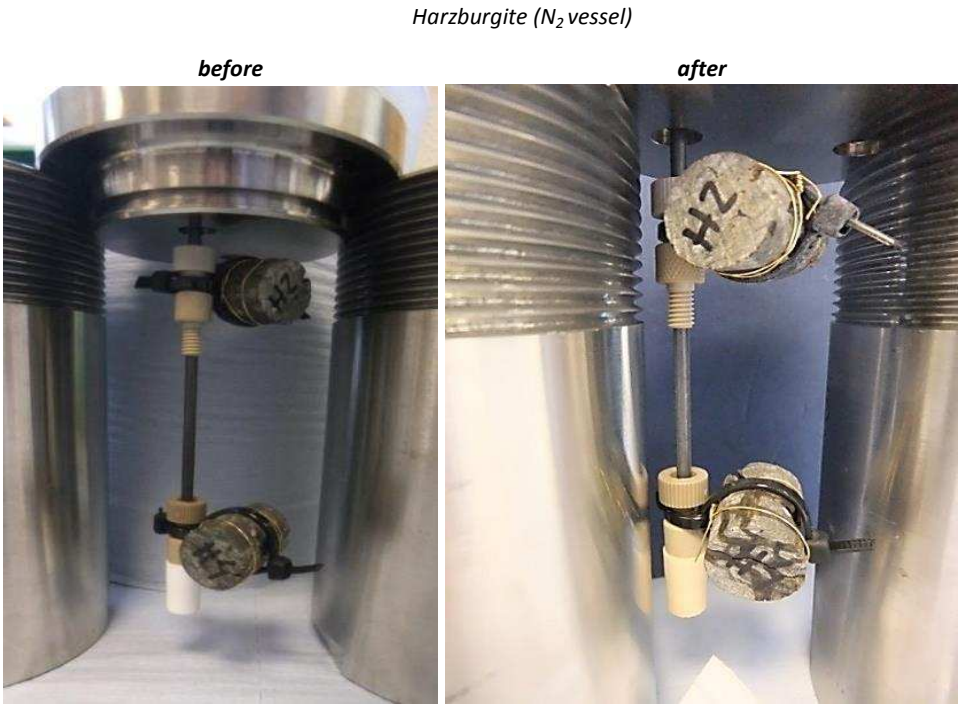


Figure 5.28 Harzburgite cores before and after the experiment in the N_2-pressurised vessel.

Harzburgite under pressurised CO_2 conditions

The experimental transformations of harzburgite under pressurised CO_2 conditions was manifested by a change of core colour, from a typical dark green to whitish, with distinct white zones for the top core and characteristic orange-brown for the bottom core (Figure 5.29). The colour changes were attributed to:

- ***Top core*** – the precipitation of a finely crystalline magnesite crust, usually in the form of nodular aggregates, generally distributed along pre-existing fractures. The extent of magnesite mineralisation, however, was very low.
- ***Bottom core*** – the precipitation of a thin (< 0.5 mm) veneer of iron oxy/hydroxides.

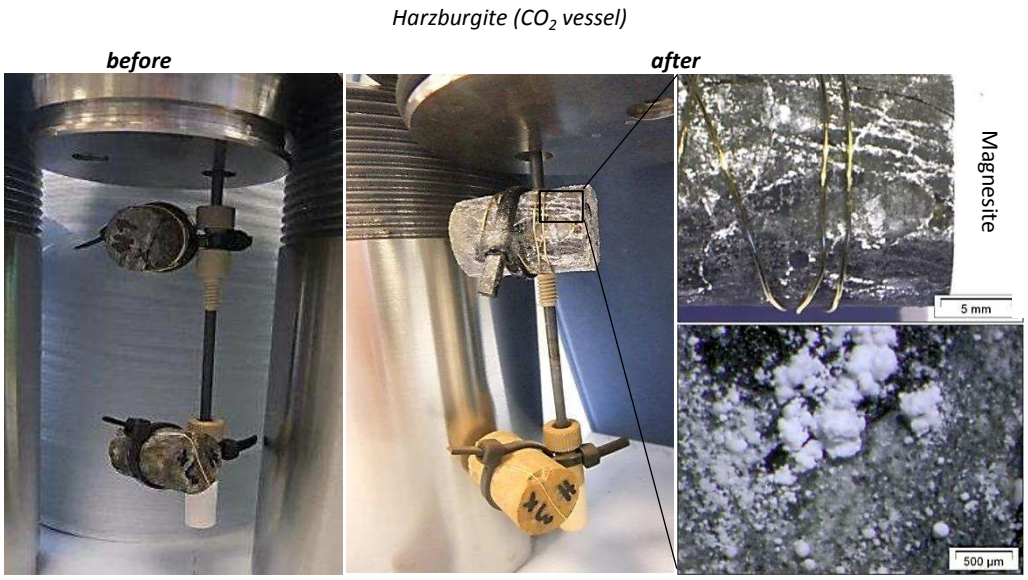


Figure 5.29 Harzburgite cores before and after the experiment in the CO_2-pressurised vessel.

Microanalysis of harzburgite core from wet $scCO_2$

Figure 5.30 Post-experiment core covered by magnesite along the fractures and core-cross section



The most prominent experimental transformation in harzburgite was related to the presence of < 100 μm nodules of authigenic Mg-carbonate, distributed on the surface of the core and locally within the core fractures, and where fractures intersected the core surface (Figures 5.31a,b). Detailed examination revealed that some original, mineralised fractures were reactivated during the experiment, with original infilling carbonate being partially dissolved (Figures 5.31c,d).

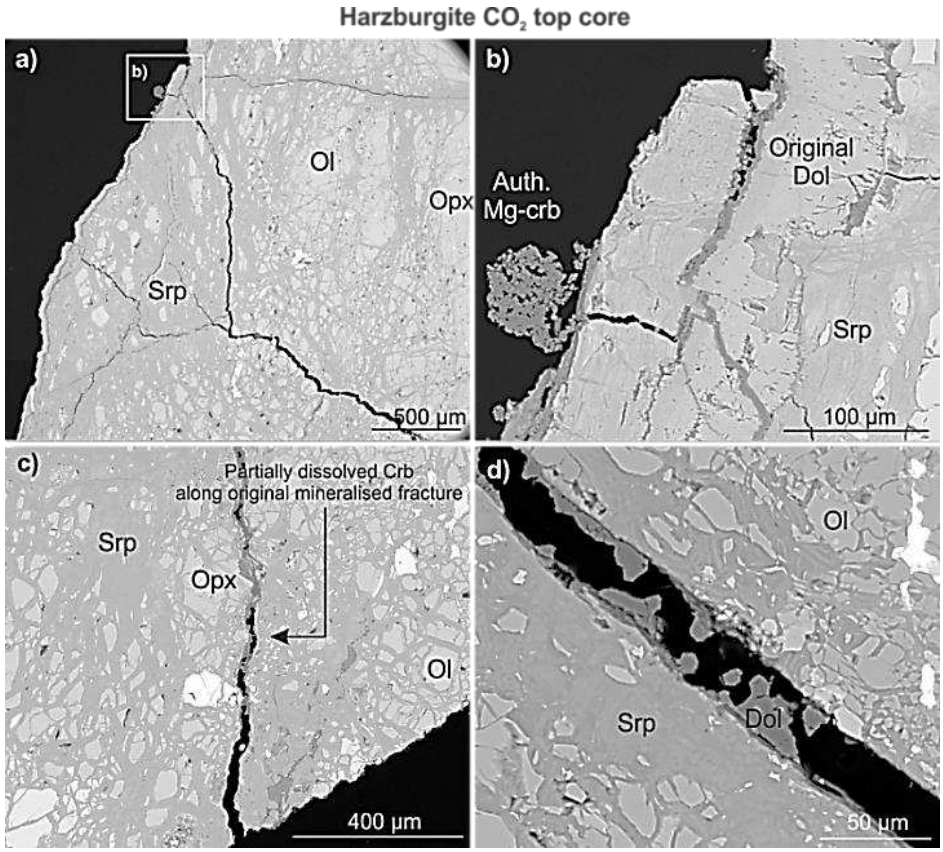


Figure 5.31 BSE images of a cross-sectioned harzburgite core following reaction with wet $scCO_2$; a,b) an induced fracture at the end of which < 100 µm nodular aggregates of finely crystalline Mg-carbonate were found; c,d) a fracture that was probably reactivated during processing, showing remnants of pre-existing partially corroded carbonate.

Microanalysis of dunite core from CO_2-saturated brine

Figure 5.32 Post-experiment core covered by Fe oxide/oxyhydroxides and core-cross section



Transformations of the lower core of harzburgite were characterised mainly by the precipitation of iron oxide/oxyhydroxide, hematite and/or goethite, forming a < 1 µm, uneven coating on the outside surface (Figure 5.33a), similar to that observed for the dunite bottom core. The Fe^{2+} originated from dissolution of primary silicates, it was then oxidised in the solution (CO_2 is a weakly oxidiser) and precipitated as Fe^{3+}-bearing oxide and /or oxyhydroxides.

Further, as illustrated in Figure 5.33b, zones directly adjacent to the induced fractures were serpentinised and although the original harzburgite rock contained veins of serpentine, it is possible that further serpentinisation occurred during the experiment.

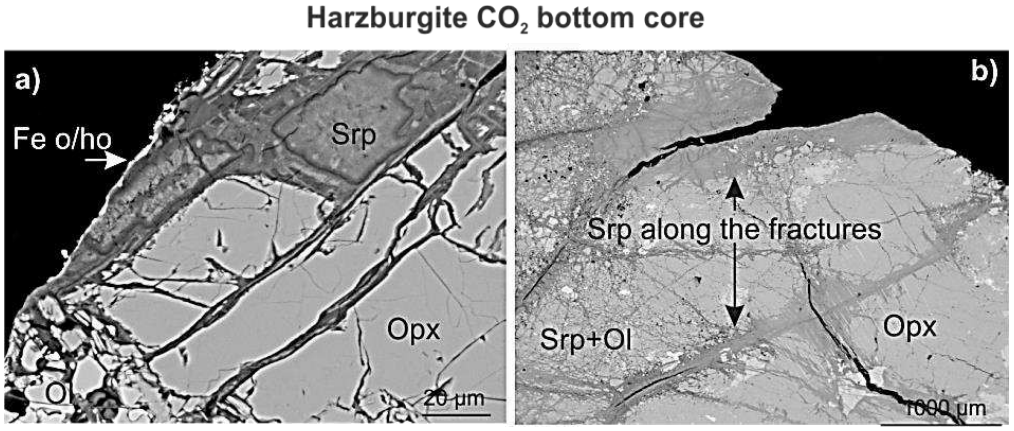


Figure 5.33 BSE images of harzburgite following reaction with CO_2 saturated brine showing: a) a thin < 1 µm veneer of hematite/goethite forming an irregular coating on the outside of the core; and b) evidence for in situ serpentinisation along the induced fractures.

Serpentinite under pressurised N_2 conditions

The lower serpentinite core that reacted with the brine was partially covered by clusters of acicular, up to 1 mm long, crystals of aragonite (Figure 5.34). In places, the distribution of aragonite matched that of the pre-existing fractures. The source of CO_2 for aragonite originated from dissolution of pre-existing carbonates.

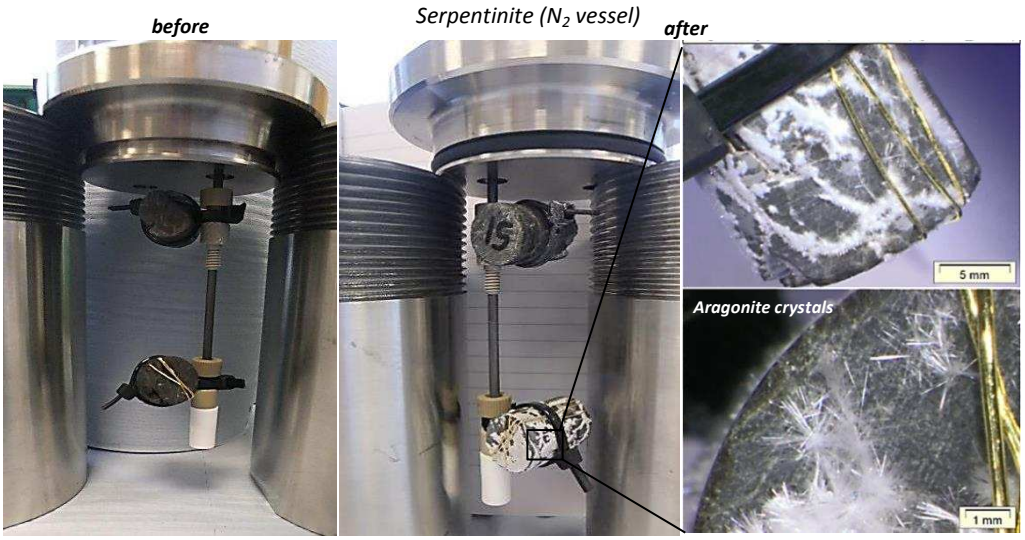


Figure 5.34 Serpentinite cores before and after the experiment in the N_2-pressurised vessel.

Serpentinite under pressurised CO_2 conditions

Samples of serpentinite from the CO_2 vessel showed the most prominent transformations amongst all the samples analysed in this study. On cessation of the experiment, both cores (top and bottom) were covered by a white, magnesite-dominated crust (Figure 5.35). The thickness of the crust was difficult to estimate due to the very friable nature of the solid precipitate combined with significant displacement of the minerals on vessel opening and subsequent handling. However, a visual estimate suggested the uneven thickness did not exceed 3 mm. In both samples, the crust consisted mostly of nodular aggregates of fine < 1 mm crystals. Also, the very first layer of the crust mimicked the dendritic network of the original serpentine veinlets.

The two cores (bottom and top) differed in their resultant post-experimental texture: the bottom core resembled the size and shape of the original sample; whilst the core that reacted with wet $scCO_2$ was damaged pronouncedly, with approximately a third of the core missing at the end of the experiment (Figure 5.35), having fallen down in the experimental vessel.

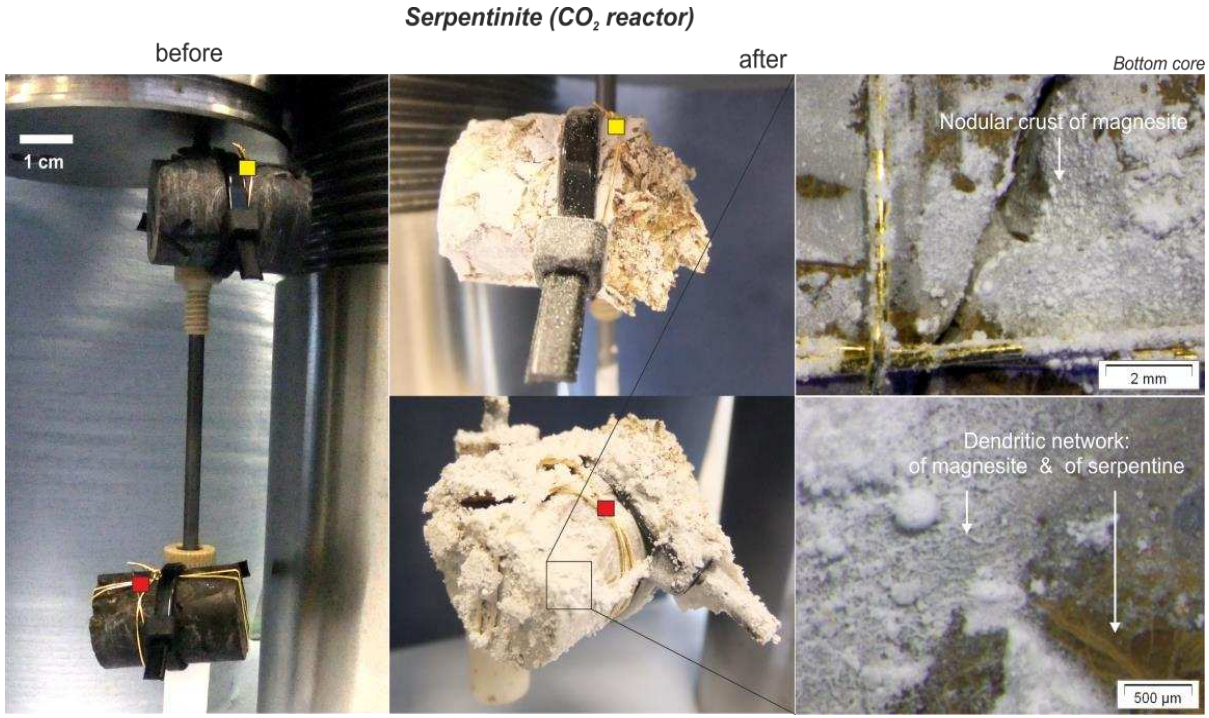
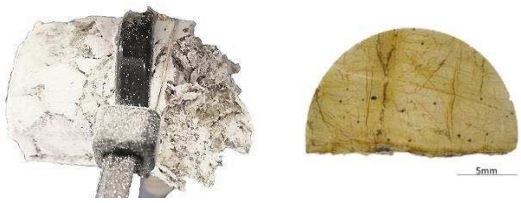


Figure 5.35 Transformational features of the serpentinite cores during fluid-rock interaction in the CO_2 – pressurised vessel. The white crust is magnesite.

Microanalysis of serpentinite core from wet $scCO_2$

Figure 5.35 Post-experiment core covered by aragonite and core-cross section



The core of serpentinite that reacted with wet $scCO_2$ displayed a wide range of experimental transformations, most prominently related to formation of a magnesite-dominated crust on the outside surface of the core and a complex Mg-carbonate paragenesis within the induced fractures. However, no clear evidence for sequential dissolution of host rock was found.

Mineralisation in the crust

The crust on the outside surface of the core was dominated by fine < 1 µm crystals of Mg-carbonate (Figure 5.36a), confirmed by XRD as ferroan-magnesite and magnesite. The crystals were commonly clustered into < 1 mm semi-nodular clusters (Figure 5.36b) or smaller < 30 µm well-developed spheres (Figure 5.36c). Apart from the ubiquitous Mg-carbonates, the crust also contained trace amounts of Ca-carbonate, with a “dog-tooth” crystal morphology typical of calcite (Figures 5.36c,d).

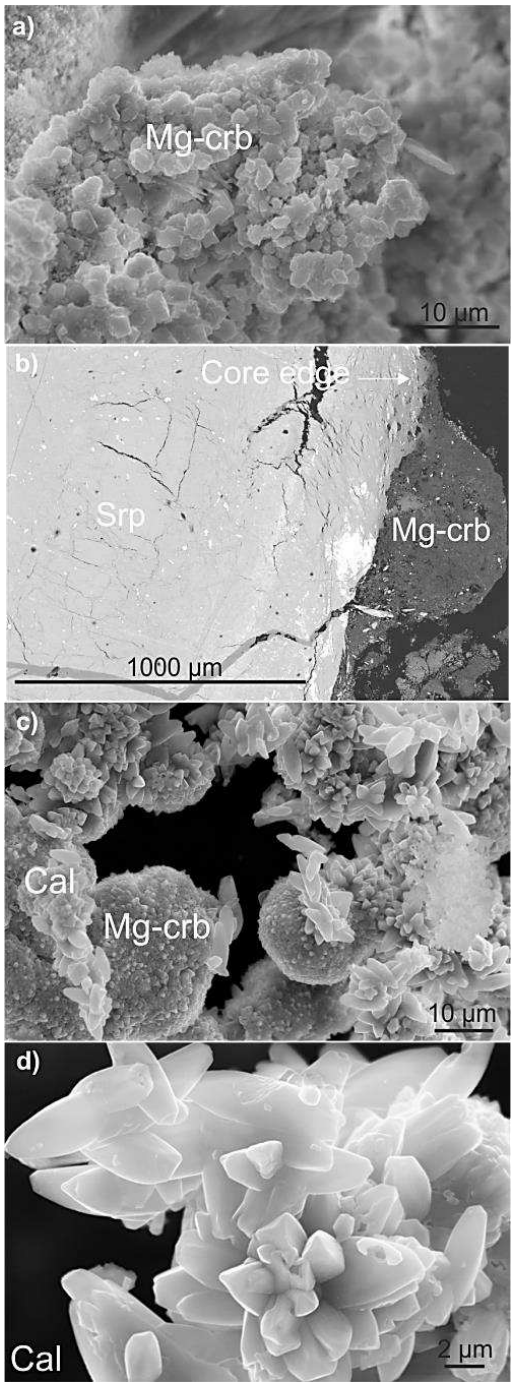


Figure 5.36 Morphology of the carbonate crust, as observed in serpentinite following reaction with wet $scCO_2$. The mineralisation was dominated by magnesite, ferroan magnesite and calcite.

Mineralisation in the fractures

Two distinctively different forms of Mg-carbonate within the fractures were identified: (i) well-developed, hemispherical aggregates and (ii) branching aggregates. The hemispheres were found on both sides of fracture walls, with sizes ranging from 10 - 50 µm, and locally clustered into groups of three or more. Optical microscopy revealed that most hemispheres exhibited radial internal texture (Figure 5.37). Figure 5.38c and the associated elemental distribution line profiles show that the nodules were chemically zoned, exhibiting an Fe-enriched core and an Fe-poor shell. The subtly darker band between the two zones was related, possibly, to discrete hydration or a localised increase in micro-porosity. Quantitative SEM-EDS analyses revealed 31 - 33 wt% MgO and ~ 3 wt% Fe-O in the Fe-rich zones, with the collective totals of these phases at ~ 36 wt%, being distinct from pure magnesite that contains ~ 48 wt% MgO and 52 wt% CO_2. The lower totals obtained in this study were probably related to analytical difficulties, *e.g.* mineral micro-porosity or the presence of water/hydroxyl groups.



Figure 5.37 Crossed polarised light image showing radial texture of Mg-carbonate hemispheres in serpentinite, following reaction with wet scCO_2.

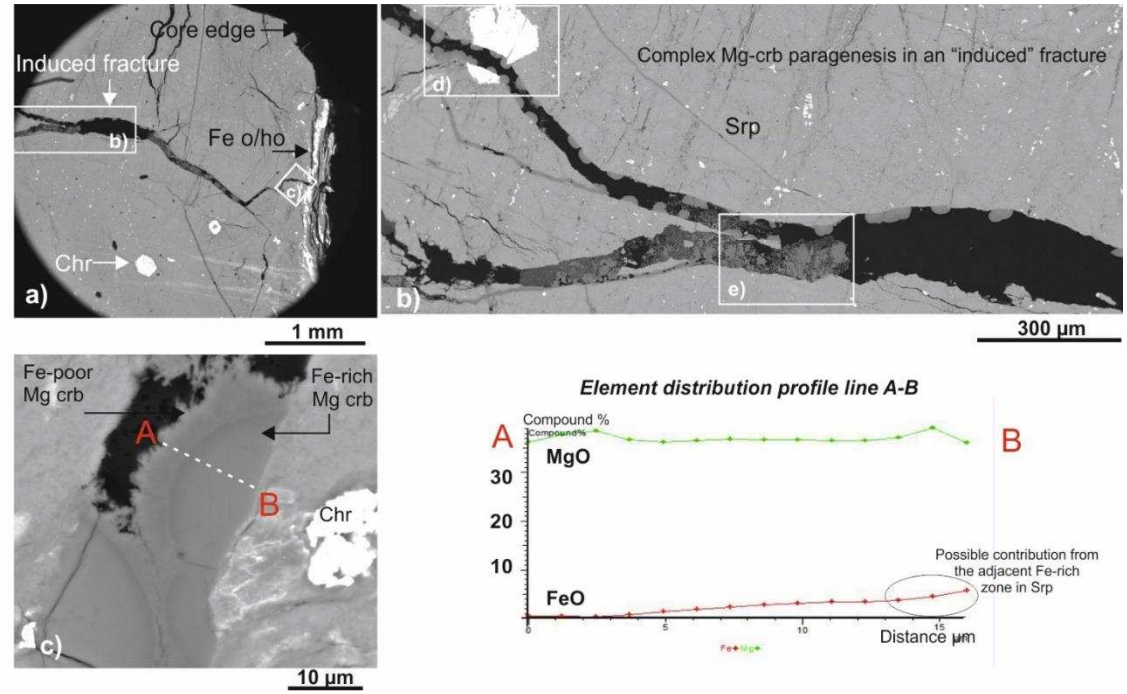


Figure 5.38A. BSE images illustrating complex mineralisation along in an induced fracture of serpentinite following reaction with wet scCO_2: a) low magnification image of a fragment of thin-section cut perpendicular to the length of the reacted core; b) distribution of hemi-spherical and branching Mg-carbonates in the fracture; c) textural and chemical details of the hemispheres

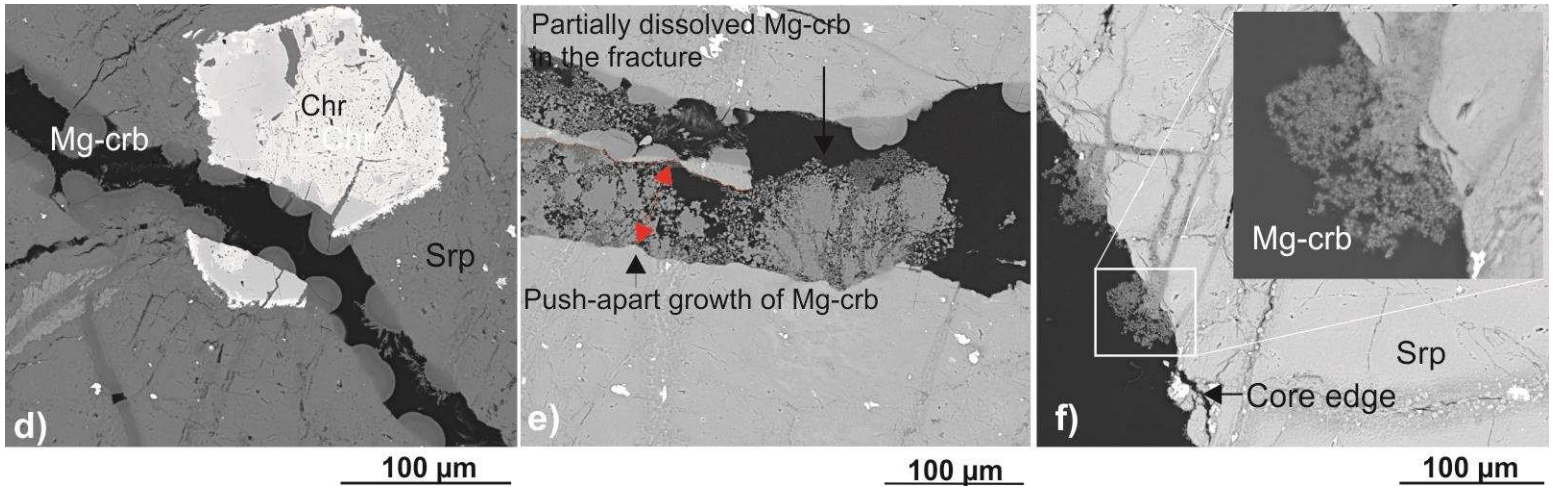


Figure 5.38B. BSE images illustrating complex mineralisation along in an induced fracture of serpentinite following reaction with wet scCO_2: d) fracture within chromite filled with hemispheres of Mg-carbonate; e) details of the texture and distribution of branching carbonates; and f) finely crystalline Mg-carbonate, as observed at the edge of the reacted core.

Carbonate fracture mineralisation (Figures 5.38b-d) was characterised by heavily corroded aggregates of fine < 1 μm domains. The aggregates displayed branching textures, particularly apparent along the deeply leached zones, along with euhedral terminations that coincided with fracture wall profiles. In several places, slivers of the original fracture surface were detached from the bulk rock with "branching" carbonate filling the spaces in-between. The textures observed pointed towards a strong crystallisation force and push-apart growth of the branching carbonate, and a detailed paragenetic sequence of carbonate growth and dissolution (Section 6.4.4).

Microanalysis of serpentinite core from the CO_2 – saturated brine

Figure 39 Post-experiment core covered by magnesite and core-cross section



The surface of the reacted serpentinite core was covered by a < 3 mm white crust of magnesite, ferroan magnesite and trace amounts of halite.

The magnesite exhibited a well-developed morphology of two dominant types: 1 – 2 µm rhombohedral and < 500 nm subhedral, equant crystals (Figures 5.40a,b). Detailed microanalysis revealed that the extent of carbonate mineralisation was largely limited to the outer surface of the reacted core and only trace amounts were found within the induced fractures. The mineral paragenesis of the induced fractures was complex and several dissolution-precipitation stages were identified. Whilst magnesite was observed on the core surface, inside the induced fractures secondary dolomite (Ca,Mg-carbonate) prevailed. It exhibited euhedral to subhedral morphology of 2-15 µm equant , rhombic to hexagonal crystals, locally corroded (Figure 5.40g), and in places covered by a < 3 µm layer of rhombic crystals of Mg-carbonate, similar to that observed on the outer surface of the core.

Some crystals of dolomite exhibited a partially dissolved core, forming intra-crystalline secondary porosity of rosette-like and dendritic morphology. This morphology provided evidence for the rapid initial crystallisation of a less stable phase and its subsequent preferential dissolution. No solid core relicts were found. The cations for the formation of secondary dolomite probably originated from partially dissolved original dolomite. Further, minor partial dissolution (mainly along zones directly adjacent to the induced fractures) of clinopyroxene (diopside - $CaMgSi_2O_6$) could have furnished the solution with Ca and Mg ions.

The diversity and extent of carbonate mineralisation, *i.e.* dolomite *versus* magnesite, suggest that the chemical micro-regimes within one core sample could have varied between the induced fracture and the outside of the core.

Source of Mg^{2+} for magnesite mineralisation

Although, some induced fracture walls were locally covered by < 3µm long, whisker–like crystals of unidentified siliceous phase (analytical limitation due to size), being a relic of incongruent dissolution of serpentine minerals from the bulk rock, the majority of Mg^{2+} (utilised in the subsequent crystallisation of magnesite) was extracted from the original serpentine-filled veins, cross-cutting the serpentinite rock core. Localised Mg-depletion from these veins is illustrated by Figure 5.40g and on the associated elemental distribution maps. The leaching of Mg resulted in siliceous residuum. It is clear that no elemental depletion was associated with the bulk rock serpentinite, suggesting that only a small percentage of the available rock was utilised in the mineral carbonation processes, with potential implications for the suitability of the host rock for CCSM.

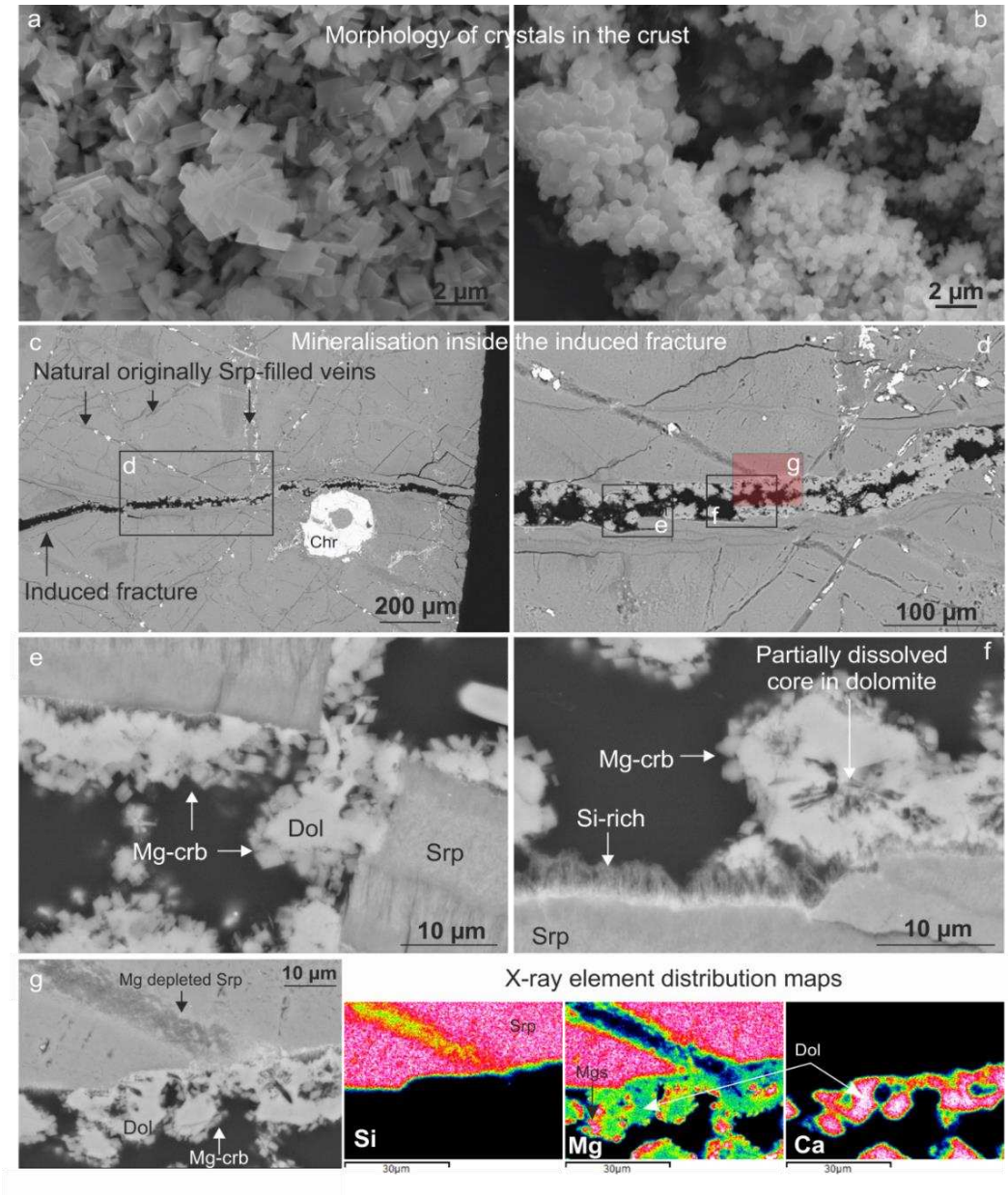


Figure 5.40 SE and BSE images of carbonate mineralisation associated with serpentinite following reaction with CO_2 saturated brine; showing a,b) fine euhedral crystals of magnesite crust; c-f) thin-section images illustrating secondary mineralisation within the induced fracture; and g) BSE image and associated elemental maps showing preferential Mg-leaching from the original serpentine-filled vein, resulting in the formation of siliceous residuum. The distribution of Mg and Ca in the carbonates correspond to dolomite ($CaMg(CO_3)_2$) overgrown by finely-crystalline magnesite ($MgCO_3$).

Microanalysis of serpentinite core from CO_2 –saturated brine

Figure 41 Post-experiment core covered by aragonite and core-cross section



Analysis of serpentinite that reacted with brine under N_2 pressurised conditions provided evidence for secondary carbonate mineralisation in a system without additional supply of CO_2. Two main types of precipitates were observed on the surface of the reacted core: acicular Sr-aragonite (orthorhombic $CaCO_3$) with chisel-like termination (Figures 5.42a-d); and rosettes of sub-rhombic platy crystals of either artrinite ($Mg_2(CO_3)(OH)_2 \cdot 3H_2O$) and/or pokrovskite ($Mg_2(CO_3)(OH)_2 \cdot 0.5H_2O$) (Figures 5.42e-f).

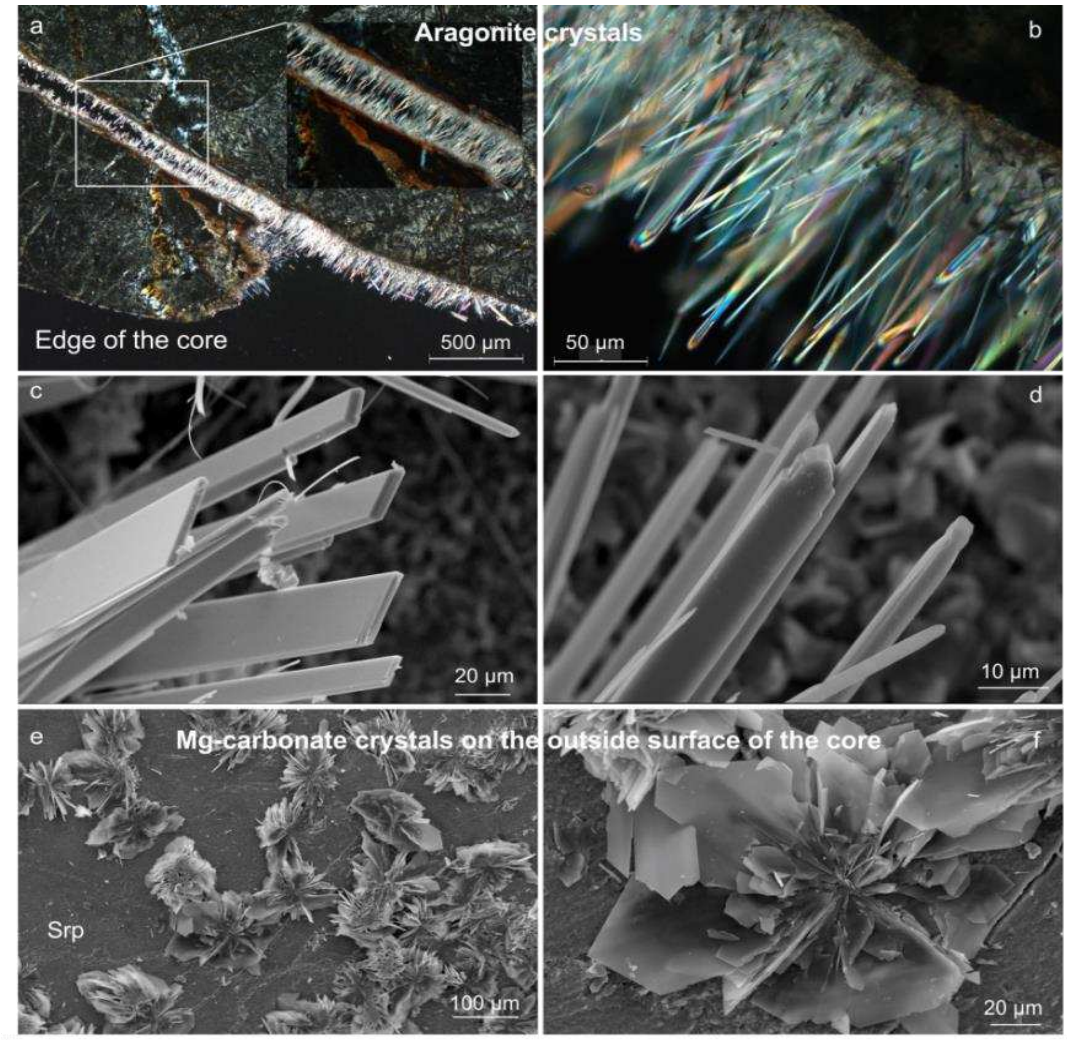


Figure 5.42 Authigenic carbonate mineralisation in serpentinite reacted with saline solution in an N_2 pressurised vessel: a) crossed polarised light OM image of aragonite on the outside surface of the serpentinite; b) acicular aragonite crystals; c,d) SE images showing the morphology of aragonite crystal; e,f) details of Mg-carbonate precipitated on the surface of the serpentinite core.

5.4. Discussion

This study was aimed at a comparison of the reactivities of ***dunite***, ***harzburgite*** and ***serpentinite*** under conditions relevant for *in situ* CCSM. The rocks' reactivity was evaluated, based on the results of eight months of fluid-rock interaction at 70°C and 100 bar, in CO_2-saturated saline solution and in wet supercritical CO_2, *i.e.* conditions approximating to the *in situ* injection of CO_2 in to ophiolite mantle rocks at *ca.* 1 km depth. A control set of experiments, using identical rocks under the same conditions, but pressurised with N_2 was also performed.

Under the broadly stated aim, several objectives were identified and the discussion below follows these objective themes.

5.4.1. The extent of rock transformation as a function of composition and texture

Three Mg-rich rock types were investigated in this study: ***dunite***, ***harzburgite*** and ***serpentinite***. All three rock types have previously been suggested as a reservoir for *in situ* CO_2 sequestration, because they offer appropriate chemistries and are present in large geological bodies.

Based on a comparison of the temporal evolution of fluid chemistry, rate of net Mg^{2+} release calculations and petrographic data for the rock samples from the CO_2-pressurised and N_2-pressurised vessels, it has been demonstrated that most of the reactions were promoted by the presence of CO_2, as expected. The extent and rate of reaction varied between the three rock types investigated and comparatively, decreased from:

serpentinite > dunite > harzburgite

This trend was consistent with serpentinite showing the highest reactivity in the accelerated acid-leaching study (Chapter 4).

Magnesium was the major element in all the rocks analysed and as illustrated by the Mg^{2+} concentration and rate of net Mg^{2+} release, the solution within the CO_2-pressurised serpentinite vessel showed the most pronounced response, categorised in to three stages:

(i) Comparatively fast rate ($1.29x10^{-08}$, being up to 2 orders of magnitude higher than for dunite and harzburgite) together with rapid initial increase in [Mg^{2+}] during the first 17 days of experiment; related to fast initial dissolution of Mg-bearing minerals, *i.e.* primary carbonate from veins and/or serpentine minerals with less stable structure, *e.g.* chrysotile or poorly crystalline lizardite. At this stage, the mineral dissolution greatly exceeded precipitation (it was difficult to establish whether precipitation did occur at this stage).

(ii) Subtle increase in [Mg^{2+}], probably related to slower dissolution of bulk rock serpentinite or indicative of conditions close to the dissolution/precipitation equilibrium (the rates of dissolution still exceeded precipitation).

(iii) Well-defined decrease in [Mg^{2+}] corresponding to rates of net Mg^{2+} release<0, from about the 60^{th} day of the experiment, during which time the precipitation of secondary phases exceeded rock dissolution. This stage was most probably related to the precipitation of Mg-carbonate, *i.e.* magnesite and ferroan magnesite.

In dunite, on the other hand, the [Mg^{2+}] in solution was initially ~ x3 lower than that of serpentinite, but was increasing continuously during the experiment. The continuous increase showed that at any time of the experiment the rate of dissolution exceeded the rate of precipitation, which nonetheless was seen to be minimal. The temporal evolution of [Mg^{2+}] in the harzburgite vessel was least prominent and after an initial steady increase, the [Mg^{2+}] fluctuated but never reached the values observed for dunite or serpentinite, suggesting overall slower reaction rates.

The reactivity of rock depended primarily on the spatial relationship of the minerals, their structures and compositions. This study showed that at 70°C and 100 bar CO_2 pressure, for a dual system of olivine-serpentine, as represented here by ***dunite*, olivine** (Fo_{87}) dissolved partially but **congruently** whilst the dissolution of serpentine was negligible. This was consistent with the observations made by Van Noort *et al.* [*van Noort et al.*, 2013], used Oman-UAE peridotite (partially serpentinised and containing 51% of olivine and 2-3% orthopyroxene), under experimental conditions of 150°C and 10 MPa CO_2, with the reported dissolution of olivine but not serpentine. This preferential dissolution may be related to the different crystal structures of the two minerals, with the presence of isolated Si-tetrahedra in olivine promoting faster dissolution than the polymerised Si-tetrahedra in serpentine. In addition, the reactivity of serpentine depended greatly on the type of mineral, with chrysotile reacting faster than lizardite in the same rock (Chapter 4, Section 4.3.3.6.).

The dissolution of olivine resulted in the development of secondary porosity that provided additional pathways for fluid ingress. These pathways may have been

interconnected and responsible for the progressive release of [Mg^{2+}] into solution, as suggested by the chemistries of the extracted leachates.

The petrographic evidence for congruent olivine dissolution was not consistent with the leachates chemistry that showed [Mg^{2+}] concentrations up to two orders of magnitude higher than that of [Si^{4+}] in all the experimental samples, pointing towards the incongruent dissolution of bulk-rock. It is accepted generally that preferential Mg-leaching is associated with the formation of a silica-rich layer, or the precipitation of secondary, silica-rich phases, and this could explain the discrepancies over the leachate chemistry. Further, the silica-rich layer, also considered to be a passivating layer, would act to limit the rate of dissolution of reactive sites, with overall negative feedback on the dissolution of mineral and rock [*Daval et al.*, 2011; *Johnson et al.*, 2014 and references therein]. Although, it is possible that a passivation layer formed in the initial stages of these experiment, as proposed by Johnson *et al.* [*Johnson et al.*, 2014], no evidence for such phases was observed in these eight-month reacted samples.

Consequently, to explain the discrepancies between the amount of Mg^{2+} and Si^{4+} in the leachates, it is suggested that minerals other than olivine may have furnished the solutions with Mg^{2+} and, although no clear evidence for such was provided by the petrographic study, it is considered that the serpentines may have dissolved incongruently. Alternatively, extensive precipitation of silica could explain the imbalance, but apart from a minor amount of secondary silica nodules, no further evidence for this was present. The fate of silica in this system requires further investigation.

It is noted that although the experimental study by Johnson *et al.* [*Johnson et al.*, 2014] was conducted under similar conditions as this study, the source materials used were different, *i.e.* isolated olivine grains *versus* olivine crystals embedded in a matrix of serpentinised dunite. As suggested by Van Noort [*van Noort et al.*, 2013] the microstructure of polymineralic peridotites (such as dunite used here) has a strong influence on the apparent dissolution rates, as compared to the dissolution of powdered single minerals phases (such as the olivine used by Johnson *et al., idem*.). In mineralogically heterogeneous and texturally complex rocks, the reactive fluids are never in direct and even contact with all the phases present, unlike with isolated homogenous mineral grains. This may result in the generation of reaction fronts with varied geochemical micro-regimes, *e.g.* localised pH differences and solution compositions, in turn leading to variable degrees of dissolution and precipitation, as observed in this study.

In the virtually monomineralic ***serpentinite sample***, the dissolution rates were much faster than in the partially serpentinised dunite. Interestingly, the major cation source in serpentinite was an array of serpentine-filled veins rather than the bulk rock serpentinite. Our related investigations (Chapter 4) demonstrated that many serpentine vein minerals were either chrysotile and/or widely spaced or poorly crystalline lizardite; and all, due to their crystal structures, were generally less stable. The preferential release of Mg^{2+} from the original serpentine veins was also consistent with the distribution of magnesite on the surface of the reacted core, mimicking the original patterns. It is likely that after the initial vein dissolution, with a continuous supply of fresh solution (unlike in our experiment), bulk rock serpentine minerals may start to dissolve, however, no clear evidence for this was found in this eight-month experimental study. The preferential leaching of Mg^{2+} from serpentine

veins resulted in a porous siliceous residue that provided pathways for fluid ingress into deeper parts of the sample and increased the overall dissolution of the sample. This positive feedback is of high importance to the real CCSM scenario.

Interestingly, ***harzburgite***, despite containing olivine and serpentine, in addition to the major component of pyroxene, showed the slowest rate of rock dissolution. The chemistry of the experimental leachates was in agreement with the observations of the reacted rock in hand-specimen and thin-section, with both suggesting a minimal transformation. It was observed that neither serpentine nor olivine reacted under the same conditions as used for dunite and serpentinite. It is noted, however, that the starting harzburgite rock contained lesser amounts of original veins that proved to be most reactive in the serpentinite sample. In terms of harzburgite mineralogy, the lower percentage of olivine and serpentine minerals were compensated by the presence of pyroxene (clino- and orthopyroxene collectively at ~ 23%), being generally less reactive [*Styles et al.*, 2014].

5.4.2. Secondary mineralisation

The eight-month interaction between CO_2-rich fluid and uncrushed rock samples (cores) resulted in the precipitation of:

- Fe-rich phases (probably goethite)
- Mg-carbonates (chiefly ferroan magnesite and magnesite)
- Minor Ca and Ca,Mg-carbonate (calcite and aragonite (N_2 vessel only), and dolomite, respectively)
- Silica, probably amorphous

On the cessation of the experiment, ***serpentinite*** showed the most amount of precipitate, manifested by a < 3 mm coating of a mixture of finely crystalline magnesite, ferroan magnesite and trace amounts of halite. Surprisingly, neither ***dunite*** nor ***harzburgite*** from the CO_2-saturated brine were covered by carbonate minerals on the outside surface of the reacted core. Instead, thin veneers (< 5 µm) of Fe-rich phases (goethite/hematite) were observed. After careful removal of the carbonate coating from the surface of the serpentinite core, it became apparent that a thin layer of Fe-rich minerals was present as well.

The results of both the geochemical modelling (PHREEQC) based on leachate chemistry and the microanalysis of solids have shown that the experimental conditions of 70°C and 100 bar CO_2 pressure favoured the crystallisation of magnesite, rather than any metastable form of Mg-carbonate, in agreement with previous studies [*Haenchen et al.*, 2008; *Langmuir*, 1965; *Prigiobbe and Mazzotti*, 2013]. In the light of industrial CCSM, magnesite is the desired form of Mg carbonate due to its long-term stability and highest Mg content per formula unit [*Swanson et al.*, 2014]. Hydrated minerals are less efficient in terms of the stoichiometric utilisation of Mg^{2+} *(idem.).*

Whereas the majority of magnesite in serpentinite was associated with the outside surface of the core; in dunite, a trace amount of magnesite was observed only on the induced fracture surface. A detailed analysis of olivine crystals in dunite revealed an *in situ* co-existence of magnesite and silica nodules (Figure 5.43), being the products of olivine and CO_2 reaction, and both grew in crystallographic alignment with the host olivine, in a similar fashion to that observed by *Olson et al.* [*Olsson et al.*, 2012]. This was consistent with the observations reported by Hovelman *et al.* [*Hovelmann et al.*, 2012] who reacted a peridotite for 7 days at 200°C and 16.2 - 17 MPa pCO_2, and by

Johnson *et al* [*Johnson et al.*, 2014] who used similar experimental conditions to those employed here (60°C and 100 bar CO_2) to investigate isolated olivine grains.

The *in situ,* crystallographically-determined, distribution of secondary (authigenic) phases in dunite suggests:

(i) Different behaviours for various olivine faces [*Olsson et al.*, 2012] with preferential dissolution along cleavage planes.

(ii) Negligible fluid movement and transport of dissolved species in the micro-environment around an olivine crystal, consistent with the simultaneous dissolution of olivine and the precipitation of silica and magnesite, in agreement with the observations made by Johnson *et al* [*Johnson et al.*, 2014].

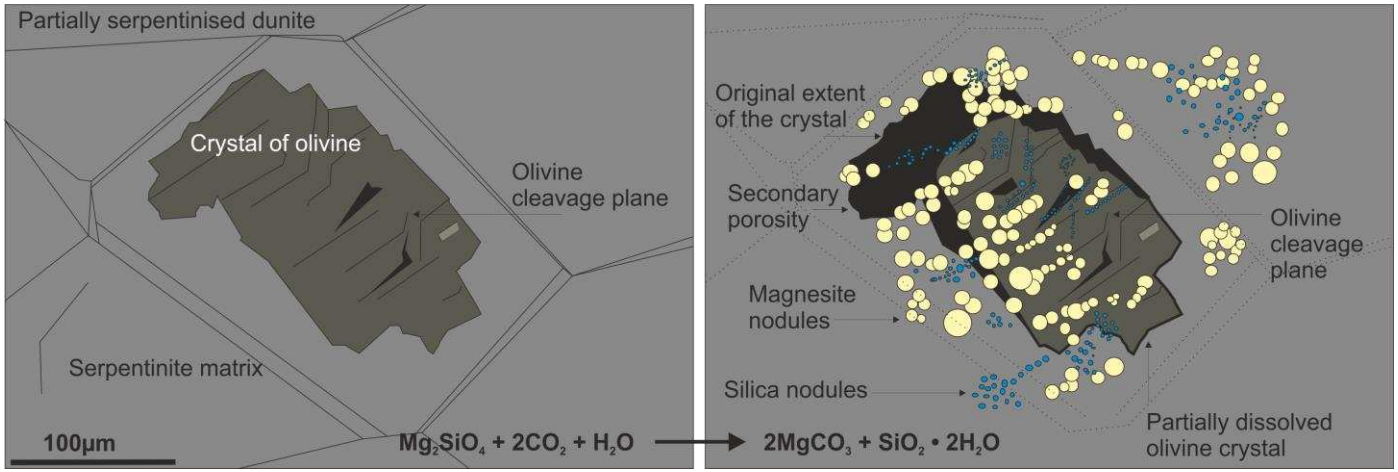


Figure 5.43 Schematic illustrating the effects of congruent dissolution of olivine in dunite. The olivine crystal dissolved stoichiometrically providing elemental substrates, i.e. Mg^{2+} and H_4SiO_4 for the subsequent in situ precipitation of magnesite (yellow) and silica nodules (blue). The dissolution of olivine also resulted in the development of secondary porosity (black zones).

Although, the extent of secondary mineralisation in dunite was negligible in comparison to serpentinite, the features observed were informative on the pathways and propagation of coupled dissolution-precipitation reactions. Petrological observations suggested that the only phases that reacted with the CO_2-rich brine, providing cations into solution, were olivine in dunite and serpentine minerals in serpentinite, both leading to the precipitation of Mg-carbonate.

A relative order of coupled dissolution - precipitation reactions, in general agreement with that proposed by Hovelmann *et al.* [*Hovelmann et al.*, 2012], is suggested here:

(i) *Dissociation of CO_2 in solution to carbonic acid, bicarbonate and carbonate ions, depending on the pH of the environment*

$CO_2 + H_2O \rightarrow H_2CO_3 \rightarrow H^+_{(aq)} + HCO_3^- \rightarrow H^+ + CO_3^{2-}$

(ii) *Dissolution of silicates*

Serpentine: $(Mg_{2.89}\,Fe_{0.1})\,Si_2O_5\,(OH)_4 + 6H^+ \rightarrow 2.89Mg^{2+} + 0.1Fe^{2+} + 2SiO_{2\,(s)} + 5H_2O$

Olivine: $(Mg_{1.82}\,Fe_{0.18})\,SiO_4 + 4H^+ \rightarrow 1.82Mg^{2+} + 0.18Fe^{2+} + H_4SiO_{4\,(aq)}$

(iii) *Precipitation of ferroan magnesite, related mainly to the top cores in $scCO_2$*

$(Mg^{2+}, Fe^{2+}) + HCO_3^- \rightarrow (Mg, Fe)CO_3 + H^+$

(iv) *a - Precipitation of magnesite*

$Mg^{2+} + HCO_3^- \rightarrow MgCO_3 + H^+$

b - Precipitation of silica (only evident from the dunite sample)

$H_4SiO_{4(aq)} \rightarrow SiO_2 \cdot 2H_2O$

The exact timing of each step is unclear, with no samples showing evidence for all these processes (*e.g.* although expected, no clear evidence for secondary silica was observed in serpentinite and hence further investigation is required). From the superposition of phases in the reacted cores, it is clear that $Fe^{3+}O(OH)$ formed first and more details on its origin are provided in Section 5.4.4.

Since no data on the changes of bicarbonate ions in solution was available, no constraints could be placed on the exact timing of carbonate precipitation. The results of net Mg release rate calculations revealed that from ~ 70^{th} day of the experiment the uptake of Mg^{2+} exceeded its release, and this was attributed to the precipitation of magnesite.

Further, the dissolution of ferromagnesian silicates, such as serpentine and olivine supplies ferrous iron in to the solution. In the presence of dissolved oxygen and/or dissolved CO_2, the Fe^{2+} oxidises to ferric iron and precipitates as goethite (± hematite). These phases were present as a thin veneer covering cores reacted with the CO_2-saturated brine. Since, no iron oxide oxyhydroxides phases were observed in the core from the cores reacted with the wet $scCO_2$ fluid that was flushed with CO_2 prior to experiment; it is likely that the oxidation in the bottom part of the vessel was largely due to the presence of dissolved oxygen.

5.4.3. Quantification of CO_2 captured in magnesite, formed in the serpentinite

The solution chemistry suggested that ~ 1.4 g magnesite formed during the experiment (5.3.1.4). The calculated weight of magnesite formed could be validated by estimation of a thickness of a layer of magnesite equal to 1.4 g, assuming an even spread over the surface area of the core. Accordingly, a layer of 250 µm was returned that appeared to be much thinner than the observed crust, *i.e.* 1-3 mm.

The discrepancy might be related to:

- The morphologies of the crystals in the crust, being a mixture of acicular, radiating, nodular forms making the crust highly porous, with consequent increase in apparent layer thickness. If evenly spread and compacted, the layer would have been significantly narrower and closer match the calculated layer thickness.
- Overestimation due to additional deposition of carbonate crust particles originating from the top core. Hence, it is suggested that future experiments should be performed in a more controlled way, with just one rock core per vessel.

It is noted that the amount of magnesite as observed at the surface of the serpentinite core appeared relatively high compared to the degree of original rock dissolution. It was evident that the bulk rock serpentinite did not undergo any major compositional or textural changes (CO_2 - saturated brine), and that most of the Mg^{2+} was extracted from narrow veins of serpentine minerals cutting through the rock. However, at the end of this experiment ~ 1/3 of the top core was missing, being displaced to the bottom of the vessel where it continued to dissolve partially in to

solution (fragments were observed at the end of the experiment), consequently increasing the [Mg^{2+}]. The timing of disaggregation was unknown, however, based on the amount of white crust formed on the detachment surfaces of the top core, it was clear that it occurred during the course of the experiment and hence contributed to chemical changes in the solution.

The weight of the top core before experimentation was 16.4 g, and a third of that weight equates to ~ 5.4 g of additional serpentinite source, being dissolved partially in to solution. Due to disaggregation, this serpentinite fragment would have proportionately a higher surface area, and consequently would be expected to react slightly faster.

Direct measurement showed that 0.7 g CO_2 was captured (calculated from the stoichiometry of 1.4 g magnesite), utilising a portion of serpentine minerals from the ~ 17.3 + 5.4 g = 22.7 g of resource serpentinite, in 70°C sea water pressurised with 100 bar CO_2. Even though it was evident that serpentine veins were the dominant reactive phases, their percentage contribution was difficult to estimate. Hence, if the entire rock weight of 22.7 g was used to calculate the rate of carbonation, then after conversion to amount of CO_2 sequestered per tonne serpentinite, a value of ~ 30.8 kg of CO_2 after ~ 6.5 months was returned, corresponding to ~ 3 % carbonation.

Petrographic analyses suggested that most of the magnesite formed on the outside core surface was closely associated with the original serpentine veins. It is difficult to predict whether bulk rock serpentinite would also become reactive and at what rate, or what the influence of continuous fluid flow through the reservoir would be. It is

unclear whether any carbonate recycling or fracture clogging, hindering further reactions, would occur. Hence, the appraisal of longer-term carbonation rates would require further experimental investigation.

5.4.3.1. Comparison with the extent of natural mineral carbonation.

The extent of laboratory carbonation was compared with two natural mineral carbonation scenarios, *i.e.* carbonation of chrysotile mine tailings at Clinton Creek, Canada [*Wilson et al.*, 2006] and carbonation of peridotite in Oman [*Kelemen et al.*, 2011] (Table 5.6). A linear reaction rate was assumed.

Table 5.6 Extent of accelerated, laboratory mineral carbonation as opposed to natural processes represented by Clinton Creek chrysotile mine tailings and peridotite in Oman, data expressed as x kg CO_2 captured per tonne of rock, over six months, assuming a linear rate.

Natural carbonation of chrysotile mine tailings [*Wilson et al.*, 2006]	Natural carbonation of Semail peridotite (Oman) [*Kelemen et al.*, 2011]	Experimental carbonation of Semail peridotite (UAE) This study
0.3	**0.0001**	**30**

**Due to scarcity of available data and assumptions on the linearity of reaction, the values should be treated as rough estimates only*

Although, the values in Table 5.6 *represent a rough estimate* of the extent of the reactions, the comparison shows that the accelerated, laboratory carbonation as pursued in this study, greatly exceeded the extent of natural carbonation. This is a general agreement with previous studies, reporting that the rate of weathering of silicate minerals in the field is 1 to 3 orders of magnitude slower than the same

minerals in laboratory experiments. This, in turn, may result from differences in reactivity between freshly-crushed and weathered minerals, errors in estimating the exposed surface areas of minerals in the field, and differences in solution composition [*Drever et al.*, 1994; *Swoboda-Colberg and Drever*, 1993].

Kelemen and Matter [*Kelemen et al.*, 2011] noted that accelerated carbonation, using conditions of 185°C and 150 bar CO_2 might result in a rate of ~ 1 million times higher than that of natural carbonation. Our data, not too surprisingly, fits in between the two extreme rate predictions suggested by Kelemen and Matter [*Kelemen et al.*, 2011].

5.4.4. The reactivity of CO_2-saturated brine *versus* wet supercritical CO_2

One of the scenarios for industrial CCSM, is to inject CO_2 as a compressed supercritical fluid [*McGrail et al.*, 2014], otherwise the injected gas would become supercritical (sc) at a depth of ~ 800 m where the temperature and pressure exceed the critical point for CO_2 of 31.1°C and 7.38 MPa (Figure 5.44). The $scCO_2$ exhibits low viscosity that makes it highly diffusive [*Kwak et al.*, 2011] and consequently highly reactive. Understanding the chemical interactions between $scCO_2$ and rocks is essential for evaluating the effectiveness and safety of CO_2 sequestration [*Kerisit et al.*, 2012]. Hence, conditions allowing the persistence of supercritical CO_2 were used in this study, enabling evaluation of its effect on host rock transformation.

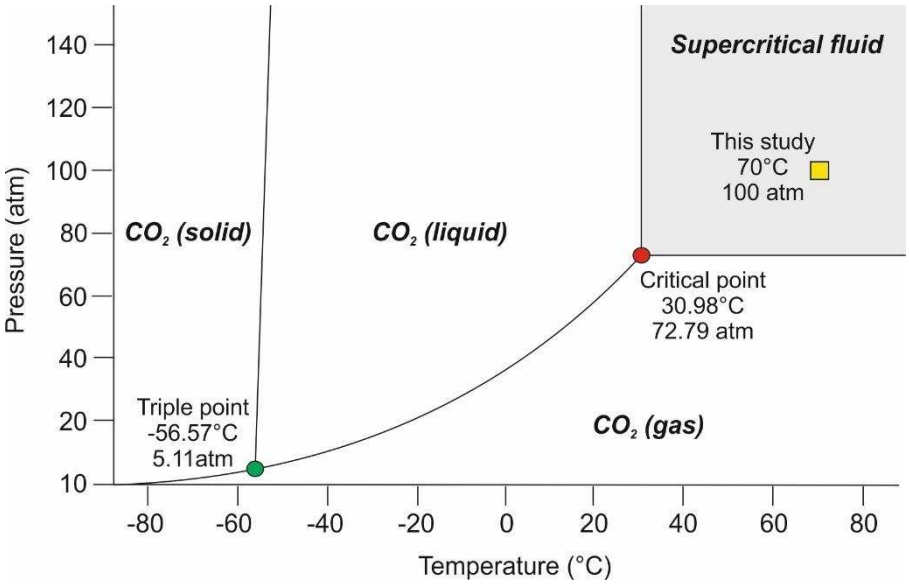


Figure 5.44 The phase diagram of CO_2 highlighting the supercritical state of CO_2 used in this study (yellow mark).

Observations of the reacted cores in hand-specimen and on a micro-scale suggested that the reactivities of the two CO_2-regimes, *i.e.* CO_2-saturated brine (bottom cores) and wet $scCO_2$ (top cores), were different. The top (headspace) cores of both dunite and harzburgite were covered by a thin, localised coating of Mg-carbonate; whereas the bottom cores that reacted with CO_2-saturated brine were coated with a thin veneer of Fe-oxyhydroxide (referred to as goethite for simplicity, hereafter). The reaction products associated with the equivalent cores of serpentinite were more complex, with goethite, magnesite and ferroan magnesite being observed on the surface of the bottom core, but only the carbonate minerals on the surface of the top core.

Two main differences attributable to the two CO_2 regimes are: (i) goethite mineralisation in all the rock samples in CO_2-saturated brine, but not in the wet $scCO_2$; and (ii) textural damage in serpentinite rock in $scCO_2$. Briefly:

5.4.2.1 CO_2-saturated brine and goethite mineralisation

Goethite was only present on the surface of cores that were immersed in the CO_2-saturated brine. It formed the very first layer of secondary precipitate, with the phase superposition being particularly well defined in serpentinite. The temporal evolution of [Fe^{total}] in the leachate solutions suggested a rapid initial release and subsequent rapid decrease within the first 33 days of the experiment. The absence of goethite on the surface of the top cores as well as in the cores from the N_2 control vessels suggest that its formation resulted from a combination of the presence of dissolved oxygen and dissolved CO_2 in the brine. The CO_2 dissociated into carbonic acid, causing a drop of pH which then enhanced the dissolution of minerals [*Gaus*, 2010]. The ferrous iron released into saline brine reacted with the dissolved oxygen and underwent rapid oxidation to ferric iron that dropped out of solution as goethite, a naturally insoluble mineral. Several mineral phases might have provided the ferrous iron, including original ferroan carbonate (pyroaurite), clay minerals or primary Fe-oxyhydroxide.

Interestingly, in the dunite sample that reacted with CO_2-saturated brine, the goethite and Mg-carbonate precipitates were mutually-exclusive. In the goethite-zone, apart from minor etch pits on the very edge of the sample, no other evidence for olivine dissolution was observed. This was consistent with observations reported elsewhere [*Olsson et al.*, 2012; *Wogelius and Walther*, 1992] and as suggested by Wogelius & Walther [*Wogelius and Walther*, 1992], the precipitation of secondary Fe^{3+}-bearing phases decreases the number of rapidly reacting surface sites, hence interfering with further dissolution. It appears that initial minor dissolution of olivine

at the very surface of the dunite core provided ferrous iron into solution that oxidised immediately to ferric iron, precipitated as goethite, which hindered further dissolution.

Accordingly, the initial precipitation of goethite on host rock requires further investigation as it may have a negative influence on the reactivity of rock as used for CCSM.

The reasons for the lack of goethite from the head-space cores and in the control (N_2) vessels are:

- ***Low level of oxygen in the head-space of the vessels.***

Prior to the experiment, the head-space was flushed with either CO_2 or N_2, thus limiting the amount of oxygen available for any reaction. The oxygen required to transform ferrous to ferric iron and thus to precipitate goethite in the head-space where $scCO_2$ prevailed probably originated from water molecules dissolved in the $scCO_2$. However, the apparatus used in the experiment did not allow for direct measurement of fluid composition in the head-space.

- ***Low rate of mineral dissolution in the N_2-pressurised vessel.*** This resulted in low concentration of Fe^{2+} in the solution and thus low degree of subsequent oxidation to Fe^{3+}.

5.4.2.2. Textural disintegration

Textural evidence suggested that reactions in the wet $scCO_2$ had an impact on sample integrity. The two serpentinite cores that reacted in the CO_2 vessel varied greatly in their resultant textures. While, the bottom core from CO_2-saturated brine retained its integrity, the top core had partially but significantly disintegrated, with

approximately a third of the original sample falling off during the experiment leaving detached fragments at the bottom of the vessel. The mechanisms for the chemical transformation of host rock minerals exposed to wet $scCO_2$ are still poorly understood [*Thompson et al.*, 2013]. The varied data from this study are intriguing but they may be explained generally by the low viscosity, high diffusivity and reactivity of the $scCO_2$ [*Felmy et al.*]. It is likely that the high diffusivity of wet $scCO_2$ allowed it to migrate along veins/fractures and grain boundaries, enhancing the overall dissolution and disaggregation of the rock. In addition, since the amount of oxygen dissolved in the wet $scCO_2$ fluid was low, no goethite, a potential reaction-inhibitor formed. The high reactivity of $scCO_2$ was accentuated by the presence of water, as it immediately caused local transformation of CO_2 into carbonic acid, promoting the localised dissolution of silicates.

5.4.3. Carbonate recycling and implications for long term system stability

Several lines of petrographic evidence indicated that the stability of carbonate minerals under the conditions investigated in this study (70°C, 100 bar CO_2) was disturbed temporally. This was manifested typically by the presence of corrosion patterns on both the original and secondary carbonates. For example, the precipitation of aragonite (calcium carbonate) on the surface of serpentinite that reacted with saline solution under N_2-pressurised conditions was facilitated probably by initial dissolution of carbonate minerals present in thin veins in the starting rock sample. Similarly, the presence of dolomite in the reacted serpentinite probably originated from the dissolution of original dolomite and subsequent re-precipitation. Further evidence was provided by a detailed petrographic study of induced-fracture mineralisation that showed dissolution of secondary magnesium carbonates in

original serpentinite that reacted with wet $scCO_2$. This is presented by means a conceptual model (Figure 5.46) of paragenetic evolution along a representative induced fracture where the following order of carbonate precipitation/dissolution was observed:

1. Before experiment: mechanical opening of non-mineralised induced fractures.
2. During experiment: radial growth of ferroan Mg-carbonate "*mc1*" on both walls of the induced fracture, with resultant hemispherical morphology. The cations, *i.e.* Fe^{T} and Mg^{2+} were probably extracted from the dissolution of primary ferromagnesian silicates and carbonates, for which pyroaurite seemed to be a likely source (Figure 5.46, plate 1-2).
3. Iso-textural overgrowth of ferroan Mg-carbonate nodules "*mc1*" with a non-ferroan Mg-carbonate "*mc2*" (Figure 5.46, plate 2-3).
4. Nucleation of a third generation of Mg-carbonate "*mc3*" and secondary fracturing. The fractures formed parallel to the originally induced fracture and it is likely that the force of crystallisation and growth of "*mc3*" caused re-activation and a subsequent "push-apart" mechanism, resulting in detachment of host-rock slivers, separated by "*mc3*". This mechanism may have potential implication for *in situ* reaction-driven cracking (Section 6.4.5.). The "*mc3*" carbonate was distinctively different from that of "*mc1"* and *"mc2*". The crystals were larger and displayed typical branching and locally dendritic morphologies. This mode of occurrence was consistent with rapid crystallisation.
5. Partial dissolution of *"mc3"* carbonate. The cause of dissolution remains unconstrained; however, it is clear that it affected *"mc3"* preferentially. This is consistent with the rapid growth and consequent poor crystallinity and poor stability of the carbonate.

The dissolution of primary (pyroaurite and dolomite) and secondary carbonates (*mc2* and *mc3*) in this eight-month experimental study showed that localised release and recycling of CO_2 is possible and should not be neglected when modelling a real CCSM scenario. More research should be devoted to the fate of CO_2 in the ultramafic carbon repository. Further, any natural rock system is compositionally and texturally complex and assumptions that the CO_2 will cause straightforward mineral dissolution and subsequent precipitation of magnesite may lead to a significant overestimate of overall CCSM efficiency.

The serpentine minerals were far from equilibrium with the experimental solution (based on PHREEQC modelling) and thus were the primary source of Mg^{2+} to form carbonates. The mechanisms driving the carbonate dissolution – re-precipitation is more difficult to elucidate. It is known that the only Mg-carbonate that was close to equilibrium was magnesite, however it is likely that the influence of reaction kinetics exceeded that of thermodynamics and some metastable carbonates formed episodically. These could have been subsequently transformed to magnesite. This is highly speculative and further research is required.

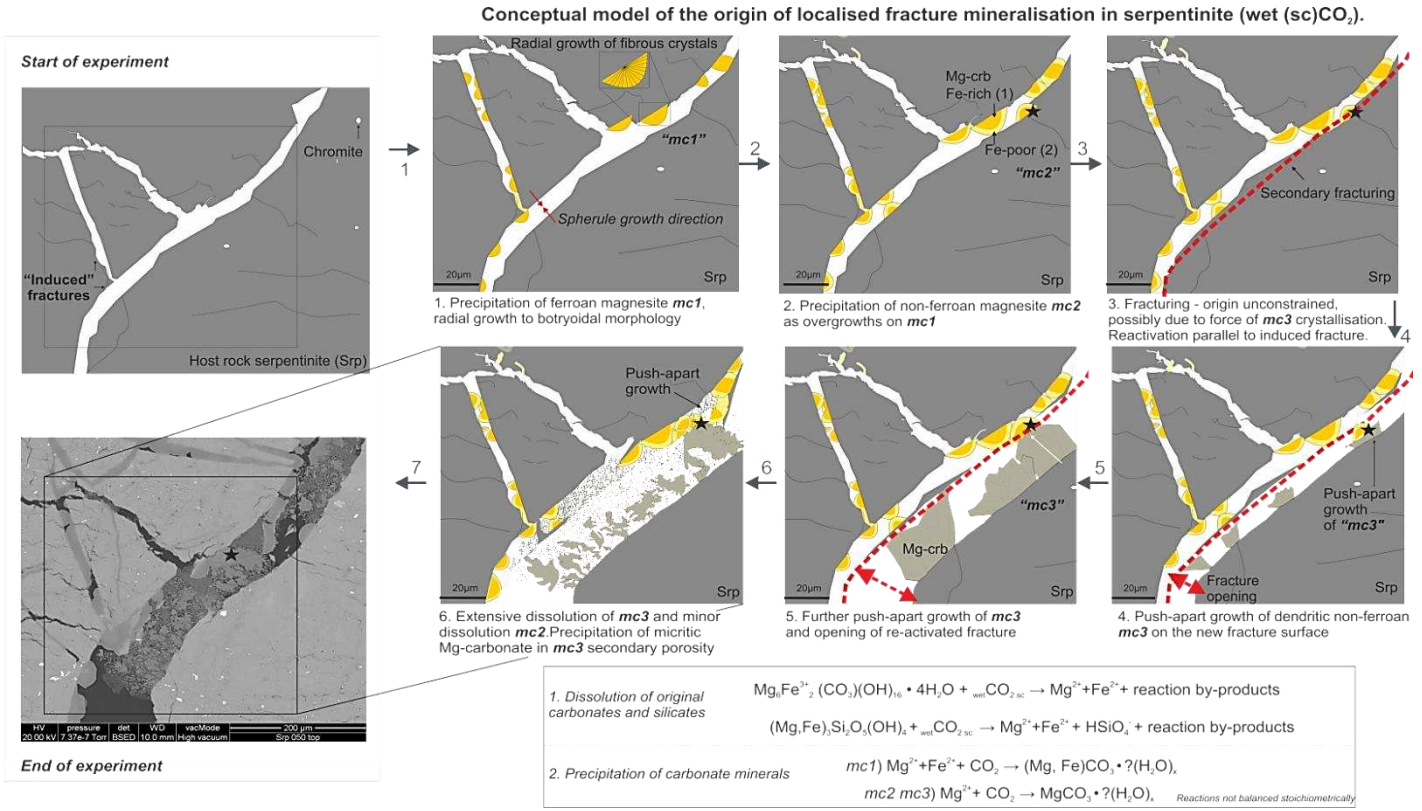


Figure 5.46 Conceptual model of an induced fracture mineralisation in serpentinite that reacted with wet supercritical CO_2. Detailed explanation of paragenetic stages is found under a corresponding plate. In summary, several stages of precipitation and dissolution of carbonate minerals have been observed; the force of crystallisation of carbonate "mc3" was sufficient to re-activate and "push-apart" previously generated fracture (mechanical fracturing prior to experiment) but not to initiate any new fracturing.

5.4.4. Reaction driven cracking

Several authors have reported on a mechanism for self-propagating fractures induced by force of crystallisation, commonly termed reaction driven cracking [*Evans*, 2004; *Plumper et al.*, 2012; *Royne et al.*, 2011]. Recently, Kelemen and Hirth [*Kelemen and Hirth*, 2012] suggested that where initial permeability is sufficient to assure continuous supply of aqueous fluids, positive feedback between reaction-driven cracking, fluid supply and reactive surface area will most likely result in nearly 100% carbonation at 185°C (accordingly, this temperature was suggested for *in situ* accelerated CCSM). Analysis of the reacted cores in this study suggested that the force of crystallisation of Mg-carbonate was sufficient to push apart and reactivate fractures in a pre-existing fracture zone but not to create new fractures (Figure 5.46).

5.5. Summary

This study focused on the reactivity of three proposed reservoir rocks, *i.e.* ***dunite***, ***harzburgite*** and ***serpentinite*** during an eight-month, closed-system, fluid-rock, interaction experiment, under conditions approximating the *in situ* injection of CO_2 into mantle peridotite, *i.e.* 70 °C and 100 bar CO_2, using saline solution.

The study showed that the reactivity of reservoir rock depended on a complex interplay between the rock's composition and texture, and the experimental conditions. The following paragraph summarises the main results significant to CCSM industry:

- Amongst the rocks tested here, serpentinite proved to be the most reactive, resulting in the fastest rates of net Mg^{2+} release and the greatest amount of secondary carbonate formed. Dunite showed low reactivity and harzburgite was virtually unreactive under the experimental conditions employed here; thus serpentinite is recommended as best resource rock for accelerated *in situ* CCSM.

- The increased reactivity of serpentinite was associated with the presence of serpentine mineral-filled veins and their preferential dissolution. This suggests that a reservoir with high density of originally mineralised fractures should be the focus of industrial geo-investigation. Dissolution of minerals from the fractures provides pathways for further fluid ingress, thereby enhancing overall CCSM efficiency.

- The extent of accelerated carbonation based on the analysis of serpentinite that reacted with CO_2-saturated brine was estimated to be ~ 3% per half year. This is 100 times greater than the rate of natural carbonation of Clinton Creek mine tailings in Canada [*Wilson et al.*, 2006] and about 200,000 times greater than the natural carbonation of peridotite in Oman [*Kelemen and Matter*, 2008]. Although the rate determined in this study may be associated with some levels of uncertainty in view of the caveats outlined in Section 6.3, it indicates the order of magnitude of carbonation under conditions approximating to the *in situ* injection of CO_2. It is also noted that the preferential reactivity of serpentine veins may have an important implication on the overall reactivity, thus longer-term experiments using a variety of serpentinites are suggested to appraise the reactivity of bulk rock, as it might be substantially lower.

- Attention should to be paid to the presence of ferrous iron, mainly originating from the dissolution of ferromagnesian minerals present in the host-rock. The ferrous iron, upon contact with oxidative solution, undergoes rapid transformation to ferric iron and precipitates as goethite. Goethite, in this study, was found to hinder further rock dissolution through a decrease of rapidly reacting surface sites [*Wogelius and Walther*, 1991]. It is recommended that a technological process is tailored to a specific natural CCSM repository and a method to mitigate the "goethite effect" should be evaluated.

- Wet $scCO_2$ proved to be highly reactive and apart from rock dissolution and carbonate precipitation, it also affected the integrity of the rock core, increasing the reactive surface area and promoting further geochemical transformations. In case of less reactive rock, *i.e.* dunite, wet $scCO_2$ rather than saline solution with dissolved CO_2 may mitigate the "goethite effect".

- The results of PHREEQC geochemical modelling were in general agreement with the outcomes of microanalysis of post-experimental solids. Accordingly, the experimental solutions were close to equilibrium with magnesite (subtle discrepancies were attributed to 5% analytical error) that has indeed formed in the solid residues. Both, nesquehonite and lansfordite were out of equilibrium, but it was clear that hydromagnesite was exhibited the furthest distance from equilibrium, being therefore an impossible secondary phase under the conditions utilised in this study.

  Further, this study has shown that serpentine minerals remained far from equilibrium in the course of the experiment, confirming their affinity to dissolution. Also, it was clear that at conditions far from equilibrium the rate of net Mg^{2+} release was independent of chemical affinity, confirming results reported by others (*Schott and Oelkers, 1995 and references therein*).

- Attention should be paid to the possibility of carbonate recycling, *i.e.* dissolution and re-precipitation. This study showed that a certain amount of carbonate recycling did take place. Dissolution of original carbonate will inevitably affect the geochemistry of solution. How this would affect the ultramafic reservoir is not known. However, the fate of injected CO_2 should be closely monitored. Thus, the commonly quoted statement that CCSM does not require long term monitoring may not be precise.

- It is recommended that any engineering planning and modelling should be site-specific; and the technological process should suit the natural repository. Assumptions on rock composition should not be made and a detailed

petrographical and geochemical study of any proposed CCSM repository should be undertaken as a part of site selection.

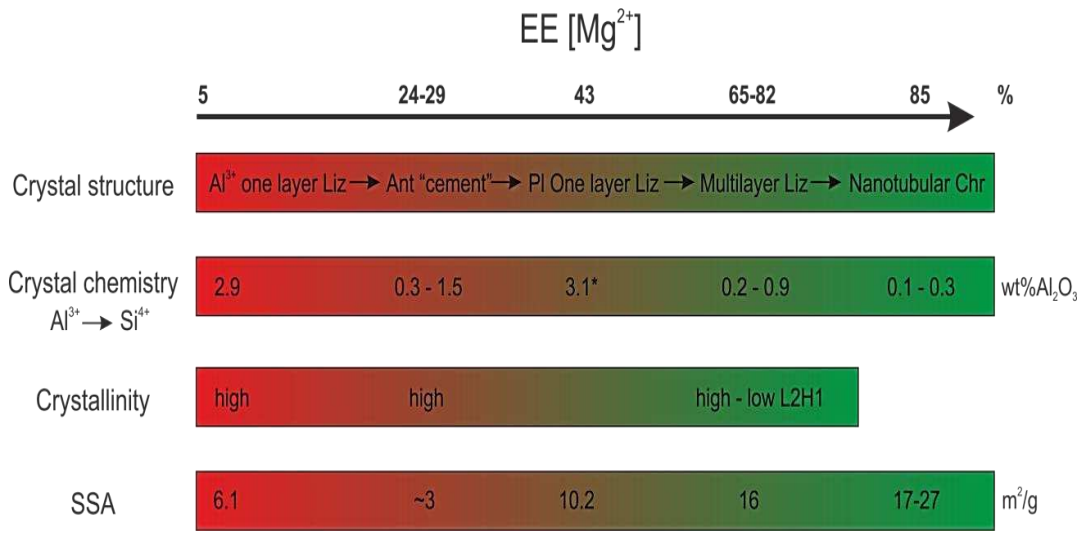
- The choice of the most suitable reservoir rock for *in situ* CCSM is essential and will significantly impact the efficiency of any proposed technology.

Chapter 6 Synthesis and conclusions

This study focused on several aspects of *ex situ* and *in situ* carbon capture and storage by mineralisation (CCSM) using serpentinites and ultramafic rocks, with the general aim of evaluating the influence of mineralogical and geochemical diversity on CCSM process efficiency. Accordingly, two sets of laboratory experiments were performed using natural rock samples and simulating *ex situ* and *in situ* processing conditions. Detailed petrographical and geochemical studies of the starting materials and reaction products provided a number of significant insights, summarised as follows.

In Chapter 3, the mineralogy and geochemistry of selected serpentinite minerals, *i.e.* resource material for *ex situ* CCSM, was investigated. The chemistries and structures of the minerals were analysed using a range of complementary techniques. The data showed that antigorite can be identified unequivocally using a combination of XRD, FTIR and/or TGA, owing to the mineral's distinctive wavy crystal structure. The polytypes of lizardite could only be identified successfully using X-ray or electron diffraction methods. Mixtures of chrysotile and lizardite proved to be most challenging, especially when finely inter-grown, however, it was noted that the use of FTIR and TGA aided mineral identification. Summarising, this study showed that a great care must be taken when analysing serpentine minerals. They are hydrous compounds with polymorphic and polytypic complexity. Further, they were found to be sensitive to high energy electron beams, and since they occurred usually as micron-scale intergrowths, this made quantitative analysis difficult.

In Chapter 4, the reactivities of serpentine minerals in acid at 70°C were evaluated, for structurally and compositionally different polymorphs and polytypes, with emphasis on the extraction efficiency (EE) of Mg^{2+}. The study showed that the reactivity of serpentine minerals in the CCSM system depends on a ***complex interplay*** between the crystal structure, crystallinity, chemistry, specific surface area and starting material texture (sample compositional homogeneity and spatial distribution of mineral components). Figure 6.1 presents a summary of serpentine mineral features that affected the efficiency of Mg^{2+} extraction and these should be considered when assessing feedstock material for *ex situ* CCSM. The colour scale from green (good) to red (bad) was used to categorise features in terms of their positive or negative influence on Mg^{2+} EE, respectively.



6.1 Overview of the relationships between extraction efficiency of Mg^{2+} and crystal structure, crystal chemistry, crystallinity and N2-BET specific surface area (SSA) for Liz – lizardite, Ant – antigorite, Chr – chrysotile and PL – polygonal serpentine.

For example, the Figure shows that low amounts of Al_2O_3, nanotubular structure and high SSA, as presented by chrysotile, are the most desirable features of feedstock material for acid extraction, providing 85% Mg^{2+} EE (after 180 minutes of acid leaching). It is noted that chrysotile rarely occurs in large amounts but the utilisation of chrysotile mine tailings may provide a viable method for small scale, localised *ex situ* CCSM, as recommended by Thom and Wilson [*Thom et al.*, 2013; *Wilson et al.*, 2006 and references therein]. Further, the use of chrysotile mine tailing in CCSM may reduce potential asbestos health hazards, but this aspect requires further investigation.

The reactivity of all remaining serpentine minerals tested in this study, described here in terms of Mg^{2+} EE, followed the order of:

Al-lizardite 1T (ca. 5%) < antigorite (24-29%) < polygonal serpentine 1M (ca. 43%) < < lizardite $2H_1$ well-crystalline (ca. 65%) < "felted"chrysotile (ca. 70%) < lizardite $2H_1$ poorly crystalline (ca. 80%) < nanotubular chrysotile (ca. 85%)

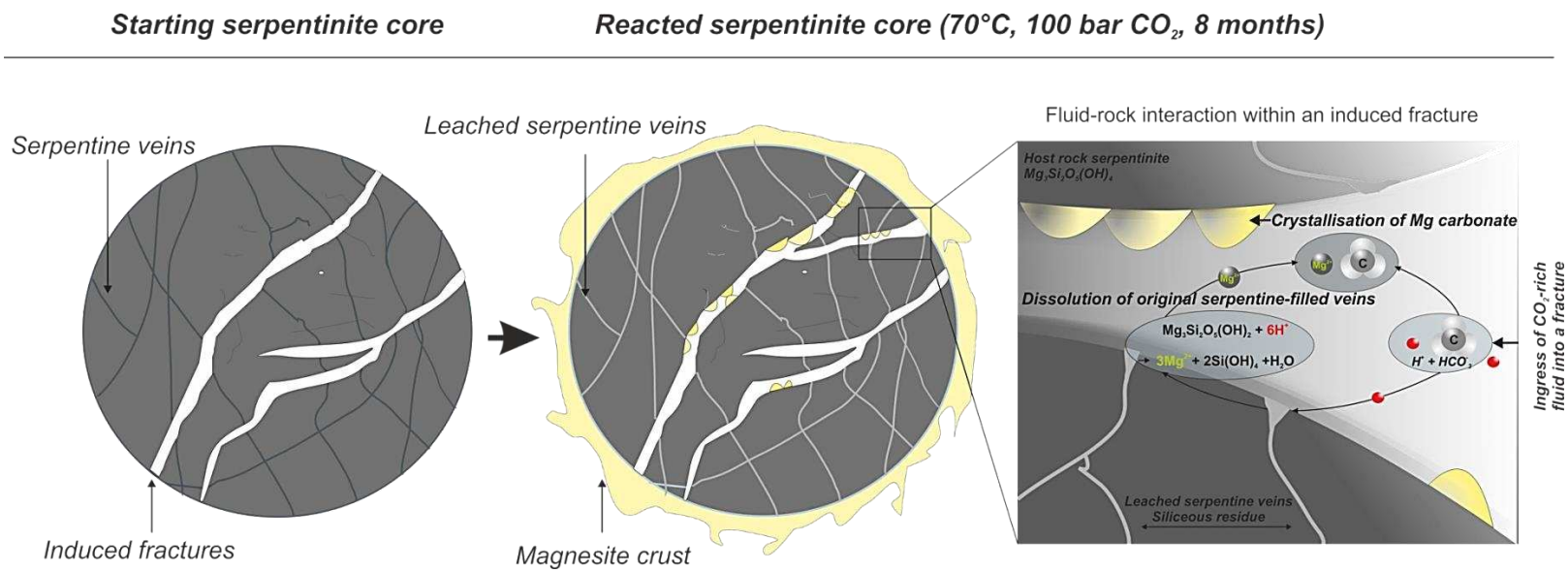
Although the selection of a single parameter most affecting reaction kinetics is not advisable for any system containing natural materials (rocks and minerals), it is noted that a mineral phase with a "disorder-rich" structure, such as nanotubular chrysotile or multilayer lizardite polytype, leading to greater intra-crystalline porosity, may provide the best resource material for CCSM. In particular, attention should be given to crystal chemistry and the selection of a phase with low amounts of aluminium may positively influence the overall kinetics of mineral dissolution.

This study has highlighted the importance of careful selection of suitable feedstock material for CCSM which if chosen correctly, should significantly reduce

the costs of an engineered CCSM process. In this context, it should be emphasized that serpentines are a structurally complex mineral group and unifying their functional properties for CCSM is inappropriate. Due to this complexity, it is essential that starting materials are analysed comprehensively, to appraise their potential for ion release, before undertaking process modelling and drawing conclusions about a minerals' potential reactivity for CCSM.

In Chapter 5, the reactivities of three proposed reservoir rocks, *i.e.* ***dunite***, ***harzburgite*** and ***serpentinite*** were investigated via eight-month, closed-system, fluid-rock interaction experiments, under conditions approximating the *in situ* injection of CO_2 into mantle peridotite. It was concluded that:

- The reactivity of serpentinite greatly exceeded that of dunite and harzburgite, and hence serpentinite is recommended as best resource rock for accelerated *in situ* CCSM. The choice of reservoir rock is critical and will significantly impact on the efficiency of any proposed technology
- The increased reactivity of serpentinite was associated with the presence of serpentine mineral-filled veins and their preferential dissolution (Figure 6.2). This suggests that a reservoir with a high density of original, serpentine-filled veins (perhaps sites where multiple serpentinisation events occurred) should be the focus of geo-investigation for CCSM. The dissolution of minerals from fractures provides pathways for further fluid ingress and overall enhanced efficiency of CCSM.
- It was noted that fracture clogging, inhibiting progressive fluid-rock interaction may occur in practice. Accordingly, further study on an open system (*i.e.* a flow-through experiment) should be performed to verify this.



6.2 Overview of Mg-carbonate mineralisation in serpentinite. The carbonate formed predominantly on the core surface and only small amounts formed within the induced fractures. Original serpentine-filled veins were the major source of cation (Mg^{2+}) and no evidence for significant dissolution of bulk rock serpentinite was observed.

- The rate of accelerated carbonation based on an analysis of magnesite crust formed on the serpentinite core surface (under CO_2-saturated brine) was estimated at ~ 3 % over the period of six months, this being ~ 100 times greater than rate of natural carbonation of Clinton Creek mine tailings in Canada [*Wilson et al.*, 2006] and about 200 000 greater than the natural carbonation of peridotite in Oman [*Kelemen and Matter*, 2008]. Although, the rate obtained in this study will be associated with some level of uncertainty, given the caveats presented in Section 5.3, it shows, nevertheless, the order of magnitude of carbonation under conditions approximating to the *in situ* injection of CO_2. It is noted also that preferential reactivity of serpentine veins over bulk serpentinite (Figure 6.2) may have important implications for overall reactivities, hence longer-term experiments using a variety of serpentinite rocks are required to appraise the reactivity of bulk rock, which might be significantly lower.
- In particular, the precipitation of goethite may hinder further dissolution of the rock and it is suggested that methods to mitigate the "goethite effect" should be investigated.
- Wet $scCO_2$ proved to be highly reactive and affected the integrity of the rock core. It is possible that the use of wet $scCO_2$ rather than CO_2-saturated brines may reduce the "goethite effect".
- Attention should be paid to the possibility of carbonate dissolution and recycling and this may impact on the overall efficiency of CCSM. The dissolution of carbonates may affect the geochemistry of local environments and although it is difficult to predict how this would affect the overall efficiency of CCSM, it is suggested that close monitoring of the post-injection fate of CO_2 is required.

Appendix A

Methodology

This study is based on two sets of fluid-rock interaction experiments performed under conditions relevant for CO_2 sequestration through mineral carbonation. The characterisation of samples before and after processing was accomplished using a combination of complementary analytical techniques, including: optical microscopy (OM), X-ray diffractometry (XRD), scanning electron microscopy (SEM), transmission electron microscopy (TEM), Fourier transform infrared spectroscopy (FTIR), X-ray fluorescence spectroscopy (XRF), thermogravimetric analysis (TGA) and inductively coupled plasma atomic emission spectroscopy (ICP-AES). Most of the analyses were performed at the British Geological Survey (BGS) laboratories, whilst TEM investigations were performed at the Faculty of Engineering, and the Nottingham Nanotechnology and Nanoscience Centre, University of Nottingham. A combination of the abovementioned analytical techniques allowed for accurate identification of serpentine minerals feedstock materials. This is prerequisite for analysis of reaction pathways. This Chapter presents details of the experimental process methodology and provides brief outline of the characterisation techniques used.

A.1. Experimental

Two fluid-rock interaction experiments were designed:

1. Extraction of Mg^{2+} ions from a range of serpentine minerals through accelerated acid-leaching. This experiment provided data on dissolution efficiency and was concerned with the first stages of chemical pre-treatment of resource rocks during *ex situ* CCSM.
2. Dissolution/carbonation of ultramafic rocks during eight months fluid-rock interaction, under P-T conditions of 100 bar and 70°C. This experiment provided data on reaction pathways and kinetics for conditions of ~ 1 km depth, relevant for *in situ* CO_2 injection.

A.1.1. Extraction of Mg^{2+} from serpentine minerals using 1.4 M ammonium bisulphate

This study was undertaken to determine the relationship between efficiency of cation removal (predominantly Mg^{2+}) and serpentine mineral crystal structure, being an important parameter in assessing the overall efficiency of *ex situ* CCSM.

To profile fully the structure-leaching inter-relationship, a mineralogically and structurally homogenous sample is required ideally. However, in natural materials, serpentine polymorphs and polytypes are intimately inter-grown and their separation is effectively impossible. Accordingly, natural serpentine vein mineralisation was appraised in this study, which provided source material with less mineralogical and structural complexity than compositionally heterogeneous host rock.

Details on sample origin and collection are presented in Chapter 3. The initial reduction from hand specimens to gravel sized particles was performed using a metal pestle and mortar. The particles were then analysed under binocular microscope to recover the purest possible sub-samples (Figure A.1). This involved the visual separation of discrete impurities such as carbonates, fragments of host rock (usually serpentinised peridotite) and chromite-magnetite grains. A hand magnet was used to

remove any magnetic minerals as well as any iron shards originating from the pestle and mortar.



Figure A.1. Lizardite sample before and after removal of host rock fragments

Approximately 70 g of sample was crushed using an agate ball-mill for approximately 5 min. The powders were then sieved to pass through a 250 µm mesh, being applicable for industrial processing with no further milling or sieving required. Special attention was given to the preparation of chrysotile asbestos-rich samples, and a protocol was produced specifically, based on BGS procedures for preparing hazardous asbestos-bearing samples, and followed at all times.

The procedure used for ion leaching was based on that of Wang and Maroto-Valer [*Sanna et al.*, 2013; *Wang and Maroto-Valer*, 2011], modified slightly to accommodate the constraints of the experimental apparatus.

1.4 M NH_4HSO_4 solution was prepared using Acros Organics extra pure ammonium hydrogen sulphate and ultrapure (Mili-Q) water (18.2 MΩ cm^{-1}). This provided an acidic solution, pH < 1. To appraise the time dependent structural and compositional modifications, leaching residues and leachates were collected at specific time intervals. Each serpentine powder sample was split into four 10 g sub-samples and poured into separate HDEP bottles filled with 200 ml of the acid pre-heated to 70°. The bottles were placed on a rotation mixer at 6 rpm (Figures A.2a, b). For each

sample set, the leaching experiments were stopped at 30, 60, 120 and 180 minute time points, whilst leachate and residuum were obtained.

Samples of leachate were extracted using a syringe with a 0.2 µm Nylon filter (Figure A.2c). The filtered leachate was split into sub-samples for:

- pH (filtered)
- ICP-AES (4ml, filtered and acidified with 0.04 ml HNO_3)
- Ion chromatography (filtered, not acidified)

After sufficient leachate was extracted, the remaining solution was filtered using a Buchner Funnel in a fume cupboard. The solid residue was then collected and split for further analyses. The residual fluid was disposed of in the fume cupboard sink and flushed with sufficient amount of water.

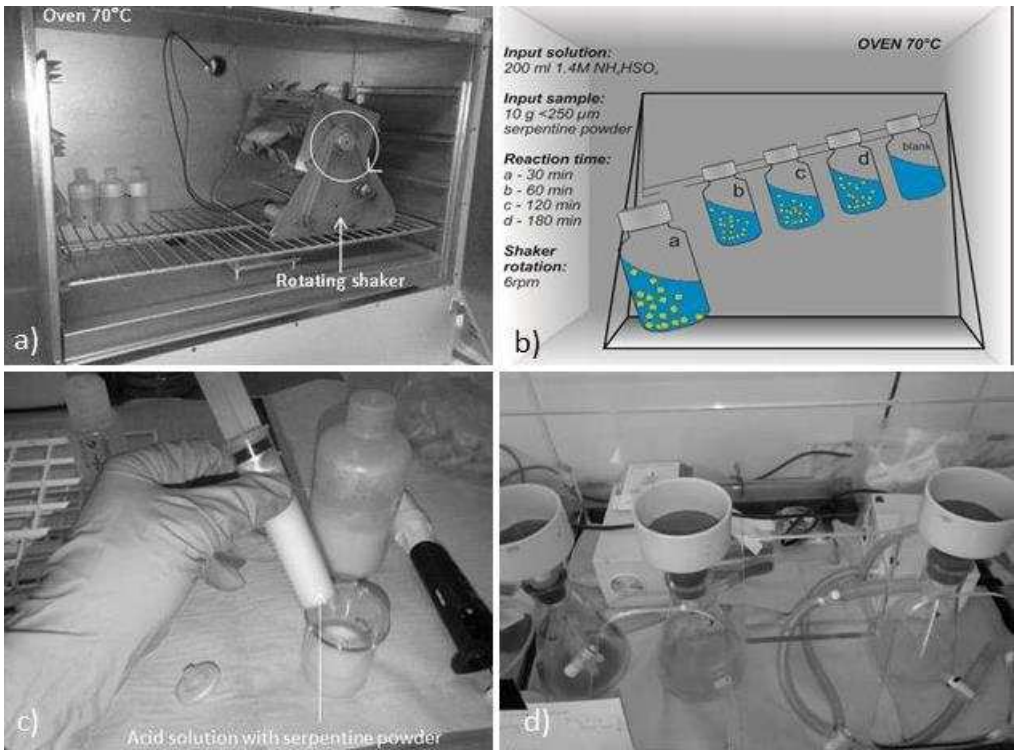


Figure A.2 Apparatus for short-term acid leaching experiments. (a, b) Bottles of powdered samples in acid on a rotating shaker in an oven heated to 70°C. (c) Extracted leachate filtered using a Nylon syringe (0.2 µm filter). (d) Solids filtered using a Buchner Funnel.

A.1.2. Dissolution and carbonation of ultramafic rocks under conditions relevant for *in situ* CO_2 injection

The reaction rates and pathways between CO_2-rich fluids and artificially fractured peridotite core-samples, maintained at constant temperature of 70°C and total CO_2 pressure of 100 bar, for 8 months, were investigated. The P-T conditions were consistent with experiments performed by Giammar *et al.* (2005), Johnson *et al. (*2014) and Van Noort *et al* (2013) and, as stated by the latter authors, approximate closely to *in situ* CCSM conditions. However, it should be noted that the temperature of 70°C is slightly higher than that anticipated with a typical geothermal gradient, being a compromise between that expected at the relevant injection conditions and the probability of reaction occurring within a time-constrained experiment. The selection of 70°C for these dissolution and carbonation experiments also allowed for data comparison with the acid leaching experiments.

In this context, the following questions were prioritised:

- What are the rates and pathways for dissolution and carbonation in the compositionally different host rocks of dunite, harzburgite and serpentinite?
- How do dissolution and carbonation reactions at fracture surfaces compare to reactions in bulk rock (serpentinised peridotite)?
- What are the differences in reactivity within CO_2-saturated brine and wet supercritical CO_2 systems?

A.1.2.1. Materials and solutions

To provide for a wide compositional and textural diversity of representative lithology at depth, dunite, harzburgite and serpentinite samples were utilised, all originating from the Semail Ophiolite, United Arab Emirates (UAE). These hand specimens were collected and provided by Dr Mike Styles. Each specimen was cut into four ~ 27 mm

long, ~ 17 mm diameter cores. In order to increase the reactive surface area, the cores were fractured using a compressive stress testing machine (maximum load between 3000-29000 N). The fractured cores were then wrapped in gold wire and mounted on sampling tubes for insertion into the pressure vessels (Figure A.3).

Six pressure vessels were utilised (Figure A.4), each containing two cores of each sample, one immersed in the aqueous phase (CO_2-saturated sea water) and one located above the solution table in the gas phase (wet supercritical CO_2). Two vessels were used per rock type (dunite, harzburgite or serpentinite): one pressurised with CO_2 and one with N_2 as a reference. The vessels were made from 316 stainless steel with wetted parts lined with polytetrafluoroethylene (PTFE); the gas inlet and sampling tubes were made of 316 stainless steel or polyetheretherketone (PEEK™) and the O-ring seals were made of Viton®. The reactors were connected to CO_2 and N_2 gas lines kept at a constant pressure of 100 bar. Each vessel contained a magnetic stirrer used every four hours for two minutes to agitate the solution.

Sea water with averaged composition, slightly modified from that given by Millero [*Millero*, 1996], was prepared and used in the current study (Table A.1). For simplification, only major cations and anions were incorporated. Most of the cations were provided by chlorides or sulphates. A trace amount of $BaCl_2$ was added as a tracer. Minor species, B and F were not included.

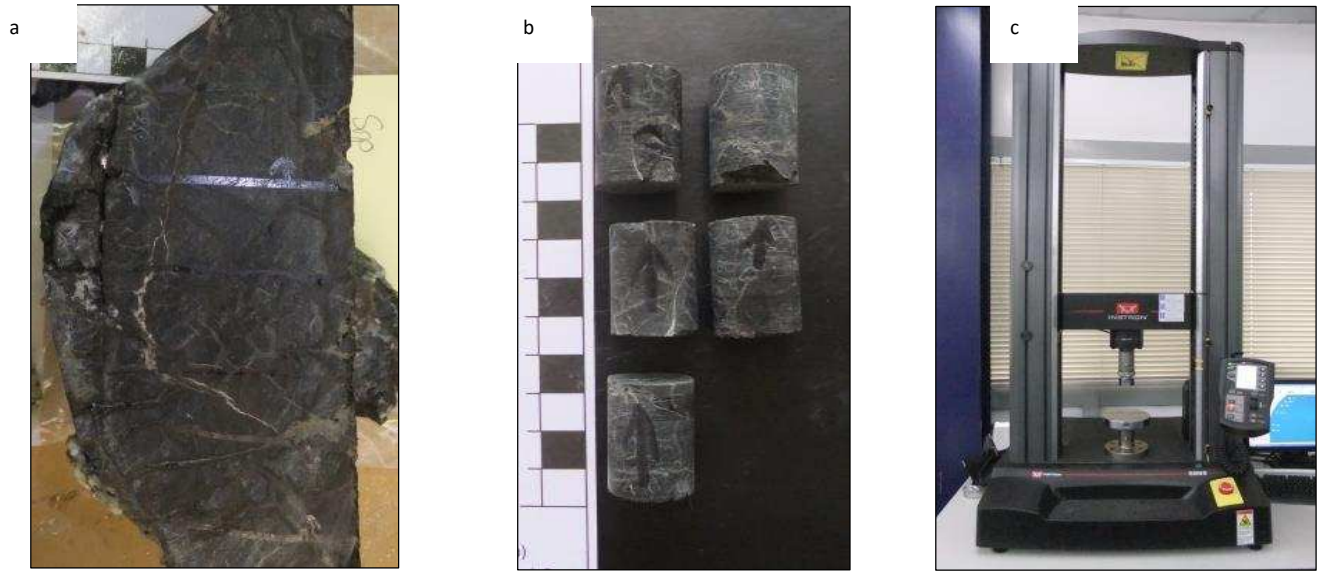


Figure A.3a Preparation of experimental cores: (a) hand specimen; (b) cores; (c, d) fracturing; (e) wrapping in gold wire; and (f) mounting on a sampling tube for insertion within the pressure vessel. The individual rectangles on the scale bars are 1 cm long.

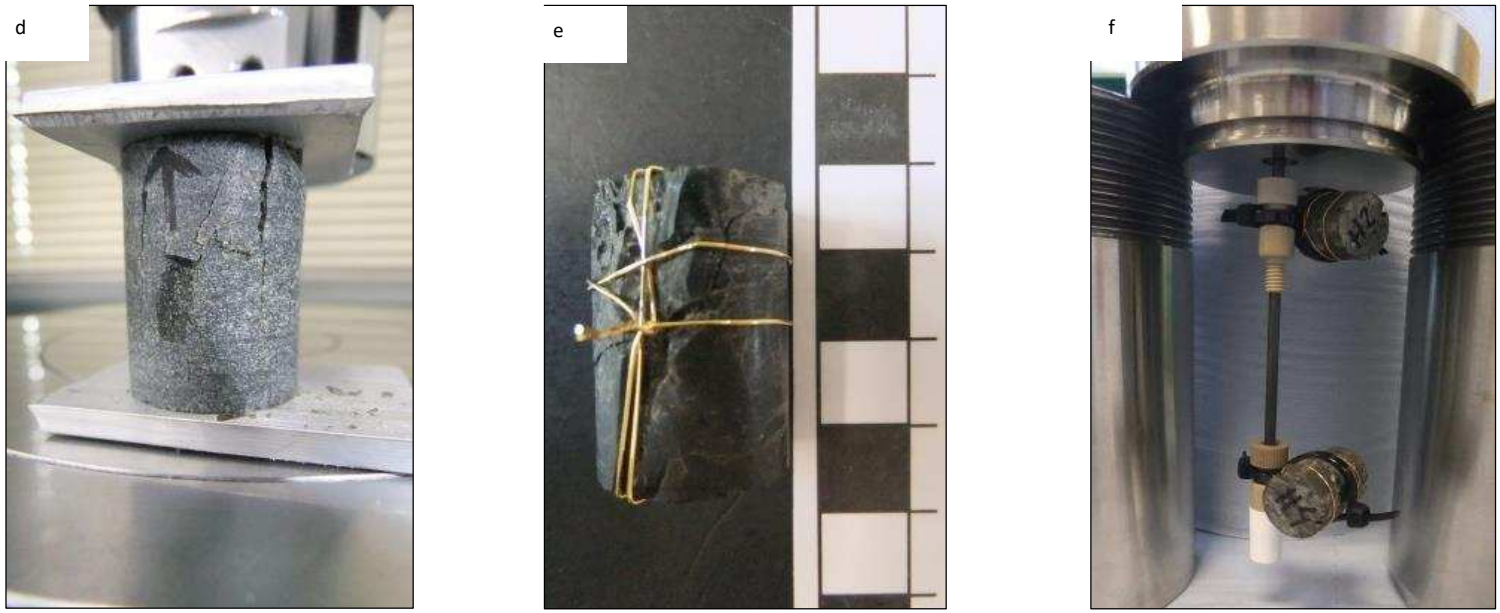


Figure A.3b Preparation of experimental cores: (d) fracturing; (e) wrapping in gold wire; and (f) mounting on a sampling tube for insertion within the pressure vessel. The individual rectangles on the scale bars are 1 cm long.

Table A.1 Composition of averaged seawater, modified from [Millero, 1996]

Ionic species	Compound used	Grade type	mol/kg solution [*Millero*, 1996]	g/mol	g of compound per litre of solution
Na^+	NaCl	ARISTAR	0.46907	58.43	**27.4**
Mg^{2+}	$MgCl_2.6H_2O$	AnalaR	0.04570	203.2	**9.28**
	$MgSO_4.7H_2O$	AnalaR	0.00714	246.36	**1.76**
Ca^{2+}	$CaCl_2.2H_2O$	AnalaR	0.01028	146.978	**1.51**
K^+	KCl	ARISTAR	0.01021	74.54	**0.76**
Sr^{2+}	$SrCl_2.6H_2O$	AnalaR	0.00009	266.52	**0.02**
Ba^{2+}	$BaCl_2$	AnalaR	0.00009	208.22	**0.02**

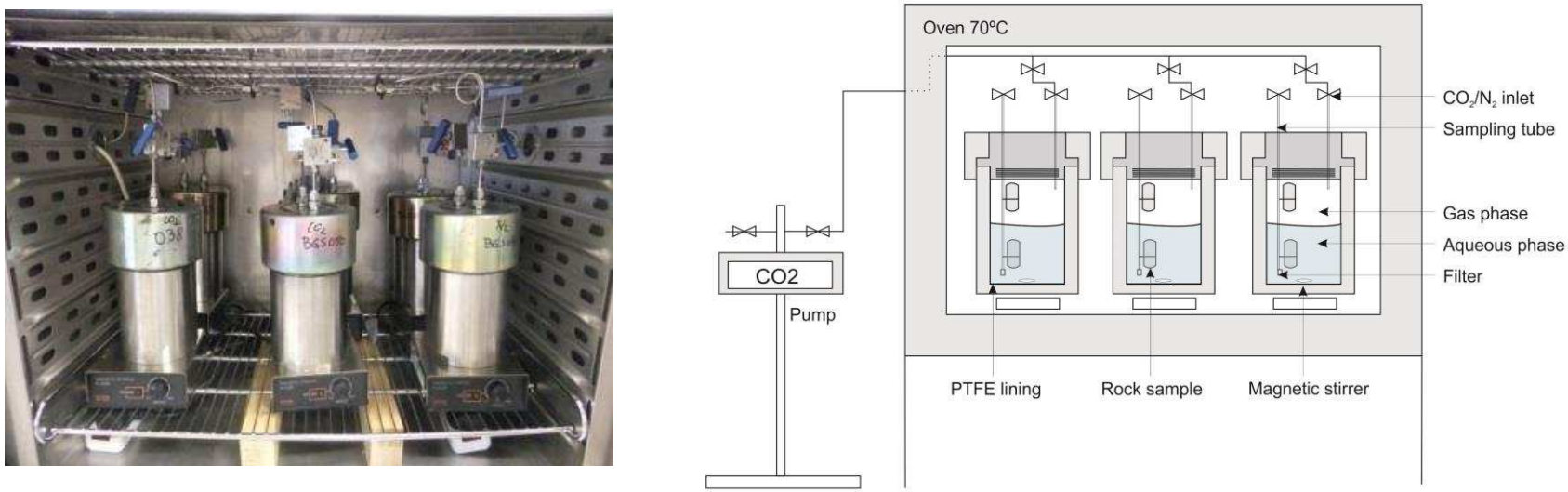


Figure A.4 Long-term CCSM experimental arrangement, a) oven with six pressurised vessels and b) corresponding schematic delineating the interior of the vessels.

Each vessel was filled with 200 ml of saline solution. The vessels, containing both solution and cores, were then placed in the oven and left overnight initially at 30°C and ambient pressure. The temperature and pressure (5 bar at a time) and were then adjusted slowly to establish the experimental conditions of 70°C (±5°C) and 100 (±5bar) bar over the course of 24 h. The incremental increase of P-T conditions is a standard procedure, as followed in the BGS hydrothermal laboratory, and provides for: (i) experimental equipment to adjust slowly to the applied conditions, *e.g.* vessel and O-ring thermal expansion; and (ii) an opportunity to monitor for any fluid leaks as pressure is established.

Each solution was sampled 11 times (including the final solution). Generally 10 ml was extracted during the first seven sampling episodes, with just 5 ml taken for the subsequent three samples, due to the decreasing amount of residual fluid (Table A.2). It should be noted that Vessel 038 (Harzburgite pressurised with CO_2) was dismantled after six weeks following a major fluid leak. The solution was replaced with 165 ml of new synthetic sea water, equivalent to the amount expected in the other vessels at that time.

Table A.2 Summary of sampling dates and the amount of solution extracted.

			Sampling date and volume (ml) of solution extracted										
Vessel	Run	**Gas**	***26.07. 2013***	***12.08. 2013***	***27.08. 2013***	***12.09. 2013***	***26.09. 2013***	***24.10. 2013***	***28.11. 2013***	***09.01. 2014***	***13.02. 2014***	***26.02. 2014***	***27.03. 2014***
032 D	1595	N_2	10	10	10	10	10	10	10	NS	NS	NS	NS
033 D	1596	**CO_2**	10	10	10	10	10	10	10	5	5	5	5
037 H	1597	N_2	10	10	10	10	10	10	10	5	5	5	5
038 H	1598	**CO_2**	10	10	10	*	10	10	10	5	5	5	5
044 S	1599	N_2	10	10	10	10	10	10	10	5	5	5	5
050 S	1600	**CO_2**	10	10	10	10	10	8	10	5	5	5	5

*Fluid replaced due to a major leak. 165 ml of new sea water solution was added to the vessel. D – dunite, H – harzburgite, S – serpentinite, NS - no sample.

Each fluid sample was passed through a 0.2 µm nylon syringe filter and split into sub-samples for analysis of chemical composition (ICP-AES and IC) and pH. All the sub-samples were the kept in the fridge (< 5°C) until sampling was complete.

Solids were collected only at the end of the experiments. The solids were slit into sub-samples for XRF, XRD and FTIR investigation; while for SEM and OM, polished thin section were prepared. Fragments of reference material were retained in a desiccator. For cases where a significant amount of carbonate had formed on the core surface, a portion was scraped off gently for analysis.

A.2. Material characterisation techniques

This section provides a brief description of the analytical techniques used to appraise sample mineralogy / structure and chemistry.

A.2.1. Optical Microscopy

Optical microscopy (OM) was used to identify the starting minerals and appraise the processed reaction products.

OM of the minerals and rocks was performed using a petrographic (polarising) microscope. The microscope contained two polarisers both located in the light pathway, one below the specimen (the lower polariser) and the other above the specimen (the analyser). Light that leaves the lower polariser is plane-polarised in the transverse direction. The light enters the mineral being examined, and depending on the crystallographic nature of the mineral, propagates in all directions with the same or different velocities, corresponding to isotropic or anisotropic minerals, respectively. In anisotropic minerals, the beam splits into two rays: termed ordinary and extraordinary. This phenomenon of birefringence or double refraction allows

interference colours to be determined that along with mineral colour, relief and pleochroism, is used as part of the process of mineral identification.

OM investigations were performed using a Zeiss Axioplan 2 polarising microscope with a high-resolution digital camera and Zeiss AxioVision software for image capture and processing. Samples were in the form of polished thin sections (~ 30 µm) cut from rock fragment, or powdered aggregate.

A.2.2. Powder X-ray Diffractometry

Powder X-ray diffractometry (XRD) enabled qualitative and quantitative appraisal of the mineral structures (phases).

Crystalline materials exhibit regular periodic arrangements of atoms in space. When an X-ray beam interacts with a crystalline material, it is scattered by atomic electron clouds. At specific angles, the scattered X-rays reinforce in phase and interfere constructively, giving rise to peaks of diffracted intensity. This is geometrically described by Bragg's Law and visualised conceptually in Figure A.5, where d is the interplanar spacing. The diffraction data is plotted usually as diffracted peak intensity vs angle 2θ, and the peak positions, intensities and profiles, provide information for structure identification.

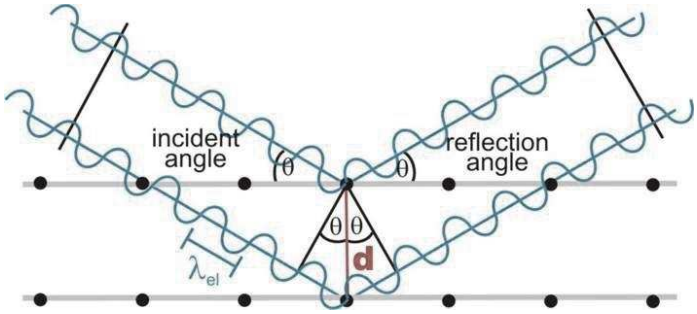


Figure A.5 Schematic illustrating the constructive interference of scattered waves (http;//www.microscopy.ethz.ch/bragg.htm).

XRD analysis was performed using a PANalytical X'Pert Pro series diffractometer equipped with an X'Celerator detector, cobalt-target tube and generator operated at 45 kV and 40 mA. The samples were supported/prepared in different ways, depending on the availability of material:

(1) ***Back-loading with quartz standard***. 4.5 g of micronized (ground to fine powder) sample + 0.5 g of quartz standard + acetone were micronized for ~ 2 minutes and then spray-dried (excluding chrysotile samples). This method was used for starting serpentine minerals for quantitative analysis.

(2) ***Back-loading without quartz standard*** - used for all processed samples. The quartz standard was omitted due to possible interference with newly formed phases.

(3) ***Silicon wafer*** - used for sample support when the availability of material was limited.

Diffraction data was analysed using PANalytical X'Pert Highscore Plus version 2.2a software, coupled to the latest version of the International Centre for Diffraction Data (ICDD) database, PDF4+. During quantitative analysis, the mineral structure was refined through Rietveld refinement using PANalytical X'Pert Highscore Plus that is designed to refine lattice cell constants, atomic positions and occupancies of the experimental pattern to allow for best fit with a calculated structure or one obtained from pure powder or single crystal X-ray diffraction.

A.2.3. Scanning Electron Microscopy

Scanning electron microscopy (SEM) was used primarily to appraise morphological, chemical and textural changes in processed materials. In addition, energy dispersive X-ray spectrometry (EDS) was used for quantitative chemical analysis.

SEM derives information from the interaction of a high energy electron beam with a sample. This interaction yields a number of secondary signals that are used to appraise sample morphology, structure and chemistry. Figure A.6 and Figure A.7 provide information on the signals produced and their information content. In practice, the main signals utilised in SEM are secondary electrons (SE), backscattered electrons (BSE) and characteristic X-rays.

Analyses were performed using a LEO 435VP variable pressure SEM and an FEI Quanta 600 environmental SEM (ESEM). Samples were analysed in the form of polished thin sections, rough surface rock chips or powders. Carbon coating (~ 25 nm) of samples was performed using an EMITECH 960L evaporation-coating unit.

Quantitative chemical analysis of the mineral phases was performed using EDS, following ASTM Standard [*(ASTM)*] recommendations (pers. comm. Dr M Styles (BGS) and Dr J Rushton (BGS)) and the procedures described by J Rushton in [*Walters et al.*, 2013]. The SEM was operated under conditions of high vacuum (< 1.2 x 10^{-4} torr) at 20 kV accelerating voltage, with 10 mm (FEI SEM) and 19 mm (LEO SEM) optimal analytical working distances, and an X-ray detector take-off angle of 45°. For EDS analysis, conditions of 1 nA beam current and 60 s acquisition times (spot mode) were used with the LEO SEM. For the FEI Quanta 600 SEM, the beam current was controlled by spot size (proportional to $\log_2$(probe current)), on a scale of 1-10, with values between 5.5 and 7 equating to beam currents of 2.45 nA and 2.8 nA, respectively, with 30 s acquisition times giving ~1 x 10^6 total counts. These experimental conditions of beam current, acquisition time and spot mode (rather than raster mode) provided optimal conditions for the analysis of major elements under conditions that prevented significant mineral de-hydroxylation under the focused electron beam.

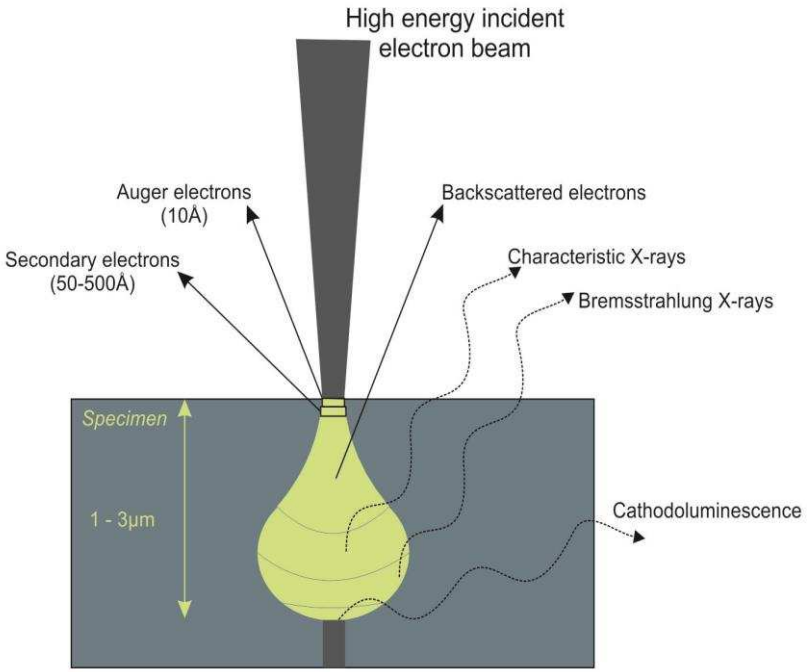


Figure A.6 Secondary signals emitted from a bulk sample upon interaction with high energy electron beam.

Signal	Event	Between	Primary information obtained
Backscattered electrons	Elastic scattering	Beam electrons and specimen nuclei or electrons	**Atomic number contrast**
Secondary electrons	Inelastic scattering	Beam or backscattered electrons and specimen electrons	**Surface morphology**
Continuum X-rays	*Inelastic scattering*	*Beam or backscattered electrons and specimen nuclei*	*N/A*
Cathodoluminescence	Secondary processes following primary process of photoionisation		*Band-gap*
Characteristic X-rays			**Elemental composition**
Auger electrons			*Surface composition*
Transmitted electrons	*Transmission*	*Beam electrons and specimen nuclei or electrons*	*Imaging / projected structure*

Figure A.7 Signals derived from the interaction between a high energy electron beam and matter (modified from Bordeaux [Bordeaux, 2011]).

Data was processed using Oxford Instruments INCA software that applied "phi-rho-z" matrix correction methods [*Pouchou et al.*, 1990]. Calibration of the X-ray analysis system was performed annually using a set of mineral standards: Mg – forsterite L134; Fe – fayalite (std #136); Si – wollastonite (std #9); Al – alumina (std #66); and Na – jadeite (std #8), and the calibration file produced was used to quantify the composition of unknown materials. Microscope performance on the day of analysis was checked using in-house secondary standards of known composition: Forsterite (Ekremseter Quarry Norway) and Frisch pyroxene (Nigeria). The analysis of secondary standards was performed at the start of every session following beam saturation and stabilisation (30-60 minutes). Once microscope performance conditions proved stable, and the relative errors of analysis for these standard materials fell to < 2% (ideally < 1%), the investigation of unknown materials could begin. Beam current stability was monitored every 10 analyses, based on a requirement of < 1 % variation in at least three consecutive analyses of a Co primary standard. The results of the quantitative analyses are presented in the form of wt% metal oxide (Chapter 3 and Appendix C), and the number of atoms per formula unit (apfu), with the mineral formula for serpentines being calculated on the basis of 7 oxygens.

X-ray elemental distribution maps were obtained similarly under conditions of 20 kV accelerating voltage, 1 nA beam current (LEO SEM) and 5.5 spot size (~ 2.5 nA) (FEI SEM), with acquisition times extended to collect ~18 x 10^6 counts.

A.2.4. Transmission Electron Microscopy

Transmission electron microscopy (TEM) was used for the high resolution imaging of starting serpentine mineral powders. TEM imaging together with electron diffraction provided information that complemented the PXRD structural analyses.

TEM employs a high-energy electron beam to appraise the morphology, structure and composition of a material on the very fine scale. A brief overview of the diffraction (Figure A.8a) and imaging (A.8b) modes of the TEM, as utilised in the present study, is now given.

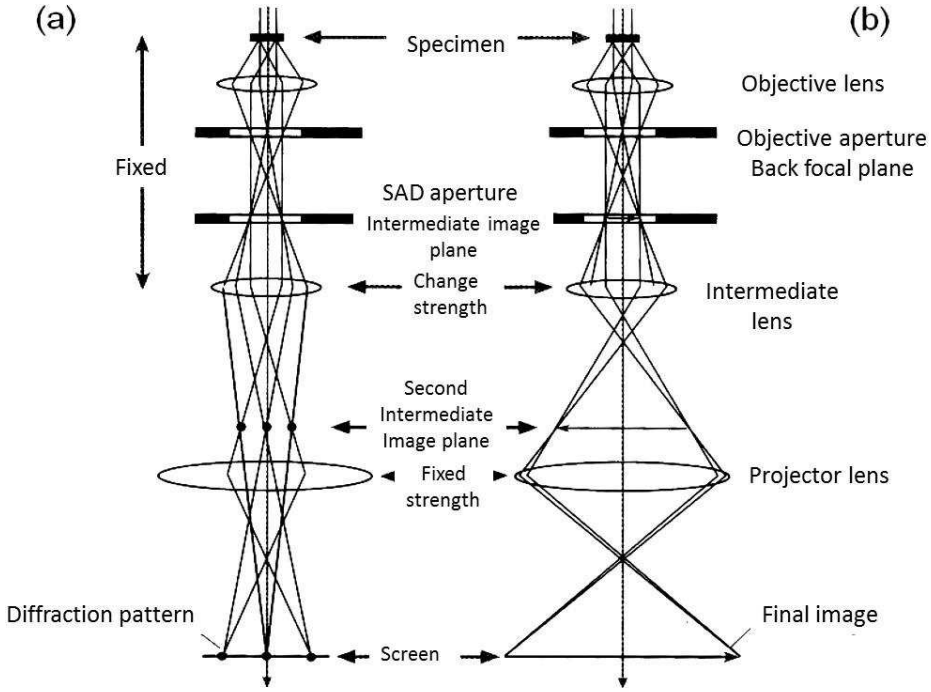


Figure A.8 Schematic diagram showing the optics for the formation of (a) electron diffraction patterns and (b) images within a TEM (Williams and Carter, 2009)

DIFFRACTION MODE (Figure A.8a). In this mode, the projection lenses are focused on the back-focal plane of the objective lens where the diffraction pattern is first formed. The utilisation of a selected area aperture in the first image plane restricts the field of view used to form the diffraction pattern as projected on to the viewing screen. The diffraction pattern essentially contains a central bright spot and an array of less intense spots around it, the distribution of which depends on the crystallographic nature of the specimen. The diffraction pattern may be interpreted with reference to reciprocal space. A point in reciprocal space represents a series of parallel crystallographic planes in real space. With reference to the Ewald sphere construction (Figure 3.9, comparison with X-ray is presented) diffraction spots will be

projected when a reciprocal lattice point is intersected by the Ewald sphere, corresponding to a set of real space crystal planes at the Bragg condition for diffraction. Lattice spacings may be determined with reference to the camera constant equation, $\lambda L = Rd$ (Figure A.10), where the camera length (L) is the effective distance between the sample and the projected image.

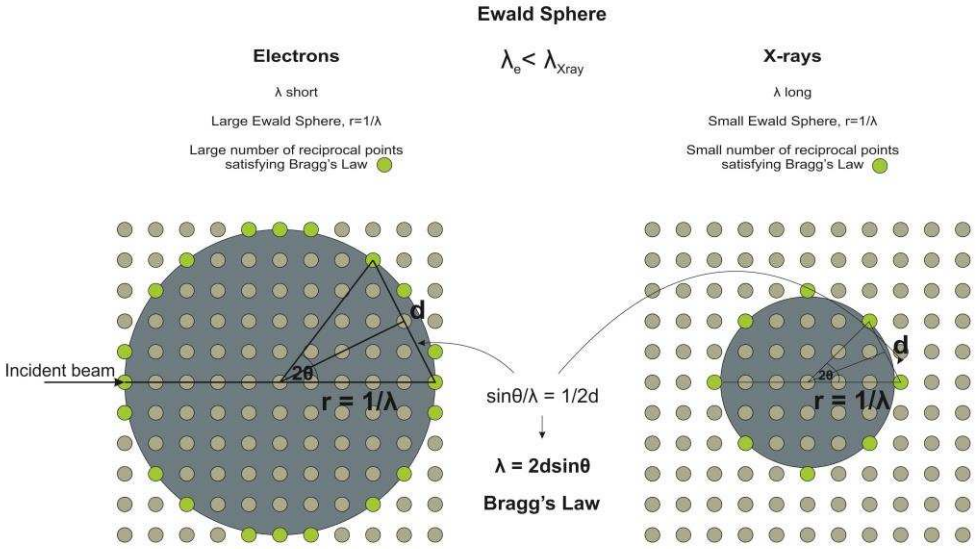


Figure A.9 Ewald sphere construction for electrons and X-rays. Ewald sphere represents in reciprocal space all possible points where planes (reflections) could satisfy the Bragg equation (green points). The difference in wavelength between electron and X-ray results in the size of Ewald Sphere and consequently the number of possible reflections satisfying Braggs Law, i.e. high for electron and low for X-rays.

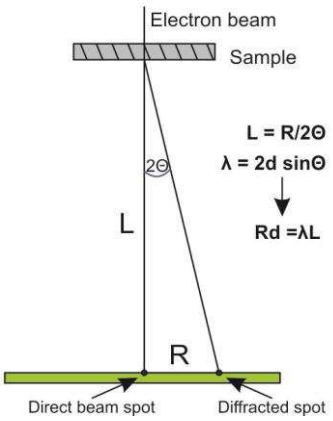


Figure A.10 Relationship between camera length (L) and the distance between the direct beam and diffracted spots or

IMAGING MODE (Figure A.8b). Bright and dark-field diffraction contrast and phase contrast (high resolution TEM (HRTEM)) are the main imaging modes in TEM. Diffraction contrast imaging is used routinely for studying crystal grain and defect structures.

A **bright-field image** is formed when an objective aperture limits the transmitted electrons to the direct beam only. Crystalline areas of sample that are at the Bragg orientation (close to a low index projection / strong scattering) will appear dark, whilst off-axis crystals (randomly oriented / weak scattering) will appear bright.

A **dark-field image** is generated when the direct beam is excluded and a selected diffracted beam only is used. In practice, the incident beam is tilted so that the diffracted beam chosen is aligned along the optic axis. Areas of sample that scatter electrons to this diffracted beam appear bright.

High resolution TEM enables observations on the atomic scale. It exploits the phenomenon of phase contrast which arises from the interference of several diffracted beams. In practice, the sample is precisely oriented such that the directly transmitted beam is aligned along a low index crystallographic projection of a grain, whilst a large diameter objective aperture is used to select the diffracted beams to form the image**.**

All TEM analyses were performed at the Nottingham University laboratories.

1. JEOL 2000FX (Wolfson building): a 200kV analytical TEM with LaB_6 electron gun. The microscope was fitted with an Oxford Instruments ISIS EDS microanalysis system comprising Si(Li) detector, and an ultra-thin window for the detection of elements as light as boron.
2. JEOL 2100F TEM (Nanotechnology and Nanoscience Centre): equipped with a field emission electron gun (FEG), providing a high brightness, high stability electron source. The point resolution of 0.19 nm enables ultrahigh resolution of materials.

A.2.5. Fourier Transform Infrared Spectroscopy

Fourier Transform Infrared Spectroscopy (FTIR) provided information on the molecules present in each sample which aided serpentine mineral identification. FTIR was used also to appraise time-constrained structural modifications within serpentine reaction residues.

Infrared spectroscopy derives information from the interaction of infrared radiation (IR) with the molecules present in a sample. The commonly used region is the Mid IR, 4000 ~ 400 cm^{-1} wavenumber, which coincides with the absorption of most organic compounds and inorganic ions. On exposure to IR, molecules absorb a portion of radiation of specific wavelength. This causes a change in the dipole moment of a molecule and a transfer of vibrational energy levels from the ground state to an excited state. The vibrational energy gap corresponds to the frequency of the absorption peak, whilst the absorption peak intensity is related to the change of dipole moment. Most molecules are infrared active, except for several homo-nuclear diatomic molecules such as O_2, N_2 and Cl_2, due to the zero dipole change in the vibration and rotation of these molecules.

FTIR was performed using a BioRad Excalibur spectrometer on an optical bench containing a 60° dynamically aligned Michelson interferometer with ceramic infrared source, an air-cooled Deuterated Tri Glycine Sulfate (DTGS) detector and a potassium bromide beam splitter. KBr discs were used as support medium for the analysis of powdered samples. Both were oven-dried overnight prior to analysis. Data was processed using Varian Resolution Pro software. 50 scans of background and sample were collected at 2 cm^{-1} spectral resolution; the processing involved the deconvolution and smoothing of peaks.

A.2.6. X-ray Fluorescence Spectroscopy

X-ray fluorescence (XRF) provided data on whole rock major element composition.

XRF provides the chemical composition of a sample following interaction with a high energy X-ray beam. The process of photoionisation describes the expulsion of an inner (core) shell electron to create an unstable, excited atom. The atom stability is regained when an electron from a higher energy level fills the vacancy, with the simultaneous emission of an X-ray photon. The energy of this photon, equal to the energy difference between the two energy levels, is characteristic of the atomic number.

XRF analysis was performed by PANanalytical Ltd, Environmental Science Centre, Nottingham. 9 g of PANalytical pre-fused 66/34 $Li_2B_4O_7/LiBO_2$ flux was weighed into a 95/5 Pt/Au crucible and fused with 0.9000 g of the sample powder at 1200°C. Loss of ignition was determined after 1 h at 1050°C. F, Cl and SO_3 represent fluorine, chlorine and sulphur retained in the fused bead after fusion at 1200°C. The analytical suite also included K, P, Sr, Zr, Ba, Cu, Zn, Pb, V and Hf, however all these were below detection limit and hence are not listed in Appendix C. Two "in-house" quality control samples and a reference serpentinite sample were investigated: Essexite QC379, Shap Granite QC377 and serpentinite SGR-1 [*Gladney and Roelandts*, 1988].

A.2.7. Inductively Coupled Plasma - Atomic Emission Spectroscopy

Inductively coupled plasma - atomic emission spectrometry (ICP-AES) was used to determine the elemental composition of leachates derived from both the short and long term experiments.

ICP-AES is another technique that relies on the emission of characteristic photons or energy by an excited atom. The excitation of sample atoms is triggered by a very hot, partially ionised gas (7000 – 10000 K), plasma. The light emitted by atoms/ions in

their excited state is collected to produce an emission spectrum. A plasma is used rather that a flame source to provide more energy and increase the number of excited atoms. ICP-AES may be used for the investigation of both metals and non-metals, up to 50 elements at a time, with detection limits as low as 10^{-6} g/l. The technique requires samples to be in solution. The dissolution of solid samples is achieved by either acid attack using HF, HNO_3 or HCl or by $LiBO_2$ fusion, a technique similar to that used in XRF. The sample solution is passed into a nebuliser to generate an aerosol mist (*i.e.* the sample is atomised). The mist is carried into an Ar plasma that thermally excites the outer-shell electrons of the sample atoms. The intensity of emitted light is proportional to the elemental concentration in the sample. In multi-elemental samples, light emission will occur simultaneously from all the elements present. An optical grating is used to separate particular characteristic wavelengths which are converted into elemental concentrations via electronic signals generated at a detector.

The analysis was performed using a Perkin Elmer Optima 7300 DV (Dual View) Inductively Coupled Plasma - Atomic Emission Spectrometer with WinLab 32 for ICP (Version 5.5) software.

A.2.8. Particle Size Distribution Analysis

Particle size distribution analysis by laser diffraction (PSD LD) was performed for starting powder samples before the short-term experiments. The data was used in evaluation of factors controlling the leaching efficiency of serpentine minerals (Chapter 5).

When a laser beam passes through a dispersed particulate sample, it is scattered with intensity that is a function of scattering angle, particle shape and size. If the relationship between the scattered intensity, angle and particle morphology are known, then the size distribution of particles of a particular shape can be

determined. In practice, laser diffraction tends to use the Mie theory of light scattering that adopts a spherical model for particles shape, with data reported as volume% of spherical diameter [*Malvern et al.*]. This is used to plot sample size distributions. In this study the cumulative undersize distribution were generated that give the amount of particle smaller than a defined size. In that context, median d_{50} (particle diameter at which half of the distribution is larger and half is smaller), and accordingly d_{10} and d_{90} values were also plotted using R Statistical Computing software.

The analysis was accomplished using an LS 13320 Laser Diffraction Particle Size Analyzer, Beckman Coulter, with a 5 mW diode laser capable of measuring particles in the range 0.017 µm to 2000 µm.

A.2.9. Specific Surface Area analysis

The specific surface area values were obtained by the physisorption Brunauer-Emmett-Teller (BET) method. The data was used in evaluation of factors controlling the leaching efficiency of serpentine minerals (Chapter 4).

Specific surface area (SSA) values were determined for the same samples analysed using PSD. The SSA is an important parameter when quantifying processes at solid/liquid interfaces, such as rates of dissolution or crystallization.

The SSA of a powder sample may be determined using the BET method that involves the physical adsorption (physisorption) of a monolayer of nitrogen gas molecules on the surface of a solid as a function of relative pressure. The amount of gas adsorbed on a surface of adsorbent as a function of pressure, at constant temperature, is plotted as an adsorption isotherm. The isotherms can be used to calculate the area of the active pores in the adsorbing material. The BET SSA is reported in m^2/g.

A Micromeritics Gemini VI 2385 C physisorption system was used in the current study. The Gemini series uses Static Volumetric Technique and a twin-tube design to generate high-speed surface area and porosity data (Kemp *et al,* 2009). Approximately 1 g of each sample was used and a detailed protocol on sample preparation and analysis can be found in Kemp *et al,* 2009.

A.2.10. Thermogravimetric Analysis

The thermogravimetric analysis was used in qualitative discrimination of serpentine minerals.

Thermal analysis covers a group of techniques in which a property of a sample is monitored against time or temperature, while the temperature of the sample is programmed, *i.e.* may involve heating or cooling. Amongst the thermal analysis techniques, thermogravimetric analysis (TGA) and differential thermal analysis (DTA were used in this study. TGA measures the weight of a sample as a function of temperature and allows to detect changes in sample mass (gain or loss), determine stepwise changes in mass, usually as a % of the initial sample mass and determine temperatures that characterise a step in the mass loss or gain curve. In DTA, the temperature difference between the sample and inert reference substance is measure as a function of temperature [*Wagner*, 2009]. In this study, single DTA was used with the reference temperature calculated from the temperature program and not taken from a measurement of a reference material.

Thermogravimetric analysis was carried out using a Mettler Toledo 851^{e} simultaneous thermogravimetric/differential thermal analyser (TGA/SDTA). The equipment was controlled and thermal analysis data analysed using the Mettler-Toledo STAR^{e} software suite. Approximately 30 - 80 mg portions of each powdered sample were heated in 150 µl aluminium crucibles from 30 to 1000˚C in a gas flow of 80 ml/minute N_2 at a heating rate of 10 ˚C/minute.

Appendix B

Precision and Accuracy of SEM-EDS analysis

Precision (P) is a measure of statistical repeatability, otherwise termed % 2 standard deviation (SD) or relative standard deviation

$$P = (2\sigma / \bar{x})*100 \qquad \text{(B.1.)}$$

Where $\bar{x}$ is the mean value of the data points and σ is the standard deviation calculated from

$$\sigma = \sqrt{\frac{\sum(x - \bar{x})^2}{N}} \qquad \text{(B.2.)}$$

Accuracy (A) is a measure of how close a measurement may be to the reference value, otherwise termed % difference:

$$A = ((\bar{x} - Y_{ref}) / Y_{ref})*100 \qquad \text{(B.3.)}$$

where Y_{ref} is the reference value.

Ten consecutive analyses of two secondary standards: Frisch Pyroxene (Table B.1.) and Forsterite #134 (Table B.2.) were performed to determine the precision and accuracy of major element measurements using scanning electron microscopy (SEM) with Energy Dispersive Spectroscopy (EDS). Two SEM/EDS systems were used: FEI Quanta 600 SEM and LEO 435 VP SEM. The details of EDS system are given in Chapter 3, Section 3.2.3.

The SEMs were operated at high vacuum (< 1.2 x 10^{-4} torr) and 20 kV accelerating voltage, with 10 mm (FEI SEM) or 19 mm (LEO SEM) working distances optimal for analysis, with fixed detector take-off angles of 45°. Conditions of 1 nA beam current and 60 s acquisition times were used with the LEO SEM. For the FEI Quanta 600 SEM, the beam current was controlled by spot size, on a scale of 1-10, with values between 5.5 and 7 being used for 30 s acquisition times, equating to beam currents of 2.45 nA and 2.8 nA, respectively (spot size is proportional to the $\log_2$(probe current)), giving ˜1 x 10^6 total spectrum counts. The conditions had previously been established as optimal for the analysis of major elements by the laboratory manager. Longer counting times could have been used to improve signal-to-noise ratio and assure sufficient signal for quantification of minor elements (Reed, 2005), but this was not required for this study.

Table B.1. Compositional precision and accuracy based on 10 consecutive analyses of Frisch Pyroxene, using an FEI Quanta 600 SEM - EDS systems

Compound	**Ref value (wt%)**	Data points x1	x2	x3	x4	x5	x6	x7	x8	x9	x10	Mean	STDEV σ	2 σ	% 2 σ Precision	% Dif. Accuracy
Na_2O	**1.30**	1.27	1.19	1.06	1.25	1.28	1.15	1.33	1.27	1.22	1.44	1.2	0.10	0.20	15.73	-4.37
MgO	**15.52**	15.41	15.29	15.31	15.1	15.16	15.36	15.37	15.68	15.23	15.53	15.3	0.16	0.32	2.09	-1.11
Al_2O_3	**7.75**	7.16	7.96	7.88	7.71	7.42	8.08	8.01	7.74	7.81	7.6	7.7	0.27	0.54	6.93	-0.15
SiO_2	**49.63**	51.06	51.58	51.27	50.35	50.3	50.7	50.83	51.3	50.02	51.54	50.9	0.52	1.03	2.03	2.55
CaO	**17.65**	17.73	17.59	17.58	17.73	17.41	17.29	17.54	17.65	17.79	17.67	17.6	0.15	0.30	1.70	-0.30
TiO_2	**0.84**	0.96	0.79	0.77	0.8	0.77	1.05	0.72	0.74	0.84	0.99	0.8	0.11	0.22	25.86	0.96
FeO	**6.15**	6	6.92	5.97	5.78	6.31	6.16	6.31	6.19	6.79	6.13	6.3	0.34	0.67	10.77	1.74
MnO	**0.14**	0.19	0.3	0.2	0.34	0.26	0	0.16	0.25	0.1	0.16	0.2	0.01	0.02	9.59	43.07

Table B.2. Compositional precision and accuracy based on 10 consecutive analyses of olivine #134, using a LEO 435 VP SEM - EDS systems

Compound	**Ref Value (wt%)**	Data points										Mean	STDEV σ	2 σ	% 2 σ Precision	% Dif. Accuracy
		x1	x2	x3	x4	x5	x6	x7	x8	x9	x10					
MgO	**51.03**	50.13	50.06	50.21	50.27	50.38	49.88	50.03	50.21	49.89	49.8	50.09	0.18	0.36	**0.71**	**-1.85**
SiO_2	**41.54**	41.0	41.31	40.95	41.19	41.31	40.66	40.86	40.88	40.7	41.21	41.01	0.23	0.45	**1.11**	**-1.28**
FeO	**6.78**	7.16	6.89	6.98	7.06	6.76	7.02	7.02	6.81	6.87	7.28	6.99	0.15	0.30	4.34	3.02
NiO	**0.38**	0.49	0.45	0.45	0.46	0.61	0.3	0.52	0.46	0.37	0.52	0.46	0.08	0.16	34.67	21.84

Table B.3. SEM-EDS quantitative analysis of lizardite 1T AML4, lizardite 2H$_1$ AML53 and AML57, and antigorite AML2 and AML59. The data for chrysotile AML60 (in grey) is shown only as an example of low analytical results arising from analytical challenges presented in Chapter 4, Section 4.4.3.2.bd=below detection, where the detection limit is 0.1wt%

		wt% oxide							Atoms per formula unit (apfu) based on 7 oxygens						
		MgO	Al_2O_3	SiO_2	FeO	NiO	MnO	Total	Mg	Fe	Ni	Al	Si	Mn	Cation total
AML4	**Lizardite 1T**														
SOI2SP4		39.92	3.01	42.00	4.07	bd	bd	89.00	2.74	0.16	bd	0.16	1.93	bd	4.99
SOI6SP7		39.36	3.19	42.15	4.23	bd	bd	88.93	2.70	0.16	bd	0.17	1.94	bd	4.97
SOI4SP6		39.01	3.39	41.41	4.45	bd	bd	88.26	2.70	0.17	bd	0.19	1.92	bd	4.98
SOI8SP4		38.96	3.37	41.52	4.34	bd	bd	88.19	2.70	0.17	bd	0.18	1.93	bd	4.98
SOI7SP5		39.36	3.10	41.74	3.88	bd	bd	88.09	2.72	0.15	bd	0.17	1.94	bd	4.98
SOI8SP3		38.97	3.26	41.55	4.07	bd	bd	87.86	2.70	0.16	bd	0.18	1.93	bd	4.97
SOI4SP7		39.02	3.15	41.36	4.18	bd	bd	87.70	2.72	0.16	bd	0.17	1.93	bd	4.98
SOI1 Sp1		38.92	3.10	41.10	4.33	bd	bd	87.45	2.72	0.17	bd	0.17	1.93	bd	4.99
SOI10SP3		38.84	3.34	41.14	4.45	bd	bd	87.77	2.71	0.17	bd	0.18	1.92	bd	4.98
SOI4SP2		38.81	3.11	40.93	4.28	bd	bd	87.12	2.72	0.17	bd	0.17	1.93	bd	4.99
AML4	**Chrysotile**										bd				
SOI6SP3		38.73	1.80	43.63	2.99	bd	bd	87.15	2.68	0.12	bd	0.10	2.03	bd	4.92
SOI6SP4		38.52	1.89	43.63	2.94	bd	bd	86.97	2.67	0.11	bd	0.10	2.03	bd	4.92
SOI3SP5		38.44	1.56	42.88	2.91	bd	bd	85.79	2.71	0.11	bd	0.09	2.02	bd	4.93
AML53	**Lizardite 2H$_1$**										bd				
SOI1 sp7		41.61	0.74	43.52	1.17	bd	bd	87.04	2.87	0.05	bd	0.04	2.01	bd	4.96
SOI7SP2		41.83	0.74	44.19	1.24	bd	bd	87.99	2.85	0.05	bd	0.04	2.02	bd	4.96
SOI7SP3		42.13	0.89	44.34	1.31	bd	bd	88.67	2.85	0.05	bd	0.05	2.02	bd	4.96
SOI8SP2		42.08	0.35	44.44	1.29	bd	bd	88.16	2.86	0.05	bd	0.02	2.03	bd	4.96
SOI8 SP1		42.28	0.12	44.69	1.06	bd	bd	88.19	2.87	0.04	bd	0.01	2.04	bd	4.95
SOI8SP3		43.21	0.00	45.53	1.10	bd	bd	89.84	2.88	0.04	bd	0.00	2.04	bd	4.96
SOI5SP5		41.28	0.40	44.05	1.71	0.01	bd	87.45	2.83	0.07	bd	0.02	2.03	bd	4.95
AML57	**Lizardite 2H$_1$**														
SOI2 SP1		41.19	0.43	44.77	1.44	0.30	bd	88.13	2.81	0.06	0.01	0.02	2.05	bd	4.94
SOI4 SP5		41.45	0.00	44.50	1.71	0.34	bd	88.00	2.84	0.07	0.01	0.00	2.04	bd	4.95

		MgO	Al_2O_3	SiO_2	FeO	NiO	MnO	Total	Mg	Fe	Ni	Al	Si	Mn	Cation total
SOI8 SP4		40.92	0.42	44.53	1.50	0.28	bd	87.64	2.80	0.06	0.01	0.02	2.05	bd	4.94
SOI1 SP13		40.76	0.52	44.59	1.49	0.28	bd	87.63	2.79	0.06	0.01	0.03	2.05	bd	4.93
SOI2 SP2		41.00	0.41	44.71	1.43	0.00	bd	87.58	2.81	0.05	0.00	0.02	2.05	bd	4.93
SSOI1 P14		40.56	0.53	44.85	1.45	0.21	bd	87.60	2.78	0.06	0.01	0.03	2.06	bd	4.92
SOI8 SP5		40.85	0.51	44.42	1.50	0.23	bd	87.51	2.80	0.06	0.01	0.03	2.04	bd	4.94
SOI1 SP12		40.69	0.65	44.34	1.59	0.24	bd	87.52	2.79	0.06	0.01	0.04	2.04	bd	4.94
SOI2 SP6		40.91	0.00	45.02	1.30	0.18	bd	87.42	2.80	0.05	0.01	0.00	2.07	bd	4.93
SOI4 SP4		41.12	0.00	44.47	1.74	0.22	bd	87.55	2.82	0.07	0.01	0.00	2.05	bd	4.95
AML2	**Antigorite**														
SOI3 SP4	39.25		1.36	44.23	3.61	0.19	bd	90.24	2.65	0.14	0.01	0.08	2.00	bd	4.93
SOI5 SP10		39.24	1.06	44.56	3.26	0.25	bd	88.36	2.68	0.12	0.01	0.06	2.05	bd	4.92
SOI3 Sp6		38.96	1.42	44.02	3.57	0.13	bd	88.40	2.67	0.14	0.01	0.08	2.03	bd	4.93
SOI3 SP3		39.08	1.30	44.30	3.41	0.15	bd	88.58	2.67	0.13	0.01	0.07	2.04	bd	4.92
SOI3 SP2		38.76	1.50	43.96	3.55	0.27	bd	88.30	2.66	0.14	0.01	0.08	2.03	bd	4.93
SOI4 SP2		38.81	1.39	44.13	3.47	0.17	bd	88.15	2.66	0.13	0.01	0.08	2.04	bd	4.92
SOI4 SP4		38.66	1.28	44.34	3.41	0.16	bd	88.17	2.67	0.13	0.01	0.07	2.05	bd	4.92
SOI3 Sp5		38.87	1.21	44.42	3.56	0.15	bd	88.16	2.65	0.14	0.01	0.07	2.05	bd	4.91
SOI4 SP5		38.83	1.17	44.57	3.29	0.11	bd	88.17	2.66	0.13	0.00	0.07	2.06	bd	4.91
SOI5 SP5		38.85	1.05	44.38	3.39	0.00	bd	87.68	2.68	0.13		0.06	2.05	bd	4.92
SOI5 SP1		38.89	0.95	44.47	3.45	0.18	bd	87.98	2.67	0.13	0.01	0.05	2.06	bd	4.92
AML59	**Antigorite-Picrolite**														
SOI4 SP2	39.14		0.29	45.49	4.63	0.00	bd	89.55	2.66	0.18	0.00	0.02	2.07	bd	4.92
SOI4 SP4		39.19	0.42	45.36	4.71	0.00	bd	89.69	2.66	0.18	0.00	0.02	2.07	bd	4.92
SOI7 SP3		39.18	0.39	45.30	4.48	0.14	bd	89.48	2.66	0.17	0.00	0.02	2.07	bd	4.92
SOI5 SP3		38.35	0.25	45.15	5.39	0.00	bd	89.15	2.63	0.21	0.00	0.02	2.07	bd	4.92
SOI5 SP1		38.42	0.20	45.14	5.07	0.00	bd	88.84	2.63	0.20	0.00	0.01	2.08	bd	4.92
SOI2 SP2		39.81	0.00	45.68	3.57	0.10	bd	89.10	2.70	0.14	0.00	0.00	2.08	bd	4.92
SOI4 SP5		38.69	0.39	45.08	4.67	0.00	bd	88.82	2.65	0.18	0.00	0.02	2.07	bd	4.92
SOI7 SP4		39.14	0.33	45.06	4.28	0.00	bd	88.81	2.68	0.16	0.00	0.02	2.07	bd	4.92
SOI3 SP4		38.63	0.33	45.01	4.59	0.09	bd	88.64	2.65	0.18	0.00	0.02	2.07	bd	4.92

		MgO	Al_2O_3	SiO_2	FeO	NiO	MnO	Total	Mg	Fe	Ni	Al	Si	Mn	Cation total
SOI7 SP1		38.82	0.15	45.26	4.22	0.12	nd	88.73	2.65	0.16	nd	0.02	2.08	nd	4.91
AML60		**Chrysotile (nanotubular)**													
SOI4SP3	34.36		bd	41.40	1.6	bd	0.2	77.57	2.67	bd	bd	0.07	2.16	0.01	4.91
SOI2SP1		34.56	bd	42.09	1.84	bd	0.24	78.74	2.62	bd	bd	0.08	2.14	0.01	4.86
SOI4SP2		35.25	bd	42.46	1.67	bd	nd	79.38	2.65	bd	bd	0.07	2.14	nd	4.86
SOI7SP1		35.32	bd	43.04	1.72	bd	0.23	80.31	2.63	bd	bd	0.07	2.15	0.01	4.85
SOI1Sp1		36.31	0.19	42.96	1.59	bd	0.17	81.78	2.67	0.01	bd	0.07	2.12	0.01	4.87
SOI6SP1		36.18	bd	43.69	1.87	bd	0.23	81.97	2.64	bd	bd	0.08	2.14	0.01	4.86
SOI6SP4		36.12	bd	44.04	1.78	bd	0.23	82.16	2.62	bd	bd	0.07	2.15	0.01	4.92
SOI5SP1		36.16	bd	43.94	1.83	bd	0.25	82.18	2.63	bd	bd	0.07	2.14	0.01	4.86
SOI6SP3		36.62	bd	44.01	1.76	bd	nd	82.39	2.65	bd	bd	0.07	2.14	nd	4.86
SOI6SP2		36.51	bd	44.03	1.81	bd	0.2	82.55	2.64	bd	bd	0.07	2.14	0.01	4.86
SOI1SP2		36.84	0.15	43.51	1.61	bd	0.19	82.91	2.67	0.01	bd	0.06	2.12	0.01	4.87

*FeO = total Fe

Appendix C

Precision and Accuracy of ICP-AES analysis (fusion solution method)

Two secondary standards: NIM-D (dunite) and PCC-1 (peridotite) were analysed by ICP-AES (fusion solution), with the results of five data sets per sample being used to calculate values for precision and accuracy. Although, ICP-AES was used in this study to determine the composition of leachate solutions only, the procedure presented here serves as a means to justify a 5 % error on the solution data. Precision and accuracy values (Table C.1.) were calculated using equations B.1, B.2 and B.3.

The standards were analysed by sodium peroxide fusion with an ICP-AES finish. Each sample (0.2 g) was weighed into a graphite crucible with sodium peroxide (1.0 g) and fused for 90 min at 500°C. The sodium peroxide fused material was dissolved in dilute hydrochloric and hydrofluoric acids, with solutions being stored in plastic Nalgene bottles prior to analysis.

The calculated error values for precision of major elements (MgO, SiO_2) ranged from *ca.* 8 – 13%, being attributable to a combination of factors, including sample homogeneity, sample preparation (fusion and dissolution), instrument performance and the number of data points acquired, in this case, five. It is accepted that due to simpler sample preparation for the acid leached solutions, *i.e.* out need for fusion & dissolution, the errors on the ICP-AES solution data are associated with lower uncertainty, being about half that of the standards data, hence a value of 5% was applied.

Table B.1. Precision and accuracy of ICP-AES (fusion solution method) based on analysis of two reference materials, dunite Nim-D, and peridotite PCC-1.

Compound analysed	**NIM-D Ref wt%**	Nim 1	Nim 2	Nim 3	Nim 4	Nim 5	**Mean (x*)**	No of values	σ	2σ	2%σ Precision	%Diff Accuracy
MgO	**43.51**	41.75	43.98	38.33	40.38	36.40	**40.17**	5.00	2.63	5.27	13.11	-7.68
Al_2O_3	**0.3**	0.25	0.26	0.22	0.22	0.20	**0.23**	5.00	0.02	0.04	17.46	-23.46
SiO_2	**38.96**	31.06	34.26	31.28	32.98	30.43	**32.00**	5.00	1.41	2.82	8.80	-17.86
CaO	**0.28**	0.44	0.45	0.39	0.40	0.38	**0.41**	5.00	0.03	0.06	14.22	46.98
NiO	**0.26**	0.23	0.24	0.21	0.21	0.20	**0.22**	5.00	0.01	0.03	12.44	-15.68
MnO	**0.22**	0.20	0.21	0.18	0.19	0.18	**0.19**	5.00	0.01	0.02	11.69	-13.13
Fe_2O_3 total	**16.96**	15.50	16.30	14.09	14.86	13.46	**14.84**	5.00	1.00	2.01	13.54	-12.50
Compound analysed	**PCC-1 Ref wt%**	PCC1	PCC2	PCC3	PCC4	PCC5	**Mean (x*)**	No of values	σ	2σ	2%σ Precision	%Diff Accuracy
MgO	**43.43**	41.85	38.77	37.92	44.27	38.32	**40.22**	5.00	2.45	4.90	12.19	-7.38
Al_2O_3	**0.675**	0.58	0.55	0.51	0.67	0.52	**0.56**	5.00	0.06	0.11	20.37	-16.47
SiO_2	**41.71**	33.62	32.55	35.32	38.51	33.83	**34.77**	5.00	2.07	4.14	11.91	-16.65
CaO	**0.52**	0.70	0.65	0.64	0.80	0.64	**0.69**	5.00	0.06	0.12	17.87	32.12
NiO	**0.3**	0.28	0.25	0.25	0.29	0.24	**0.26**	5.00	0.02	0.04	15.06	-12.48
MnO	**0.12**	0.11	0.10	0.09	0.11	0.09	**0.10**	5.00	0.01	0.02	14.91	-15.51
Fe_2O_3 total	**8.25**	7.47	6.90	6.71	7.84	6.79	**7.14**	5.00	0.44	0.88	12.32	-13.42

Appendix D

ICP-AES and XRF analytical data

The abundance of elements in the starting materials, and solid and liquid reaction products was appraised by ICP-AES and XRF. The analyses were performed at the British Geological Survey Analytical Geochemistry Laboratories and by PANanalytical Ltd, Environmental Science Centre, Nottingham. The detailed analytical protocol is presented in the Appendix A. Here, the raw data is tabulated and presented as mg/l (ppm) of element for ICP-AES and wt% oxide for XRF.

D.1. ICP AES data - short term experiments

D.2. XRF data - short term experiments

D.3. ICP-AES data - long term experiments

D.4. Concentration of anions in the liquid samples extracted from long term experiments determined by Ion Chromatography (IC)

D.5. XRF data - long term experiments

D.1. Fluid chemistry of short term experiments - ICP-AES data.

Sample Type		Reaction Time (min)	Si	Mg	Al	Mn	Fe^{Total}	Ni	Ca	Na	K	P^{Total}	Ba	Cr	Co	Cu	Zn	Sr	Li	V	Cd
			(mg l^{-1})																		
Antigorite	AML 2	30	145.24	1270.00	39.90	3.30	171.00	15.40	<1.7	<128	<18	<2.7	<0.01	9.30	0.93	0.87	0.89	<0.02	<0.11	<0.16	<0.05
		60	158.57	1660.00	51.50	4.20	231.00	17.50	<1.7	<128	<18	<2.7	0.04	12.40	0.99	0.75	1.16	<0.02	<0.11	0.22	<0.05
		120	185.23	2165.00	68.60	5.50	333.00	21.60	<1.7	<128	<18	<2.7	0.02	16.81	1.18	1.01	1.16	<0.02	<0.11	0.43	<0.05
		180	195.57	2650.00	87.40	6.80	429.00	24.90	<1.7	<128	<18	<2.7	0.03	21.44	1.39	1.11	1.24	<0.02	<0.11	0.42	<0.05
Antigorite	AML 59	30	85.47	1510.00	6.00	3.20	94.00	5.00	<1.7	<128	<18	<2.7	<0.01	3.99	0.61	<0.14	0.71	<0.02	<0.11	<0.16	<0.05
		60	126.61	2344.00	9.20	4.50	146.00	7.60	<1.7	<128	<18	<2.7	<0.01	3.99	0.88	<0.14	0.75	<0.02	<0.11	<0.16	<0.05
		120	173.51	3518.00	14.10	6.80	230.00	10.70	<1.7	<128	<18	<2.7	<0.01	4.01	1.40	<0.14	0.86	<0.02	<0.11	<0.16	<0.05
		180	190.28	4533.00	18.60	9.40	313.00	13.70	<1.7	<128	<18	<2.7	<0.01	4.00	1.89	<0.14	0.95	<0.02	<0.11	<0.16	<0.05
Lizardite 1T	AML 4	30	112.32	1594.00	74.40	4.40	167.00	3.10	58.60	<128	<18	<2.7	<0.01	0.38	0.33	<0.14	0.62	0.03	<0.11	0.29	<0.05
		30	116.33	1682.00	78.00	4.50	176.00	3.30	59.20	<128	<18	<2.7	<0.01	0.41	0.29	<0.14	0.74	<0.02	<0.11	0.25	<0.05
		60	149.12	2239.00	103.20	4.70	224.00	4.20	52.80	<128	<18	<2.7	<0.01	0.48	0.35	<0.14	0.65	<0.02	<0.11	0.25	<0.05
		120	212.97	3856.00	181.40	6.30	375.00	6.50	59.30	<128	<18	<2.7	<0.01	0.81	0.76	<0.14	0.92	0.06	0.16	0.31	<0.05
		180	232.62	5151.00	241.90	7.40	504.00	8.00	61.70	<128	<18	<2.7	0.02	1.07	1.01	<0.14	1.08	0.03	0.23	0.56	<0.05
Lizardite, Tlc, Chl	AML 46	30	154.21	2855.00	95.80	15.90	86.00	24.90	12.50	383.00	<18	<2.7	0.05	0.86	1.80	0.61	2.89	0.19	1.06	0.43	<0.05
		60	202.78	5366.00	146.10	25.40	139.00	32.60	12.60	422.00	<45	<6.8	0.04	1.15	2.86	0.41	4.01	0.21	1.45	0.70	<0.13
		120	205.50	7836.00	214.80	29.60	181.00	39.70	12.80	390.00	<45	<6.8	0.08	1.47	3.91	0.88	4.18	0.13	1.85	1.33	<0.13
		180	217.14	9536.00	281.30	34.00	226.00	45.80	15.40	404.00	<45	<6.8	0.07	1.78	4.64	0.77	4.70	0.22	2.45	1.67	<0.13
Lizardite 2H1	AML 53	30	116.03	3035.00	53.70	3.50	150.00	32.00	4.00	<128	<18	<2.7	0.02	1.37	1.01	<0.14	0.62	0.86	1.40	0.32	<0.05
		60	201.66	6727.00	107.90	6.80	312.00	56.00	6.40	<319	<45	<6.8	<0.03	1.72	1.89	<0.36	1.37	0.96	3.12	0.68	<0.13
		120	241.70	10383.00	167.20	9.40	467.00	71.50	7.20	<319	<45	<6.8	<0.03	1.86	2.65	<0.36	1.57	1.09	4.67	<0.39	<0.13

		Si	Mg	Al	Mn	Fe^{Total}	Ni	Ca	Na	K	P^{Total}	Ba	Cr	Co	Cu	Zn	Sr	Li	V	Cd
											(mg l^{-1})									
	180	210.91	10777.00	176.50	9.40	487.00	69.50	4.90	<319	<45	<6.8	<0.03	1.80	2.64	<0.36	1.50	0.97	4.73	0.69	<0.13
Lizardite 2H1	**AML 57**																			
	30	152.39	4913.00	22.00	5.40	152.00	43.30	8.70	<128	<18	<2.7	<0.01	1.27	1.14	0.27	0.71	<0.02	2.46	0.44	<0.05
	60	187.72	7873.00	28.50	7.00	200.00	53.80	12.60	<319	<45	<6.8	0.06	1.31	1.45	0.54	1.33	0.07	3.88	0.91	<0.13
	120	220.64	12000.00	43.60	9.50	291.00	73.50	10.70	<319	<45	<6.8	0.04	1.67	1.96	0.79	1.45	<0.06	5.58	1.15	<0.13
	180	207.08	13237.00	48.30	10.00	322.00	81.00	9.00	<319	<45	<6.8	<0.03	1.71	2.00	0.61	1.50	<0.06	6.38	1.39	<0.13
Polygonal serpentine	**AML 62**																			
	30	182.24	3377.17	234.78	5.72	296.74	0.63	4.73	<0.86	<0.48	<0.07	0.00	0.15	0.21	<0.01	0.63	<0.02	<0.02	0.28	<0.003
	60	217.34	4713.53	300.03	7.30	408.81	0.72	4.31	<0.86	<0.48	<0.07	0.00	0.16	0.29	<0.01	0.70	<0.02	<0.02	0.34	<0.003
	120	232.32	6393.80	404.75	9.37	547.07	0.81	4.20	<0.86	0.62	<0.07	0.00	0.16	0.40	<0.01	0.81	<0.02	<0.02	0.42	<0.003
	180	227.67	7617.17	491.73	10.15	650.77	0.91	4.17	<0.86	<0.48	<0.07	0.00	0.15	0.49	<0.01	0.86	<0.02	<0.02	0.46	<0.003
	180	226.23	7897.25	490.32	10.67	672.90	0.98	4.27	<0.86	1.21	<0.07	0.01	0.17	0.52	<0.01	1.00	<0.02	<0.02	0.46	0.03
	180	237.09	8400.82	509.40	11.05	717.05	0.95	4.40	<0.86	0.70	<0.07	0.01	0.16	0.52	<0.01	0.90	<0.02	<0.02	0.48	0.03
	180	235.32	8112.48	515.99	10.71	691.74	0.88	4.61	<0.86	0.89	<0.07	0.01	0.16	0.54	<0.01	0.92	<0.02	<0.02	0.50	0.03
Chrysotile	**AML 6**																			
	30	264.21	4768.00	25.50	4.80	225.00	5.00	51.40	<128	<18	<2.7	0.02	0.74	0.81	0.17	0.66	0.33	<0.11	<0.16	<0.05
	60	260.68	6458.00	34.60	7.00	317.00	7.20	51.50	<319	<45	<6.8	<0.03	0.88	1.08	<0.36	1.49	0.29	<0.27	<0.39	<0.13
	60	226.96	6386.00	34.30	6.90	314.00	7.30	51.00	<319	<45	<6.8	<0.03	0.81	1.17	<0.36	1.25	0.26	<0.27	<0.39	<0.13
	120	205.78	8466.00	45.50	9.60	434.00	10.40	54.90	<319	<45	<6.8	0.08	0.76	1.86	<0.36	1.57	0.29	<0.27	<0.39	<0.13
	180	204.26	10029.00	52.90	11.90	533.00	12.70	56.30	<319	<45	<6.8	0.05	0.81	2.17	<0.36	1.72	0.77	<0.27	<0.39	<0.13
Chrysotile	**AML 60**																			
	30	227.21	4052.00	15.50	63.30	252.00	0.10	607.60	<128	<18	<2.7	0.02	<0.06	<0.09	<0.14	1.96	0.73	4.16	<0.16	<0.05
	60	199.07	5397.00	18.90	66.10	316.00	0.20	560.80	<319	<45	<6.8	<0.03	<0.15	<0.23	<0.36	2.99	0.65	4.57	<0.39	<0.13
	120	178.37	9040.00	27.70	82.60	497.00	0.40	594.20	<319	<45	<6.8	<0.03	<0.15	<0.23	<0.36	3.90	0.78	6.14	<0.39	<0.13
	180	175.20	10631.00	33.80	90.70	591.00	0.30	626.10	<319	<45	<6.8	0.05	<0.15	<0.23	<0.36	4.22	0.81	7.27	0.51	<0.13

D.2. Whole rock XRF analysis data for starting materials (StMat) and reaction residues (30, 60, 120, 180 min) from the short term acid-leaching experiments. Major element data is reported to two decimal places, sulphur to only one due to potential loss during sample preparation resulting in greater uncertainty. The XRF instrument was calibrated using units of Fe_2O_3 hence total iron data is reported as Fe_2O_3t. For the following elements the values were below detection: P <0.01%, Sr <0.01%, Zr <0.02%, Ba <0.02%, Cu <0.01%, Zn <0.01%, Pb <0.01%, V <0.01%, Hf <0.01% and F <0.01% and are not included in the table.

	Time of leaching	SiO_2	TiO_2	Al_2O_3	Fe_2O_3t	Mn_3O_4	MgO	CaO	Na_2O	K_2O	SO_3	Cr_2O_3	NiO	Cl	Total	LOI
		wt%	wt%	wt%	wt%	wt%	wt%	%	%	%	%	wt%	wt%	%	%	%
Antigorite AML 2	**Start Mat**	**41.58**	**<0.01**	**1.54**	**6.63**	**0.09**	**39.14**	**<0.01**	**<0.05**	**<0.01**	**<0.1**	**0.30**	**0.22**	**<0.1**	**89.51**	**12.10**
	30	38.91	<0.01	1.28	5.91	0.08	33.81	<0.01	<0.05	<0.01	3.7	0.27	0.17	<0.1	84.13	20.62
	60	38.35	<0.01	1.21	5.99	0.07	32.36	<0.01	<0.05	<0.01	2.7	0.26	0.16	<0.1	81.10	20.67
	120	35.45	<0.01	1.16	6.17	0.07	30.94	<0.01	<0.05	<0.01	6.5	0.26	0.16	<0.1	80.72	26.95
	180	33.76	<0.01	1.05	5.19	0.06	27.73	<0.01	<0.05	<0.01	8.5	0.23	0.14	<0.1	76.66	32.63
Antigorite AML 59	**Start Mat**	**43.70**	**0.01**	**0.29**	**4.15**	**0.13**	**40.82**	**<0.01**	**<0.05**	**<0.01**	**<0.1**	**0.01**	**0.09**	**<0.1**	**89.19**	**12.52**
	30	42.34	0.01	0.28	3.82	0.12	35.97	<0.01	<0.05	<0.01	2.8	0.01	0.08	<0.1	85.41	18.65
	60	43.91	0.01	0.28	3.91	0.13	35.83	<0.01	<0.05	<0.01	2.4	0.01	0.08	<0.1	86.54	18.12
	120	45.29	0.01	0.26	3.78	0.12	33.03	<0.01	<0.05	<0.01	2.8	0.01	0.07	<0.1	85.35	18.68
	180	46.65	0.01	0.26	3.66	0.12	30.93	<0.01	<0.05	<0.01	3.2	0.01	0.07	<0.1	84.89	19.50
Lizardite 1T AML 4	**Start Mat**	**39.99**	**<0.01**	**2.93**	**4.28**	**0.04**	**40.34**	**0.14**	**<0.05**	**<0.01**	**<0.1**	**0.01**	**0.04**	**<0.1**	**87.77**	**13.20**
	30	40.53	<0.01	2.77	3.99	0.03	37.09	<0.01	<0.05	<0.01	1.9	<0.01	0.03	<0.1	86.34	17.25
	30	39.68	<0.01	2.69	3.85	0.03	35.83	<0.01	<0.05	<0.01	2.4	0.01	0.03	<0.1	84.52	17.91
	60	40.82	<0.01	2.64	3.77	0.03	34.77	<0.01	<0.05	<0.01	2.6	<0.01	0.03	<0.1	84.66	19.07
	120	43.33	<0.01	2.62	3.73	0.03	33.42	<0.01	<0.05	<0.01	2.6	0.01	0.02	<0.1	85.76	19.41
	180	44.26	<0.01	2.53	3.58	0.03	31.55	<0.01	<0.05	<0.01	2.5	<0.01	0.02	<0.1	84.47	18.96
Lizardite 1T, Chlorite, Talc, AML 46	**Start Mat**	**43.09**	**0.16**	**2.80**	**1.36**	**0.12**	**37.85**	**0.05**	**0.90**	**0.11**	**<0.1**	**0.02**	**0.19**	**0.50**	**87.18**	**14.93**
	30	40.78	0.14	2.27	1.05	0.07	27.88	0.03	<0.05	0.07	7.5	0.02	0.12	<0.1	79.95	27.01
	60	43.05	0.14	2.23	1.00	0.06	23.21	0.03	0.07	0.08	8.3	0.01	0.10	<0.1	78.30	30.60
	120	42.54	0.14	1.96	0.85	0.04	14.99	0.02	0.09	0.08	12.1	0.01	0.09	<0.1	72.92	38.43
	180	41.11	0.13	1.75	0.76	0.03	11.79	0.02	0.09	0.08	11.3	<0.01	0.08	<0.1	67.15	43.02

		SiO_2 wt%	TiO_2 wt%	Al_2O_3 wt%	Fe_2O_3t wt%	Mn_3O_4 wt%	MgO wt%	CaO %	Na_2O %	K_2O %	SO_3 %	Cr_2O_3 wt%	NiO wt%	Cl %	Total %	LOI %
Lizardite 2H1 AML 53	**Start Mat**	**42.39**	**0.01**	**0.89**	**1.85**	**0.03**	**42.25**	**0.01**	**<0.05**	**<0.01**	**<0.1**	**0.01**	**0.20**	**<0.1**	**87.62**	**13.94**
	30	45.35	0.01	0.70	1.50	0.02	34.47	<0.01	<0.05	<0.01	2.4	0.01	0.11	<0.1	84.55	18.00
	60	51.54	0.01	0.59	1.26	0.02	27.63	<0.01	<0.05	<0.01	3.2	0.01	0.07	<0.1	84.31	19.38
	120	59.20	0.01	0.44	0.93	0.01	19.23	<0.01	<0.05	<0.01	3.6	0.01	0.03	<0.1	83.44	20.71
	180	62.61	0.01	0.31	0.75	0.01	14.84	<0.01	<0.05	<0.01	4.0	0.01	0.02	<0.1	82.53	21.51
			0.01													
Lizardite 2H1 AML 57	**Start Mat**	**42.65**	**0.01**	**0.20**	**1.04**	**0.03**	**42.08**	**0.02**	**<0.05**	**<0.01**	**<0.1**	**0.01**	**0.21**	**<0.1**	**86.24**	**14.46**
	30	49.00	0.01	0.15	0.70	0.02	32.36	<0.01	<0.05	<0.01	1.9	0.01	0.12	<0.1	84.25	17.26
	60	57.30	0.01	0.13	0.55	0.01	22.62	<0.01	<0.05	<0.01	2.9	0.01	0.08	<0.1	83.59	19.57
	120	66.07	0.01	0.09	0.37	0.01	12.90	<0.01	<0.05	<0.01	3.3	0.01	0.04	<0.1	82.77	20.35
	180	70.99	0.01	0.07	0.27	0.01	8.39	<0.01	<0.05	<0.01	3.1	0.01	0.03	<0.1	82.85	19.46
Polygonal Serpentine AML 62	**Start Mat**	**40.06**	**<0.01**	**3.17**	**3.29**	**0.04**	**40.97**	**0.02**	**<0.05**	**<0.01**	**<0.1**	**<0.01**	**<0.01**	**<0.1**	**87.55**	**13.60**
	30	45.33	<0.01	2.70	2.84	0.03	35.40	<0.01	<0.05	<0.01	0.7	<0.01	<0.01	<0.1	87.00	14.57
	60	44.85	<0.01	2.36	2.50	0.02	31.30	<0.01	<0.05	<0.01	3.0	<0.01	<0.01	<0.1	84.03	18.87
	120	41.90	<0.01	2.00	2.14	0.02	26.48	<0.01	<0.05	<0.01	6.9	<0.01	<0.01	<0.1	79.44	28.12
	180	35.73	<0.01	1.49	1.59	0.01	19.63	<0.01	<0.05	<0.01	13.1	<0.01	<0.01	<0.1	71.55	39.97
	180	46.61	<0.01	1.76	1.86	0.01	22.95	<0.01	<0.05	<0.01	6.4	<0.01	<0.01	<0.1	79.59	26.76
	180	47.70	<0.01	1.81	1.91	0.01	23.46	<0.01	<0.05	<0.01	5.5	<0.01	<0.01	<0.1	80.39	25.41
Chrysotile AML6	**Start Mat**	**38.26**	**0.01**	**0.28**	**11.19**	**0.08**	**38.06**	**0.13**	**<0.05**	**<0.01**	**<0.1**	**0.01**	**0.07**	**<0.1**	**88.07**	**13.23**
	30	35.66	0.01	0.15	8.64	0.05	23.20	0.02	<0.05	<0.01	8.7	0.01	0.05	<0.1	76.47	31.87
	60	38.33	0.01	0.11	10.55	0.06	20.78	0.01	<0.05	<0.01	7.4	0.01	0.05	<0.1	77.29	29.85
	120	41.37	0.01	0.09	9.94	0.05	15.75	<0.01	<0.05	<0.01	8.4	0.01	0.04	<0.1	75.64	32.55
	180	43.51	0.01	0.04	11.52	0.06	12.28	<0.01	<0.05	<0.01	7.6	0.01	0.04	<0.1	75.05	31.89
	180	39.55	0.01	0.09	11.92	0.07	20.81	<0.01	<0.05	<0.01	6.3	0.01	0.06	<0.1	78.80	26.80
												0.01				
		SiO_2 wt%	**TiO_2 wt%**	**Al_2O_3 wt%**	**Fe_2O_3t wt%**	**Mn_3O_4 wt%**	**MgO wt%**	**CaO %**	**Na_2O %**	**K_2O %**	**SO_3 %**	**Cr_2O_3 wt%**	**NiO wt%**	**Cl %**	**Total %**	**LOI %**

AML 60 Chrysotile	**Start Mat**	**37.77**	**0.01**	**0.12**	**1.82**	**0.26**	**34.64**	**7.96**	**<0.05**	**<0.01**	**<0.1**	**0.01**	**<0.01**	**<0.1**	**82.58**	**18.16**
	30	28.61	0.01	0.05	0.94	0.08	18.45	5.04	<0.05	<0.01	16.7	0.01	<0.01	<0.1	69.87	43.23
	60	29.68	0.01	0.02	0.77	0.07	15.22	5.18	<0.05	<0.01	16.9	0.01	<0.01	<0.1	67.84	45.92
	120	31.50	0.01	0.01	0.45	0.04	8.38	5.51	<0.05	<0.01	20.3	0.01	<0.01	<0.1	66.18	50.50
	180	37.53	0.01	0.01	0.32	0.03	5.35	6.55	<0.05	<0.01	18.6	0.01	<0.01	<0.1	68.38	44.91
AML 60 Chrysotile	**30**	48.51	<0.01	0.28	5.37	0.06	31.81	<0.01	<0.05	<0.01	0.5	<0.01	0.04	<0.1	86.57	14.56
	60	53.88	<0.01	0.17	6.02	0.05	25.23	0.01	<0.05	<0.01	0.4	<0.01	0.04	<0.1	85.80	14.77
	120	52.96	<0.01	0.11	3.69	0.03	14.99	<0.01	<0.05	<0.01	6.3	<0.01	0.02	<0.1	78.10	27.54
	180	69.06	<0.01	0.06	6.53	0.03	11.10	0.01	<0.05	<0.01	0.3	<0.01	0.02	<0.1	87.11	15.75
Dunite	**Start Mat**	**35.06**	**<0.01**	**0.23**	**7.52**	**0.11**	**44.43**	**0.14**	**<0.05**	**<0.01**	**0.1**	**0.86**	**0.25**	**<0.1**	**88.70**	**12.15**
	30	49.46	<0.01	0.30	3.86	0.04	25.11	0.11	<0.05	<0.01	4.0	1.13	0.17	<0.1	84.18	19.00
	60	53.72	<0.01	0.34	3.40	0.03	21.44	0.12	<0.05	<0.01	3.7	1.14	0.15	<0.1	84.05	18.54
	120	47.81	<0.01	0.29	2.35	0.02	14.00	0.09	<0.05	<0.01	8.6	0.89	0.10	<0.1	74.15	33.74
	180	53.10	<0.01	0.31	2.24	0.02	11.93	0.10	<0.05	<0.01	7.2	1.18	0.10	<0.1	76.18	29.14
Serpentinite	**Start Mat**	**34.10**	**<0.01**	**0.30**	**8.27**	**0.13**	**39.56**	**0.17**	**<0.05**	**<0.01**	**<0.1**	**0.52**	**0.20**	**<0.1**	**83.25**	**17.85**
	30	53.29	<0.01	0.32	5.30	0.02	19.78	0.21	<0.05	<0.01	3.0	0.58	0.02	<0.1	82.52	19.81
	60	48.70	0.01	0.30	4.64	0.02	13.68	0.19	<0.05	<0.01	7.9	0.57	0.02	<0.1	76.03	31.36
	120	57.23	0.01	0.34	4.93	0.02	10.26	0.22	<0.05	<0.01	5.5	0.67	0.02	<0.1	79.20	25.88
	180	51.46	0.01	0.28	4.28	0.01	7.76	0.19	<0.05	<0.01	6.8	0.58	0.02	<0.1	71.39	30.88
Harzburgite	**Start Mat**	**40.82**	**0.04**	**2.06**	**8.38**	**0.13**	**38.24**	**2.04**	**<0.05**	**<0.01**	**<0.1**	**0.37**	**0.27**	**<0.1**	**92.36**	**8.22**
	30	44.05	0.04	2.30	5.32	0.08	24.81	2.13	<0.05	<0.01	5.6	0.42	0.16	<0.1	84.93	20.97
	60	43.28	0.04	2.32	4.31	0.06	20.42	2.18	<0.05	<0.01	7.1	0.44	0.13	<0.1	80.29	25.60
	120	43.33	0.04	2.45	3.56	0.06	16.91	2.31	<0.05	<0.01	9.5	0.46	0.10	<0.1	78.74	30.38
	180	45.60	0.04	2.48	3.05	0.05	14.55	2.36	<0.05	<0.01	8.8	0.48	0.08	<0.1	77.50	30.51

The Total is a Sum of all measured elements and should equate to 100 %. The difference from 100% represents the loss of volatiles in the starting serpentine that are mostly related to structural OH. Loss on ignition (LOI) was determined after 1 h at 1050°C. The LOI data were not included in the totals and are reported for information only. This is due to the samples being chemically altered and outside the accredited scope of materials tested by the subcontractor laboratory. The totals in the samples fail one routine QC criteria (Totals between 99 and 101%) but pass all other QC criteria.

D.3. Fluid chemistry of long term experiments as determined by ICP-AES (Time interval measured from 26th July 2013 as the start of experiment. Duration of experiment 246 days)*

Date of sampling	Time interval *	Sample Code		pH	Ca	Mg	Si	Total Fe	Al	Na	K	Total S	Ba	Sr	Mn	Cr	Co	Ni	Cu	Zn
													mg l^{-1}							
13364-0051	**0**	**original solution**		**6.20**	**454**	**1447**	**<0.416**	**<0.061**	**0.29**	**11646**	**438.80**	**225**	**0.88**	**9.20**	**<0.014**	**<0.028**	**0.04**	**<0.046**	**0.08**	**<0.036**
12.08.2013	17	1595_1		7.64	425	1376	0.83	0.08	<0.197	11334	418.37	251	0.37	9.44	<0.014	<0.028	0.03	<0.046	<0.078	0.11
27.08.2013	33	1595_2		7.83	445	1439	0.78	0.08	0.27	11738	439.02	268	0.38	9.91	<0.014	<0.028	<0.022	<0.046	<0.078	0.10
12.09.2013	49	1595_3		8.53	548	1995	114.06	0.61	<0.197	12787	475.39	260	0.27	11.92	2.34	<0.028	0.15	3.02	<0.078	0.39
26.09.2013	63	1595_4	N_2 Dunite	7.92	481	1493	1.43	0.90	1.62	12626	451.46	278	0.41	10.72	0.05	<0.028	<0.022	<0.046	<0.078	0.07
24.10.2013	92	1595_5		8.70	463	1472	1.31	0.85	1.54	11998	463.28	270	0.40	10.33	0.03	<0.028	0.03	<0.046	<0.078	0.11
28.11.2013	127	1595_6		8.40	473	1513	1.85	0.89	1.57	12397	467.59	282	0.40	10.55	0.03	<0.028	0.02	<0.046	<0.078	0.06
13364-0051	**0**	**original solution**		**6.20**	**454**	**1447**	**<0.416**	**<0.061**	**0.29**	**11646**	**438.80**	**225**	**0.88**	**9.20**	**<0.014**	**<0.028**	**0.04**	**<0.046**	**0.08**	**<0.036**
12.08.2013	17	1596_1		7.27	463	2379	128.80	13.19	1.48	12135	455.13	260	0.35	10.24	3.08	0.20	0.23	3.41	0.08	0.13
27.08.2013	33	1596_2		7.40	483	2685	146.64	2.16	1.59	12934	473.82	260	0.36	10.78	3.07	<0.028	0.23	3.11	<0.078	0.17
12.09.2013	49	1596_3		7.14	448	2673	141.13	0.66	0.38	11875	437.61	261	0.33	10.10	3.02	<0.028	0.21	3.08	<0.078	0.11
26.09.2013	63	1596_4		7.36	453	2770	141.03	3.33	0.33	12005	452.30	249	0.36	9.48	2.86	<0.028	0.23	3.12	<0.078	0.09
24.10.2013	92	1596_5		7.30	454	2998	143.21	0.70	0.43	12308	459.59	264	0.36	10.39	2.81	<0.028	0.22	2.95	<0.078	0.11
28.11.2013	127	1596_6	CO_2 Dunite	7.52	454	3185	142.77	1.41	0.31	12260	460.53	267	0.38	10.41	2.62	<0.028	0.20	2.91	<0.078	0.11
09.01.2014	169	1596_7		7.77	205	3218	99.86	0.14	0.34	11905	440.59	250	0.07	4.11	1.40	<0.028	0.15	2.38	<0.078	0.06
13.02.2014	204	1596_8		7.65	420	3342	131.96	0.45	0.66	11784	435.40	250	0.36	9.74	1.95	<0.028	0.16	2.41	0.11	0.08
26.03.2014	246	1596_9		7.60	411	3487	133.56	0.34	0.32	11866	433.81	260	0.38	9.69	1.68	<0.028	0.15	2.27	0.13	0.05

Date of sampling	Time interval *	Sample Code		pH	Ca mg l^{-1}	Mg	Si	Total Fe	Al	Na	K	Total S	Ba	Sr	Mn	Cr	Co	Ni	Cu	Zn
13364-0051	**0**	**original solution**		**6.20**	**454**	**1447**	**<0.416**	**<0.061**	**0.29**	**11646**	**438.80**	**225**	**0.88**	**9.20**	**<0.014**	**<0.028**	**0.04**	**<0.046**	**0.08**	**<0.036**
12.08.2013	17	1597_1	N_2 Harzburgite	7.11	460	1484	2.28	6.57	0.42	12158	443.33	228	0.45	10.23	0.08	0.03	<0.022	0.28	<0.078	0.05
27.08.2013	33	1597_2		7.02	454	1450	2.49	2.88	0.44	11808	444.08	222	0.43	9.59	0.07	<0.028	0.02	0.16	<0.078	0.08
12.09.2013	49	1597_3		7.28	467	1496	3.18	1.65	0.41	12206	448.77	236	0.45	10.51	0.08	<0.028	0.03	0.11	<0.078	0.06
26.09.2013	63	1597_4		7.55	434	1380	3.05	0.51	0.31	11232	425.32	208	0.41	9.19	0.05	<0.028	0.04	<0.046	<0.078	0.06
24.10.2013	92	1597_5		7.50	447	1420	3.52	1.46	0.54	11596	437.52	214	0.41	9.05	0.06	<0.028	0.04	0.08	<0.078	0.05
28.11.2013	127	1597_6		7.60	438	1412	4.31	0.38	0.55	11687	427.43	229	0.44	9.92	0.04	<0.028	<0.022	<0.046	<0.078	0.06
09.01.2014	169	1597_7		7.79	477	1537	4.96	0.80	0.48	12478	460.73	237	0.43	10.85	0.05	<0.028	<0.022	<0.046	<0.078	0.06
13.02.2014	204	1597_8		7.86	426	1368	4.92	0.49	0.63	11112	421.80	210	0.41	8.99	0.04	<0.028	<0.022	<0.046	<0.078	0.05
26.03.2014	246	1597_9		7.98	441	1407	5.44	0.29	0.39	11423	426.32	219	0.40	9.99	0.05	<0.028	<0.022	<0.046	<0.078	0.04
13364-0051	**0.00**	**original solution**		**6.20**	**454**	**1447**	**<0.416**	**<0.061**	**0.29**	**11646**	**438.80**	**225**	**0.88**	**9.20**	**<0.014**	**<0.028**	**0.04**	**<0.046**	**0.08**	**<0.036**
12.08.2013	17	1598_1	CO_2 Harzburgite	6.97	475	1647	113.31	0.59	0.39	11165	411.42	216	0.29	9.91	1.57	0.05	0.14	1.99	0.09	0.18
27.08.2013	33	1598_2		6.82	534	1898	142.33	0.19	0.30	12120	463.29	232	0.22	10.28	2.13	<0.028	0.13	2.56	0.10	0.16
26.09.2013	63	1598_4		6.60	506	1724	108.80	1.16	<0.197	12187	457.14	230	0.33	10.70	1.16	<0.028	0.14	2.09	0.21	0.16
24.10.2013	92	1598_5		6.80	494	1822	136.08	0.22	0.24	11764	433.58	220	0.32	10.34	1.94	<0.028	0.15	2.70	0.13	0.10
28.11.2013	127	1598_6		7.10	488	1882	139.08	0.19	0.32	11242	425.65	219	0.28	9.34	2.38	<0.028	0.13	2.82	0.08	0.12
09.01.2014	169	1598_7		7.49	529	2170	129.32	0.11	0.31	12580	464.78	243	0.32	10.39	2.90	<0.028	0.13	3.11	0.22	0.09
13.02.2014	204	1598_8		7.19	492	2091	144.19	0.10	0.34	11886	430.68	225	0.34	10.43	3.09	<0.028	0.14	3.10	<0.078	0.11
26.03.2014	246	1598_9		7.22	476	2044	139.24	0.14	<0.197	11130	417.17	215	0.33	9.56	3.21	<0.028	0.15	2.88	<0.078	0.10
13364-0051	**0.00**	**original solution**		**6.20**	**454**	**1447**	**<0.416**	**<0.061**	**0.29**	**11646**	**438.80**	**225**	**0.88**	**9.20**	**<0.014**	**<0.028**	**0.04**	**<0.046**	**0.08**	**<0.036**
12.08.2013	17	1599_1	N_2 Serpentinite	7.91	275	1514	1.04	<0.061	<0.197	11961	449.71	227	0.42	6.63	<0.014	0.31	0.04	<0.046	0.09	0.07
27.08.2013	33	1599_2		8.01	215	1489	1.22	<0.061	<0.197	11980	447.69	227	0.42	5.46	<0.014	0.34	0.04	<0.046	<0.078	0.06
12.09.2013	49	1599_3		8.06	180	1509	1.49	0.10	<0.197	12134	439.12	226	0.45	4.75	<0.014	0.33	0.04	<0.046	<0.078	<0.036
26.09.2013	63	1599_4		8.02	161	1555	1.76	0.09	0.26	12101	447.74	224	0.42	4.43	<0.014	0.33	0.03	<0.046	<0.078	0.05
24.10.2013	92	1599_5		8.08	124	1482	1.96	0.10	0.26	11556	436.82	209	0.39	3.66	<0.014	0.33	<0.022	<0.046	<0.078	0.05
28.11.2013	127	1599_6		8.10	107	1509	2.30	<0.061	<0.197	12012	438.08	216	0.40	3.30	0.07	0.25	0.03	0.05	0.23	0.04
09.01.2014	169	1599_7		8.15	97	1526	3.10	0.07	<0.197	12063	456.25	212	0.43	3.10	0.01	0.22	<0.022	0.05	<0.078	0.04
13.02.2014	204	1599_8		8.35	94	1479	4.37	<0.061	0.28	11631	437.78	204	0.42	3.01	<0.014	0.24	<0.022	<0.046	0.13	<0.036

26.03.2014	246	1599_9		8.37	89	1372	5.23	0.20	<0.197	11090	407.32	192	0.37	2.80	0.11	<0.028	0.03	0.10	0.14	0.05
13364-0051	**0**	**original solution**		**6.20**	**454**	**1447**	**<0.416**	**<0.061**	**0.29**	**11646**	**438.80**	**225**	**0.88**	**9.20**	**<0.014**	**<0.028**	**0.04**	**<0.046**	**0.08**	**<0.036**
12.08.2013	17	1600_1		7.65	140	4171	48.56	<0.061	<0.197	12689	475.46	261	0.05	2.71	1.00	<0.028	0.16	2.62	<0.078	0.08
27.08.2013	33	1600_2		7.71	42	4661	39.28	<0.061	<0.197	12074	443.84	254	0.02	0.68	0.26	<0.028	0.13	1.77	<0.078	<0.036
12.09.2013	49	1600_3	CO_2 Serpentinite	7.63	35	4899	39.25	0.07	<0.197	11885	455.67	253	0.02	0.56	0.05	<0.028	0.06	1.28	<0.078	<0.036
26.09.2013	63	1600_4		7.58	60	5067	40.82	<0.061	<0.197	12564	465.47	267	0.02	1.50	0.08	<0.028	0.07	1.13	<0.078	0.04
24.10.2013	92	1600_5		7.60	92	4689	39.30	<0.061	<0.197	12125	453.62	257	0.37	6.33	<0.014	<0.028	0.03	0.67	<0.078	<0.036
28.11.2013	127	1600_6		7.60	28	3984	35.69	<0.061	0.22	11222	425.51	237	0.40	6.35	0.13	<0.028	0.03	0.36	<0.078	<0.036
09.01.2014	169	1600_7		7.74	36	3616	39.70	<0.061	<0.197	11453	433.81	245	0.37	6.76	0.17	<0.028	0.04	0.31	<0.078	<0.036
13.02.2014	204	1600_8		7.59	82	3275	142.22	0.18	<0.197	11435	429.94	243	0.34	7.08	0.11	<0.028	0.03	0.26	<0.078	<0.036
26.03.2014	246	1600_9		7.42	97	3041	134.15	0.14	<0.197	11166	415.29	243	0.34	7.32	0.09	<0.028	0.05	0.21	0.09	0.04

D.4. Concentration of anions in liquid samples extracted from long term experiments, as determined by Ion Chromatography (IC). Multiply the values by 4!!!! Apart from the higher one!

Date of sampling	Time interval	Sample code	Cl^- mg l^{-1}	SO_4^{2-} mg l^{-1}	NO_3^- mg l^{-1}	Br^- mg l^{-1}	NO_2^- mg l^{-1}	HPO_4^{2-} mg l^{-1}	F^- mg l^{-1}
Dunite N_2		**Starting fluid**	20940	**153**	**<12**	**<4**	**<2**	**<4**	**<2**
12.08.2013	17	1595_1	20100	163	<12	<4	<2	<4	<2
27.08.2013	33	1595_2	21416	176	<12	<4	<2	<4	<2
12.09.2013	49	1595_3	20860	176	<12	<4	<2	<4	<2
26.09.2013	63	1595_4	21504	182	<12	<4	<2	<4	<2
24.10.2013	92	1595_5	21344	179	<12	<4	<2	<4	<2
28.11.2013	127	1595_6	21036	185	<12	<4	<2	<4	<2
Dunite CO_2		**Starting fluid**	**20940**	153	**<12**	**<4**	**<2**	**<4**	**<2**
12.08.2013	17	1596_1	19900	151	<12	<4	<2	<4	<2
27.08.2013	33	1596_2	21320	163	<12	<4	<2	<4	<2
12.09.2013	49	1596_3	21020	162	<12	<4	<2	<4	<2
26.09.2013	63	1596_4	20980	164	<12	<4	<2	<4	<2
24.10.2013	92	1596_5	21208	169	<12	<4	<2	<4	<2
			Cl^-	**SO_4^{2-}**	**NO_3^-**	**Br^-**	**NO_2^-**	**HPO_4^{2-}**	**F^-**

28.11.2013	127	1596_6	21120	165	<12	<4	<2	<4	<2
09.01.2014	246	1596_9	21106	734	<12	<4	<2	<4	<2
Harzburgite N_2		**Starting fluid**	**20940**	**153**	**<12**	**<4**	**<2**	**<4**	**<2**
12.08.2013	17	1597_1	19844	146	<12	<4	<2	<4	<2
27.08.2013	33	1597_2	21248	162	<12	<4	<2	<4	<2
12.09.2013	49	1597_3	21596	163	<12	<4	<2	<4	<2
26.09.2013	63	1597_4	20864	163	<12	<4	<2	<4	<2
24.10.2013	92	1597_5	21164	165	<12	<4	<2	<4	<2
28.11.2013	127	1597_6	21400	163	<12	<4	<2	<4	<2
26.03.2014	246	1597_9	21143	676	<12	<4	<2	4.44	<2
Harzburgite CO_2		**Starting fluid**	**20940**	**153**	**<12**	**<4**	**<2**	**<4**	**<2**
12.08.2013	17	1598_1	20960	156	<12	<4	<2	<4	<2
27.08.2013	33	1598_2	21148	162	<12	<4	<2	<4	<2
26.09.2013	63	1598_4	20760	157	<12	<4	<2	<4	<2
24.10.2013	92	1598_5	20992	159	<12	<4	<2	<4	<2
28.11.2013	127	1598_6	20820	155	<12	<4	<2	<4	<2
26.03.2014	246	1598_9	20956	657	<12	<4	<2	<4	<2
Serpentinite N_2		**Starting fluid**	**20940**	**153**	**<12**	**<4**	**<2**	**<4**	**<2**
12.08.2013	17	1599_1	19728	156	<12	<4	<2	<4	<2
27.08.2013	33	1599_2	20504	154	<12	<4	<2	<4	<2
12.09.2013	49	1599_3	20644	153	<12	<4	<2	<4	<2
26.09.2013	63	1599_4	20416	147	<12	<4	<2	<4	<2
24.10.2013	92	1599_5	20648	154	<12	<4	<2	<4	<2
28.11.2013	127	1599_6	20772	148	<12	<4	<2	<4	<2
26.03.2014	246	1599_9	20772	631	<12	<4	<2	<4	<2
Serpentinite CO_2		**Starting fluid**	**20940**	**153**	**<12**	**<4**	**<2**	**<4**	**<2**
12.08.2013	17	1600_1	20388	156	<12	<4	<2	<4	<2
27.08.2013	33	1600_2	20748	155	<12	<4	<2	<4	<2
12.09.2013	49	1600_3	21056	160	<12	<4	<2	<4	<2
26.09.2013	63	1600_4	20752	154	<12	<4	<2	<4	<2
28.11.2013	127	1600_6	21188	169	<12	<4	<2	<4	<2
26.03.2014	246	1600_9	21242	729	<12	<4	<2	<4	<2

IC was performed by the BGS Analytical Geochemistry Laboratories; the samples were analysed as received at 400x dilution which has been corrected for.

Analysis Details:

Determinands	Test Method	Procedure	Notes
Cl^-, SO_4^{2-}, NO_3^-, NO_2^-, Br^-, F^-, HPO_4^{2-}	Ion chromatography	AG 2.3.19	UKAS

D.5. Whole rock XRF analysis data of starting materials and reaction residues of eight-months carbonation experiments. Major element data is reported to two decimal places, sulphur to only one due to potential loss during sample preparation resulting in greater uncertainty. The XRF instrument was calibrated using units of Fe_2O_3 hence the total iron data is reported as

Fe_2O_3t. For the following elements the values were below detection: P <0.01%, Sr <0.01%, Zr <0.02%, Ba <0.02%, Cu <0.01%, Zn <0.01%, Hf <0.01% and F <0.01% and are not included in the table.

Description	Sample name	Vessel	SiO_2 wt%	MgO wt%	Al_2O_3 wt%	Fe_2O_3t wt%	Mn_3O_4 wt%	CaO %	TiO_2 wt%	Na_2O %	K_2O %	SO_3 %	Cr_2O_3 wt%	NiO wt%	PbO %	V_2O_5 %	Cl %	Total %	LOI %
Dunite start			**35.06**	**44.43**	**0.23**	**7.52**	**0.11**	**0.14**	**<0.01**	**<0.05**	**<0.01**	**0.1**	**0.86**	**0.25**	**<0.01**	**<0.01**	**<0.1**	**88.70**	**12.15**
Dunite T	**MPLU614**	N_2 t	34.83	44.21	0.23	7.46	0.11	0.14	<0.01	<0.05	<0.01	<0.1	0.85	0.25	<0.01	<0.01	<0.1	88.08	12.58
Dunite 3	**MPLU615**	N_2 b	35.23	44.56	0.23	7.54	0.11	0.14	<0.01	<0.05	<0.01	<0.1	0.85	0.25	<0.01	<0.01	0.10	89.01	12.34
Dunite 2	**MPLU617**	CO_2 t	34.64	43.56	0.27	7.48	0.11	0.14	0.01	<0.05	<0.01	<0.1	0.99	0.24	<0.01	<0.01	<0.1	87.44	13.51
Dunite 1	**MPLU618**	CO_2 b	36.62	44.12	0.39	7.90	0.11	0.19	<0.01	<0.05	<0.01	<0.1	0.88	0.26	<0.01	<0.01	<0.1	90.47	12.64
Harzburgite start			**40.82**	**38.24**	**2.06**	**8.38**	**0.13**	**2.04**	**0.04**	**<0.05**	**<0.01**	**<0.1**	**0.37**	**0.27**	**<0.01**	**0.01**	**<0.1**	**92.36**	**8.22**
Hzb 2	**MPLU619**	N_2 t	40.94	37.93	2.14	8.31	0.13	2.26	0.04	<0.05	<0.01	<0.1	0.39	0.27	<0.01	0.01	<0.1	92.42	8.27
Hzb 4	**MPLU620**	N_2 b	40.76	38.52	1.97	8.40	0.13	2.18	0.04	0.05	<0.01	<0.1	0.35	0.27	<0.01	0.01	<0.1	92.68	8.41
Hzb 1	**MPLU621**	CO_2 t	40.52	37.85	2.06	8.22	0.12	2.38	0.05	<0.05	<0.01	<0.1	0.37	0.26	0.01	0.01	<0.1	91.85	8.57
Hzb 3	**MPLU622**	CO_2 b	41.47	37.67	2.15	8.52	0.12	2.60	0.04	0.07	<0.01	<0.1	0.39	0.27	<0.01	0.02	<0.1	93.32	7.66
Serpentinite start			**34.10**	**39.56**	**0.30**	**8.27**	**0.13**	**0.17**	**<0.01**	**<0.05**	**<0.01**	**<0.1**	**0.52**	**0.20**	**<0.01**	**<0.01**	**<0.1**	**83.25**	**17.85**
Srp 1	**MPLU623**	N_2 t	34.31	38.98	0.31	7.88	0.12	0.30	0.01	<0.05	<0.01	<0.1	0.49	0.20	<0.01	<0.01	<0.1	82.60	17.85
Srp 5	**MPLU624**	N_2 b	33.36	39.17	0.32	8.33	0.12	0.61	0.01	<0.05	<0.01	<0.1	0.59	0.20	<0.01	<0.01	0.50	83.21	18.50
Srp 4	**MPLU625**	CO_2 t	31.18	37.11	0.18	9.08	0.14	0.25	<0.01	<0.05	<0.01	<0.1	0.31	0.17	<0.01	<0.01	<0.1	78.42	22.56
Srp 2	**MPLU626**	CO_2 b	37.37	35.19	0.35	8.97	0.11	0.58	0.01	0.27	0.01	<0.1	0.53	0.21	<0.01	<0.01	0.20	83.80	17.31

**t – top of the vessel, gaseous phase*

**b – bottom of the vessel, liquid phase*

Appendix E

Repeatability of short-term acid-leaching experiments

To assess experimental repeatability, four samples were run as duplicates and one sample was run three times, under the same experimental conditions, *i.e.* the same reactive fluid, temperature and pressure. Discrepancies between the duplicates may have been related to experimental factors such as: weight of solid sample input into the experimental vessel resulting in variable solid : liquid ratio, exact time of fluid-rock interaction and degree of solid agitation inside the vessel.

Experimental repeatability was appraised on the basis on XRF data of reaction residues and is presented in Figure E.1 and Table E.1. The experimental repeatability was assessed to be good generally, apart from one outlier in sample AML62 returning significantly different values. In addition to the experimental factors, this discrepancy may have been related to inhomogeneity of the staring solid material.

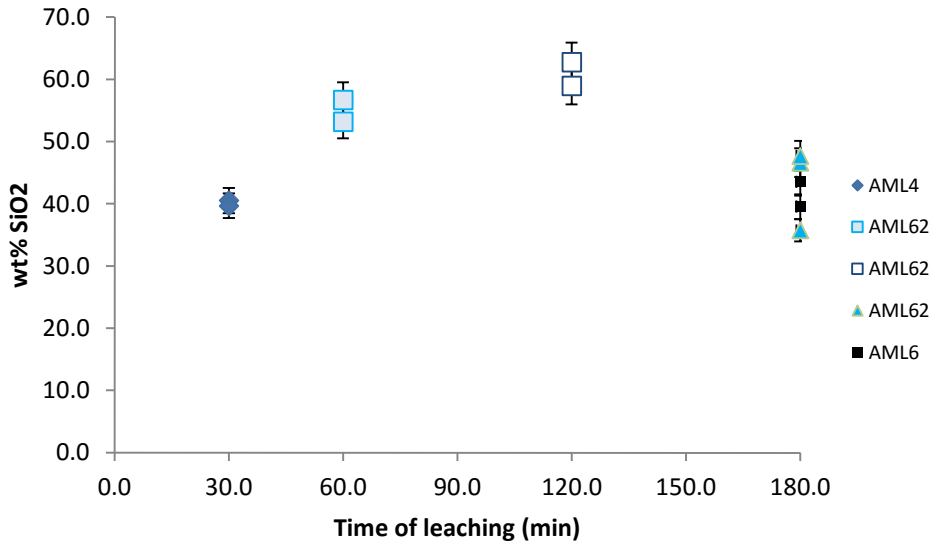


Figure E.1. The repeatability of short term acid leaching experiment based on XRF measurement of SiO_2. The same symbols represent sample duplicates, i.e. AML4 – lizardite 1T, 30 min residuum; AML62 – polygonal serpentine, 60, 120 and 180 min residuum; AML6 – chrysotile, 180 min residuum. The error bars are related to the 5% error associated with XRF analysis. Comparable results were obtained for other analysed elements, as summarised in Table D.1.

Table E.1. XRF data of experimental duplicates as indicator of experimental repeatability. Data for SiO_2 is plotted in Figure D.1.

Sample duplicates	Time of leaching	SiO_2	TiO_2	Al_2O_3	Fe_2O_{3t}	Mn_3O_4	MgO	CaO	Na_2O	K_2O	P_2O_5	SO_3	Cr_2O_3	Total	LOI
AML4	30	40.5	<0.01	2.77	3.99	0.03	37.09	<0.01	<0.05	<0.01	<0.01	1.9	<0.01	86.3	17.3
AML4	30	39.7	<0.01	2.69	3.85	0.03	35.83	<0.01	<0.05	<0.01	<0.01	2.4	0.01	84.5	17.9
AML4	180	43.5	0.01	0.04	11.52	0.06	20.81	<0.01	<0.05	<0.01	<0.01	7.6	0.01	75.1	31.9
AML6	180	39.6	0.01	0.09	11.92	0.07	12.28	<0.01	<0.05	<0.01	<0.01	6.3	0.01	78.8	26.8
AML62	60	53.2	0.0	1.11	5.48	0.05	21.81	<0.01	<0.05	<0.01	<0.01	2.3	0.40	84.5	18.5
AML62	60	56.7	0.0	1.21	5.70	0.05	22.36	<0.01	<0.05	<0.01	<0.01	<0.1	0.46	86.6	14.2
AML62	120	58.9	0.0	1.09	4.58	0.04	15.76	<0.01	<0.05	<0.01	<0.01	2.4	0.42	83.3	19.0
AML62	120	62.8	0.0	1.15	4.78	0.03	16.04	<0.01	<0.05	<0.01	<0.01	<0.1	0.44	85.3	14.6
AML62	180	35.73	<0.01	1.49	1.59	0.01	19.63	<0.01	<0.05	<0.01	<0.01	13.1	<0.01	71.55	39.97
AML62	180	46.61	<0.01	1.76	1.86	0.01	22.95	<0.01	<0.05	<0.01	<0.01	6.4	<0.01	79.59	26.76
AML62	180	47.70	<0.01	1.81	1.91	0.01	23.46	<0.01	<0.05	<0.01	<0.01	5.5	<0.01	80.39	25.41

References

- Adler, H. H., and P. F. Kerr (1963) "Infrared spectra, symmetry and structure relations of some carbonate minerals" The American Mineralogist, 48 (July-August), 839-853.
- Alexander, G., M. M. Maroto-Valer, and P. Gafarova-Aksoy (2007) "Evaluation of reaction variables in the dissolution of serpentine for mineral carbonation" Fuel, 86 (1-2), 273-281.
- Alfredsson, H. A., B. S. Hardarson, H. Franzson, and S. R. Gislason (2008) "CO_2 sequestration in basaltic rock at the Hellisheidi site in SW Iceland: stratigraphy and chemical composition of the rocks at the injection site" Mineralogical Magazine, 72 (1), 1-5.
- Alves dos Anjos, A. P., A. Sifeddine, C. J. Sanders, and S. R. Patchineelam (2011) "Synthesis of magnesite at low temperature" Carbonates and Evaporites, 26 (3), 213-215.
- Amouric, M., and A. Baronnet (1983) "Effect of early nucleation conditionss on synthetic muscovite polytypism as seen by high resolution transmission electron microscopy" Physics and Chemistry of Minerals, 9 (3-4), 146-159.
- Anbalagan, G., G. Sivakumar, A. R. Prabakaran, and S. Gunasekaran (2010) "Spectroscopic characterization of natural chrysotile" Vibrational Spectroscopy, 52 (2), 122-127.
- Aradottir, E. S. P., and E. Gunnlaugsson (2013) "CarbFix and SulFix sequestration project" GEORG W2V seminar, May 8th 2013.
- American Society for Testing Materials (ASTM). Standard Guide for Quantitative Analysis by Energy-Dispersive Spectroscopy, ASTM E1508-12a.
- Baciocchi, R., A. Polettini, R. Pomi, V. Prigiobbe, V. N. Von Zedwitz, and A. Steinfeld (2006) "CO_2 sequestration by direct gas-solid carbonation of air pollution control (APC) residues" Energy & Fuels, 20 (5), 1933-1940.
- Bailey, S. W. (1969) "Polytypism of trioctahedral 1:1 layer silicates" Clays and Clay Minerals, 17, 355-371.
- Bailey, S. W. (1988) "X-ray diffraction identification of the polytypes of mica, serpentine and chlorite" Clays and Clay Minerals, 36 (3), 193-213.
- Bailey, S. W., and J. F. Banfield (1995) "Derivation and identification of nonstandard serpentine polytypes" American Mineralogist, 80 (11-12), 1104-1115
- Balan, E., A. M. Saitta, F. Mauri, C. Lemaire, and F. Guyot (2002) "First-principles calculation of the infrared spectrum of lizardite" American Mineralogist, 87 (10), 1286-1290.
- Ballirano, P., C. De Vito, S. Mignardi, and V. Ferrini (2013) "Phase transitions in the Mg-CO_2-H_2O system and the thermal decomposition of dypingite, $Mg_5(CO_3)_4(OH)_2$ center x $5H_2O$: Implications for geosequestration of Carbon dioxide" Chemical Geology, 340, 59-67.
- Banfield, J. F., S. W. Bailey, W. W. Barker, and R. C. Smith (1995) "Complex polytypism: Relationships between serpentine structural characteristics and deformation" American Mineralogist, 80 (11-12), 1116-1131.

- Barnes, I., J. R. Oneil, and J. J. Trescases (1978) "Present day serpentinisation in New-Caledonia, Oman and Yugoslavia" Geochimica Et Cosmochimica Acta, 42 (1), 144-145.
- Baronnet, A., M. Mellini, and B. Devouard (1994) "Sectors in polygonal serpentine - a model based on dislocations" Physics and Chemistry of Minerals, 21 (5), 330-343.
- Bearat, H., M. J. McKelvy, A. V. G. Chizmeshya, R. Sharma, and R. W. Carpenter (2002) "Magnesium hydroxide dehydroxylation/carbonation reaction processes: Implications for carbon dioxide mineral sequestration" Journal of the American Ceramic Society, 85 (4), 742-748.
- Beckman and Coulter (2011) LS 13 320 Laser Diffraction Particle Size AnalyserRep.
- Bishop, J., E. Murad, and M. D. Dyar (2002) "The influence of octahedral and tetrahedral cation substitution on the structure of smectites and serpentines as observed through infrared spectroscopy" Clay Minerals, 37 (4), 617-628.
- Bodenan, F., F. Bourgeois, C. Petiot, T. Auge, B. Bonfils, C. Julcour-Lebigue, F. Guyot, A. Boukary, J. Tremosa, A. Lassin, E. C. Gaucher, P. Chiquet (2014) "*Ex situ* mineral carbonation for CO_2 mitigation: Evaluation of mining waste resources, aqueous carbonation processability and life cycle assessment (Carmex project)" Minerals Engineering, 59, 52-63.
- Boillot, G., S. Grimaud, A. Mauffret, D. Mougenot, J. Kornprobst, J. Mergoildaniel, and G. Torrent (1980) "Ocean-continent boundary off the Iberian Margin – a serpentinite diapir west of the Galicia Bank" Earth and Planetary Science Letters, 48 (1), 23-34.
- Bonati, E., and P. R. Hamlyn (1981) "Oceanic ultramafic rocks, The Sea, The oceanic lithosphere, edited by Cesare Emiliani" 7, 241-283.
- Bordeaux, N. (2011), Backscattered Electron Emission, power point presentation.
- Boschi, C., A. Dini, L. Dallai, G. Ruggieri, and G. Gianelli (2009) "Enhanced CO_2-mineral sequestration by cyclic hydraulic fracturing and Si-rich fluid infiltration into serpentinites at Malentrata (Tuscany, Italy)" Chemical Geology, 265 (1-2), 209-226.
- Boschi, C., A. Dini, F. Bedini, I. Baneschi, C. Natali, and L. Dallai (2013) "Carbonation of serpentine mine tailings: the example of Montecastelli mine (Tuscani, Italy)" paper presented at Goldschmidt 2013, Florence, Italy.
- Brantley, S. L., Mellott, N. P. (2000) "Surface area and porosity of primary silicate minerals". American Mineralogist, 85, 1767-1783
- Brantley, S. L., J. D. Kubicki, and A. F. White (2008) "Kinetics of water-rock interaction" Book, 833 pp., Springer Science+Business Media, New York, NY 10013.
- Bromiley, G. D., and A. R. Pawley (2003) "The stability of antigorite in the systems MgO-SiO_2-H_2O (MSH) and MgO-Al_2O_3-SiO_2-H_2O (MASH): The effects of Al^{3+} substitution on high-pressure stability" American Mineralogist, 88 (1), 99-108.
- Butt, D. P., K. S. Lackner, C. H. Wendt, S. D. Conzone, H. Kung, Y. C. Lu, and J. K. Bremser (1996), "Kinetics of thermal dehydroxylation and carbonation of magnesium hydroxide" Journal of the American Ceramic Society, 79 (7), 1892-1898.
- Buttner, W., and R. Saager (1982) "Rapid XRD determination of the chrysotile lizardite ratios in asbestos-bearing serpentinites" Tschermaks Mineralogische Und Petrographische Mitteilungen, 30 (3), 177-187.
- Capitani, G., and M. Mellini (2004) "The modulated crystal structure of antigorite: The m=17 polysome" American Mineralogist, 89 (1), 147-158.
- Caruso, L. J., and J. V. Chernosky, Jr. (1979) "The stability of lizardite" Canadian Mineralogist, 17, 757-769.
- Case, D. H., F. Wang, and D. E. Giammar (2011) "Precipitation of Magnesium Carbonates as a Function of Temperature, Solution Composition, and Presence of a Silicate Mineral Substrate" Environmental Engineering Science, 28(12), 881-889.

- Cavallo, A., and B. Rimoldi (2013) "Chrysotile asbestos in serpentinite quarries: a case study in Valmalenco, Central Alps, Northern Italy" Environmental Science-Processes & Impacts, 15(7), 1341-1350.
- Chen, Z.-Y., W. K. O'Connor, and S. J. Gerdemann (2006) "Chemistry of aqueous mineral carbonation for carbon sequestration and explanation of experimental results" Environmental Progress, 25 (2), 161-166.
- Christ, C. L., and P. B. Hotetler (1970) "Studies in the system MgO-SiO_2-CO_2-H_2O (II): The activity-product constant of magnesite" American Journal of Science, 268, 439-453.
- CO_2Now.org, edited, http://co2now.org/Current-CO2/CO2-Now/global-carbon-emissions.html.
- Coleman, R. G. (1971) "Petrologic and geophysical nature of serpentinites" Geological Society of America Bulletin, 82 (4), 897-&.
- Cressey, G., B. A. Cressey, and F. J. Wicks (2008) "Polyhedral serpentine: a spherical analogue of polygonal serpentine" Mineralogical Magazine 72 (6), 1229-1242.
- Cressey, G., B. A. Cressey, and F. J. Wicks (2008) "The significance of the aluminium content of a lizardite at the nanoscale: the role of clinochlore as an aluminium sink" Mineralogical Magazine, 72 (3), 817-825.
- Culka, A., J. Jehlicka, and I. Nemec (2009) "Raman and infrared spectroscopic study of boussingaultite and nickelboussingaultite" Spectrochimica Acta Part a-Molecular and Biomolecular Spectroscopy, 73 (3), 420-423.
- DaCosta, H. F., M. Fan, and A. T. Russell (2010) "Method to sequester CO_2 as mineral carbonate" United States Patent Application Publication, US2010/0221163 A1.
- Daval, D., et al. (2011) "Influence of amorphous silica layer formation on the dissolution rate of olivine at 90 degrees C and elevated pCO_2" Chemical Geology, 284 (1-2), 193-209.
- Daval, D., R. Hellmann, I. Martinez, S. Gangloff, and F. Guyot (2013) "Lizardite serpentine dissolution kinetics as a function of pH and temperature, including effects of elevated pCO_2" Chemical Geology, 351, 245-256.
- Davies, P. J., and B. Bubela (1973) "The transformation of nesquehonite into hydromagnesite" Chemical Geology, 12, 289-300.
- Deer, W. A., R. A. Howie, and J. Zussman (2009) "Rock-forming minerals. Layered silicates excluding micas and clay minerals" Published by Geological Society, 3B, 314.
- DePaolo, D. J., and D. R. Cole (2013) "Geochemistry of Geologic Carbon Sequestration: An Overview, in Geochemistry of Geologic CO_2 Sequestration" edited by D. J. DePaolo, D. R. Cole, A. Navrotsky and I. C. Bourg, pp. 1-14.
- Dick, H. J. B., J. Lin, and H. Schouten (2003) "An ultraslow-spreading class of ocean ridge" Nature, 426 (6965), 405-412.
- Dilek, Y., and H. Furnes (2011) "Ophiolite genesis and global tectonics: Geochemical and tectonic fingerprinting of ancient oceanic lithosphere" Geological Society of America Bulletin, 123 (3-4), 387-411.
- Drever, J. I., K. M. Murphy, and D. W. Clow (1994) "Field weathering rates versus laboratory dissolution rates: an update" Mineralogical Magazine, *58A*.
- Eloneva, S., S. Teir, J. Salminen, C.-J. Fogelholm, and R. Zevenhoven (2008) "Fixation of CO_2 by carbonating calcium derived from blast furnace slag" Energy, 33 (9), 1461-1467.
- Evans, B. W. (2004) "The serpentinite multisystem revisited: Chrysotile is metastable" International Geology Review, 46 (6), 479-506.
- Evans, B. W. (2010) "Lizardite versus antigorite serpentinite: Magnetite, hydrogen, and life" Geology, 38 (10), 879-882.
- Fabian, M., M. Shopska, D. Paneva, G. Kadinov, N. Kostova, E. Turianicova, J. Briancin, I. Mitov, R. A. Kleiv, and P. Balaz (2010) "The influence of attrition milling on carbon

dioxide sequestration on magnesium-iron silicate" Minerals Engineering, 23 (8), 616-620.

- Farmer, V. C. (1974) "The layer silicates" in The Infrared Spectra of Minerals, edited, pp. 331-363, The Mineralogical Society London
- Felmy, A. R., D. A. Dixon, J. Z. Hu, E. S. Ilton, K. M. Rosso, J. R. Rustad, and Z. Wang "The role of interfacial processes on mineral transformations in wet supercritical CO_2" in Proposal of project, edited, not published.
- Field CB, Barros VR, Dokken Dj, Mach KJ, Mastrandrea MD, Bilir TE, Chatterjee M, Ebi KL, Estrada YO, Genova RC, Girma B, Kissel ES, Levy AN, MacCracken S, Mastrandrea PR, White LL (2014) IPCC, Summary for Policymakers. In: Climate Change 2014: Impacts, Adaptation, and Vulnerability. Part A: Global and Sectoral Aspects. Contribution of Working Group II to the Fifth Assesment Report of the Intergovernmental Panel on Climate Change. In, vol., Cambridge University Press, Cambridge, UK and New York, USA, p 32
- Frondel, C., and C. Palache "Retgersite, $NiSO_4 \times 6H_2O$, a new mineral". Contribution from the Department of Mineralogy and Petrography, Harvard University, No 301.
- Fuchs, Y., J. Linares, and M. Mellini (1998) "Mossbauer and infrared spectrometry of lizardite-1T from Monte Fico, Elba" Physics and Chemistry of Minerals, 26 (2), 111-115.
- Garcia, A. V. (2005) "Measurement and modelling of scaling minerals" Technical University of Denmark, Lyngby.
- Gaus, I. (2010) "Role and impact of CO_2-rock interactions during CO_2 storage in sedimentary rocks" International Journal of Greenhouse Gas Control, 4(1), 73-89.
- Giacomini, F., V. Boerio, S. Polattini, M. Tiepolo, R. Tribuzio, and A. Zanetti (2010) "Evaluating asbestos fibre concentration in metaophiolites: a case study from the Voltri Massif and Sestri-Voltaggio Zone (Liguria, NW Italy)" Environmental Earth Sciences, 61 (8), 1621-1639.
- Giammar, D. E., R. G. Bruant, and C. A. Peters (2005) "Forsterite dissolution and magnesite precipitation at conditions relevant for deep saline aquifer storage and sequestration of carbon dioxide" Chemical Geology, 217 (3-4), 257-276.
- Gillespie, M. R., and M. T. Styles (1999), BGS rock Classification Scheme, British Geological Survey Research Report, 2nd edition (RR 99-06), 52.
- Gislason, S. R., et al. (2010) "Mineral sequestration of carbon dioxide in basalt: A pre-injection overview of the CarbFix project" International Journal of Greenhouse Gas Control, 4(3), 537-545.
- Gislason, S. R., and E. H. Oelkers (2014), "Carbon Storage in Basalt" Science, *344*(6182), 373-374.
- Gladney, E. S., and I. Roelandts (1988) "1987 Compilation of elemental concentration data for USGS BHVO-1, MAG-1, QLO-1, RGM-1, SCO-1, SDC-1, SGR-1 AND STM-1" Geostandards Newsletter, 12 (2), 253-362.
- Global, CCS, Institute (2014), website http://www.globalccsinstitute.com/
- Greenpeace (2014), 15 key findings from the IPCC mitigation report, edited, http://www.greenpeace.org.uk/newsdesk/energy/news/15-key-findings-ipcc-mitigation-report
- Gregorkiewitz, M., B. Lebech, M. Mellini, and C. Viti (1996) "Hydrogen positions and thermal expansion in lizardite-1T from Elba: A low-temperature study using Rietveld refinement of neutron diffraction data" American Mineralogist, 81 (9-10), 1111-1116.
- Gualtieri, A. F., and G. Artioli (1995) "Quantitative determination of chrysotile asbestos in bulk materials by combined Rietveld and RIR methods" Powder Diffraction, 10 (4), 269-277.

- Gualtieri, A. F., C. Giacobbe, and C. Viti (2012) "The dehydroxylation of serpentine group minerals" American Mineralogist, 97(4), 666-680
- Gualtieri, A. F., S. Pollastri, N. Bursi Gandolfi, F. Ronchetti, C. Albonice, A. Cavallo, G. Zanetti, P. Marini, and O. Sala (2014) "Determination of the concentration of asbestos minerals in highly contaminated mine tailings: An example from abandoned mine waste of Cretaz and Emarese (Valle d'Aosta, Italy)" American Mineralogist, 99.
- Hänchen, M., V. Prigiobbe, R. Baciocchi, and M. Mazzotti (2008) "Precipitation in the Mg-carbonate system - effects of temperature and CO_2 pressure" Chemical Engineering Science, 63(4), 1012-1028.
- Hänchen, M., V. Prigiobbe, R. Baciocchi, and M. Mazzotti (2008) "Precipitation in the Mg-carbonate system - effects of temperature and CO_2 pressure" Chemical Engineering Science, 63 (4), 1012-1028.
- Hellmann, R., C. M. Eggleston, M. F. Hochella, and D. A. Crerar (1990) "The formaiton of leached layers on albite surfaces during dissolution under hydrothermal conditions" Geochimica Et Cosmochimica Acta, 54 (5), 1267-1281.
- Hellmann, R., J. C. Dran, and G. DellaMea (1997) "The albite-water system .3. Characterization of leached and hydrogen-enriched layers formed at 300°C using MeV ion beam techniques" Geochimica Et Cosmochimica Acta, 61 (8), 1575-1594.
- Hellmann, R., J. M. Penisson, R. L. Hervig, J. H. Thomassin, and M. F. Abrioux (2003) "An EFTEM/HRTEM high-resolution study of the near surface of labradorite feldspar altered at acid pH: evidence for interfacial dissolution-reprecipitation" Physics and Chemistry of Minerals, 30 (4), 192-197.
- Hess, H. H., R. J. Smith, and G. Dengo (1952) "Antigorite from the vicinity of Caracas, Venezuela" American Mineralogist, 37 (68), 8.
- Hopkinson, L., K. Rutt, and G. Cressey (2008) "The transformation of nesquehonite to hydromagnesite in the system CaO-MgO-H_2O-CO_2: An experimental spectroscopic study" Journal of Geology, 116 (4), 387-400.
- Hovelmann, J., H. Austrheim, and B. Jamtveit (2012) "Microstructure and porosity evolution during experimental carbonation of a natural peridotite" Chemical Geology, 334, 254-265.
- Hovelmann, J., H. Austrheim, A. Beinlich, and I. A. Munz (2011) "Experimental study of the carbonation of partially serpentinized and weathered peridotites" Geochimica Et Cosmochimica Acta, 75 (22), 6760-6779.
- Huijgen, W. J. J., and R. N. J. Comans (2003a) "Carbon dioxide sequestration by mineral carbonation_Literature review" Unpublished report, part of PhD thesis.
- Huijgen, W. J. J., and R. N. J. Comans (2003b) "Carbon dioxide sequestration by mineral carbonation_Literature review Update 2003-2004" Unpublished report, part of PhD thesis.
- Jacobs, A. D., and M. Hitch (2011) "Experimental mineral carbonation: approaches to accelerate CO_2 sequestration in mine waste materials" International Journal of Mining Reclamation and Environment, 25(4), 321-331.
- Johnson, N. C., B. Thomas, K. Maher, R. J. Rosenbauer, D. Bird, and G. E. Brown, Jr. (2014) "Olivine dissolution and carbonation under conditions relevant for *in situ* carbon storage" Chemical Geology, 373, 93-105.
- Kaszuba, J. P., D. R. Janecky, and M. G. Snow (2005) "Experimental evaluation of mixed fluid reactions between supercritical carbon dioxide and NaCl brine: Relevance to the integrity of a geologic carbon repository" Chemical Geology, 217 (3-4), 277-293.

- Kaviratna, H., and T. J. Pinnavaia (1994) "Acid hydrolysis of octahedral Mg^{2+} sites in 2:1 layered silicates – an assessment of edge attack and gallery access mechanisms" Clays and Clay Minerals, 42 (6), 717-723.
- Kelemen PB, Matter J (2008) "*In situ* carbonation of peridotite for CO_2 storage" Proceedings of the National Academy of Sciences of the United States of America 105 (45):17295-17300 doi:10.1073/pnas.0805794105
- Kelemen, P. B., and G. Hirth (2012) "Reaction-driven cracking during retrograde metamorphism: Olivine hydration and carbonation" Earth and Planetary Science Letters, 345-348, 81-89.
- Kelemen, P. B., J. Matter, E. E. Streit, J. F. Rudge, W. B. Curry, and J. Blusztajn (2011) "Rates and Mechanisms of Mineral Carbonation in Peridotite: Natural Processes and Recipes for Enhanced, *in situ* CO_2 Capture and Storage" in Annual Review of Earth and Planetary Sciences, Vol 39, edited by R. Jeanloz and K. H. Freeman, pp. 545-576.
- Kemp, S. J., Turner, G., Wagner, D. (2009) "Initial testing and a laboratory manual for the Micrometrics Gemini VI physisorption system". British Geological Survey, Internal report, IR/08/086, 41 pp.
- Kerisit, S., J. H. Weare, and A. R. Felmy (2012) "Structure and dynamics of forsterite-scCO_2/H_2O interfaces as a function of water content" Geochimica Et Cosmochimica Acta, 84, 137-151.
- Kline, W. E., and H. S. Fogler (1981) "Dissolution kinetics-the nature of the particle attack of layered silicates in HF" Chemical Engineering Science, 36 (5), 871-884.
- Kirby, G. A. (1979) "The Lizard Complex as an ophiolite" Nature, 282, 58-61.
- Kosuge, K., K. Shimada, and A. Tsunashima (1995) "Micropore formation by acid treatment of antigorite" Chemistry of Materials, 7 (12), 2241-2246.
- Krevor, S. C., and K. S. Lackner (2009) "Enhancing Process Kinetics for Mineral Carbon Sequestration" Greenhouse Gas Control Technologies 9, 1 (1), 4867-4871.
- Krevor, S. C., C. R. Graves, B. S. Van Gosen, and A. E. McCafferty (2009) "Delineation of Magnesium-rich Ultramafic Rocks Available for Mineral Carbon Sequestration in the United States" Greenhouse Gas Control Technologies 9, 1 (1), 4915-4920.
- Krevor, S. C. M., and K. S. Lackner (2011) "Enhancing serpentine dissolution kinetics for mineral carbon dioxide sequestration" International Journal of Greenhouse Gas Control, 5 (4), 1073-1080.
- Krstanovic, I. (1997) "Serpentine mineral from Crni Kamen, Serbia" Neues Jahrbuch Fur Mineralogie-Monatshefte (10), 451-465.
- Kwak, J. H., J. Z. Hu, R. V. F. Turcu, K. M. Rosso, E. S. Ilton, C. Wang, J. A. Sears, M. H. Engelhard, A. R. Felmy, and D. W. Hoyt (2011) "The role of H_2O in the carbonation of forsterite in supercritical CO_2" International Journal of Greenhouse Gas Control, *5* (4), 1081-1092.
- Lacinska, A. M., and M. T. Styles (2013) "Silicified serpentinite - a residuum of a Tertiary palaeo-weathering surface in the United Arab Emirates" Geological Magazine, 150 (3), 385-395.
- Lacinska, A. M., M. T. Styles, and A. R. Farrant (2014) "Near surface diagenesis of ophiolite-derived conglomerates if the Barzaman Formation in the United Arab Emirates: a natural analogue for permanent CO2 sequestration via mineral carbonation of ultramafic rocks" From Rollinson, H. R., Searle, M. P., Abbasi, I. A., Al-Lazki, A. & Al Kindi, M. H. (eds). Tectonic Evolution of the Oman Mountains. Geological Society, London, Special publications, 392, 343-360.
- Lackner, K. S. (2002) "Carbonate chemistry for sequestering fossil carbon" Annual Review of Energy and the Environment 27, 193-232.

- Lackner, K. S., D. P. Butt, and C. H. Wendt (1997) "Progress on binding CO_2 in mineral substrates" Energy Conversion and Management, 38, S259-S264.
- Lackner, K. S., C. H. Wendt, D. P. Butt, E. L. Joyce, and D. H. Sharp (1995) "Carbon-dioxide disposal in carbonate minerals " Energy, 20 (11), 1153-1170.
- Langmuir, D. (1965) "Stability of carbonates in the system $MgO-CO_2-H_2O$" in The Journal of Geology, edited by E. C. Olson, The University of Chicago Press, Chicago.
- Larachi, F., I. Daldoul, and G. Beaudoin (2010) "Fixation of CO_2 by chrysotile in low-pressure dry and moist carbonation: Ex-situ and in-situ characterizations" Geochimica Et Cosmochimica Acta, 74 (11), 3051-3075.
- Larachi, F., J. P. Gravel, B. P. A. Grandjean, and G. Beaudoin (2012) "Role of steam, hydrogen and pretreatment in chrysotile gas-solid carbonation: Opportunities for pre-combustion CO_2 capture" International Journal of Greenhouse Gas Control, 6, 69-76.
- Le Maitre, R. W., et al. (2002), Igneous rocks. A classification and glossary of terms, Cambridge University Press, 2nd edition (ISBN 0 521 66215 X).
- Lin, F. C., and C. V. Clemency (1981) "The dissolution kinetics of brucite, antigorite, talc and phlogopite at room temperature and pressure" American Mineralogist, 66 (7-8), 801-806.
- Lin, P.-C., C.-W. Huang, C.-T. Hsiao, and H. Teng (2008) "Magnesium hydroxide extracted from a magnesium-rich mineral for CO_2 sequestration in a gas-solid system" Environmental Science & Technology, 42 (8), 2748-2752.
- Liu, Y., A. Wang, and J. J. Freeman (2009) RAMAN, MIR and NIR spectroscopic study of calcium sulfates: gypsum, bassanite and anhydrite., paper presented at 40th Lunar and Planetary Science Conference.
- Luce, R. W., R. W. Bartlett, and G. A. Parks (1972) "Dissolution kinetics of magnesium silicates" Geochimica Et Cosmochimica Acta, 36 (1), 35-&.
- Ludwig, C., and W. H. Casey (1996) "On the mechanisms of dissolution of bunsenite NiOs and other simple oxide minerals" Journal of Colloid and Interface Science, 178(1), 176-185.
- Macht, F., K. U. Totsche, K. Eusterhues, and G. Pronk (2010) "Topography and surface properties of clay minerals analyzed by atomic force microscopy" in 19th World COngress of Soil Science, Soil Solution for a Changing World, edited, Publiushed on DVD, Brisbane, Australia.
- Madejova, J. (2003) "FTIR techniques in clay mineral studies" Vibrational Spectroscopy, 31, 1-10.
- Malvern, Instruments, website, and http://www.malvern.com/en/products/technology/laser-diffraction/ Laser Diffraction, Particle size distributions from nanometers to milimeters, edited.
- Marion, G. M. (2001) "Carbonate mineral solubility at low temperatures in the $Na-K-Mg-Ca-H-Cl-SO_4-OH-HCO_3-CO_3-CO_2-H_2O$ system" Geochimica Et Cosmochimica Acta, 65(12), 1883-1896.
- Maroto-Valer, M. M., M. E. Kuchta, Y. Z. Zhang, J. M. Andresen, and D. J. Fauth (2004) "Comparison of physical and chemical activation of serpentine for enhanced CO_2 sequestration" Abstracts of Papers of the American Chemical Society, 227, U1095-U1095.
- Maroto-Valer, M. M., D. J. Fauth, M. E. Kuchta, Y. Zhang, and J. M. Andresen (2005) "Activation of magnesium rich minerals as carbonation feedstock materials for CO_2 sequestration" Fuel Processing Technology, 86(14-15), 1627-1645.
- Matter, J. M., and P. B. Kelemen (2009) "Enhanced *in situ* carbonation of peridotite for permanent CO_2 storage" Geochimica Et Cosmochimica Acta, 73 (13), A848-A848.

- Matter, J. M., et al. (2011) "The CarbFix Pilot Project - Storing Carbon Dioxide in Basalt" 10th International Conference on Greenhouse Gas Control Technologies, 4, 5579-5585.
- McGrail, B. P., H. T. Schaef, A. M. Ho, Y.-J. Chien, J. J. Dooley, and C. L. Davidson (2006) "Potential for carbon dioxide sequestration in flood basalts" Journal of Geophysical Research-Solid Earth, 111(B12).
- McGrail, B. P., F. A. Spane, C. R. Amonette, C. R. Thompson, and C. F. Brown (2014) "Injection and monitoring at the Wallula Basalt Pilot Project" Energy Procedia, *63*, 2939-2948.
- Mellini, M. (1982) "The crystal structure of lizardite 1T - hydrogen bonds and polytypism" American Mineralogist, 67(5-6), 587-598.
- Mellini, M., and P. F. Zanazzi (1987) "Crystal structures of lizardite 1T and lizardite 2H1 from Coli, Italy" American Mineralogist, 72 (9-10), 943-948.
- Mellini, M., and C. Viti (1994) "Crystal structure of lizardite-1T from Elba, Italy" American Mineralogist, 79 (11-12), 1194-1198.
- Mellini, M., Y. Fuchs, C. Viti, C. Lemaire, and J. Linarès (2002) "Insights into the antigorite structure from Mössbauer and FTIR spectroscopies" European Journal of Mineralogy, 14 (1), 97-104.
- Mellini, M., G. Cressey, F. J. Wicks, and B. A. Cressey (2010) "The crystal structure of Mg end-member lizardite-IT forming polyhedral spheres from the Lizard, Cornwall" Mineralogical Magazine, 74 (2), 277-284.
- Mellini, M. (2013) "Structure and microstructure of serpentine minerals" in Minerals at the Nanoscale, edited by F. Nieto and K. J. T. Livi, pp. 153-179.
- Melezhik, V. A., A. E. Fallick, P. V. Medvedev, and V. V. Makarikhin (2001), Palaeoproterozoic magnesite: lithological and isotopic evidence for playa/sabkha environments, Sedimentology, 48 (2), 379-397.
- Metz, B., O. Davidson, H. C. De Corninck, M. Loos, and L. A. e. Meyer (2005), IPCC Special Report on Carbon Dioxide Capture and Storage, Cambridge University Press, Cambridge, United Kingdom and New York, NY, USA, 442.
- Midgley, H. G. (1951) "A serpentine mineral from Kennack Cove, Lizard, Cornwall" Mineralogical Magazine, 29, 4.
- Millero, F. J. (1996), Chemical Oceanography, 469 pp., CRC Press, Boca Raton, FL.
- Muir, I. J., and H. W. Nesbitt (1997) "Reactions of aqueous anions and cations at the labradorite-water interface: Coupled effects of surface processes and diffusion" Geochimica Et Cosmochimica Acta, 61 (2), 265-274.
- Mullin, J. W. (1961 (2001)) Crystallization, 4th 2001 ed., Butterworth Heinemann.
- Munz, I. A., J. Kihle, O. Brandvoll, I. Machenbach, J. W. Carey, T. A. Haug, H. Johansen, and N. Eldrup (2009) "A continuous process for manufacture of magnesite and silica from olivine, CO(2) and H_2O" Greenhouse Gas Control Technologies 9, 1(1), 4891-4898.
- Murphy, W. M., E. H. Oelkers, and P. C. Lichtner (1989) "Surface-reaction versus diffusion control of mineral dissolution and growth-rates in geochemical processes" Chemical Geology, 78 (3-4), 357-380.
- O'Connor, W. K., D. C. Dahlin, D. N. Nilsen, G. E. Rush, R. P. Walters, and P. C. Turner (2001), CO_2 storage in solid form: A study of direct mineral carbonation, 322-327 pp.
- O'Connor, W. K., C. L. Dahlin, D. N. Nilsen, S. J. Gerdemann, G. E. Rush, L. R. Penner, R. P. Walters, and P. C. Turner (2002) "Continuing studies on direct aqueous mineral carbonation for CO_2 sequestration" in 27th International Technical Conference on Coal Utilisation & Fuel Systems, edited, p. 13, Clearwater, Florida.
- Oelkers EH, Gislason SR, Matter J (2008) "Mineral Carbonation of CO_2" Elements 4 (5):333-337 doi:10.2113/gselements.4.5.333

- Oelkers, E. H. (2001) "General kinetic description of multioxide silicate mineral and glass dissolution" Geochimica Et Cosmochimica Acta, 65 (21), 3703-3719.
- Oelkers, E. H., and J. Schott (2001) "An experimental study of enstatite dissolution rates as a function of pH, temperature, and aqueous Mg and Si concentration, and the mechanism of pyroxene/pyroxenoid dissolution" Geochimica Et Cosmochimica Acta, 65 (8), 1219-1231.
- Oelkers, E. H., S. V. Golubev, C. Chairat, O. S. Pokrovsky, and J. Schott (2009) "The surface chemistry of multi-oxide silicates" Geochimica Et Cosmochimica Acta, 73 (16), 4617-4634.
- O'Hanley, D. S., J. V. Chernosky, and F. J. Wicks (1989) "The stability of lizardite and chrysotile" Canadian Mineralogist, 27, 483-493.
- O'Neil, J. R., and I. Barnes (1971) "C^{13} and O^{18} compositions in some fresh water carbonates associated with ultramafic rocks and serpentinites-Western United States" Geochimica et Cosmochimica Acta, 35 (7), 687-697.
- Olajire, A. A. (2013) "A review of mineral carbonation technology in sequestration of CO_2", Journal of Petroleum Science and Engineering, 109, 364-392.
- Olsson, J., N. Bovet, E. Makovicky, K. Bechgaard, Z. Balogh, and S. L. S. Stipp (2012) "Olivine reactivity with CO_2 and H_2O on a microscale: Implications for carbon sequestration" Geochimica Et Cosmochimica Acta, 77, 86-97.
- Ostwald, W. (1897) "Studien uber die Bildung und Umwandlung fester Korper" Zeitschrift fuer physikalische Chemie, XXII.
- Page, N. J. (1968) "Chemical difference among the serpentine polymorphs" The American Mineralogist, 53.
- Park, A. H. A., and L. S. Fan (2004) "CO_2 mineral sequestration: physically activated dissolution of serpentine and pH swing process" Chemical Engineering Science, 59 (22-23), 5241-5247.
- Parkhurst, D. L. and Appelo C. A. J. (1999) User's guide to PHREEQC (Version 2): a computer program for speciation, batch-reaction, one-dimensional transport, and inverse geochemical calculations. Water-Resources Investigation Report. US Geological Survey.
- Paukert AN, Matter JM, Kelemen PB, Shock EL, Havig JR (2012) "Reaction path modeling of enhanced *in situ* CO_2 mineralization for carbon sequestration in the peridotite of the Samail Ophiolite, Sultanate of Oman" Chemical Geology 330:86-100
- Pauling, L. (1930) "The structure of the chlorites" Proceedings of the National Academy of Sciences of the United States of America, 16 (9), 578-582.
- Pasquier, L.-C., G. Mercier, J.-F. Blais, E. Cecchi, and S. Kentish (2014) "Reaction Mechanism for the Aqueous-Phase Mineral Carbonation of Heat-Activated Serpentine at Low Temperatures and Pressures in Flue Gas Conditions" Environmental Science & Technology, 48 (9), 5163-5170.
- Petit JR, Basile I, Leruyuet A, Raynaud D, Lorius C, Jouzel J, Stievenard M, Lipenkov VY, Barkov NI, Kudryashov BB, Davis M, Saltzman E, Kotlyakov V (1997) Four climate cycles in Vostok ice core. Nature 387(6631):359-360 doi:10.1038/387359a0
- Pfaff, F. W. (1894) "Beitrage zur Erklarung uber die Entstehung des Magnesits und Dolomits" Neues Jahrbuch Fur Mineralogie-Abhandlungen, IX, 485-507.
- Plumper, O., A. Royne, A. Magraso, and B. Jamtveit (2012) "The interface-scale mechanism of reaction-induced fracturing during serpentinization" Geology, 40 (12), 1103-1106.

- Pouchou, J. L., F. Pichoir, and D. Bovin (1990), The XPP procedure applied to quantitative EDS X-ray analysis in the SEM, in Microbeam analysis, edited by J. R. Michael and P. Ingram, pp. 120-126, San Francisco Press, San Francisco.
- Power, M. R., R. K. Shail, A. C. Alexander, and P. W. Scott (1997) "Alteration and vein mineralisation within the Lizard complex, south Cornwall: Constraints on the timing of serpentinisation" in Proceedings of the Ussher Society, Vol 9, Pt 2 - 1997, edited by B. J. Williams, pp. 188-194.
- Power, I. M., S. A. Wilson, J. M. Thom, G. M. Dipple, J. E. Gabites, and G. Southam (2009) "The hydromagnesite playas of Atlin, British Columbia, Canada: A biogeochemical model for CO_2 sequestration" Chemical Geology, 260(3-4), 286-300.
- Power, I. M., G. M. Dipple, and G. Southam (2010) "Bioleaching of Ultramafic Tailings by Acidithiobacillus spp. for CO_2 Sequestration" Environmental Science & Technology, 44 (1), 456-462.
- Power IM, Harrison AL, Dipple GM, Wilson SA, Kelemen PB, Hitch M, Southam G (2013) "Carbon Mineralization: From Natural Analogues to Engineered Systems" In: DePaolo DJ, Cole DR, Navrotsky A, Bourg IC (eds) Geochemistry of Geologic CO_2 Sequestration, vol 77. pp 305-360
- Prichard, H. M. (1979) "A petrographic study of the process of serpentinisation in ophiolites and the ocean crust" Contributions to Mineralogy and Petrology, 68 (3), 231-241.
- Prigiobbe, V., and M. Mazzotti (2013) "Precipitation of Mg-carbonates at elevated temperature and partial pressure of CO_2" Chemical Engineering Journal, 223, 755-763.
- Prigiobbe, V., M. Haenchen, M. Werner, R. Baciocchi, and M. Mazzotti (2009) "Mineral carbonation process for CO_2 sequestration" Greenhouse Gas Control Technologies 9, 1 (1), 4885-4890.
- Pundsack, F. L., and N. J. Somerville (1967) "Recovery of silica, iron oxide and magnesium carbonate from the treatment of serpentine with ammonium bisulfate" United States Patent Office.
- Putnis, A. (2009) "Mineral replacement reactions" in Reviews in Mineralogy & Geochemistry, pp. 87-124.
- Radoslovich, E. V. (1963) "The cell dimensions and symmetry of layer-lattice silicates" Interatomic forces., American Mineralogist, 48, 76-99.
- Rao, K. V., D. Purushottam, and D. Vaidyanadham (1975) "Uptake of fluoride by serpentine" Geochimica Et Cosmochimica Acta, 39 (10), 1403-1411.
- Reddy, K. J., S. John, H. Weber, M. D. Argyle, P. Bhattacharyya, D. T. Taylor, M. Christensen, T. Foulke, and P. Fahlsing (2011) "Simultaneous capture and mineralization of coal combustion flue gas carbon dioxide CO_2" 10th International Conference on Greenhouse Gas Control Technologies, 4, 1574-1583.
- Rice, N. M., and L. W. Strong (1974) "The leaching of lateritic nickel ores in hydrochloric acid" Canadian Metallurgical Quarterly, 3.
- Royne, A., P. Meakin, A. Malthe-Sorenssen, B. Jamtveit, and D. K. Dysthe (2011) "Crack propagation driven by crystal growth" Europhysics Letter 96 (2).
- Rucklidge, J. C., and J. Zussman (1965) "The crystal structure of the serpentine mineral, lizardite $Mg_3Si_2O_5(OH)_4$" Acta Crystallographica, B25, 925-946.
- Ruiz-Agudo, E., C. V. Putnis, C. Rodriguez-Navarro, and A. Putnis (2012) "Mechanism of leached layer formation during chemical weathering of silicate minerals" Geology, 40 (10), 947-950.
- Sandvik, K. L., R. A. Kleiv, and T. A. Haug (2011) "Mechanically activated minerals as a sink for CO_2" Advanced Powder Technology, 22 (3), 416-421.

- Sanna, A., M. Dri, and M. Maroto-Valer (2013) "Carbon dioxide capture and storage by pH swing aqueous mineralisation using a mixture of ammonium salts and antigorite source" Fuel, 114, 153-161.
- Sanna A, Wang X, Lacinska A, Styles M, Paulson T, Maroto-Valer MM (2013) "Enhancing Mg extraction from lizardite-rich serpentine for CO_2 mineral sequestration" Minerals Engineering, 49, 135-144
- Sanna A, Lacinska A, Styles M, Maroto-Valer MM (2014) "Silicate rock dissolution by ammonium bisulphate for pH swing mineral CO_2 sequestration" Fuel Processing Technology, 120, 128-135
- Schaef, H. T., B. P. McGrail, and A. T. Owen (2011) "Basalt Reactivity Variability with Reservoir Depth in Supercritical CO_2 and Aqueous Phases" 10th International Conference on Greenhouse Gas Control Technologies, 4, 4977-4984.
- Scholtzova, E., and L. Smrcok (2005) "On local structural changes in lizardite-1T: $\{Si^{4+}/Al^{3+}\}$, $\{Si^{4+}/Fe^{3+}\}$, Mg^{2+}/Al^{3+} , Mg^{2+}/Fe^{3+} substitutions" Physics and Chemistry of Minerals, 32(5-6), 362-373.
- Schott, J., and E. H. Oelkers (1995), "Dissolution and crystallization rates of silicate minerals as a function of chemical affinity." Pure and Applied Chemistry, 67(6), 903-910.
- Schott, J., O. S. Pokrovsky, and E. H. Oelkers (2009) "The Link Between Mineral Dissolution/Precipitation Kinetics and Solution Chemistry" in Thermodynamics and Kinetics of Water-Rock Interaction, edited by E. H. Oelkers and J. Schott, pp. 207-258.
- Schott, J., and E. H. Oelkers (1995) Dissolution and crystallization rates of silicate minerals as a function of chemical affinity Pure and Applied Chemistry, 67(6), 903-910.
- Schulze, R. K., M. A. Hill, R. D. Field, P. A. Papin, R. J. Hanrahan, and D. D. Byler (2004) "Characterization of carbonated serpentine using XPS and TEM" Energy Conversion and Management, 45(20), 3169-3179.
- Shoval, S., Y. Ginott, and Y. Nathan (1991) A new method for measuring the crystallinity index of quartz by infrared-spectroscopy" Mineralogical Magazine 55 (381), 579-582.
- Seifritz, W. (1990) "CO_2 disposal by means of silicates" Nature, 345, 486.
- Serna, C. J., J. L. White, and B. D. Velde (1979) "The effect of aluminium on the infra-red spectra of 7A trioctahedral minerals" Mineralogical Magazine, 43, 141-148.
- Siever, R., and N. Woodford (1979) "Dissolution kinetics and the weathering of mafic minerals" Geochimica Et Cosmochimica Acta, 43(5), 717-724.
- Sipila, J., S. Teir, and R. Zevenhoven (2008) "Carbon dioxide sequestration by mineral carbonation_Literature review update 2005-2007". Faculty of technology, Åbo Akademi University report 2008-1
- Smyth, J. C. H. (1913) "The relative solubilities of the chemical constituents of rocks" The Journal of Geology, 21 (2), 15.
- Stephen, A. L., G. R. T. Jenkin, M. T. Styles, D. J. Smith, J. Naden, A. J. Boyce, M. J. Leng, and I. L. Millar (2013) "Tracing carbon: natural mineral carbonation and the incorporation of atmospheric vs recycled CO_2" Energy Procedia, 37, 5897 - 5904.
- Streckeisen, A. L. (1973), Plutonic rocks. Classification and nomenclature recommended by the IUGS. Subcommission on the systematics of igneous rocks, Geotimes, 18(no 10), 4.
- Styles, M. T., and G. A. Kirby (1980) "New investigations of the Lizard complex, Cornwall, England and a discussion of an ophiolite model" in Proceedings of the International Ophiolite Symposium, Cyprus, 1979, edited.
- Styles, M. T., A. Sanna, A. M. Lacinska, J. Naden, and M. Maroto-Valer (2014) "The variation in composition of ultramafic rocks and the effect on their suitability for carbon

dioxide sequestration by mineralization following acid leaching" Greenhouse Gases-Science and Technology, 4(4), 440-451.

- Swanson, E. J., K. J. Fricker, M. Sun, and A.-H. A. Park (2014) "Directed precipitation of hydrated and anhydrous magnesium carbonates for carbon storage" Physical chemistry chemical physics: PCCP, 16(42), 23440-23450.
- Swoboda-Colberg, N. G., and J. I. Drever (1993), "Mineral dissolution rates in plot-scale field and laboratory experiments" Chemical Geology, *105*(1-3), 51-69.
- Tans P, Keeling R (2014) Mauna Loa, NOAA/ESRL data.
- Teir, S., H. Revitzer, S. Eloneva, C.-J. Fogelholm, and R. Zevenhoven (2007) "Dissolution of natural serpentinite in mineral and organic acids" International Journal of Mineral Processing, 83 (1-2), 36-46.
- Huifang, X., M. Zhou, F. zhang, H. Konishi, Z. Shen, H. Teng (2013) "Interface induced carbonate mineralization: a fundamental geochemical process relevant to carbon sequestration" The George Washington University Technical Report, DOE-EW-0-01929 27DT
- Thompson, C. J., J. S. Loring, K. M. Rosso, and Z. Wang (2013) "Comparative reactivity study of forsterite and antigorite in wet supercritical CO_2 by *in situ* infrared spectroscopy" International Journal of Greenhouse Gas Control, 18, 246-255.
- Tokunaga, T. K., and J. Wan (2013) "Capillary Pressure and Mineral Wettability Influences on Reservoir CO_2 Capacity" in Geochemistry of Geologic CO_2 Sequestration, edited by D. J. DePaolo, D. R. Cole, A. Navrotsky and I. C. Bourg, pp. 481-503.
- Uibu, M., R. Kuusik, L. Andreas, and K. Kirsimaee (2011) "The CO_2-binding by Ca-Mg-silicates in direct aqueous carbonation of oil shale ash and steel slag" 10th International Conference on Greenhouse Gas Control Technologies, 4, 925-932.
- Van Essendelft, D. T. (2008) "Kinetics of the acid digestion of serpentine with concurrent grinding for the purpose of carbon dioxide sequestration" The Pennsylvania State University, PhD Thesis.
- Van Noort, R., C. J. Spiers, M. R. Drury, and M. T. Kandianis (2013) "Peridotite dissolution and carbonation rates at fracture surfaces under conditions relevant for *in situ* mineralization of CO_2" Geochimica Et Cosmochimica Acta, 106, 1-24.
- Vaneldik, R., and D. A. Palmer (1982) "Effects of pressure on the kinetics of the dehydration of carbonic acid and the hydrolisis of CO_2 in aqueous solution" Journal of Solution Chemistry, 11 (5), 339-346.
- Viti, C. (2010) "Serpentine minerals discrimination by thermal analysis" American Mineralogist, 95 (4), 631-638.
- Viti, C., and M. Mellini (1997) "Contrasting chemical compositions in associated lizardite and chrysotile in veins from Elba, Italy" European Journal of Mineralogy, 9 (3), 585-596.
- Wagner, M. (2009) "Thermal Analysis in Practice" Mettler Toledo Collected Applications.
- Walters, A. S., K. M. Goodenough, H. S. R. Hughes, N. M. W. Roberts, A. G. Gunn, J. Rushton, and A. Lacinska (2013) "Enrichment of rare earth elements during magmatic and post magmatic processes: a case study from the Loch Loyal Syenite Complex, northern Scotland" Contributions to Mineralogy and Petrology, 166, 1177-1202.
- Wang, X., and M. M. Maroto-Valer (2011) "Dissolution of serpentine using recyclable ammonium salts for CO2 mineral carbonation" Fuel, 90 (3), 1229-1237.
- Ward, D. B., and P. V. Brady (1998) "Effect of Al and organic acids on the surface chemistry of kaolinite" Clays and Clay Minerals, 46(4), 453-465.
- Weissbart, E. J., and J. D. Rimstidt (2000) "Wollastonite: Incongruent dissolution and leached layer formation" Geochimica Et Cosmochimica Acta, 64 (23), 4007-4016.

- Werner, M., S. B. Hariharan, A. V. Bortolan, D. Zingaretti, R. Baciocchi, and M. Mazzotti (2013), "Carbonation of activated serpentine for direct flue gas mineralization" International Journal of Greenhouse Gas Control *11*, *37*, 5929-5937.
- Westrich, H. R., R. T. Cygan, W. H. Casey, C. Zemitis, and G. W. Arnold (1993) "The dissolution kinetics of mixed-cation orthosilicate minerals" American Journal of Science, 293(November), 869-893.
- Whittaker, E. J., and J. Zussman (1956) "The characterisation of serpentine minerals by X-ray diffraction" Mineralogical Magazine, 31, 107-126.
- Wicks, F. J., and E. J. W. Whittaker (1975) "A reappraisal of the structures of the serpentine minerals" Canadian Mineralogist, 13, 227-243.
- Wicks, F. J., M. C. Corbeil, M. E. Back, and R. A. Ramik (1995) "Microbeam X-ray diffraction in the analysis of minerals and materials" Canadian Mineralogist, 33, 313-322.
- Wicks, F. J. (2000) "Status of the reference X-ray powder-diffraction patterns for the serpentine minerals in the PDF database – 1997" Powder Diffraction, 15(1), 42-50.
- Wicks, F. J., and E. J. Chatfield (2005) "Scrolling of thin crystals of lizardite: An expression of internal stress" Canadian Mineralogist, 43, 1993-2004.
- Wieland, E., and W. Stumm (1992) "Dissolution kinetics of kaolinite in acidic aqueous solutions at 25°C" Geochimica Et Cosmochimica Acta, 56(9), 3339-3355.
- Wilson, S. A., M. Raudsepp, and G. M. Dipple (2006) "Verifying and quantifying carbon fixation in minerals from serpentine-rich mine tailings using the Rietveld method with X-ray powder diffraction data" American Mineralogist, 91 (8-9), 1331-1341.
- Wogelius, R. A., and J. V. Walther (1991) "Olivine dissolution at 25°C – effects of pH, CO_2, and organic acids" Geochimica Et Cosmochimica Acta, 55 (4), 943-954.
- Wolf, G. H., A. V. G. Chizmeshya, J. Diefenbacher, and M. J. McKelvy (2004) "*In situ* observation of CO_2 sequestration reactions using a novel microreaction system" Environmental Science & Technology, 38 (3), 932-936.
- Yan, H., J. Zhang, Y. Zhao, and C. Zheng (2013) "CO_2 Sequestration from flue gas by direct aqueous mineral carbonation of wollastonite" Science China-Technological Sciences, 56 (9), 2219-2227.
- Yariv, S., and L. Heller-Kallai (1975) "The relationship between the infrared spectra of serpentinites and their structures" Clays and Clay Minerals, 23, 145-152.
- Yoo, K., B.-S. Kim, M.-S. Kim, J.-c. Lee, and J. Jeong (2009) "Dissolution of Magnesium from Serpentine Mineral in Sulfuric Acid Solution" Materials Transactions, 50 (5), 1225-1230.
- Ziomek-Moroz, M., W. K. O'Connor, and S. Bullard (2012) "Investigations of localized corrosion of stainless steel after exposure to supercritical CO_2" Corrosion, Paper C2012-0001597.